Electronic Thesis and Dissertation Repository

6-16-2017 12:00 AM

Morphological Bedload Transport in Gravel-Bed Braided Rivers

Sarah E. K. Peirce, *The University of Western Ontario*

Supervisor: Dr. Peter Ashmore, *The University of Western Ontario*
A thesis submitted in partial fulfillment of the requirements for the Doctor of Philosophy degree in Geography
© Sarah E. K. Peirce 2017

Abstract

Gravel-bed braided rivers, defined by their multi-thread planform and dynamic morphology, are commonly found in proglacial mountainous areas. With little cohesive sediment and a lack of stabilizing vegetation, the dynamic morphology of these rivers is the result of bedload transport processes. Yet, our understanding of the fundamental relationships between channel form and bedload processes in these rivers remains incomplete. For example, the area of the bed actively transporting bedload, known as the active width, is strongly linked to bedload transport rates but these relationships have not been investigated systematically in braided rivers. This research builds on previous research to investigate the relationships between morphology, bedload transport rates, and bed-material mobility using physical models of braided rivers over a range of constant channel-forming discharges and event hydrographs. Morphology changes were estimated using the morphological method, which infers information from changes in channel topography over time, from an extensive dataset of digital elevation models (DEMs) generated using digital photogrammetry and 'Structure-from-Motion' principles. Results suggest that the active width is highly variable even at constant discharge but increases with stream power and is positively related to bedload transport rates, bulk change (i.e., total volume of erosion and deposition), and active braiding intensity. Morphologically-derived sediment budgets provided reasonable estimates of bedload transport rates that were similar to independent measurements of bedload transport rates from sediment baskets. In addition, grain size distributions and bed mobility evolved from a state of partial mobility towards equal mobility with increasing discharge. This is rare in most gravel-bed rivers, but in braided rivers the high levels of sediment supply and lack of armouring allow for greater mobility of the channel bed and subsurface. Finally, the lower detection threshold for the morphological active width, bedload transport, and transition to selective mobility all coincided with a dimensionless stream power of ~0.08. Overall, these results suggest that while braided rivers are dynamic, they may be restricted in ways like their single-threaded counterparts so that measures of morphology (i.e., the active width) can be used as general predictors of bedload transport rates and the morphological stability of the river. This knowledge contributes to our overall understanding of braided river

morphodynamics while also building on theory for use in applied geomorphology and engineering practices for the management, conservation, and restoration of complex braided rivers systems.

Keywords

Acknowledgements

I would first like to acknowledge and thank my thesis advisor, Dr. Peter Ashmore. I am grateful your guidance, patience, wisdom, and general love of braided rivers.

Along with my advisor, I would like to thank all of those who had a direct hand in making this Ph.D. possible. Dr. Pauline Leduc, whose brilliant ideas on physical modelling and coding made it possible collect (and process) the rather ridiculous amount of data that was measured in the flume. Furthermore, your guidance and friendship was truly invaluable throughout my Ph.D. experience. I also want to thank Lara Middleton, who spent endless hours in the flume, in the dark, collecting data with me. Thank you for your help, friendship, and of course, for your enthusiasm for braided rivers. Thank you Danie Barr for everything, but especially for all of your support throughout the last two years. I also want to extend my gratitude to Dr. Matidle Welber for sharing her wisdom about statistics, flumes, and cooking with me.

Thank you to all of those who came to the flume to help out including Erika Hill, Sarah McFadden, Cliff Davidson, Clayton Cook, Chris Vandelaar, and in particular Cody Ruthman, who often came at a moment's notice to save the day! I also want to thank Dr. Darren Sjogren, Dr. Joe Wheaton, Wally Macfarlane, and Dr. Chris Hugenholtz for their help and experience in the field.

I would like to thank Dr. Andy Binns, Dr. Marco Van De Wiel, Dr. Adam Yates, Dr. Katrina Moser, and Dr. Cheryl McKenna-Neuman for taking the time to challenge me as part of my thesis and examination committees. A special thank you to Dr. Desmond Moser, my second reader, for your time and feedback on my manuscript. Thank you to all of the wonderful staff at the university including Lori Johnson, Joe Smrekar, Karen Vankerkoerle, Kathy Tang, Angelica Lucaci, and Rita Mendis-Mogenson for all of your help.

Last but not least, I want to thank my family and friends for their continued love and support throughout these last few years. Like so many other graduate students I can honestly say that my Ph.D. experience did not go exactly as planned, but I am so lucky to

have people encourage me to just keeping going. Thank you to my mom and brother, Michael, I could not have done this without you. I also want to thank my Dad, whom I miss every day, for bestowing on me a love of learning and teaching that helped make this journey possible. Finally, I want to thank my husband, Aaron. I am not sure I can even find the words to express my gratitude to you but we both know I would not be submitting this thesis if it wasn't for your unwavering love and support. Thank you for everything.

Table of Contents

List of Tables

List of Figures

List of Notations

Symbol	Definition	Units
b	average wetted width	m
Q_i	bedload input	g s^{-1}
Q_o	bedload output	g s^{-1}
Q_b	bedload transport rate	g s^{-1}
γ_s	bulk density of sediment	kg m^{-3}
D_{90L}	D_{90} of the bedload	mm, m
D_{90S}	D_{90} of the subsurface	mm, m
qb*	dimensionless bedload flux	
w*	dimensionless stream power	
Q	discharge	l s^{-1} or m^3 s^{-1}
H	Water height	cm, m
d	Flow depth	cm, m
Fr	Froude number	
Re*	grain Reynolds number	
D_x	grain size	mm, m
g	gravitational constant	m s^{-1}
Rh	hydraulic radius	m
v	kinematic viscosity	m^2 s^{-1}
$\bar{x}$	mean	
U	mean velocity	m s^{-1}
δS	net change	m^3
L_t	path length	m
ρ_s	particle density	kg m^{-3}
L_r	reach length	m
Δ	relative submerged weight	
τ	shear stress	N m^{-2}
u*	shear velocity	m s^{-1}

ϑ	Shields parameter	
S	slope	
γ	specific weight of water	kN m^{-3}
σ	standard deviation	
SE	standard error of the estimate	
D*	subsurface D_{50}/bedload D_{50}	
t	time	s, min, h
Ω	total stream power	W m^{-1}
V_d	volume of deposition	m^3
V_e	volume of erosion	m^3
ρ	water density	kg m^{-3}

Chapter 1

1 Introduction

1.1 Thesis Format and Research Objectives

1.1.1 Thesis Rationale

High-energy, multi-thread, or braided, rivers in Canada and around the world have been subject to human interference through flow regulation, gravel-extraction, channelization, and changing flow regimes following land-use changes. These changes can result in flooding, damage to infrastructure, and reduction in ecological functioning. Given these major changes there has been increasing regulatory pressure to better manage and restore morphological and ecological functioning to braided rivers. For these management initiatives to be successful, they will require an understanding of gravel-bed river dynamics for improved channel design and prediction of future morphologies under altered flow and sediment regimes. Specifically, the reliable prediction of sediment transport as bedload will be central to any application of fluvial geomorphology to river hazard assessment, long-term management, conservation, and restoration. However, methods for predicting bedload transport based on conventional hydraulic sediment transport theory may perform poorly or are difficult to apply in braided rivers because of their complex, unstable, and multi-channeled morphology. Furthermore, traditional methods don't account for important spatial and temporal interactions between channel morphodynamics and bedload transport. Therefore, our current understanding of the relationships between braided river form and processes remains incomplete.

1.1.2 Purpose and Methodological Background

As an alternative to traditional hydraulics-based formula and sampling techniques, the morphological, or inverse, method infers information about bedload transport rates from changes in channel topography over time (Ashmore & Church, 1998). By focusing on changes in river topography and morphology, the morphological method allows for greater insight into the spatial and temporal patterns of bedload transport and channel change. The morphological method has become increasingly popular in the past decade due to

improvements in technologies used for collecting topographic data, such as digital photogrammetry, GPS, and terrestrial laser scanning, which allow data to be collected at high spatial and temporal resolutions (Brasington et al., 2003; Rumsby et al., 2008). In addition, software to process high-resolution topographic data has become increasingly user-friendly, inexpensive, and efficient (Brasington & Smart, 2003). As a result, it is now possible to investigate ideas and theories about the morphodynamics of braided river systems in more detail than ever before in both the field and the laboratory.

This research uses measurements of morphological change and bedload in gravel-bed braided rivers to investigate important relationships between channel form and process. For example, previous research has suggested that the morphological active width, defined by the overall river area actively transporting bedload, is related to hydraulic and morphological parameters, including dimensionless stream power and active braiding intensity. Yet, these relationships have not been investigated systematically or over a range of river morphology (Bertoldi et al., 2009a; Ashmore et al., 2011). In addition, while the morphological method has been used to create morphological sediment budgets, few studies have characterized the spatial and temporal variability of those budgets over a range of stream power. Finally, few studies have looked at the linkages between channel morphology, bedload transport, and the evolution of grain size distributions in braided rivers.

Therefore, the general objective of this research was to further our knowledge of gravel-bed braided river morphodynamics by characterizing the relationships between the morphological active width, bedload transport rates, and bedload grain size distributions over a range of discharge and stream power. The research used physical models of gravel-bed braided rivers to control formative conditions (discharge, slope, and grain size), allow for high-resolution measurement of channel topography and bedload transport rate, and extend results from previous physical model experiments on gravel-bed braided river morphodynamics (Ashmore, 1991b; Paola et al., 2009; Bennett et al., 2015).

1.1.3 Thesis Format and Research Objectives

This thesis is written in a monograph format so that the core chapters address discrete research objectives but all are focused on the general theme of linking bedload transport

processes and morphological change in gravel-bed braided rivers. As such, there is a global literature review (Chapter 2) and methods chapter (Chapter 3) followed by three results chapters, each addressing specific research objectives and questions, outlined below (Chapters 4-6). The conclusion (Chapter 7) provides a summary and integration of the main findings as well as a discussion about additional research prospects.

Specific research questions and hypotheses are given in each of the main results chapters but the overall aims of this research can be summarized by the following objectives:

1. Quantify the morphological active width in a physical model over a range of gravel-bed river morphologies and characterize its relationship with wetted width, braiding indices, and dimensionless stream power for a range of flow conditions (Chapter 4).
2. Characterize the relationship between the active width and bedload transport flux under channel forming conditions and variable discharge conditions (Chapter 4).
3. Calculate the morphological sediment budget for gravel-bed braided rivers over a range of stream power conditions with a known sediment output and under minimum budget conditions (Chapter 5).
4. Investigate the spatial and temporal dynamics of bedload transport in experimental gravel-bed braided rivers using morphological methods (Chapter 5).
5. Characterize the evolution of bedload grain size distributions across three experimental hydrographs, including fractional transport rates (Chapter 6).
6. Characterize the range of bed mobility conditions in terms of partial, selective, or equal mobility over three experimental hydrographs in a gravel-bed braided river (Chapter 6).

Chapter 2

2 Background

2.1 Conditions for Braiding in Gravel-Bed Rivers

Braided rivers are characterized by multiple channels separated by mid-channel bars, often called braid bars (Ashmore, 2013) (Figure 2.1). The braided river planform and bed topography is dynamic and modifications to channel pattern geometry, bar form, and the number of individual channels, or anabranches, can occur within only a few hours under high flow conditions (Wheaton et al., 2013). Braiding occurs in a variety of environmental conditions, but it is often found in proglacial mountainous areas, alluvial fans, and lower gradient coastal and continental plains that are abundant in non-cohesive sand and gravel (Ashmore, 2013). While braided rivers often include a wide range of bed material sizes from sand (< 2 mm) to boulder (> 64 mm), they are often classified as sand-bed or gravel-bed, where the finer-grained sand-bed rivers are defined as having less than 25% gravel on the bed (Bristow & Best, 1993). In general, braided rivers are more common in gravel than sand, possibly due to differences in bedload transport rates and vegetation coverage, and therefore will be the focus of this thesis (Kleinhans & van den Berg, 2011).

Figure 2.1 – Sunwapta River in Alberta, Canada, a proglacial, gravel-bed braided river. Arrow indicates flow direction.

In general, the conditions necessary for braiding include a high sediment supply of coarse bedload, non-cohesive erodible banks, and high total stream power (Ω) relative to particle size:

$$\Omega = \rho g Q S \tag{2.1}$$

where ρ is the mass density of water, g is the acceleration due to gravity, Q is discharge, and S is water surface slope (Robert, 2003; Charlton, 2008; Hicks et al., 2008; Ashmore, 2013). The high bedload transport and erodible banks help maintain the braided river morphology by providing the high level of dynamism (i.e., sediment transport) that prevents the establishment of stabilizing vegetation, both in-channel and in the riparian zones (Gurnell et al., 2012; Wheaton et al., 2013). Erodible banks and lack of vegetation promote lateral migration and channel widening generating the relatively high width-depth ratios important for the development of mid-channel bars (Kleinhans, 2010; Ashmore, 2013; Wheaton et al., 2013). Although some early researchers believed that variable discharge was necessary for braiding, experimental laboratory studies in river flumes have shown that a braided planform can evolve under constant channel-forming discharge conditions (Ashmore, 1982). Discharge variation is, however, still important in determining the character and morphology of a braided river because it can influence the number of anabranch channels present (Egozi & Ashmore, 2009). Furthermore, large floods can completely modify morphology in a relatively short amount of time and can prevent the establishment of vegetation, which further promotes a braided morphology (Ashmore, 2013; Gurnell et al., 2012) (Figure 2.2).
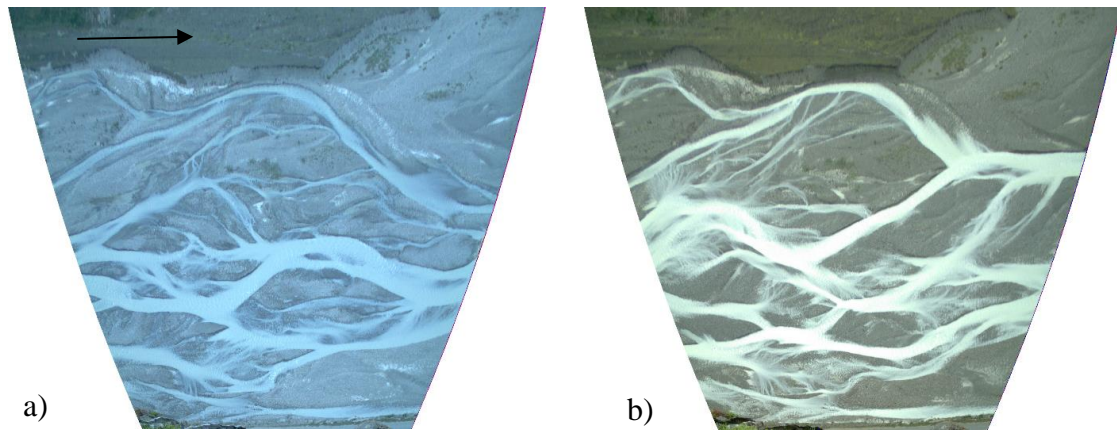
Figure 2.2 – Planform changes over a two-week period in the Sunwapta River between a) July 8, 2012 and b) July 24, 2012. Images taken for similar discharges and the arrow indicates flow direction.

2.2 Morphological Characteristics of Braided Channels

The form, or morphology, of braided rivers is the result of the interactions between flow, bed topography, and bedload transport. The flow hydraulics (i.e., velocity, bed shear stress, and stream power) are responsible for the initiation and maintenance of bedload transport, which is the movement of coarse grains via sliding, rolling, or saltating (i.e., hopping) along the channel bed (Haschenburger, 2013). Bed topography, including microscale and macroscale bedforms, influences flow conditions by determining the nature of local resistance and bed shear stress. Finally, bedload transport contributes to morphology through the creation, migration, and destruction of bedforms and banks (Ashmore, 2013). In multi-thread braided rivers, the interactions between flow and the uneven bed topography result in bed shear stresses that are spatially and temporally variable (Ashworth & Ferguson, 1986; Lane, 1995). Combined with variable sediment supply (either from the bed or upstream), braided channel morphology and bedload transport can be highly dynamic both spatially and temporally, even at constant discharge (Ashworth & Ferguson, 1986; Hoey & Sutherland, 1991; Ashmore, 2007).

Yet, even with their inherent complexity, braided river morphology can still be defined by several characteristic units and processes. These include the individual anabranch channels, bar unit and complex braid bars, confluences and bifurcations, and braiding intensity which

all contribute to the distinctive three-dimensional morphology of braided rivers (Ashmore, 2013; Wheaton et al., 2013) (Figure 2.3).
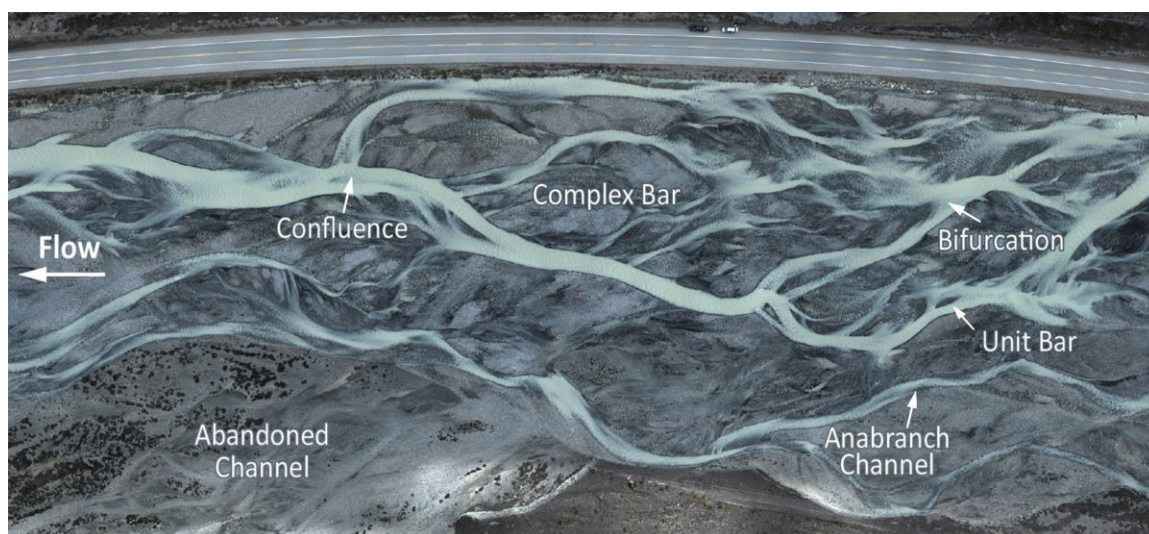
Figure 2.3 – Main morphological characteristics of gravel-bed braided rivers.

2.2.1 Bar Unit

Bars are found in all types of alluvial channels and represent sites of sediment deposition and storage. There are many ways to classify bars, including by sediment composition (sand or gravel), formative processes, location in the channel, and ability to migrate. For example, unit bars are depositional features that have been unmodified by erosion while complex bars are the result of multiple erosional and depositional events (Ashmore, 1988; 2013). Forced bars are those that are fixed into position due to channel configuration and flow conditions (e.g., point bars in meander bends), while free bars can migrate and form spontaneously in response to flow and sediment interactions (Zolezzi et al., 2012). The mid-channel bar, sometimes called a braid bar, is a free complex bar (Figure 2.3) and a distinguishing feature in braided rivers.

The bar unit contributes to the dynamic planform appearance of braided rivers due to their changing role with flow stage. At low flow, bars are exposed and flow is restricted to the multiple anabranches of a braided river. At high flow, however, bars can become submerged, changing the overall planform appearance of the river (Figure 2.4). It is also during this high flow stage that bars are actively formed, aggraded, and mobilized by the

flow. In reality, most braided rivers have exposed bars at high and low discharges (Bristow & Best, 1993).

a)
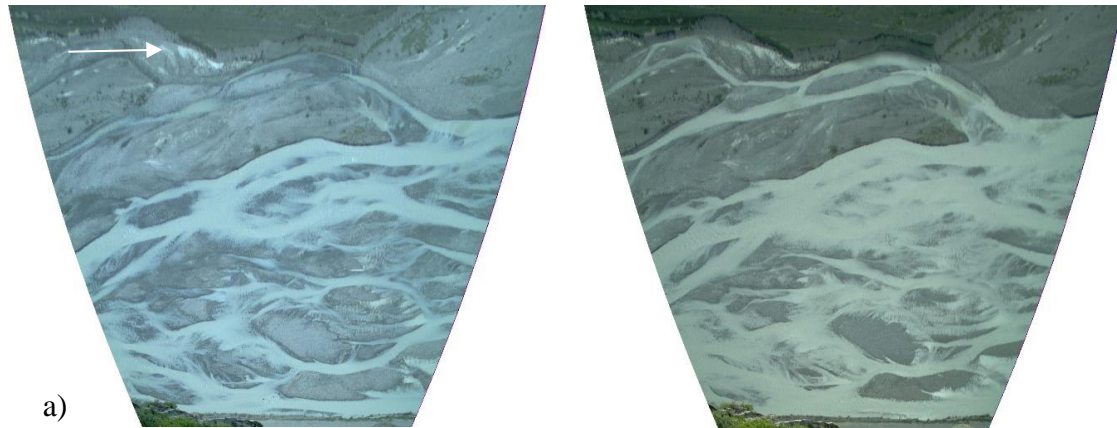
Figure 2.4 – Diurnal changes in planform appearance due to bars at a) low discharge becoming submerged at b) high discharge. Both photos were taken on August 14, 2013 at the Sunwapta River, Alberta, Canada. Arrow indicates flow direction.

While bars are themselves morphological units within alluvial rivers, they can also be considered part of a pool-bar unit. At the upstream end of the pool-bar unit is a deep pool that widens in the downstream direction. Downstream of the pool there is a lobe front that aggrades vertically and downstream so that the downstream edge of the lobe is an exposed bar (Bunte and Abt, 2001) (Figure 2.5). While the exposed bars and pools generally switch from one bank to the other in straight and meandering channels, they can exist in two or more parallel rows in braided channels (Ferguson, 1993). Therefore, each mid-channel bar is contributing to three separate pool-bar units, where the bar head is the end of an upstream bar unit and each side of the bar belong to lateral bar units (Ferguson, 1993) (Figure 2.5). Pools are connected by thalwegs, zones of deepest flow, and in braided channels multiple thalwegs converge and diverge downstream. Thus, individual anabranches can have bends like a meandering channel (Ferguson, 1993; Robert, 2003).
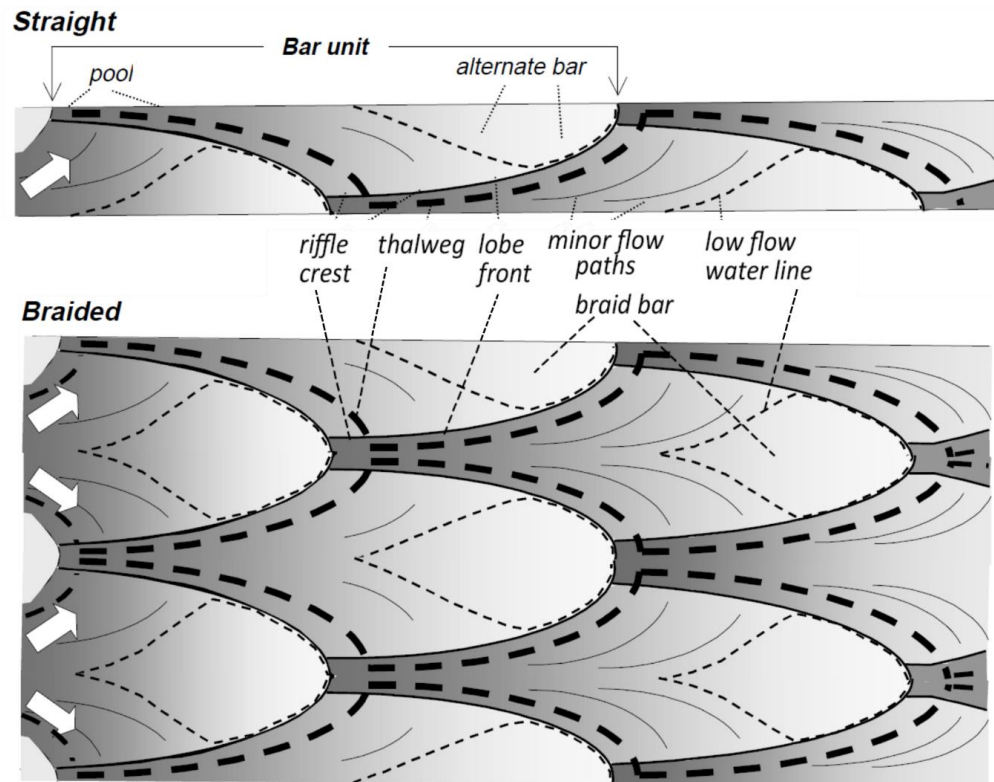
Figure 2.5 – Pool-bar unit in straight and braided alluvial channels. White arrows indicate flow direction and thick black lines represent the thalweg, or zone of deepest water flow. Water depth is represented by the shading so that dark areas indicate deep water and light areas represent bars exposed during low flow. Figure adapted from Bunte and Abt (2001).

Conceptual models of braided river development have described several processes, both depositional and erosional, that are responsible for generating and maintaining mid-channel bars. Originally defined by Ashmore (1991b), the four principle mechanisms of braided channel dynamism are central bar deposition, transverse bar conversion, chute cut-off, and lobe dissection (Ashmore, 1991b; Ferguson, 1993; Wheaton et al., 2013). The central bar deposition and transverse bar conversion are both depositional processes associated with the movement and deposition of a bedload sheets, which are mobile microscale bedforms 1-2 grains thick, and the subsequent growth into mid-channel bars (Ashmore, 1991b; Ferguson, 1993). Chute-cut off and multiple bar dissection are erosional processes related to the development of narrow chute channels over already developed unit and complex bars. Once braiding is initiated there is a positive feedback loop that promotes

the repetition of these main braiding processes (Ashmore, 2013). For example, initial formation of a mid-channel bar results in flow diversion towards outer banks, promoting bank erosion, and increasing the width-depth ratio and the local sediment supply, all of which encourage additional propagation of braid bars downstream (Bristow & Best, 1993) (Figure 2.5). All of the current models for the development of mid-channel bars and braiding morphology involve multiple processes, both erosional and depositional (Wheaton et al., 2013). Overall, the development, erosion, and flow diversion caused by bars all contribute to the complex sediment transport and morphological dynamics in braided rivers (Ferguson, 1993).

2.2.2 Confluences and Bifurcations

Another fundamental feature of a braided channel is the presence of multiple anabranching channels that meet at confluences and separate at diffluences, more commonly called bifurcations (Ashmore, 1991b; Tubino & Bertoldi, 2007) (Figure 2.3). The main characteristics of a braided confluence are 1) the presence of at least two anabranching channels, which can differ in geometry; 2) a scour hole, whose depth and shape are a function of the angles and discharges of the incoming anabranches and; 3) a mid-channel downstream bar (Ashmore, 1993) (Figure 2.6). While these features are common in confluences, not all confluences will have all of these characteristics, and the exact form of each will depend on local flow and sediment conditions (Ashmore & Gardner, 2008).
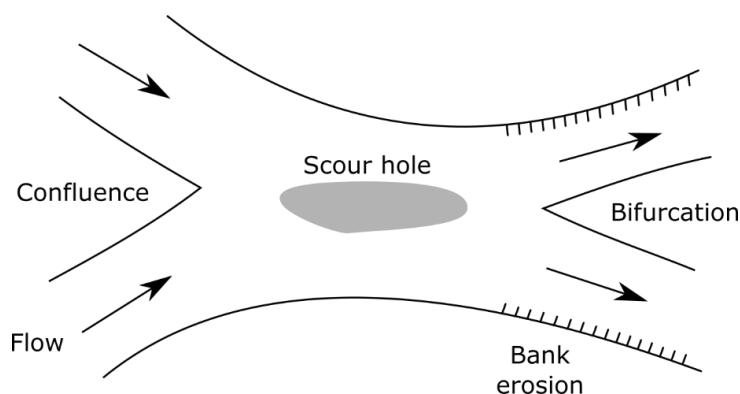
Figure 2.6 – General structure of a confluence-bifurcation unit. Flow (black arrows) from two individual anabranch channels meet at a confluence and create a scour hole. Downstream, the flow is split at a bifurcation diverting water towards the outer bank causing local bank erosion. Image modified from Ashmore (1993).

Research on confluences and bifurcations suggest that these features have a characteristic length that is linearly related to channel width so that the length from the confluence to the head of the downstream bifurcation is approximately four to five times greater than channel width (Hundey & Ashmore, 2009). In addition, studies on sediment transport in confluences suggest that they are areas of increased bedload transport. The maximum transport rate occurs at the downstream end of the erosional scour hole, which is followed by a downstream decrease in shear stress resulting in deposition on the bar (Ashmore, 1993; Ashmore & Gardner, 2008). Therefore, scour holes are a result of the locally high rates of sediment transport that result from confluences (Wheaton et al., 2013). Bifurcations may also contribute to avulsion, or channel switching, when the flow becomes concentrated to one side, choking the other anabranch into abandonment (Ashmore, 1993; Ferguson, 1993) Therefore, the formation, migration, and abandonment of confluences contributes to the spatial and temporal variability in bedload transport and morphology in braided rivers.

2.2.3 Braiding Intensity

Braiding intensity is a measure of the complexity of the braided anabranch network and is considered a fundamental measure of the braided channel pattern morphology (Egozi & Ashmore, 2008). While there are several different braiding indices, one of the most common is the channel count index, which reflects the average number of channels

conveying water based on a series of river transects (Egozi & Ashmore, 2008; Ashmore, 2009).

Egozi & Ashmore (2008) define a total braiding intensity (BI) as the average number of channels with observable water discharge (i.e., "wetted") and the active braiding intensity (ABI) as the number of channels actively transporting bedload. The active braiding intensity is considered important because this subset of the total braiding intensity is responsible for conveying bedload and therefore is strongly related to channel morphodynamics (Egozi & Ashmore, 2008). Experimental results suggest that total braiding intensity reaches a stable average for a given stream power or discharge, although the instantaneous braiding intensity can fluctuate (Ashmore, 2009; Egozi & Ashmore, 2009). In the field, Mosley (1982) found that while depth, velocity, and water surface area all increased with increasing discharge in the Ohau River, a braided river in New Zealand, that new channels emerging at higher discharge helped maintain a relatively stable braiding intensity regardless of discharge. This general rule can be complicated by changes in channel morphology. For example, Ashmore et al. (2011) found that while active braiding intensity generally increased with discharge over an event hydrograph, different channel configurations of the same river resulted in variable active braiding intensity at the same discharge. Therefore, natural variation in braiding intensity results in a measurement precision of ~20% of the mean value in a braided river reach (Egozi & Ashmore, 2008).

Flume experiments suggest that the active braiding intensity correlates positively with dimensionless stream power (ω^*) (Ashmore, 2009; Bertoldi et al., 2009b):

$$\omega^* = \frac{QS}{b\sqrt{g\Delta D_{50}^3}}$$

(2.2)

where Q is discharge, S is slope, D_{50} is mean grain size, Δ is relative submerged density, b is the average wetted width and g is the acceleration due to gravity. By using a dimensionless variable that considers grain size, this measure of stream power allows for comparison between rivers of difference sizes, including physical models (Bertoldi et al., 2009a). Comparing the two braiding intensities, Egozi and Ashmore (2008) found that active braiding intensity responded quickly to changing discharge while total braiding

intensity responded more slowly. The ratio of active channels to total channels (ABI/BI) varies from 0.3 to 0.8 with an average of ~0.5, depending on the dimensionless stream power (Ashmore, 2009; Bertoldi et al., 2009b; Egozi & Ashmore, 2009). The exact reason for the active braiding intensity stabilizing around half of the total braiding intensity is not fully known but may be related to asymmetrical bifurcations. Specifically, bifurcations in gravel-bed braided rivers are often asymmetrical such that while both anabranches convey water, only one remains competent enough to convey bedload (Ashmore, 2009).

These results suggest that the complexity of braided channels is controlled and limited by some measure of slope and discharge (i.e., dimensionless stream power and/or dimensionless discharge), so that total braiding intensity, active braiding intensity, and even the ratio of the two, represent regime properties of braided channels.

2.2.4 Channel Geometry

Hydraulic geometry aims to predict how a river will change its form in response to changing discharge based on the following continuity equation:

$$Q = wdv \tag{2.3}$$

where Q is discharge, w is mean width, d is mean depth, and v is mean velocity (Ferguson, 1986). Leopold and Maddock (1953) applied this idea to single-thread channels and established "at-a-station" and "downstream" (longitudinal) hydraulic geometry relations. At-a-station hydraulic geometry refers to changes in flow width, depth, and velocity at a specific river cross-section as discharge changes over time. The downstream hydraulic geometry considers how channel geometry varies with a given discharge, usually bankfull or an equivalent channel-forming discharge, longitudinally and between rivers (Ferguson, 1986; Dingman, 2009).

Unlike their single-threaded counterparts, multi-thread rivers have a complex and unstable cross-sectional geometry that varies laterally, longitudinally, and temporally (Hoey & Sutherland, 1991; Redolfi et al., 2016). As discussed, some of this dynamism is the result of locally high stream power causing active erosion and deposition of bars and banks (Ferguson, 1993). Furthermore, the presence of confluences and bifurcations causes large, local changes in sediment transport capacity as well as large changes in the cross-sectional

geometry longitudinally. Finally, Hoey & Sutherland (1991) suggest that braided river instability is partially due to the fact that even at the same overall discharge, flow is constantly re-distributed among the individual anabranch channels.

Braided rivers are often characterized by a high width/depth ratio (i.e., greater width than depth), especially compared to their single-threaded counterparts. Recent research by Redolfi et al. (2016) found that unlike single-thread rivers, most changes in discharge in braided rivers are accommodated by changes in channel width, with only slight changes in channel depth. This is supported by Ashmore and Sauks (2006) who found that in general, at-a-station changes in braided river discharge were accommodated by changes in channel width and braiding intensity and that channel depth and velocity remained relatively unchanged. One of the implications of these results is that small reductions in water depth can result in a significant reduction in flow competence and bedload deposition. Downstream hydraulic geometry data for braided rivers show that despite the complex morphology, mean river width and depth as well as the width and depth of individual anabranches vary in a way similar to that of stable, single-threaded channels (Ashmore, 2009). For instance, research in the field and in the laboratory suggest that at the reach scale the statistical properties of braided rivers are controlled by bankfull discharge, slope, and sediment size in a similar way to single-thread channels (Chew & Ashmore, 2001; Ashmore, 2009, 2013; Redolfi et al., 2016). Therefore, for a given slope and grain size, increasing channel-forming discharges will result in greater mean widths and depths as well as an increase in braiding intensity as the river occupies more of the braidplain (Bertoldi et al., 2009b).

The importance of braided river geometry, and how it changes over time, is that it is strongly related to bedload transport processes, both at-a-station and longitudinally. For example, as discharge increases, channel width increases, and therefore a larger area of submerged bed is exposed to shear stresses required for bedload transport (Bristow & Best, 1993; Wheaton et al., 2013; Mueller & Pitlick, 2014). As a result, research suggests that changes in sediment transport may be restricted to specific zones of the channel which are likely a function of the wetted width (Gomez, 1991; Hoey, 1992; Bertoldi et al., 2009a; Mueller & Pitlick, 2014).

2.3 Bedload Transport Processes

Bedload refers to the portion of the total sediment load being transported by a river that moves close to or on the channel bed by sliding, rolling and saltating (Gomez, 1991; Haschenburger, 2013). The initiation of bedload transport is fundamentally the result of the hydraulic force (i.e., shear stress) at the bed (Yager & Schott, 2013).

2.3.1 Active Layers and Phase Flow

The channel bed can be classified into three vertical layers: the exposed surface , the active subsurface, and the inactive subsurface (Haschenburger, 2013; Church & Haschenburger, 2017). Grains can be actively transported from the exposed surface and from the active subsurface as those grains become exposed to the flow. In general, the depth of this active layer (i.e., surface and active subsurface) will increase with discharge (Haschenburger, 2013). Therefore, it is possible to classify bedload transport rates in gravel-bed rivers in terms of two phases. During Phase I, bedload transport rate is low and consists mostly of fine grains moving over a stable bed surface (Ryan et al., 2002). Phase II involves the mobilization of coarser grains from the surface causing grains from the active subsurface to be exposed and entrained. Consequently, Phase II has a significantly greater sediment transport rate and grain size range than Phase I flow (Ryan et al., 2002). As a result, the amount of bedload transported and the size of grains transported will increase with flow but in a non-linear fashion due to local variation in bed shear stress and sediment supply from the active layer (Ashworth & Ferguson, 1986; Haschenburger, 2013).

2.3.2 Bedload Pulses

The changes in bedload transport rate across a particular cross-section over a short period of time is referred to as a bedload pulse (Hoey & Sutherland, 1991; Hoey, 1992). Instantaneous bedload pulses may appear as migrating bedload sheets, and are a result of the stochastic variability in sediment entrainment due to local differences in shear stress (Hoey, 1992). These bedload sheets are often associated with pulses of bedload material migrating downstream and play a very important role in the morphology, surface texture, and sediment sorting pattern in gravel-bed rivers, all of which influence local sediment transport processes (Gomez, 1991; Robert, 2003). As a bedload pulse moves through a

system, it will either be transported (translated), deposited (attenuated) or removed (dissipated), and all of these outcomes can be caused by different conditions (Hoey, 1992). Therefore, some of the streamwise variations in bedload transport rate are in response to temporal variations at-a-point.

The temporal differences in bedload transport at the micro-scale are often associated with the movement of bedload sheets and at a larger scale, related to patterns of scour and fill during rising and falling discharge (Gomez, 1991). In addition, the continuous formation and destruction of bars under flood conditions in braided rivers can also result in bedload pulses in these systems (Hoey, 1992). The presence of bedload pulses due to a variety of braiding processes and morphological dynamism could be one of the reasons that bedload transport in braided rivers is temporally variable even at a constant discharge (Ashmore, 1988; Goff & Ashmore, 1994; Shvidchenko & Kopaliani, 1998). Figure 2.7 highlights that bedload is highly variable at a constant discharge, but that on average it increases with increasing discharge and total stream power (Doeschl et al., 2006). Hoey and Sutherland (1991) found that there was an inverse relationship between channel pattern complexity (total channel length in a reach) and the measured sediment output rate in a model of a gravel-bed braided river. This result could indicate that, even though channel complexity (braiding intensity) increases, bedload transport rate is still restricted to a relatively small area of the bed. This concentrated area of active transport that expands and contracts is also called the active width.
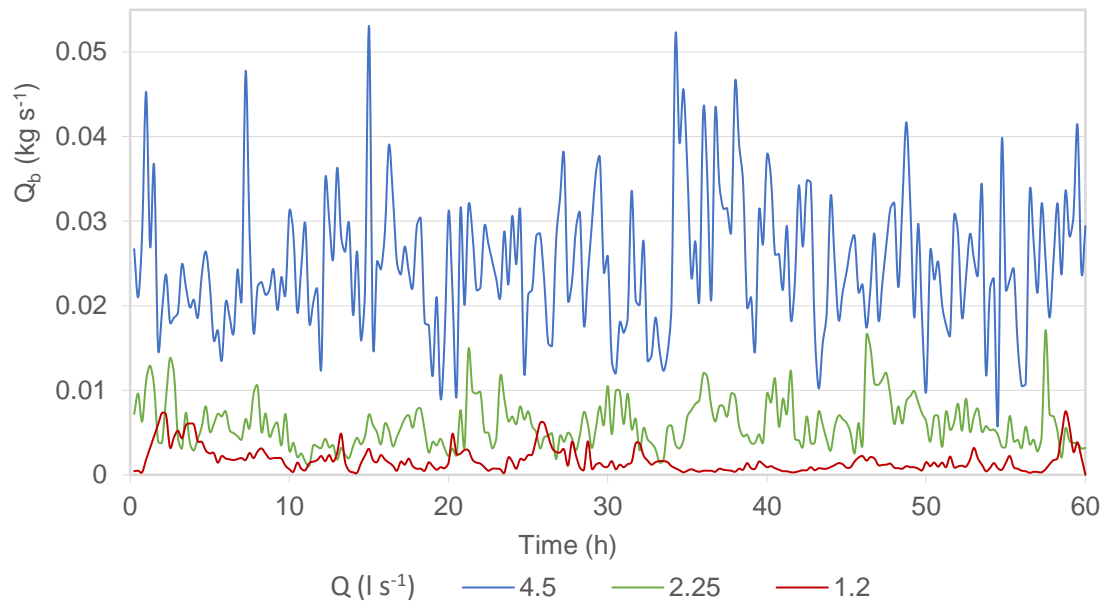
Figure 2.7 – Temporal variability in bedload transport rate (Q_b) from three experimental gravel-bed braided rivers run at constant discharge (Q). Data from Ashmore (1988).

The collective movement of individual bed particles creates and interacts with the channel morphology, particularly at the scale of the local pool-bar unit (Pyrce & Ashmore, 2003a). The total streamwise distance travelled by a grain from initial erosion to final deposition is called the path length (Pyrce & Ashmore, 2003a). While the path length is often comprised of multiple steps as a function of flow conditions and the bed surface, research by Kasprak et al. (2015) found that the path length in braided rivers is strongly controlled by local morphology. Specifically, the majority (81%) of tracers seeded in a river-modelling flume were deposited on local downstream bar heads and bar margins regardless of the initial seed site. Ferguson et al. (1992) found that in a gravel-bed braided river coarse sediment moving from a chute would be deposited onto the downstream bar because of its high forward momentum rather than follow the flow of the water into the anabranches. In a positive feedback loop, the deposition of coarse material on the bar head traps additional coarse material resulting in the upstream growth of the bar and overall imbrication and armouring of the bar head with coarse grains (Ferguson et al., 1992; Bristow & Best, 1993; Lane, 1995).

2.3.3 Bed Mobility

The transport of the available particle sizes in the active layers defines the bed mobility. In gravel-bed rivers the three main mobility conditions, shown in Figure 2.8, are defined (Parker, 2008; Venditti et al., 2017) as:

- Partial mobility – The grain size distribution of the bedload and bed surface are different so that the bedload is less coarse than the surface.
- Selective mobility – The grain size distribution of the bedload and bed surface are different so that all the grain sizes are represented in both, but the bedload is finer than the bed surface.
- Equal mobility – The grain size distribution of the bedload and bed surface are equal.

Venditti et al. (2015) defined a fourth condition, which they described as a special case of selective mobility, in which the particle size distribution of the bedload and the subsurface sediment are equal, but both are finer than the surface grain size distribution. In all cases, except equal mobility, the bedload grain size distribution is finer than that of the surface, which is fundamentally a function of microtopography and sediment supply conditions (Ashworth et al., 1992; Lane, 1995; Parker & Toro-Escobar, 2002). For example, it is characteristic in gravel-bed channels to have surface coarsening, called armour (Bunte & Abt, 2001; Yager & Schott, 2013). Large protruding grains can provide shelter for finer grains that would otherwise become entrained at a lower shear stress. As a result, fine grains on a mixed-bed may require a greater shear stress to become entrained than would be estimated based on the grain size or weight alone (Ashworth et al., 1992; Parker & Toro-Escobar, 2002). The effect of armouring has been found to change with sediment supply. In channels with high sediment supply the bed surface armouring is diminished which results in relative surface fining and bedload coarsening, and an overall shift towards equal mobility along with increase in bedload transport rates (Mueller & Pitlick, 2013; Venditti et al., 2017). In channels with a low sediment supply, coarse patches on the bed expand (i.e., more armouring) reducing bedload transport rates as the surface grain size becomes coarser and requires greater shear stresses to breach the armour and mobilize the smaller particles hidden in the subsurface (Mueller & Pitlick, 2013; Venditti et al., 2017).
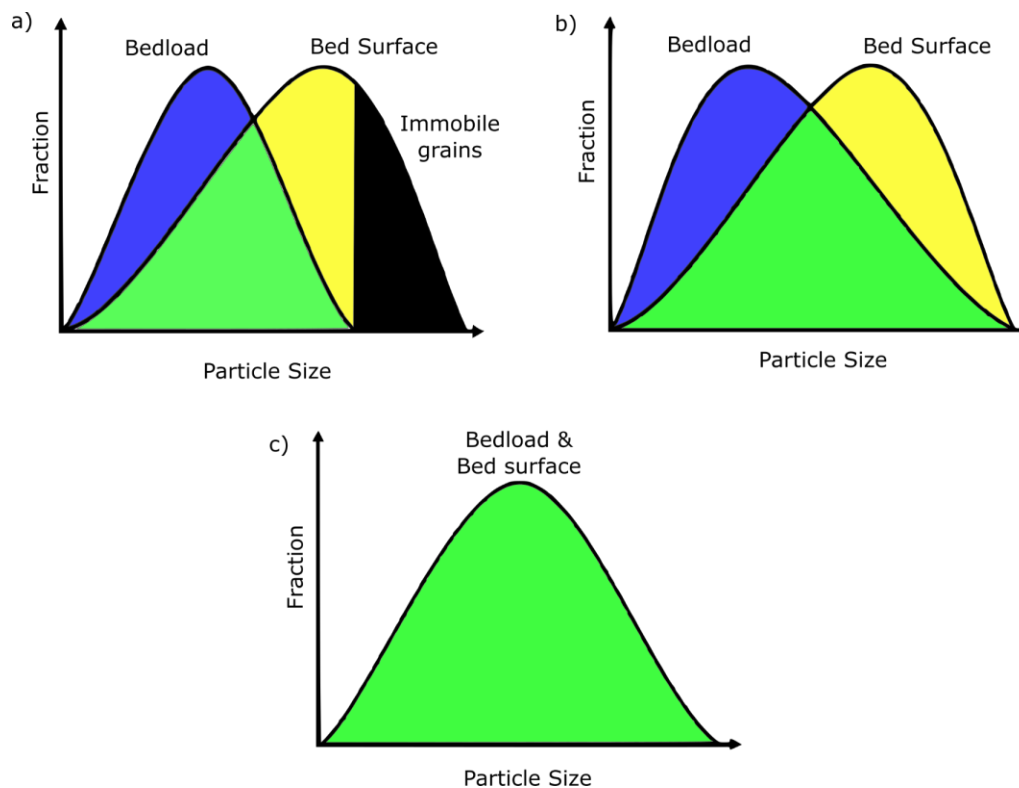
Figure 2.8 – Conceptual diagram of bed mobility functions in terms of bedload grain size distribution and bed surface grain size distribution where a) represents partial mobility, b) selective mobility, and c) equal mobility. This image is adapted from Venditti et al. (2015).

Previous research suggests that most gravel-bed rivers exist in a condition of partial mobility but can reach selective mobility under higher bankfull discharges (Venditti et al., 2017). For true equal mobility, surface armouring would need to be diminished so that all grain sizes in the active layer would be equally available for transport, which is expected to be rare in gravel-bed rivers. Interestingly, when Mueller and Pitlick (2013) looked at a range of channel morphology, the conditions under which the bedload and subsurface grain size ratio approached unity were predominately found in braided rivers. Their results also confirmed that braided channels have, on average, higher concentrations (ratio of bedload discharge to water discharge) of bedload compared to their single-thread counterparts. One of the important implications of that research was that changes in bed structure and channel morphology may reflect changes in bed load sediment concentration and sediment transport processes and vice versa (Mueller & Pitlick, 2013). Ashworth et al. (1992) also

found that gravel-bed braided rivers with high sediment supplies and frequent high flows lacked well-structured beds (i.e., armouring). Thus, the importance of armouring and hiding in determining sediment availability and bedload transport rates may be reduced in gravel-bed braided rivers, but this has not been investigated in detail.

The area of the bed that is mobile at any given time will shift spatially and temporally in response to changes in discharge (i.e., shear stress) and sediment supply (e.g., armouring). For example, Haschenburger & Wilcock (2003) found that an area of the bed classified as partially mobile would expand during a flood into areas that were previously immobile. In addition, the area of the bed that was partially mobile at low discharge could become fully mobilized (i.e., selective mobility) at higher discharges. This implies that with increasing discharge not only is a greater area of the bed mobilized, but a wider range of grain sizes is being mobilized as well.

2.4 The Morphological Active Width

The active zone of bedload transport in a river, that expands and contracts based on discharge and sediment supply conditions, is known as the active width. The active width can be defined in two ways. The instantaneous active width refers to areas where particle movement was directly observed, either visually or with direct sediment sampling. Quantifying the instantaneous active width is challenging because it can be difficult to directly observe and measure particle movement in a channel. Portable samplers, intensive surveying, and tracers could be used, but these methods are time-consuming and may not be reliable in capturing the spatial and temporal variability of bedload transport (Ashmore et al., 2011). On the other hand, the morphological active width (herein called the active width) relies on identifying and characterizing the active zones of transport based on measuring areas of significant bed-material displacement over time. This approach can be applied using repeat surveys of the river providing a time-integrated active width (Ashmore et al., 2011). It is expected that this application of the morphological method might underestimate active width for two reasons: 1) only areas of significant elevation change are considered and; 2) areas that have an overall zero net change (i.e., bed elevation change from erosion and deposition both occur but are equal in the measurement time interval) may not be detected (Lindsay & Ashmore, 2002; Ashmore et al., 2011). To manage these

problems, it is important to use an appropriate detection level and time interval between surveys. This requires balance because the interval must be long enough to allow for a detectable amount of morphological change but short enough that major changes in morphology are not compensated.

Although research on the active width is limited, Bertoldi et al. (2009a) found that increases in mean bedload transport rates in braided rivers were largely driven by changes in the active (and therefore, wetted) width, rather than bed shear stress (i.e., water depth) as previously assumed. This means that in braided rivers, quantifying the variability in the active width should be more meaningful for estimating bedload transport rates than methods relying on bed shear stress, such as standard bedload formulas used for single channels. Furthermore, because the morphological active width is related to bedload transport rate, it can provide additional insights into the spatial and temporal patterns of bedload transport rates, although these relationships in gravel-bed braided rivers are not completely understood (Ashmore et al., 2011).

Ashmore et al. (2011) investigated the active width using field data, a physical model, and simple computations from bedload formulas. The authors found that the active width generally increased with discharge once the threshold discharge for bedload transport was exceeded, but there was considerable scatter in the active width on a given day and even between days with similar discharges in the field. In a scaled physical model of the Sunwapta River, Ashmore et al. (2011) found that the active width could vary up to a factor of 6, even at constant discharge. The authors attribute this variability to changes in the number of active channels, the convergence and divergence of flow, and the local patterns of erosion and deposition caused by bar formation, avulsion, and bifurcation in braided rivers. The active width seems to be especially variable and unpredictable close to the threshold discharge for gravel entrainment. Above this threshold there is a steep increase in the active width with increasing discharge which also reflects an increase in bedload transport rate as more areas of the bed exceed the critical bed shear stress required for entrainment (Ashmore et al., 2011). Although spatially variable the active width can occupy as much as 50% of the wetted width at formative discharge, but in general occupies 10-40% of the channel (Ashmore et al., 2011).

Ashmore et al. (2011) also investigated the relationship between the active width and simple hydraulic parameters and found that dimensionless active width (non-dimensionalized using the wetted width) has an approximately linear relationship with dimensionless stream power. This could suggest that the morphological active width represents a fundamental property of braided rivers that responds to variations in discharge and stream power both between rivers and within a given river (Ashmore et al., 2011). Research has already found that the active width is correlated with the active braiding intensity, and therefore the total braiding intensity as well as wetted width. Consequently, it may be possible to estimate the active width with relatively little data on channel morphology such as channel dimensions and discharge. In addition, the inherent relationship between active width and bed-material transport suggests that it could serve as a general predictor of reach-averaged bedload transport (Ashmore et al., 2011).

To date these results are based on relatively few observations and rely on predictions from simplified hydraulics. Better understanding of the relationship between the active width, flow, and bedload transport flux requires an extensive set of experiments in which the bedload flux, hydraulic parameters, and morphology are all being monitored and (ultimately) complemented by field observations (Ashmore et al., 2011). This kind of dataset would make it possible to see if the variability in the active width matches local changes in erosion and deposition, therefore confirming and enhancing understanding of the connection between active width, as a measure of channel morphodynamics, and bedload flux. Finally, Ashmore et al. (2011) suggest that additional research is required to understand the role of the active depth (i.e., depth of active layer), in relation to bedload transport. In combination, knowledge about the active width and active depth allows for the estimation of a morphological bedload transport flux, which would contribute to our ability to manage, monitor, conserve and restore gravel-bed braided rivers (Ashmore et al., 2011; Ashmore, 2013).

2.5 Morphological Methods for Estimating Bedload Transport Rates

The need to determine bedload transport rates in gravel-bed rivers originally surfaced to determine bedload, discharge, and river channel evolution for engineering projects (i.e., to

train rivers and design navigable channels) (Gomez, 1991). There were two main approaches: 1) development and application of bedload transport formulae and 2) sampling bedload transport directly or indirectly to generate empirical relations for a given field site (McLean & Church, 1999). These methods are challenging to implement in channels like braided rivers where sediment transport dynamics are complicated and difficult to measure (Ashmore & Church, 1998). More recently, another approach referred to as the morphological method has been adopted into bedload transport research as an alternative to hydraulic methods, which generally perform poorly in braided rivers (Ashmore & Church, 1998). Due to the spatial and temporal variation in bedload flux which is often considered the result of the evolution (formation, migration, and dispersion) of bedload sheets, surface armour, and bedforms, there is still no universally accepted method for determining bedload transport rates under all conditions (Gomez, 1991; Diplas et al., 2008).

The morphological method came out of the growing recognition that detailed information about channel form and topography could provide new insights into channel processes (Martin & Church, 1995; McLean & Church, 1999; Brasington et al., 2003). Even at extremely small spatial and temporal scales, bedload transport in alluvial channels results in local changes in bed elevation, channel location, and channel form (Hoey & Sutherland, 1991; Lane & Richards, 1997; Church, 2006; Parker, 2008; Buffington, 2012). Therefore, morphological change (e.g., changes to elevation and form due to erosion and deposition) can provide information on both sedimentary processes and estimate sediment transport rates, specifically bedload transport (Hoey & Sutherland, 1991; Goff & Ashmore, 1994; Ashmore & Church, 1998).

The development of the fundamental principles of the morphological method are often credited to Popov (1962), who suggested that an estimate of sediment transport could be derived from changes in the sediment budget of a reach (Ashmore & Church, 1998). This method was further developed by Neill (1971, 1987) who looked at bank erosion rates in single-thread meandering rivers (Hoey & Sutherland, 1991; Martin & Church, 1995; Ashmore & Church, 1998). More recently there has been a resurgence in using the morphological method, which is largely related to improvements in data resolution and

automated post-processing techniques (Brasington & Smart, 2003; Surian & Cisotto, 2007; Westoby et al., 2012).

There are several variations of the morphological method that can be used to estimate bedload transport rates in channels including the commonly used reach-budget method (Hoey & Sutherland, 1991; Martin & Church, 1995; Ashmore & Church, 1998; Surian & Cisotto, 2007). The reach-budget method is based on the continuity principle for sediment in each reach so that:

$$S_o = S_i - \delta S \qquad\qquad (2.4)$$

where S_o is the sediment output, S_i is the sediment input and δS is the change in storage for a given reach (Hoey & Sutherland, 1991; Martin & Church, 1995; Surian & Cisotto, 2007) (Figure 2.9). The change in storage is the net difference between erosion of bars, banks and the channel bed and the deposition of sediments on bars, in scour holes, and on the floodplain (Hoey & Sutherland, 1991; McLean & Church, 1999). Based on this equation, if two of the terms are known then it is possible to estimate the third within the margin of error of the known terms (Martin & Church, 1995).
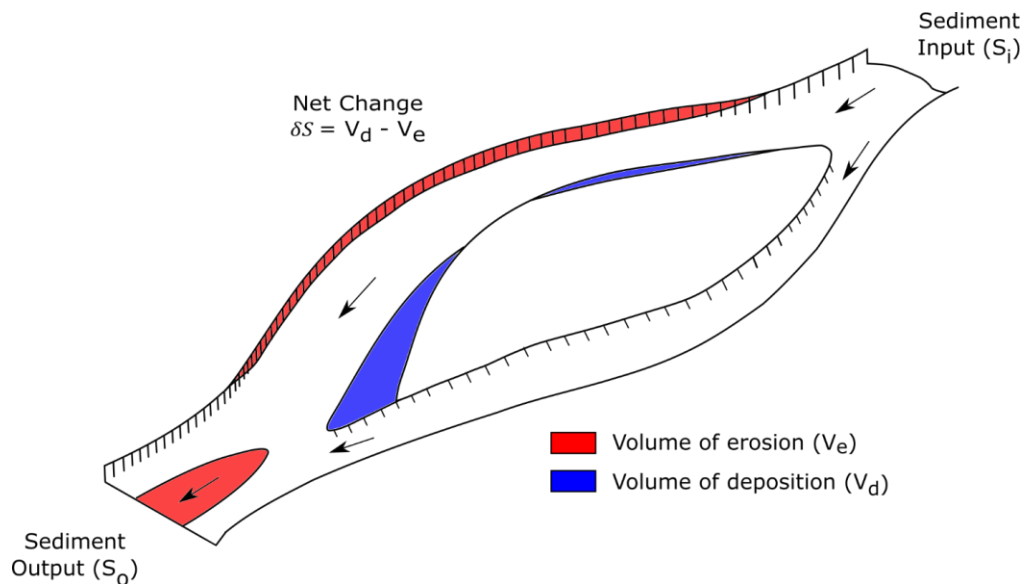
Figure 2.9 – Conceptual diagram of the morphological reach-budget method for estimating bedload transport rates, where S_i is sediment input, net change (δS) is the difference between volumes of deposition and volumes of erosion within the reach, and S_o is sediment output. Image adapted from Brewer & Passmore (2002).

The reach-budget equation can also be expressed as a mean transport rate integrated over time to become:

$$Q_o = Q_i - \rho \delta S / \delta t \tag{2.5}$$

where Q_o is the mass transport output from the reach, Q_i is the mass transport into the reach, ρ is the sediment bulk density, δS is the volumetric change in sediment storage (i.e., volume of deposition – volume of erosion) and δt is the time interval (Hoey & Sutherland, 1991; Martin & Church, 1995; Brasington & Smart, 2003; Brasington et al., 2003; Surian & Cisotto, 2007).

The reach-budget approach was first used in a braided river by Griffiths in 1979 on the Waimakariri River in New Zealand (Ashmore & Church, 1998). He estimated volumes of erosion and deposition between surveyed cross-sections by averaging the end areas of the enclosing prism. As a result, Griffiths was able to estimate changes in erosion and deposition over time as well as estimate mean gravel transport rates (Ashmore & Church, 1998).

Applying the reach-budget method requires 3 to 4 steps depending on data availability (Ashmore & Church, 1998; Surian & Cisotto, 2007):

1) Estimate the net change in area for each cross-section in each reach;
2) Estimate the net change in volume of sediment for a given reach;
3) Estimate of grain size and porosity;
4) Identification of a cross-section where sediment transport is known.

Estimating the net change in area and volume can be difficult but is commonly done using repeat surveys of channel cross-sections or using more advanced techniques such as remote sensing, digital photogrammetry, and/or LiDAR to create continuous digital elevation models (DEM) of the surface (Surian & Cisotto, 2007; Williams et al., 2011; Bakker & Lane, 2016). Early methods relied solely on cross-sectional data, which required interpolation between the cross-sections and resulted in limited insight into the spatial distribution of change (Goff & Ashmore, 1994; Brewer & Passmore, 2002; Brasington et al., 2003). Newer techniques often provide spatially continuous measures of topography change making it possible to investigate the spatial pattern in bedload transport for the time

interval between surveys. While providing higher spatial and temporal resolution, newer data acquisition methods like LiDAR and DEM Differencing are subject to potentially high levels of uncertainty and error propagation (Wheaton et al., 2009; Williams, 2012).

Since the reach-budget method requires knowledge of sediment transport rate across one cross-section (boundary condition), this method is ideal in locations where bedload transport rate can be measured or be assumed to be zero at some boundary, such as at deltas or gravel-sand transitions (McLean & Church, 1999; Surian & Cisotto, 2007). In situations where the bedload transport rate cannot be known, it is common to use the assumptions of a minimum budget, in which the sediment input is either assumed to be zero or is adjusted so that the resulting downstream budget remains positive (Surian & Cisotto, 2007). Once the bedload transport is known or estimated at one cross-section, the sediment budget calculations can be extended upstream and downstream as Q_i from one reach is Q_o from the upstream reach (Martin & Church, 1995; Ashmore & Church, 1998; McLean & Church, 1999).

Under some circumstances where the bedload transport rate (Q_b) cannot be known or assumed to be zero, it can alternatively be estimated from an equation for the mass rate of bedload transport:

$$Q_b = V_e(L_t/L_r)/t \tag{2.6}$$

where V_e is the volume of mobilized bedload (i.e., volume of eroded sediment), L_t is path length, L_r is the reach length, and t is the interval between surveys (Ashmore & Church, 1998). This method has been used in small rivers where Ve, Lr and t are relatively easy to determine and L_t can be estimated from tracers (Haschenburger & Church, 1998). In larger rivers and braided rivers, however, it might be challenging to determine L_t. One possible solution is to rearrange equation 2.6 so that if Q_b is known, estimates of Lt can be used in subsequent calculations:

$$Q_b = V_e L_t/\alpha \tag{2.7}$$

$$L_t = Q_b\alpha/V_e \tag{2.8}$$

where $\alpha = L_r*t$, so that for a given reach and time interval, α is constant. Based on equation 2.8, path length could be estimated as the ratio of bedload transport to the volume of

mobilized sediment. Pyrce & Ashmore (2003a) looked at the distributions of path lengths in meandering rivers and found that tracers were preferentially deposited on downstream bars (50-75%). This research agrees with Kasprak et al. (2014) who found that tracers in braided rivers were preferentially deposited on bars (81%) regardless of where tracer particles are seeded within the flow. Consequently, since confluences and bifurcations have a characteristic length scale, path length may be nearly constant for a given morphology based on a characteristic length scale (Hundey & Ashmore, 2009). If path length is nearly constant for a given morphology, then based on equation 2.8, changes in bedload transport rate could be explained by changes in the volume of mobilized sediment alone, although these relationships have not been investigated systematically or over a range of river morphologies.

2.5.1.1 Advantages of the Morphological Method

The main advantage to the morphological method is that unlike the variables and parameters used in the forward method (e.g., near-bed velocity and bed shear stress), morphology is relatively easy to measure (Ashmore & Church, 1998). This makes it possible to monitor spatially extensive sites and complex morphologies over long temporal scales, none of which are possible with hydraulically-based formulas or field sampling, which may be limited due to practical or financial constraints (Goff & Ashmore, 1994; McLean & Church, 1999; Brewer & Passmore, 2002). Consequently, McLean & Church (1999) concluded that morphological methods may be the most generally applicable method for estimating bedload transport rates. Furthermore, continued improvements in technology have made the morphological method an attractive alternative to at-a-point sampling and bedload formulas (Brasington & Smart, 2003; Brasington et al., 2003; Haschenburger, 2013).

By considering the direct link between sediment transport processes and morphology, with less emphasis on hydraulic parameters, it may be possible to gain new knowledge about sedimentary and fluvial processes (Martin & Church, 1995; McLean & Church, 1999). For example, the reach-budget method is able to provide a time-integrated bedload transport rate (e.g., transport during a single flood event) but can also provide insight into the spatial

and temporal patterns of transport that traditional sampling and formulae cannot (Ashmore & Church, 1998; McLean & Church, 1999; Williams et al., 2011).

In addition to the advantages of using the morphological method, it has already been successfully used in many different geomorphological applications. This includes estimating short-term event-based sediment transport rates as well as long-term sediment budgets at a variety of spatial and temporal scales and river types (Ashmore & Church, 1998; Brewer & Passmore, 2002; Brasington & Smart, 2003; Surian & Cisotto, 2007; Williams et al., 2011). Knowledge of bed material displacement and changes in sediment storage along a reach provides a direct assessment of channel stability, which is also of interest to river engineers (Martin & Church, 1995; Ashmore & Church, 1998; McLean & Church, 1999; Brewer & Passmore, 2002).

According to Ashmore and Church (1998), the morphological method is ideal for use on braided rivers since their complex and dynamic nature make all other methods for estimating bedload transport largely inappropriate and impractical. Furthermore, braided river morphology is dominated by bedload transport and frequent topography changes, making it possible to detect changes in morphology over relatively short time intervals.

2.5.1.2 Uncertainty in the Morphological Method

Data Collection and Quality

The reliable application of the morphological method is fundamentally a function of the density, frequency, and quality of the topography data collected (Ashmore & Church, 1998; Brasington et al., 2003). The ability to collect high-resolution data at a high enough density and frequency will depend heavily on the resources available, the sampling method used, and the dynamism of the river (Ashmore & Church, 1998; McLean & Church, 1999). For example, estimates of net storage changes coming from the construction of DEMs of Difference (DoD) will be limited by DEM quality, which in turn is a function of the sampling method, the quality of the point data, the topographic complexity, and surface composition as well as the interpolation methods applied (Wheaton et al., 2009).

In addition, the frequency of repeat surveys poses another challenge. It is expected that rivers are likely to experience compensating erosion and deposition (scour and fill) between surveys leading to a negative bias on net change estimates (Ashmore & Church, 1998; McLean & Church, 1999; Lindsay & Ashmore, 2002). While little data is available on the specific impacts of survey frequency, it is expected that larger temporal spacing will result in larger negative biases on volumetric change estimates (Ashmore & Church, 1998). While a greater temporal frequency is desirable, it is also limited on the lower end by the precision of the change detection. Therefore, the choice of time interval will be a trade-off between choosing an interval short enough to minimize compensating scour and fill while remaining long enough to allow for detectable morphological change (Ashmore & Church, 1998).

Uncertainty in Volumetric-Based Analyses

One of the main challenges with applying the morphological reach-budget method in the field is that it may not be possible to know the boundary conditions (sediment input or output) required for sediment budgeting (McLean & Church, 1999; Brasington et al., 2003). Without a direct bedload flux measurement, this method will have to rely on bedload estimates from formulae which may not be practical for use in braided rivers (Ashmore & Church, 1998). Due to the challenges of determining an accurate bedload transport rate in the field, it is possible that the morphological method cannot be properly tested in the field where local bedload transport rates are difficult to measure for both constraining the budget and comparing morphological transport estimated with 'known' average bedload flux (Warburton in Ashmore and Church, 1998).

In addition, morphological sediment budgets can only account for the gross or net change in sediment and does not consider any sediment that was transferred through the system without exchange with the bed morphology (McLean & Church, 1999; Brewer & Passmore, 2002). As a result, these methods will generally underestimate sediment transport rates (Martin & Church, 1995; Brewer & Passmore, 2002; Surian & Cisotto, 2007). Martin and Church (1995) suggest that this challenge can be addressed by ensuring that the study reach is longer than the path lengths of the sediment. Ashmore et al. (2011) suggest that some of these challenges can be addressed by using a fixed-integration time

or integrating the morphological change over an entire event hydrograph. For example, in gravel-bed rivers with moderate rates of bed material transport, the use of a short time interval could address this issue (Martin & Church, 1995). Similarly, the reach-budget method only provides estimates of the bed-material load, and cannot account for any throughput or wash load that passes through the reach without interacting with the bed or morphology (McLean & Church, 1999).

The use of the morphological method for a volumetric sediment budget is also subject to error and uncertainty propagation. This method is limited by the quality of not just one DEM, but two, therefore errors and uncertainties in each DEM will be carried forward into the volume estimates (Ashmore & Church, 1998; Brasington et al., 2003; James et al., 2012). In the case of the reach-budget method, sediment transport calculations can be carried upstream and downstream if the bed-material transport rate is known at one location in the reach. Therefore, the error increases as the calculations are propagated farther from a cross-section of known transport (Martin & Church, 1995; McLean & Church, 1999). As a result, it is expected that DoD methods will be most effective and reliable in areas where geomorphic change is much higher than the levels of uncertainty (Williams et al., 2011; James et al., 2012).

Overall it is expected that the morphological method will provide an estimate of the lower-limits of sediment transfers with information being lost due to the data quality, sediment throughout, and compensating scour and fill (Martin & Church, 1995; Ashmore & Church, 1998). Some of these challenges, however, can be addressed in an experimental setting where there is control over the governing conditions as well as measurement precision and frequency.

2.6 Measuring Morphological Change

Monitoring of geomorphic change was historically done using repeat surveys of planform, cross-sections, and/or longitudinal profiles (Wheaton et al., 2009). Additional research has successfully used aerial photographs and detailed contour maps to measure morphological sediment budgets (Brewer and Passmore, 2002). While these methods provide a coarse measure of volume change, cross-sectional data provides sparse information on the spatial

distribution of channel change (Brasington et al., 2003). Also, while maps and photos can provide information on the long-term changes in sediment sources and transfers, they lack detailed information on changing bed morphology and may have limited temporal resolution. Fortunately, advancements in technology have made it possible to capture, monitor, and model channel morphology and morphological change at spatial and temporal resolutions never before possible (Rumsby et al., 2008; Wheaton et al., 2009; Redolfi et al., 2016). Specifically, morphological analysis is no longer restricted to one- and two-dimensions, but techniques such as remote sensing, LiDAR, and digital photogrammetry have opened the way for high-resolution 3D images and DEMs of channel morphology (Rumsby et al., 2008; Redolfi et al., 2016). These methods have much higher spatial sampling resolution than the cross-sectional datasets of the past (Brasington et al., 2003). With repeat topographical surveys it is possible to create DEMs of the river and DEMs of Difference (DoDs) through the comparison of two DEMs taken at different times (Brasington et al., 2003; Wheaton et al., 2009; James et al., 2012). Not only can this provide a basis for sediment budgeting through quantification of changes in sediment storage, but DoDs allow us to visualize and quantify spatial and temporal patterns of channel morphology change (Brasington et al., 2003; Wheaton et al., 2009; Williams et al., 2011; James et al., 2012; Williams, 2012). This '4D' (x, y, z and time) approach has already been applied to several different types of geomorphological practices including the assessment of bank erosion and drainage basin evolution, both in the field and in the laboratory (Brasington et al., 2003; James et al., 2012).

2.6.1 Digital Photogrammetry

Photogrammetry is the science of using photographs, usually aerial or remotely sensed imagery, to make quantitative measurements (James et al., 2012). Over recent years, digital photogrammetry has become more popular for creating digital elevation models (DEMs) from a set of overlapping digital photographs (Chandler, 1999; Gardner & Ashmore, 2011; Westoby et al., 2012). Recently, the emergence of 'Structure-from-Motion' (SfM) photogrammetric techniques represents a technological revolution in geomatics and geomorphological terrain analysis (Westoby et al., 2012; Bakker & Lane, 2017). SfM follows the same basic principles of traditional digital photogrammetry by reconstructing

3D structures from overlapping, offset images. The main difference is that SfM is heavily automated, allowing for camera positions and the geometry of the scene to be solved automatically and simultaneously, whereas traditional methods required a priori knowledge of camera positions, fixed and calibrated geometry (usually vertical stereo photos), and/or the real-world 3D locations of a network of ground control points (GCP) (Westoby et al., 2012; Fonstad et al., 2013). With SfM image-processing algorithms being automated, data that would have been impossible to process using older manual photogrammetric methods can now be processed at high-resolution (Chandler, 1999; Brasington & Smart, 2003). In addition, the availability of inexpensive high-resolution digital cameras and photogrammetric software to produce DEMs means that the resolution and quality of the DEMs is now only limited by the resolution and quality of the input imagery (Chandler, 1999; Brasington & Smart, 2003; Rumsby et al., 2008). The advancements in software also mean that it is possible to capture high-resolution DEMs for analysis without advanced photogrammetric training, which has also made this approach desirable and increasingly available for researchers and engineers alike (Chandler, 1999; Brasington & Smart, 2003; Fonstad et al., 2013; Smith et al., 2016).

Geomorphologists are taking advantage of these new technologies and have used digital photogrammetry to monitor and model landscapes from flumes to large, dynamic braided rivers in the field (Brasington & Smart, 2003; Morgan et al., 2016; Bakker & Lane, 2017). One area that has particularly evolved in the advent of improved photogrammetric techniques is the morphological method. With easy-to-acquire high-resolution DEMs, it is now possible to monitor geomorphological change and sediment transport through DEM comparison or differencing (Brasington & Smart, 2003; Wheaton et al., 2009; James et al., 2012; Williams, 2012; Bakker & Lane, 2017). While originally developed for remote sensing and vertical aerial photogrammetry, automated digital photogrammetry software can be used effectively at close-range micro-scales, which is advantageous for laboratory research (Chandler, 1999; Morgan et al., 2016). At these micro-scales there is an added advantage that cost-effective digital cameras can be used to capture digital images of a sufficient resolution for DEM generation (Chandler, 1999).

Some of the challenges with using digital photogrammetry in fluvial geomorphology includes capturing elevation data from wetted areas, where ground surveys are required (Ashmore & Church, 1998). According to Brasington and Smart (2003), this combined approach can lead to variable data coverage and therefore variable reliability. As a solution to this problem, some researchers have used physical models in which the flow can be turned off, the model surface allowed to drain, and the wetted areas revealed before turning the flow back on (Brasington & Smart, 2003). This modelling approach not only provides full data coverage of the model surface, but at a consistent data coverage and resolution (Gardner & Ashmore, 2011; Kasprak et al., 2015; Leduc et al., 2015).

SfM allows for the creation of a dense point cloud without a priori knowledge of camera or target locations, but reference to 'real-world' position still requires independent ground control points for georeferencing (Fonstad et al., 2013). In addition, the automation of the photogrammetry may still necessitate long data-processing times (Westoby et al., 2012). The extraction of and matching of keypoints between images and the construction of both sparse and dense point clouds is computationally demanding (see Chapter 2). Therefore, while SfM may be faster than traditional methods, the final choice of survey method should consider the time-cost for covering large topographic areas at high-resolution.

Overall, digital photogrammetry is now able to reproduce DEMs with sufficient resolution to generate morphological sediment budgets with high temporal frequency (Rumsby et al., 2008; Morgan et al., 2016). The advantages of faster data acquisition and semi-automation have made this method a preferred method in geomorphology (Fonstad et al., 2013). In addition, given the relatively low cost to implement and growing availability of general photogrammetric software, these techniques have been used at close-range in the flume as well as in the field (Brasington et al., 2003; Gardner & Ashmore, 2011; Kasprak et al., 2015; Leduc et al., 2015; Morgan et al., 2016; Bakker & Lane, 2017). Therefore, SfM digital photogrammetry was used to acquire high-resolution DEMs for this research in an experimental laboratory setting.

2.7 Experimental Geomorphology

While field observations are still the basis for much of geomorphology, there are several limitations which have driven fluvial geomorphology to find complementary methods. One of the most commonly cited issues in field observation and measurement is that many of the phenomena that interest fluvial geomorphologists occur at large spatial and temporal scales that make field research impractical or incomplete (Kleinhans, 2010). Also, given the complexity of natural systems it may be impossible to observe certain features or phenomena directly or even indirectly. This can be due to inaccessibility, unsuitable equipment, or because some measurement techniques alter or disturb the phenomena being measured (Kleinhans, 2010). Furthermore, Lane & Richards, (1997) point out that contextual interactions between form and process at particular field sites may also raise questions about the general applicability of a given set of observations. Given the challenges to studying fluvial processes and morphology in the field, many researchers have turned to experimental geomorphology, including the use of physical, or hardware, models, to better understand river processes (Paola et al., 2009).

2.7.1 Physical Modelling

Peakall et al. (1996) defines four general types of physical models used in fluvial geomorphology: 1) 1:1 models, which maintain the same spatial and temporal scale as the prototype model; 2) Froude-scale models, which attempt to accurately scale Froude numbers between model and prototype (Church, 1984); 3) distorted scale models, which exaggerate one or many aspects of the prototype (e.g., vertical or horizontal distances); and finally 4) analogue models, which are used for those phenomena which occur at such large spatial and temporal scales that a they cannot be studied directly (Peakall et al., 1996).

Froude-scale models, which are often used in fluvial geomorphology to model river processes, are founded on the principles of similarity theory (Yalin, 1971). A scaled model has geometric, kinematic and dynamic similarity with its prototype (Peakall et al., 1996). Geometric similarity holds a constant ratio of geometric (length) dimensions. Kinematic similarity attempts to hold constant ratios for both length and time. Finally, dynamic similarity holds constant ratios across length, time, and mass (Young and Warburton,

1996). As a result, models with dynamic similarity produce similar force ratios in the model and prototype and are therefore required when modelling fluvial processes (Peakall et al., 1996; Warburton, 1996; Young & Warburton, 1996; Ashmore, 2007). Practically, it is generally not possible to achieve perfect similarity because some properties of the fluvial system cannot be scaled, for example, the density (ρ) and viscosity (μ) of water and the acceleration due to gravity (g) (Peakall et al., 1996; Young and Warburton, 1996).

Froude-scale models are so named because the Froude number (*Fr*), which describes the conditions of flow in a dimensionless number, is equal between the model and its prototype (Ritter et al., 2011) (Details in Appendix A). By maintaining the Froude number, the Reynolds number (*Re*), another dimensionless number characterizing flow turbulence (i.e., the ratio of inertial to viscous forces), must be relaxed (Ritter et al., 2011). For a prototype river with 'rough-turbulent flow' hydraulic theory shows that if the grain Reynolds number (*Re**, the state of turbulence at the bed) and the Reynolds number in the model are high enough to also allow for rough-turbulent flow ($Re^* > 70$; $Re > 2000$), the critical dimensionless bed shear stress is fairly constant above these values, and therefore, the exact *Re* value will not substantially influence dynamics of the flow and sediment transport (Paola et al., 2009; Young and Warburton, 1996). As a result, these models have approximate dynamic similarity (Young & Warburton, 1996). Froude-scale modelling is well suited for modelling gravel-bed rivers because it is easier to maintain the relatively high hydraulic roughness required to generate the rough turbulence flow and dimensionless bed shear stresses needed for model and prototype similarity (McKenna Neuman et al., 2013).

When modelling gravel-bed braided rivers specifically, Warburton (1996a) describes general characteristics required for the physical model. As already mentioned, there must be dynamic similarity between the model and a braided river system. This can be achieved when the length dimensions are scaled in a linear way and the principles of Froude-scale modelling are applied. It is common in geomorphology to allow river channels in models to self-form, so the bed and banks of the channel must be deformable. Third, the bed-material must reflect the bed-material of the prototype. The bed and bank materials should be kept granular and non-cohesive, where the grain size is determined by the length scale

(Warburton, 1996a; Young and Warburton, 1996). Using mainly fine-grained sediment (< 0.6 mm) could result in the formation of ripples and other bedforms, as well as cohesion effects that change the resistance of the bed and alter local sedimentary processes. As a result, it is common practice in hydraulic modelling to truncate the smaller grain sizes when scaling the sediment material to avoid cohesive behaviour or to use non-cohesive materials such as silica flour and beads (McKenna Neuman et al., 2013). Warburton (1996a) suggests that the slope of the bed be kept steep while others suggest that the slope be equal between the model and prototype to satisfy the requirements of a true Froude-scaled model (Ashmore, 1982; Young and Warburton, 1996). Following these general guidelines will provide a model with approximate dynamic similarity and similar sedimentary features to a real braided river (Warburton, 1996a). Finally, verification of physical models across a range of scales helps to ensure that the model is providing relevant data (Peakall et al., 1996). Qualitative visual verification is common when comparing model form with prototype form but the challenges associated with characterizing and defining a braided channel can make this difficult (Young and Warburton., 1996). Other methods attempt to quantify and compare channel geometry (dimensions) and channel complexity (sinuosity) between the model and prototype (Young & Warburton, 1996; Doeschl et al., 2006).

Advantages of Physical Models

While all models are simplifications and abstractions of reality, physical models have three major benefits over field research: control, comprehensive data collection, and replication (Mosley & Zimpfer, 1978; Wainwright & Mulligan, 2013; Bennett et al., 2015). Physical models provide control over the governing conditions of rivers (i.e., slope, discharge, and sediment calibre and supply) making it possible to investigate a range of river conditions and morphologies, something that cannot be done systematically in the field (Mosley & Zimpfer, 1978). This control also makes it possible to run experiments under constant geomorphic forcing conditions. For example, it is relatively common to use constant channel-forming discharge in flumes to speed up initial channel evolution and the rate at which geomorphic events cause morphological change to occur (McKenna Neuman et al., 2013). As a result, physical models can allow for the measurement of rare and unpredictable geomorphic events, which may be hard to capture with relatively infrequent field surveys (McKenna Neuman et al., 2013). Therefore, control allows researchers to

isolate, manipulate, observe, and measure geomorphic events and processes in an experimental way that contributes to our understanding of geomorphic systems (Mosley & Zimpfer, 1978; Young & Warburton, 1996; McKenna Neuman et al., 2013; Bennett et al., 2015; Yager et al., 2015).

Secondly, physical models simplify complex natural systems so that underlying mechanisms and processes can be observed and measured in a controlled experimental setting (Mosley & Zimpfer, 1978; McKenna Neuman et al., 2013; Bennett et al., 2015). This means that physical models allow for measurements not possible in the field because the site of interest is inaccessible, difficult to measure, or hazardous. At the same time models allow for the geomorphic evolution of rivers to be observed at a reduced spatial and temporal scale (Ashmore, 1982; Young and Warburton, 1996). In a Froude-scaled model specifically, it is possible relate the length (λ_l) scale to the time (λ_t), mass (λ_m) and discharge (λ_Q) scales using the following relations:

$$\lambda_t = \sqrt{\lambda_l} \qquad\qquad (2.9)$$

$$\lambda_m = \lambda_l^3 \qquad\qquad (2.10)$$

$$\lambda_Q = \lambda_l^{2.5} \qquad\qquad (2.11)$$

The time scale applies to all motion in the model (i.e., fluid and grain motion), and the mass scale only holds true when the density of the fluid and sediment are in unity in the model and prototype (Young and Warburton, 1996). These reduced scales allow for multiple processes to be measured and monitored simultaneously and precisely (Young and Warburton, 1996). In combination, the ability to gather information not accessible from the field over reduced space and time has allowed physical models to accumulate large comprehensive datasets on geomorphic processes. In some cases, physical models have been the only option for investigating complex geomorphic processes (Mosley & Zimpfer, 1978; Shvidchenko & Kopaliani, 1998). For example, Ashmore (1982, 1988, 1991b) was able to describe the fundamental processes leading to the initiation and maintenance of braiding, which would have been impossible in the field. Finally, models allow for

replication of experimental runs and simulations. This not only provides confidence in the results but promotes the development of new hypotheses and theories.

Overall, one of the most important benefits of using scale models is that even simple models are relatively successful at recreating complex geomorphic landscapes (Shvidchenko & Kopaliani, 1998; Paola et al., 2009; Bennett et al., 2015). Research has shown that small-scale physical models are able to reproduce channel morphology and braided river behaviour at a variety of scales (Ashmore, 1991b, 2007; Paola et al., 2009; Redolfi et al., 2016). This suggests that even with only approximate dynamic similarity, physical models are still able to reproduce the basic processes and forces found in real rivers (Paola et al., 2009; Kleinhans, 2010). As a result, and given the highly dynamic nature of these channels in nature, flumes are a fundamental source of knowledge and understanding on braided river processes (Ashmore, 1991b; Warburton, 1996; Shvidchenko & Kopaliani, 1998; Paola et al., 2009).

Limitations of Physical Models

The main limitation to using a physical model is the scaling difficulties caused by the simplifications and abstractions from reality. For example, certain processes and variables cannot be scaled down, including particle settling velocities and the physical properties of water (e.g., viscosity and density) (Peakall et al., 1996; Young and Warburton, 1996). Also, while it is generally accepted in Froude-scale modelling to use a lower Reynolds (Re) number if the Froude (Fr) number is maintained, the lower limit of Re is poorly defined and the effect of averaging Re is not fully understood (Young and Warburton, 1996). The result may be imperfect dynamic similarity between the model and prototype (Peakall et al., 1996; Young and Warburton, 1996; Paola et al., 2009).

In addition, natural landscapes are highly variable in climate, bedrock material, vegetation, anthropogenic interference, water quality and quantity etc. but this variability is too complex to model. Therefore, even generic models may be too simplified to allow for generalizable statements (Mosley & Zimpfer, 1978; Church, 2011; Bennett et al., 2015). This is especially a problem because certain features, such as vegetation, precipitation, and habitat, are likely to influence bank stability but are rarely modelled in flumes (Young and Warburton, 1996).

A practical problem is managing boundary conditions. Unlike nature, which is an open system, models are closed with finite amounts of water, sediment, and space. Therefore, there can be complications with how to manage sediment, edge effects as well as inlet and outlet effects in the model (Bennett et al., 2015).

Use of Physical Models in Braided River Research

Flume experiments and physical models have been vital to the progression of fluvial geomorphology and braided river research. Physical models are also ideal for investigating the morphological method in braided rivers where it is possible to obtain high-resolution topography, determine bedload transport rates directly, and control the governing conditions of river systems (Ashmore and Church, 1998).

Gravel-bed braided rivers are particularly good candidates for research in physical models because they are relatively easy to reproduce in a flume, leading some researchers to suggest that braiding is the default morphology of non-cohesive channels without lateral constraints (Murray & Paola, 2003; Ashmore, 2009; Paola et al., 2009). As a result, the use of physical models to investigate braided rivers and bedload transport became more popular in the eighties with research lead by Schumm, Ashmore, and Warburton (Metivier & Meunier, 2003).

Physical models have been paramount in understanding the processes leading to the development of braided rivers. Given that the necessary variables are impractical to alter in the field, the ability to alter discharge and slope in the flume allows for the development of a braided channel from an originally straight channel. Using a model, researchers are able to compress the evolution of a braided channel both spatially and temporally so it can be examined in great detail. For instance, Leopold and Wolman (1957) and later Ashmore (1991) were able to describe the mechanisms of braided channel development over time. In addition to braided river development, most of the knowledge on bedload transport rates in braided rivers comes from physical models (Ashmore, 1988; Young & Davies, 1990; Yager et al., 2015).

Physical modelling experiments have also helped confirm some of the behaviours and processes occurring in braided rivers. For example, models have confirmed the dynamic

steady-state of braiding as well as the tendency of channels to widen and multiply with increasing discharge (Paola et al., 2009; Bertoldi et al, 2009b; Egozi and Ashmore, 2008). More recently, flume experiments have shown that bedload transport, and therefore morphological change, in braided rivers does not span the entire channel width but is limited to what is now known as the active width (Ashmore et al, 2011; Welber et al., 2012). This means that morphological changes could be limited to a small number of main branches even at bankfull discharge (Egozi and Ashmore, 2009; Paola et al., 2009; Welber et al., 2012). In another study, Tal and Paola (2010) were able to cause a braided channel form to evolve into a much more meandering form through the introduction of alfalfa sprouts in the flume. More studies like this could provide additional insights into the role of vegetation and habitat on river functioning, something that has not adequately been done in the flume or field.

2.8 Research Rationale

Braided rivers continue to be of interest to geomorphologists, geologists, and engineers. For fluvial geomorphologists braided rivers are interesting because of their morphological complexity, dynamic erosion and bedload transport, and because of their relative abundance, especially in proglacial mountainous environments (Bristow & Best, 1993; Ashmore, 2013). Geologists study braided rivers to investigate sedimentary deposits and the local geology to determine their use as aquifer systems, as hydrocarbon reservoirs, and for the mining of sand and gravel (Bristow & Best, 1993). Finally, the lateral instability, high rates of sediment transport, and possible channel switching means that engineering and management is often important for the protection of populated areas, infrastructure (such as bridge piers and roads), and natural resources (Bristow & Best, 1993; Lane, 2000; Church, 2006; Piegay et al., 2006) (Figure 2.10).

Anthropogenic interference including lateral confinement, changes in flow and sediment regimes, gravel mining, and dredging have all been linked to the destruction of braiding morphology in many places around the world (Piegay et al., 2006; Surian & Cisotto, 2007; Ashmore, 2013). Yet, in other areas of the world, increased sediment production as a result of human activities have caused other river planforms to evolve into a braided planform (Piegay et al., 2006). Additionally, some braided rivers such as the Fraser River in British

Columbia, have important ecological functions including providing fish, bird, and invertebrate habitats (Piegay et al., 2006). As a result, there has been pressure to better understand the mechanics of braided rivers, and in particular bedload transport in braided rivers, for improved mining, restoration, and management of these systems (Bristow & Best, 1993; Piegay et al., 2006).

Figure 2.10 – Braided river instability creates challenges for maintaining infrastructure. The arrow indicates flow direction and the red circle highlights a location where the river is dangerously close to flooding the road. As a major tourist road, it is likely that the banks will be stabilized and the primary river channel moved away from the road.

However, estimating and predicting bedload transport fluctuations in gravel-bed braided rivers continues to be a challenge due to their complex and dynamic morphology (Bertoldi et al., 2009a). Yet, the dynamic morphology of braided rivers and their spatially and temporally variable bedload transport regimes are fundamentally linked. This relationship opens the possibility of using a morphological method for estimating bedload fluxes, where other traditional methods of formulae and sampling are insufficient (Ashmore & Church, 1998; McLean & Church, 1999). Specifically, consideration of the morphological active

width could help improve our predictions and understanding of bedload transport processes in gravel-bed and braided rivers. As morphologically-driven systems where bedload transport is spatially and temporally variable, the morphological method may be a more appropriate way to estimate transport than traditional formulae (McLean & Church, 1999). Given the challenges to collecting both bedload transport and active width data in the field, the use of a physical model provides an ideal location to investigate the relationships between morphology, bedload transport, and sedimentary processes over a range of channel-forming conditions (i.e., slope and discharge). To do this, close-range digital photogrammetry was used to capture high-resolution DEMs at a high temporal frequency in a physical model (Kasprak et al., 2015; Leduc et al., 2015; Morgan et al., 2016). Also, with the opportunity to directly measure the bedload transport rate in a physical model, this research investigates the evolution of grain size distributions and bed mobility with changes in discharge and stream power, something that has not previously been done adequately for braided rivers.

Uses of the morphological method already have shown that there is a clear link between hydraulic processes and channel geomorphology (Ashmore & Church, 1998; McLean & Church, 1999). Although there are clear advantages to morphological methods, including the direct applicability to engineering works and assessments of channel stability, there are still challenges. For example, the need to know sediment transport rate at one location in the reach continues to be a problem in the field and until a systematic monitoring system is put in place, these methods will continue to rely on estimates from formulae or estimates of sediment path length (Ashmore & Church, 1998; McLean & Church, 1999). A better understanding of active width and its relationship to bedload transport may not only improve the ability to correctly estimate bedload transport rates but may help bridge the conceptual knowledge gap between single-thread and multiple-thread channel dynamics (Bertoldi et al., 2009a; Paola et al., 2009; Egozi and Ashmore, 2009). Finally, the ability to link hydraulic parameters, bedload transport, bed mobility, and channel morphology quantitatively is expected to improve numerical model predictions of bedload transport rates and braided river evolution, something that has not been adequately done in the past.

The results of this research have been broken up into three chapters (Chapters 4-6), each related to understanding the linkages between channel morphology and bedload transport processes in gravel-bed braided rivers. Although individual research objectives and questions are presented in the introduction of each chapter, the main research questions can be summarized as the following:

1. The Variability in the Morphological Active Width (Chapter 4)
   - What is the variability in the morphological active width over a range of stream power and how does this variability relate to bedload transport rates as well as other morphological and hydraulic parameters?

2. Morphometric Estimates of Bedload Transport Rate (Chapter 5)
   - What are the spatial and temporal differences in braided river morphology and bedload transport rate and how do these differences impact estimates of bedload transport rates using of the morphological reach-budget method for a known sediment output and under the assumptions of the minimum budget?

3. Grain Size Evolution and Bed Mobility in Gravel-Bed Braided Rivers (Chapter 6)
   - How does grain size distribution and bed mobility change over event hydrographs in a braided river and are these changes related to channel morphology?

Chapter 3

3 Experimental Methods

3.1 Chapter Structure

The following chapter presents all the experimental methods used for this thesis research. Section 3.2 begins by introducing the experimental model used in the primary data collection. Section 3.3 outlines the details of operating the physical model. The next section, section 3.4, outlines the specific experimental conditions used in this research in terms of slope, discharge, and initial channel evolution. Section 3.5 outlines the main data collection procedures for capturing photographs of the model surface. Section 3.6 describes the main steps in data processing, specifically the generation of digital elevation models (DEMs) and the creation of DEMs of Difference (DoDs). Section 3.7 describes the procedures used to measure and characterize channel morphology and bedload transport flux. The last section briefly summarizes the data set and assessment of the methods.

3.2 Experimental Setting

3.2.1 Physical model

This research was based on data gathered from small-scale physical models of gravel-bed rivers in a river modelling flume located at the Boundary Layer Wind Tunnel Laboratory at The University of Western Ontario (UWO) (Figure 3.1). Affectionately known as "Flo", the flume was 18.3 m long and 3 m wide with an upstream head tank, a downstream tail tank, and a moveable bridge that spanned the width of the flume (Figure 3.2). The flume had adjustable slope and discharge that could reach a maximum of 2.5 % and ~2.7 l s^{-1}, respectively. In addition, five metal sediment baskets with a mesh size of 0.1 mm spanned the length of the tail tank to collect all sediment output from the flume (Figure 3.2).

Figure 3.1 – Image of the physical gravel-bed river flume in the Boundary Layer Wind Tunnel Laboratory at the University of Western Ontario. Arrow indicates flow direction.
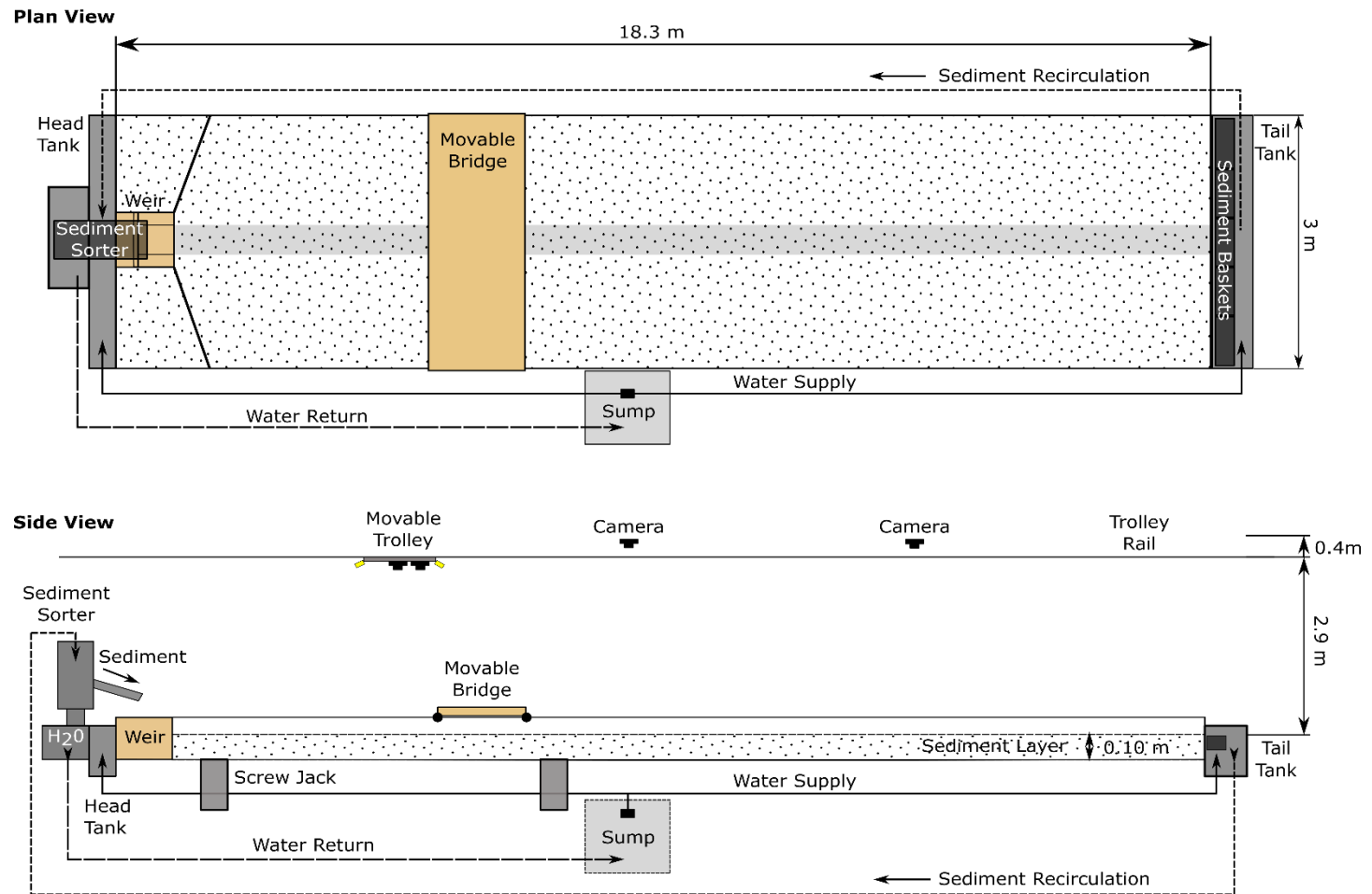
Figure 3.2 – Schematic of the river modelling flume . Plan view (top) and side view (bottom) showing the locations of the upstream head tank, sediment sorter, downstream tail tank, sump pump, screw jacks, and cameras.

The grain size distribution in the flume ranged from 0.18 mm to 16 mm, with a D_{10} of 0.32 mm, D_{50} of 1.18 mm and D_{90} of 3.52 mm (Figure 3.3). The grain size distribution of the flume corresponds to a distribution scaled by 1:35 from the Sunwapta River in Alberta, Canada (Figure 3.3). The Sunwapta River is a proglacial braided river located in Jasper National Park in Alberta, Canada that has a median grain size of 41 mm and an approximate slope of 1.5 % (Figure 3.4). Grain size distributions for the Sunwapta River were collected in 1999 and 2003 by a research team organized by Dr. Peter Ashmore. To reduce cohesion and bedforms (e.g., ripples), the lower limit of the grain size distribution was truncated so that grains smaller than 0.18 mm were excluded from the flume grain size distribution. For more details on the principles of Froude-scaled physical models, refer to Section 2.7.1 and Appendix A.
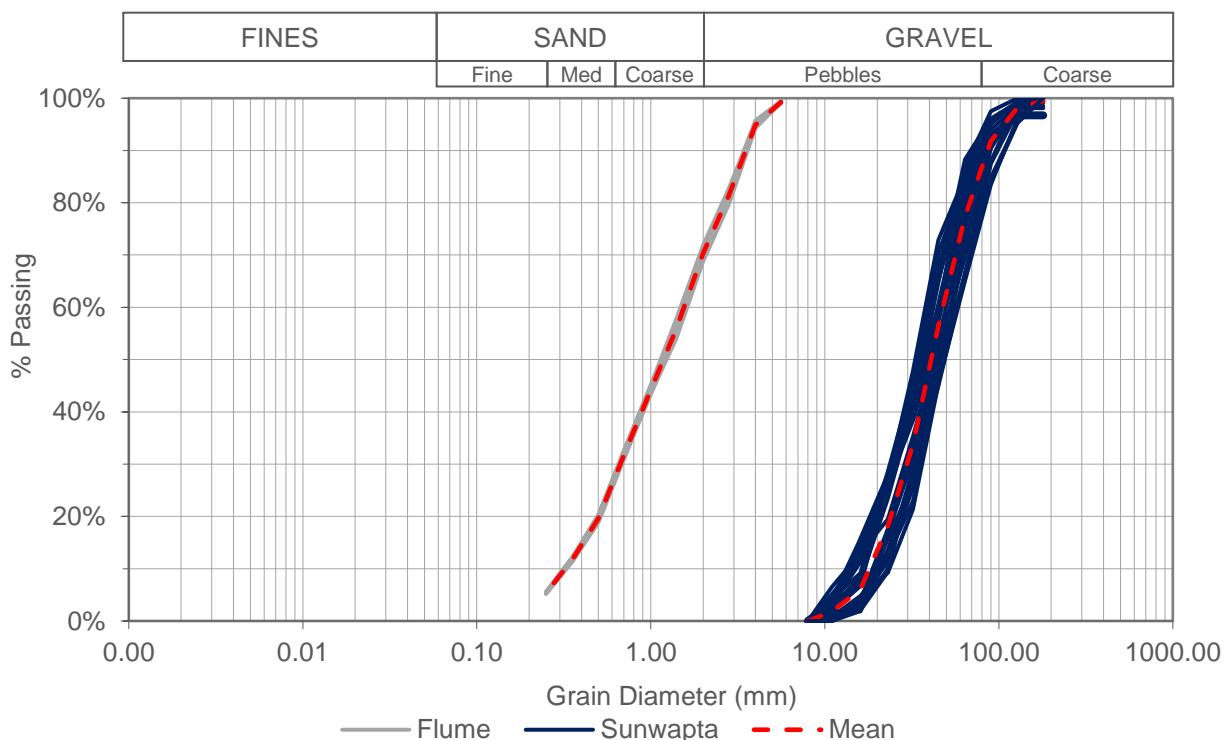
Figure 3.3 – Grain size distribution of the UWO flume and the Sunwapta River. **The Sunwapta River grain sizes represent the surface grain size distribution while the flume results shown are based on subsurface (below the surface) samples.**

Figure 3.4 – Image of the Sunwapta River, a proglacial gravel-bed braided river in Alberta, Canada that was used to scale the grain size distribution of the UWO flume. Arrow indicates flow direction.

3.2.2 Visual Verification

While all the experiments performed were not modelled after the Sunwapta River specifically, the scaled-down grain size distribution makes it the most appropriate prototype for visual verification. Cameras placed on the adjacent hillslopes at the Sunwapta River from June-October between 2012 and 2016 provided time-lapse planform photos of river morphology every 30 minutes. These time-lapse photos served as a visual verification of similarity in channel morphology between a field prototype and the models (Figure 3.5). Specifically, photos from the field and flume were compared for similarity in channel form, number of anabranch channels (i.e., braiding intensity), and general structure of bars and confluences.

a)

b)
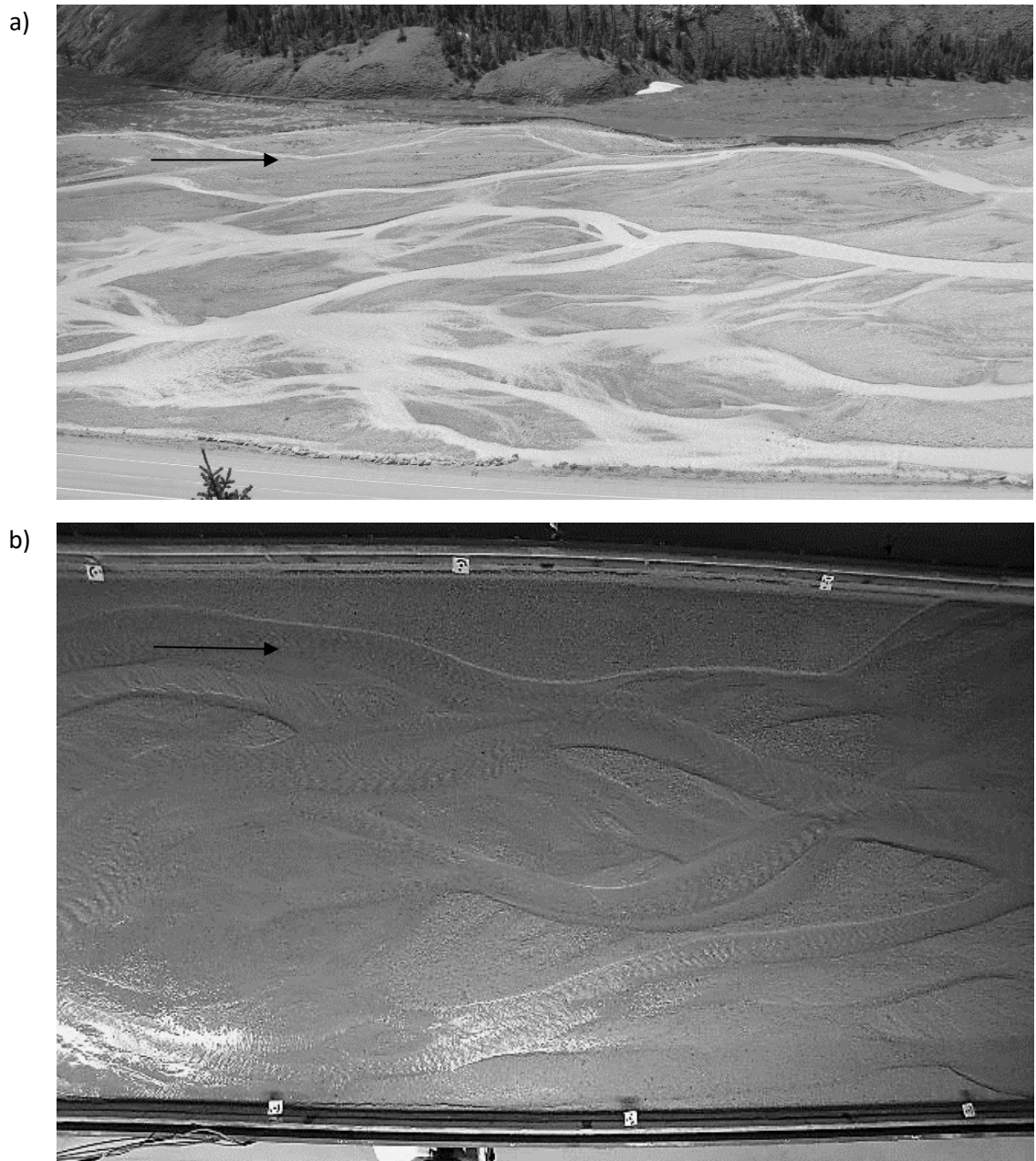
Figure 3.5 – Visual comparison of the a) prototype gravel-bed river and b) the river modelling flume. **Arrows indicate flow direction.**

3.3 Experimental Set-up

3.3.1 Slope

The slope of the model could be adjusted between 0 - 2.5 % using four screw jacks situated under the upstream end of the flume (Figure 3.2). All experiments for this research were completed at 1.5 % with the exception of one experiment, which was completed at 2 %. The slope of 1.5 % reflects the average slope of the upper reach of the prototype river, the Sunwapta River. Increasing the slope to 2 % extended the range of total stream powers modelled, and therefore the channel morphologies that could be investigated. The slope of the flume was determined using a Leica TCA 1800 total station using the same general procedure used for the target survey (details below). The complete slope survey of the model was completed each time the slope was changed and any additional measurements of slope were extracted from the digital elevation models (DEMs) generated from the flume surface.

3.3.2 Discharge

Discharge was estimated from the height of the water overflowing the upstream calibrated trapezoidal weir (Figure 3.6). The height of the water was adjusted using a valve situated at the sump pump and during experiments was measured from a measuring tape located in the head tank to 1 mm precision (Figure 3.2). Calibration of the weir determined the relative error on the linear interpolation of the discharge as a function of the water height (H) in the head tank and was approximately 4.5 % (additional details in Appendix B).
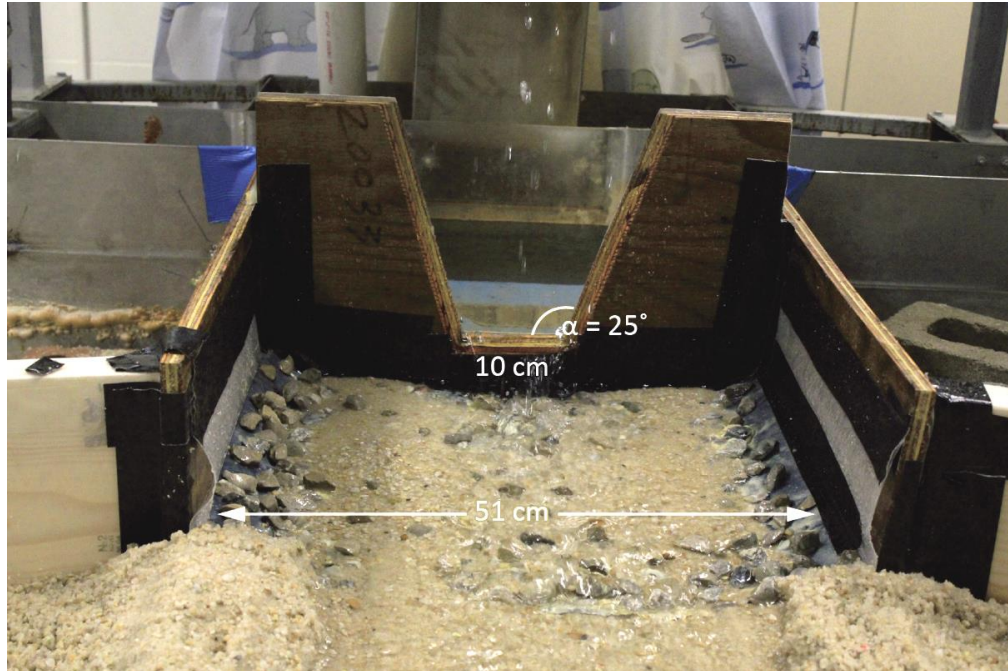
Figure 3.6 – View of the upstream calibrated weir below the head tank of the flume. Flow is towards camera.

3.3.3 Sediment Recirculation

The flume had an automated sediment recirculation system which brings water and sediment from the downstream tail tank and delivers it to an upstream sediment sorter positioned over the weir (Figure 3.2 and Figure 3.7). Any sediment deposited in the tail tank was used as the sediment input for the next experimental run, maintaining an overall sediment balance within the model.

The sediment sorter separated most of the water from the sediment using an internal mesh, so that water was returned to the head tank and sediment ran off the end of the sorter and onto the weir (Figure 3.7). To prevent the sediment from resting or building up on the slide, a vibrator attached to the sorter shook the unit to encourage the continual movement of sediment into the flume. Although water and sediment were mostly separated by the sorter, some water flowed onto the sediment slide as well. While this assisted moving sediment down the slide, it is also an additional source of water that was not accounted for in the weir discharge calibrations. Several tests were done to determine the contribution of water from the sediment sorter, which had an average of $0.12 \, \mathrm{l \, s^{-1}}$ (see Appendix C for details).

Since this value was well below the error for the discharge measurement, no additional adjustments were made to the overall discharge estimates.

Figure 3.7 – Image of the upstream sediment sorter. A water and sediment mixture from the sediment pump is propelled through the sediment pipe into the sorter. The sorter returned water to the head tank as sediment rolled down a slide onto the weir.

3.4 Experimental Runs

In total, six experiments were used in the data analysis of this research project (Table 3.1). Most of the experiments were divided into four stages: initial evolution, experimental round 1, a second evolution phase, and experimental round 2. At the beginning of each experiment, the bed of the flume was flattened using a large metal blade that spanned the width of the flume. A relatively small, straight, initial channel was carved into the flat bed to concentrate the flow over the bed and speed up initial evolution (Figure 3.8). The dimensions of the initial channel width increased with discharge from 25 cm ($0.7 \, \mathrm{l \, s^{-1}}$) to

65 cm at the highest discharge (2.5 l s^{-1}) while initial channel depth varied between 2 and 3 cm (Table 3.1).
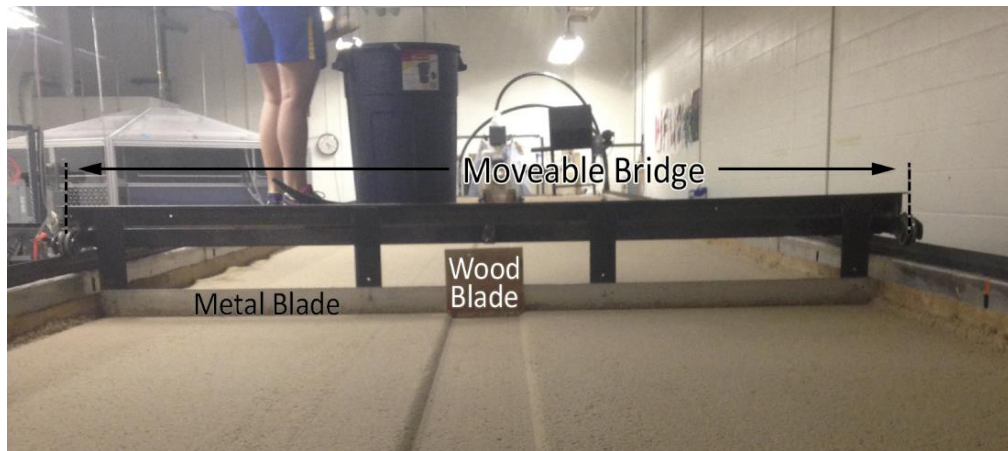
Figure 3.8 – Flattening of the flume bed with a metal blade attached to the movable bridge. A small wooden board attached to the blade was used to carve the initial straight channel.

During the evolution stage, the initially straight channel was left to self-form towards a dynamically stable morphology, defined by a steady average wetted width and braiding intensity. The length of time to reach the final dynamically stable morphology was different for each experiment and generally decreased with increasing stream power (Table 3.1). The exception was experiment 1, which did not braid, and represented a channel on the low end of the morphodynamic spectrum. After 16 hours of little channel change and a stable wetted width, the experimental runs for experiment 1 were started.

Table 3.1 - Summary of the experimental conditions. The experiment number represents the order in which the experiments were completed, the slope refers to the % slope of the flume, the discharge (Q) is the estimated model discharge (±4.5 %, l s⁻¹), total stream power (Ω) is the estimated model total stream power ($\Omega=\rho g Q S$) and the initial width and depth refer to the dimensions of the initial straight channel. The evolution time and experimental run time are the total hours for the difference stages of the experiment resulting in a final total run time (in hours) for each experiment.

Experiment	Initial Channel Conditions					Evolution Time			Experimental Run Time	Total Time
	Slope	Q	Ω	Width	Depth	Initial	2nd round	Total	Total	
	%	l s⁻¹	W m⁻¹	cm	cm	h	h		h	h
1	1.5	0.70	0.10	25	2.0	16	8		17.17	41.17
4	1.5	1.65	0.24	36	2.5	42	9		17	68
9	1.5	2.10	0.31	50	2.5	28.25	8		18.25	54.5
12	1.5	2.50	0.37	65	3.0	20	2		16.5	38.5
13	2	2.10	0.41	50	2.5	12	0.75		16.5	29.25
11	1.5	0.7 - 2.1	0.10 - 0.31	50	2.5	24	-		30.25	54.25
Total									111.75	285.67

Following initial evolution to a steady wetted width, 8 hours of experimental runs were completed during experimental round 1, divided into 15 or 30 minute intervals. At the end of each 15 or 30 minute experimental run, the flow of water to the flume was turned off and photos of the dry bed surface were taken for digital photogrammetric processing. In addition to photo surveys, the downstream sediment baskets were individually weighed at the end of each experimental run. Initially, intervals of 15 minutes were chosen based on the estimated rate of morphological change and the capacity of the downstream sediment baskets. It is important that the time interval between surveys be long enough to allow for detectable morphological change, so the time interval was extended to 30 minutes for experiment 1 after several 15 minute runs had barely detectable morphological change or bedload transport (Ashmore & Church, 1998; James et al., 2012).

The third stage of the experiment was a second shorter stage where the channel was left to evolve for several hours. This second evolution stage was to allow the channel to rework its morphology and to support research being done by Dr. Pauline Leduc on grain size mapping for which longer intervals of morphological change (rather than 15 minutes) were desirable. The final stage of the constant-discharge experiments was a second 8 hour round of experimental runs divided into 15 or 30 minute intervals. In total, each experiment included at least 16 hours of experimental runs and a variable number of evolution hours (Table 3.1). At the end of each experiment, the flume was 'reset' via flattening the bed and carving a new initial channel.

Except for experiment 11 (described in detail below), all other experiments were run at a constant channel-forming discharge for all four stages of the experiment (initial evolution, round 1, second evolution, round 2) (Table 3.1). Experiments 2, 3, 5, 7, and 10 were abandoned during the initial evolution stage because of excessive flooding on the flume bed. Flooding was avoided because it could lengthen the time for channel evolution and may result in channels forming along the edge of the flume, introducing unnecessary edge effects. Experiments 6 and 8, which were completed in full, were not included in the final analysis due to poor DEM quality. Therefore, the constant discharge experiments completed in full and included in the final analysis were experiments 1, 4, 9, 12, and 13 (Table 3.1).

The experimental conditions for the constant discharge experiments were originally chosen to cover a range of estimated total stream powers ($\Omega = \rho g D S$) (Figure 3.9 and Table 3.1). Experiment 9 and 13 were completed for the same discharge, but the increase in slope from 1.5 to 2 % for experiment 13 increased the stream power to 0.41 W m^{-1} from the 0.31 W m^{-1} of experiment 9 (Figure 3.9). Experiment 8 was completed at 1.14 l s[-1] (0.17 W m^{-1}) but was abandoned resulting in the gap between experiments 1 and 4.
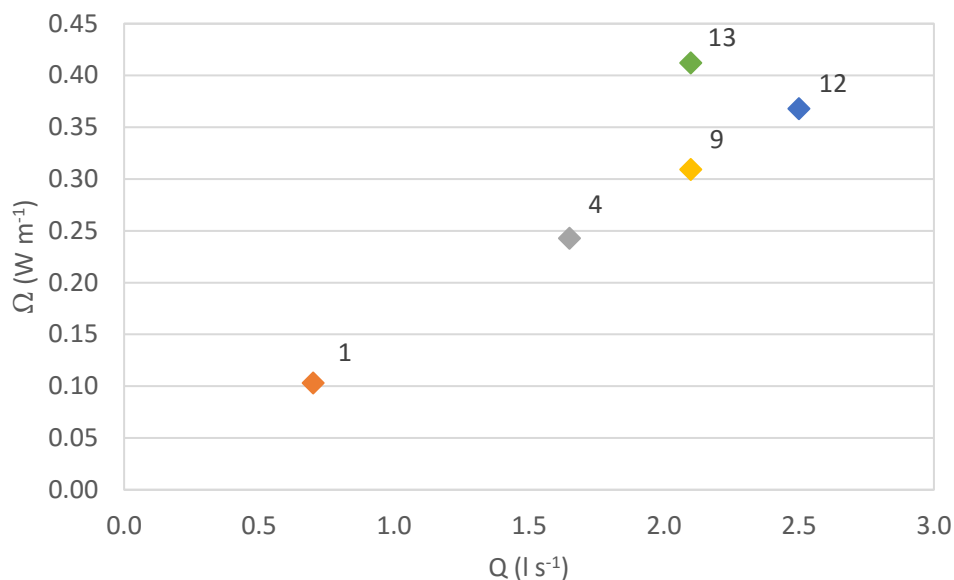
Figure 3.9 – Estimated total stream power (Ω) for the constant discharge experiments as a function of the model discharge (Q).

These constant channel-forming discharge models are considered generic models (i.e., they are not modelling a specific river prototype). Therefore, while the Froude numbers need not be exactly the same between the model and a particular field prototype, the Froude and grain Reynolds number help to characterize the flow characteristics of the different experiments (Table 3.2). The Froude (*Fr*) numbers and grain Reynolds (*Re**) numbers were calculated using the following equations:

$$Fr = U/\sqrt{gd} \qquad\qquad 3.1$$

$$Re* = U^* D_{90}/\upsilon \qquad\qquad 3.2$$

where U is the average velocity, g is the acceleration due to gravity, d is the average cross-sectional depth, U^* is the shear velocity ($U^* = \sqrt{\tau/\rho}$), D_{90} is the 90th percentile for grain size, and v is the kinematic viscosity (1.00×10^{-6} m^{2}s^{-1} at 20°C). The average velocity was estimated from Manning's equation ($U = \frac{1}{n}Rh^{2/3}S^{1/2}$) using an n= 0.03.

The estimated range of Froude numbers was between 0.52-0.68, which corresponds to subcritical flow, and are within the range commonly found in braided Froude-scaled models with similar conditions (Ashmore, 1988, 1991a, 1991b; Young & Davies, 1990; Peakall et al., 1996). The estimated average grain Reynolds numbers, which are a measure of the bed roughness with respect to the thickness of the viscous sublayer, ranged from 96.45 -167.06 so were much greater than 70 required for rough turbulent flow (Yalin, 1971; Peakall et al., 1996; Young & Warburton, 1996) (Table 3.2).

Table 3.2 - Summary of model hydraulic parameters for the constant-discharge (Q) experiments. Average depths (d) were estimated from river cross-sections and average velocity (U) was estimated from Manning's equation using an n=0.03. Fr is the Froude number and Re* is the particle Reynolds number.

Experiment	Q	d	U	Fr	Re*
	l s^{-1}	m	m s^{-1}		
1	0.7	0.005	0.12	0.52	96.5
4	1.65	0.006 - 0.008	0.13 - 0.16	0.54 - 0.56	105 - 122
9	2.1	0.007 - 0.012	0.15 - 0.21	0.56 - 0.60	114 - 149
12	2.5	0.008 - 0.015	0.16 - 0.24	0.57 - 0.62	122 - 167
13	2.1	0.008 - 0.010	0.18 - 0.21	0.66 - 0.68	122 - 136

Although the constant-forming discharges are generic models, experiment 11 had varying discharge designed to reflect the rising and falling limb of a hypothetical hydrograph. The hydrographs modelled were similar to experiments completed by Egozi & Ashmore (2008) based on the diurnal hydrograph of the Sunwapta River. The grain size in the model has been scaled down 1:35 with the Sunwapta River therefore, the corresponding discharges in the prototype can be estimated using the length scale based on equation 2.11. The result is

that discharges used in the model (0.7- 2.1 l s^{-1}) cover a range of discharges from 5.07-15.22 m^3 s^{-1} in the prototype (Table 3.3).

Table 3.3 – Discharge (Q) scaling between physical model and field prototype. The prototype is the Sunwapta River, Alberta, Canada and the scaling is based on the 1:35 ratio between the grain size distributions.

Model Q		Prototype Q
l s^{-1}	m^3 s^{-1}	m^3 s^{-1}
0.70	0.0007	5.07
0.83	0.0008	6.02
0.93	0.0009	6.74
1.14	0.0011	8.26
1.35	0.0014	9.78
1.65	0.0017	11.96
1.86	0.0018	13.48
2.10	0.0021	15.22

Experiment 11 was started from a flat surface and the same initial conditions as experiment 9 (1.5 % slope, initial channel dimensions of 50 x 2.5 cm, 2.1 l s^{-1} discharge) (Table 3.1). Experiment 11 then evolved to a stable morphology at constant discharge (2.1 l s^{-1}) followed by three successive experimental hydrographs, herein referred to as hydrographs A, B, and C (Figure 3.10 and Table 3.4). The slope was held constant for the length of the experiment, therefore differences in total stream power are due to changes in discharge alone. In total, 117 experimental runs were completed across all three hydrographs. The peak discharge of 2.1 l s^{-1} used for all three hydrographs was chosen as the approximate average peak discharge in the Sunwapta River based on the 1:35 scaling of the grain size. Therefore, while these hydrographs were not designed to replicate a specific event hydrograph in the Sunwapta, they do cover the average range of discharges found in the prototype river.
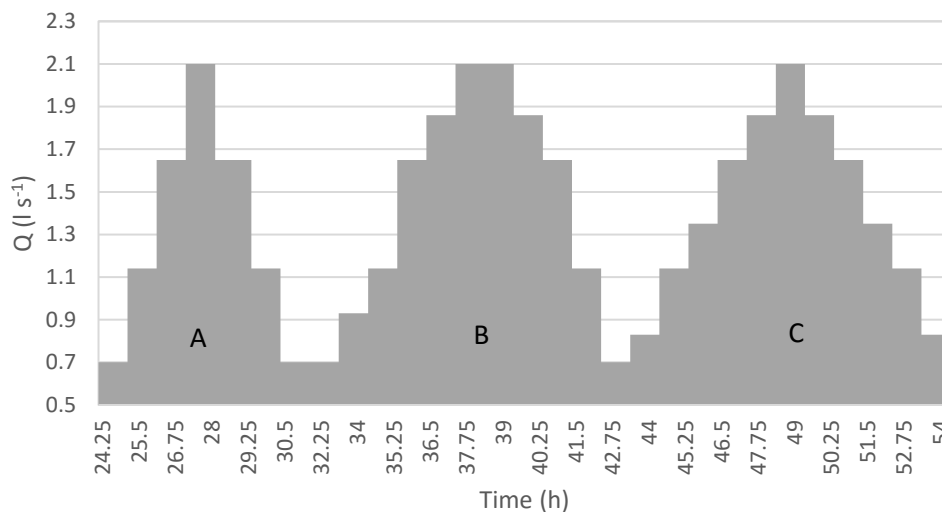
Figure 3.10 – Experimental design of the hydrograph experiment (experiment 11) after initial evolution, where Q is discharge and each hydrograph is represented by the letter A, B, or C.

Table 3.4 - Summary of the experimental conditions of the three hydrographs (A, B, and C) completed for experiment 11. Number of runs refers to the total number of experimental runs completed for each hydrograph, time is the total length of time to complete each hydrograph, minimum Q and maximum Q refer to the minimum and maximum discharges, and different Q refers to the total number of different discharges used in each hydrograph.

Hydrograph	Number of Runs	Time	Minimum Q	Maximum Q	Different Q
		(h)	$l\,s^{-1}$	$l\,s^{-1}$	
A	29	7.25	0.70	2.10	4
B	44	12	0.70	2.10	6
C	44	11	0.83	2.10	6

The discharges chosen for hydrograph A are the same as the ones used in the constant discharge experiments described above (Table 3.5). Each step of the hydrograph was run for 1 hour, divided into 15 minute intervals.

During the rising limb of hydrograph B, the runs for 0.7 l s^{-1} were completed over 30 minutes (Figure 3.10). This change, like that done for experiment 1, was an adjustment made to allow for greater morphological change between intervals. New discharges (0.93 and 1.86 l s^{-1}) were added to this hydrograph to better define the trends in morphology and bedload transport rates as a function of changing discharge (Table 3.5).

New discharges (0.83 and 1.35 l s^{-1}) were also used in hydrograph C to fill some of the discharge gaps from the previous 2 hydrographs. To save on time, 0.7 l s^{-1} was not used for this hydrograph so the lowest discharge used was 0.83 l s^{-1} (Table 3.4). Overall, the number of runs completed for each discharge was variable, with only three discharges being used in every hydrograph (Table 3.5).

Table 3.5 - Summary of the discharges used during the three hydrograph experiments. The discharge (Q) refers to the model discharge used, the number of runs refers to the total number of experimental runs completed at each discharge, while the hydrograph states in which hydrographs each discharge was used.

Model	Number of Runs	Hydrograph
Q (l s^{-1})		
0.70	16	A, B
0.83	8	C
0.93	4	B
1.14	24	A, B, C
1.35	8	C
1.65	21	A, B, C
1.86	20	B, C
2.10	16	A, B, C
Total	117	

Figure 3.11 shows how the model discharges and total stream powers used for the hydrographs compared to those of the constant discharge experiments. The hydrograph experiments covered a range of total stream power from $0.10 - 0.30$ W m^{-1}, corresponding with the stream power of experiments 1, 4, and 9 (Figure 3.11).
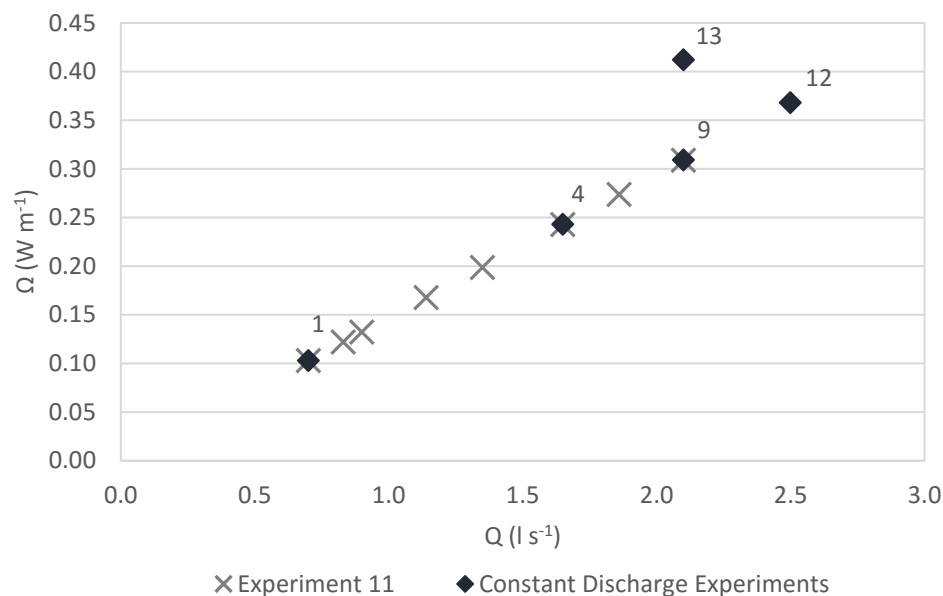
Figure 3.11 – Total stream power (Ω) for all experiments as a function of discharge (Q).

3.5 Data Collection

During each 15 or 30-minute experimental run, photos from two stationary cameras were taken of the model surface at regular intervals as an ongoing record of morphological change. At the end of each experimental time interval, the flow was turned off, the downstream sediment baskets were weighed and emptied, and the surface of the model was drained. Once drained, high-resolution images of the dry bed surface were taken using two additional cameras for later DEM generation. Once the dry bed photo surveys were completed, the flow was turned back on for the next experimental run. Details of targets locations as well as camera locations and settings are outlined below.

3.5.1 Coded Targets

The high-resolution topography of the flume surface required for this research was collected using digital photogrammetry. Coded survey ground control targets were required for image stitching as well as to generate a coordinate system and scale during DEM generation (Agisoft, 2016). The coded targets used were printed from Agisoft PhotoScan (version 1.0.0.1, herein called Agisoft), which was also used for DEM

generation. Each ~ 7 x 7 cm printed target was attached to one of the inside walls of the flume via industrial Velcro (Figure 3.12). A total of 18 targets were used (9 on each side of the flume) so that there were multiple targets in every image taken (Figure 3.13).

Figure 3.12 – Example of a coded target in the flume used for digital photogrammetry georeferencing.

Targets locations for georeferencing were determined using a total station and the angle intersection method, which is used to determine a point location from two or more stations with known locations (Chandler, 1999). The general survey method was adopted from previous experiments (see Gardner, 2009), where two station locations (Survey Station 1 and Survey Station 2 in Figure 3.13) were used for each survey. The locations of three external control points on the laboratory walls (1B, 3L and 3LB in Figure 3.13) determined at the beginning and end of each survey were used to ensure precision (<0.002") of coordinates and survey orientation. Once each coded target was surveyed twice from each of the two survey station locations, the average horizontal and vertical angles were converted into a 3D (xyz) position using trigonometry and exported as a text file for use in Agisoft's automatic target detection process (see Appendix D for additional details on surveying methods).
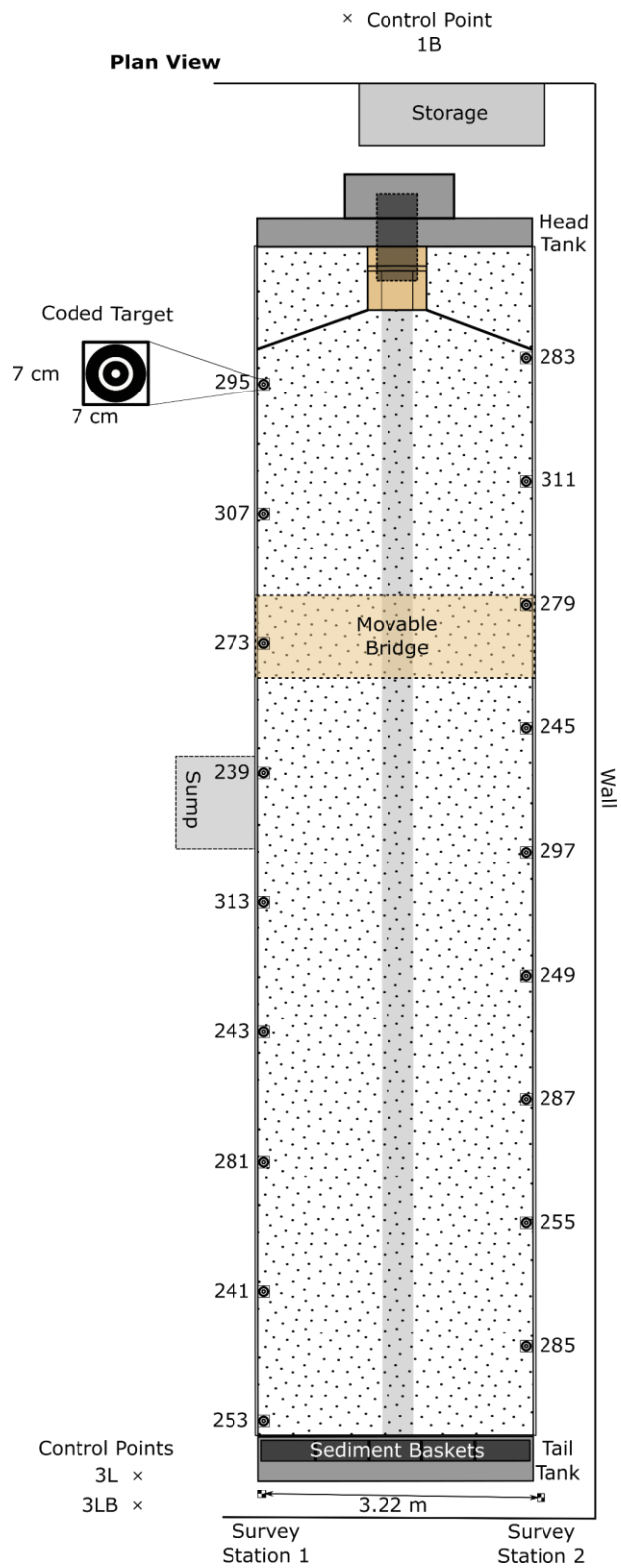
Figure 3.13 – Locations of the coded targets, control points, and survey stations from a plan view of the flume.

3.5.2 Camera Settings and Locations

During each run, two Olympus C5060 cameras located in fixed positions 3 m above the flume were used to provide a continuous record of braidplain evolution (Figure 3.2). These images were used in the measurement of braiding intensity and wetted width. Each Olympus camera had a wide-angled lens that covered the full width of the flume and a length of 5.4 m, allowing for a total coverage of 10 m with ~ 0.5 m overlap between the two images (Figure 3.14). These cameras captured photos simultaneously every 2.5 minutes (150 s) during experimental runs using the software program Camera Controller. The settings for the Olympus cameras were slightly different but these differences were corrected in post-processing using Adobe Photoshop by converting the images to greyscale. Adobe Photoshop was used for lens correction, cropping, and final image stitching (Figure 3.14).
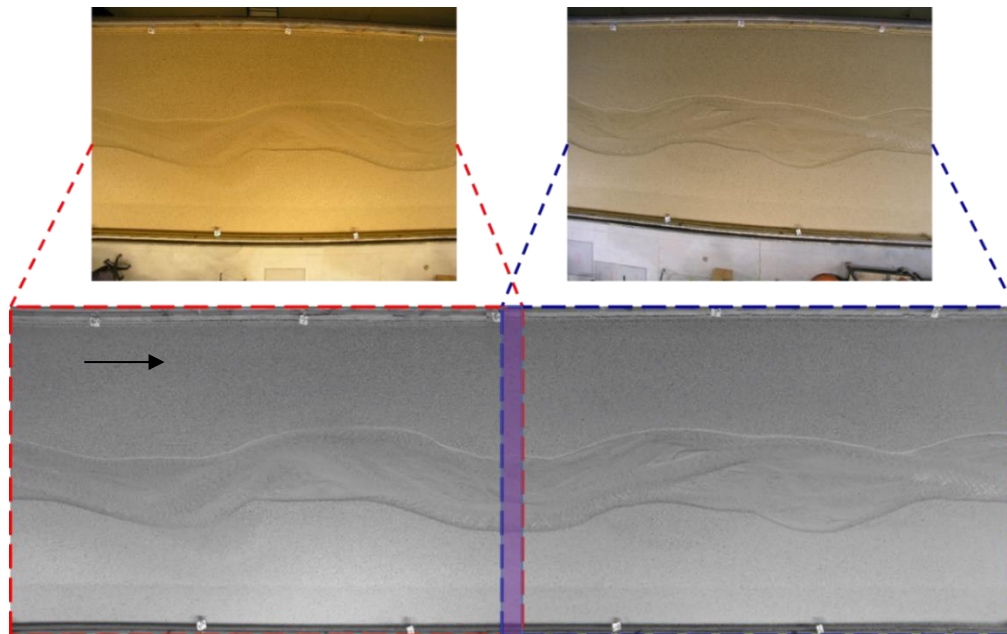
Figure 3.14 – Olympus image lens and colour correction for the upstream (top left) and downstream (top right) cameras. The purple section outlined in the bottom image shows the 0.5 m overlap between the two images. Arrow indicates flow direction.

At the end of each experimental run, high-resolution images of the flume surface were taken with two Canon T5i cameras with a standard 20 mm lens. The Canon cameras were stationed on a movable trolley situated 2.9 m above the flume bed (Figure 3.2 and Figure

3.15). The cameras were positioned in a convergent geometry on either side of the trolley so that there was ~80 % overlap between photos over the center area of the model where morphological change was expected to be greatest. The convergent positions of the cameras were determined through extensive testing of possible arrangements. It was found that slightly oblique photos from multiple angles provided better precision for the Structure-from-Motion (SfM) photogrammetry methods used than vertical images from a single camera. In addition, strictly vertical images can cause a doming effect during processing due to incorrect determination of the camera parameters (Smith et al., 2016). Therefore, convergent imagery was preferred. During each photo survey, a photo was taken from each camera every 30-50 cm. In total, it took an average of 100 photos (50 photos from each camera) to cover the entire length of the flume. Both Canon cameras were connected to a single computer on the floor and the software program DigiCamControl was used to trigger both cameras simultaneously. A 24 mm lens was used during experiment 9 while repairs were being made to the 20 mm lenses. While there was no difference in the average DEM quality between the two lenses, the 20 mm offered greater image overlap and therefore was used for the remaining experiments (i.e., experiments 11, 12 and 13). Additional camera details are in Appendix E.
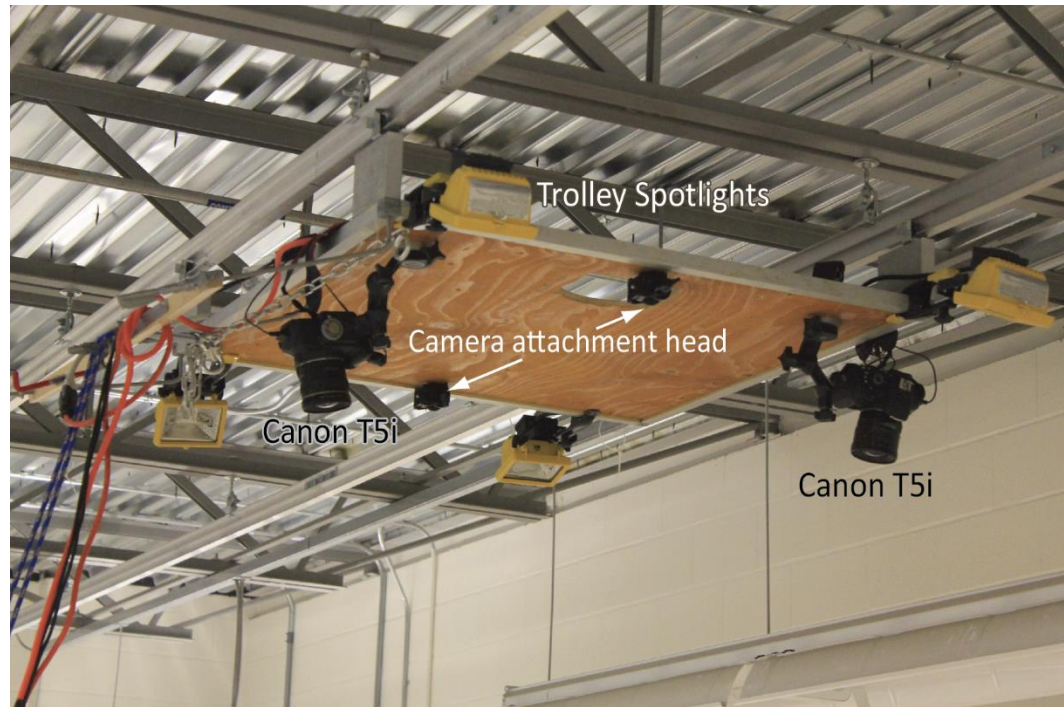
Figure 3.15 – Camera locations on the moveable trolley approximately 3 m above the flume surface. The trolley had two additional camera attachment heads as well as adjustable spotlights at each corner.

For the dry bed photos taken at the end of each run, the flume was left to drain until there was no obvious standing water in the deepest scour holes (Figure 3.16). This was done because water distorts the surface and therefore does not provide an accurate topography of the channel bed during DEM processing (Smith et al., 2016). The time it took to drain the flume was highly variable (~20-90 minutes) and was strongly dependent on the depth of scour holes. Two dry bed photo surveys were taken of each dry surface before moving on to the next experimental run.

Figure 3.16 – Example of a dry flume surface from experiment 11. Image taken from the downstream end facing upstream.

In addition to the dry bed photo survey, a shortened photo survey was taken of the downstream half of the flume surface during the last minute of each experimental run (i.e., the wet bed photo survey) (Figure 3.17). Photos were only taken in the last minute to ensure minimal morphological change between the wet bed photo survey and the subsequent dry bed photo survey. These photos were used in the quantification of the wetted width and braiding intensity. Photos were only taken for the downstream half of the flume because that is approximately how much area could be covered quickly in 1 minute using the available camera setup.

Figure 3.17 – Demonstration of a wet photo survey being completed at the end of an experimental run. Arrow indicates flow direction.

During all photo surveys, only the spotlights attached to the camera trolley are turned on to minimize shadows and create an evenly lit surface where the photos were being taken (Figure 3.15 and Figure 3.17). In addition, turning off the ceiling lights during the wet bed photo survey helped to minimize reflection off the flowing water surface.

3.5.3 Sediment Baskets

The five sediment baskets located at the downstream end of the flume were weighed at the end of each experimental run using a load cell, which provided a digital readout of mass in kilograms (Figure 3.18). Testing the load cell with calibration weights established that there was a minor 0.5 % underestimation error.

The wet sediment weight determined from the downstream baskets was converted to an equivalent dry weight. To determine the conversion, a pre-measured mass of dry sediment was placed into a downstream sediment basket hooked up to the load cell, wetted, and then the mass was recorded every minute for 10 minutes. In addition to providing a sediment conversion factor, this test quantified the effect of changing sediment moisture content over time. Results showed that the moisture content of the wet sediment was greatest during the first minute after being wetted and then remained constant so that the wet sediment weight averaged 1.22 times the dry sediment weight. It is assumed that since the baskets were generally weighed within the first 10 minutes after the completion of a run but after the baskets had drained, the differences in mass due to moisture content would be minimal. For additional details on moisture content tests and sediment mass conversions, see Appendix F.
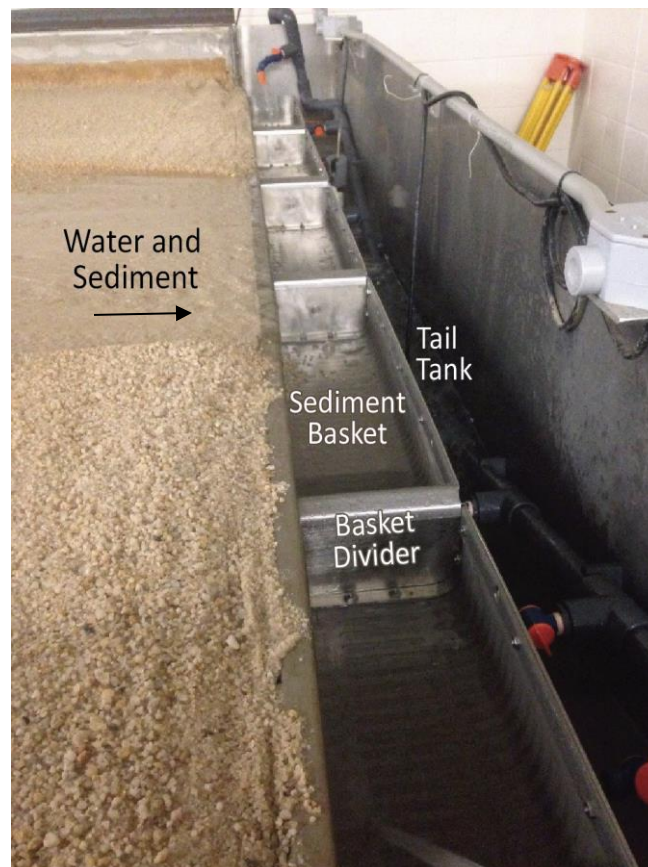
Figure 3.18 – Image of the five sediment baskets located in the downstream tail tank.

3.6 Data Processing and DEM Generation

3.6.1 Image Processing

The software package Agisoft PhotoScan 1.0.0.1 was used for photogrammetric processing to convert both the dry and wet bed photo surveys into high-resolution digital elevation models (DEMs). This method of DEM generation was chosen because it produced similar high-resolution results to previous photogrammetry applications (±1 mm) but Agisoft's built-in target detection made it faster and more flexible to use (Gardner and Ashmore, 2011; Kasprak et al., 2014).

There are four stages used by Agisoft to create a DEM and orthophoto from each photo survey: 1) camera alignment 2) dense point cloud creation 3) mesh creation and finally 4) orthophoto generation and adding texture to the mesh (Figure 3.19). During camera alignment, the program searches for common points on the photos (e.g., detects coded targets) and matches them while simultaneously estimating camera positons. The result is a sparse point cloud, but more importantly, it automatically refines the camera self-calibration parameters. With the matched photos and camera positions, Agisoft creates a dense point cloud next which is used in stage 3 to create a 3D polygonal mesh of the model surface (Figure 3.19).
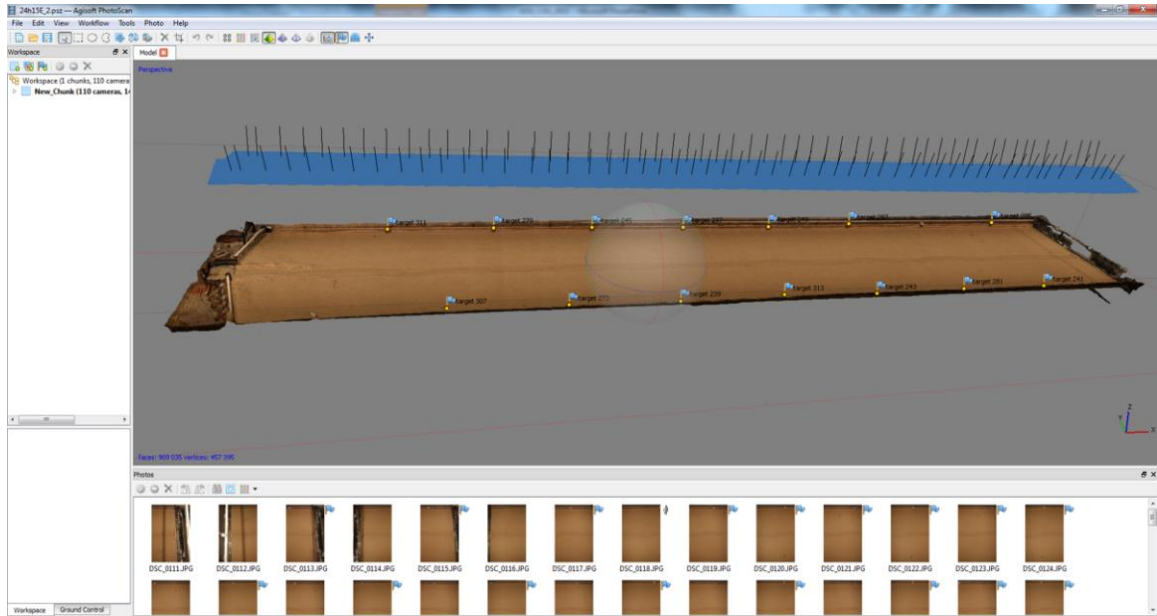
Figure 3.19 – Agisoft PhotoScan processing screen shot. Individual images from the photo survey appear at the bottom of the screen, the blue area above the 3D model surface represents the automatically detected camera locations, and the small flags on the middle image are the locations of coded targets that were automatically detected.

Each photo survey of the full flume took approximately 5 hours of processing time to generate a high-resolution DEM in Agisoft. Therefore, several weeks of continuous processing was needed for each experiment just to produce the raw DEMs of the experimental runs. To ensure that the data were processed continually, Dr. Pauline Leduc wrote a simple Python script that allowed for batch processing of the photo surveys. The input for the script was the images from the photo surveys, code target locations, and initial camera calibration parameters. While this process was time consuming, the automation made it possible to continuously process photos and generate >1000 high-resolution DEMs across all experiments. The output of the batch processing script was an orthophoto and a DEM of the flume surface with 1.5 mm pixels, which is similar to the D_{50} of the model at 1.18 mm. The script additionally exported a report on the Agisoft project, indicating the number of photos used, the image overlap, and the estimated error on target detection. Once exported, the orthophoto provided a record of braiding evolution as well as an opportunity

to visually inspect photo processing. The DEMs, which were used to quantify the areas and volumes of morphological change, underwent additional processing as outlined below.

3.6.2 DEM Correction

To correct systematic errors in the DEMs, the following steps were completed:

1. Removal of high frequency noise
2. Initial vertical correction using the downstream metal bar as a datum
3. Decision between DEM_1 and DEM_2 based on mean error
4. Fine vertical adjustments
5. Fine lateral adjustments (required for experiments 1, 4 and 9 only)
6. Slope detrending

With the exception of the manually defined final mask in step 3, each step of this process was automated using a script developed by Dr. Pauline Leduc in the open-source general analysis and software visualization program Scilab. Details of each step are described below.

The initial raw DEMs generated in Agisoft had the dimensions 13332 x 2346 cells with a cell size of 1.5 mm (19.99 x 3.52 m). High frequency noise was removed using a running averaged filter on height (z) with a step of 10 cells and the following equation:

$$Z_{corrected(x)} = \frac{z_x + z_{x-1} + \cdots + z_{x-(s-1)}}{s}$$

(3.1)

All values above 2 m and below -100 m were removed as obvious error points. There is a metal bar at the downstream end of the flume where the water flows into the metal sediment baskets. This bar was used as a preliminary vertical correction so that all DEMs were adjusted to have the same height at that metal bar. Unfortunately, some DEMs (especially the wet surface DEMs) are missing this bar, so the correction is not consistent and an additional convolution smoothing matrix was applied later. Brasington et al. (2003) used a similar smoothing matrix to normalize local variability based on a filter created through trial and error.

Following these initial corrections, a decision was made about which of the two DEMs, one from each of the dry photo surveys of each experimental run, to use in subsequent analysis. The quality of the DEMs was inconsistent, and the choice was made based on the distribution of error in a DEM of difference (DoD) created with the two DEMs (DEM_1 or DEM_2) of the same surface:

$$DoD(t) = DEM_2(t) - DEM_1(t) \qquad (3.2)$$

Since the DEMs were taken of the same surface, only minutes apart, any differences in elevation values are expected to be small. When the mean error of the DoD is less than 0.5 mm, the DEMs were deemed very similar and DEM_1 was used for further analysis. If the error is greater than 0.5 mm, additional DoDs were created to determine which of the DEMs, DEM_1 or DEM_2, was more appropriate for use. Under these circumstances two additional DoDs were created using a DEM from the closest experimental run where the DEM decision had already been made (called DEM_D) so that:

$$Dod_1 = DEM_D - DEM_1 \qquad (3.3)$$

$$Dod_2 = DEM_D - DEM_2 \qquad (3.4)$$

Again, the mean error value was evaluated and the DEM with the lowest error value was picked for further analysis. This decision-making process reduced the number of DEMs used in the final analysis to one DEM for each run, rather than two (Table 3.6). Only DEMs created during experiment runs (i.e., not the evolution stages) are included in Table 3.6.

Table 3.6 - Final DEM count for each experiment. Numbers are based on experimental runs only.

Experiment	Number of DEMs
1	39
4	69
9	72
12	67
13	67
11	118
Total	430

After the initial decision making process, many of the DEMs required additional adjustment and correction including vertical or lateral shifting. These issues could be due to the cameras shifting during the photo surveys, blurry images, or insufficient target detection. Each experiment had unique challenges and therefore each experiment was corrected as a batch.

To make fine vertical adjustments in the individual DEMs a final binary mask (M_f) was made for each experiment. To create the mask, the final DEM for each experiment was used so that areas defined as non-moving (e.g., areas near the edges of the flume) were manually classified as 1 while all other areas of the flume where morphological change occurred were classified as 0 (Figure 3.20). Then, an individual mask (M_{ind}) was created for each DEM automatically using the same classification system as the final mask (1= non-moving areas; 0= changing areas). Finally, a reference mask (M_{ref}) was created when the final mask was applied to the very first DEM (t=0) within each experiment.
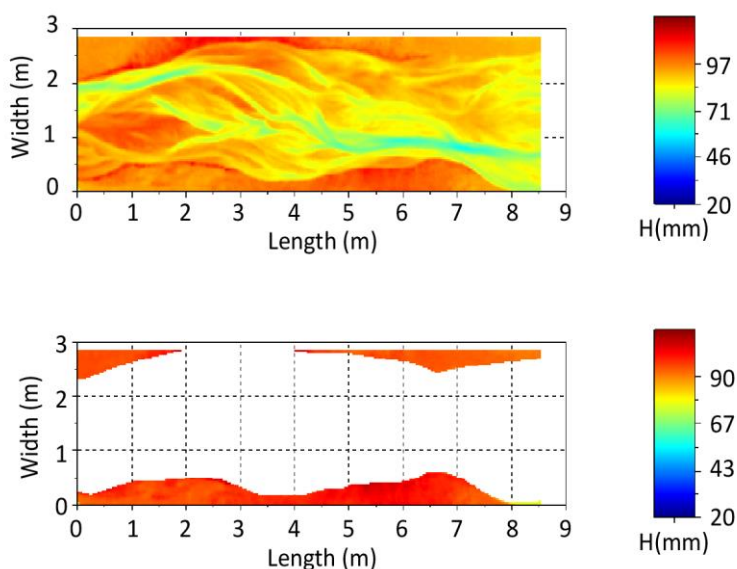
Figure 3.20 – Example binary mask used to define non-moving areas with a 1, and moving areas with a 0. The result is the lower image where all of the active areas are removed. H refers to elevation.

The mean values of the final mask, M_f, were intersected ($\cap$) with each DEM within a given experiment and the resulting value was compared to the values of the reference mask (M_{ref}).

As seen in Figure 3.21, an adjustment coefficient (α) was applied to reduce any difference between the values so that:

$$\propto (t) = DEM(t) \cap M_f - M_{ref} \tag{3.5}$$

$$DEM(t)_{correced} = DEM(t) - \propto (t) \tag{3.6}$$

Experiment 1, 4, and 9 had a lateral shift that required additional adjustments, which follow the same general procedure just described for the vertical correction.
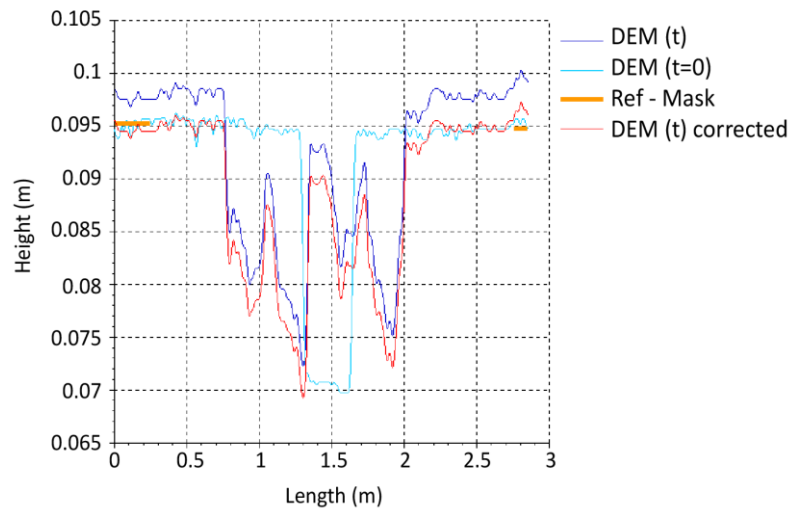
Figure 3.21 – Example of the vertical DEM correction using the reference mask.

Finally, to remove the slope of the flume from the DEMs, a correction matrix was created using the flume slope (S in %, where S = σ1.5 % except for experiment 13 where S = 2 %) and the cell size (0.0015 m) for every row (i) of the DEM (Figure 3.22).

$$D(i) = \frac{Sd(n - i)}{100} \tag{3.7}$$
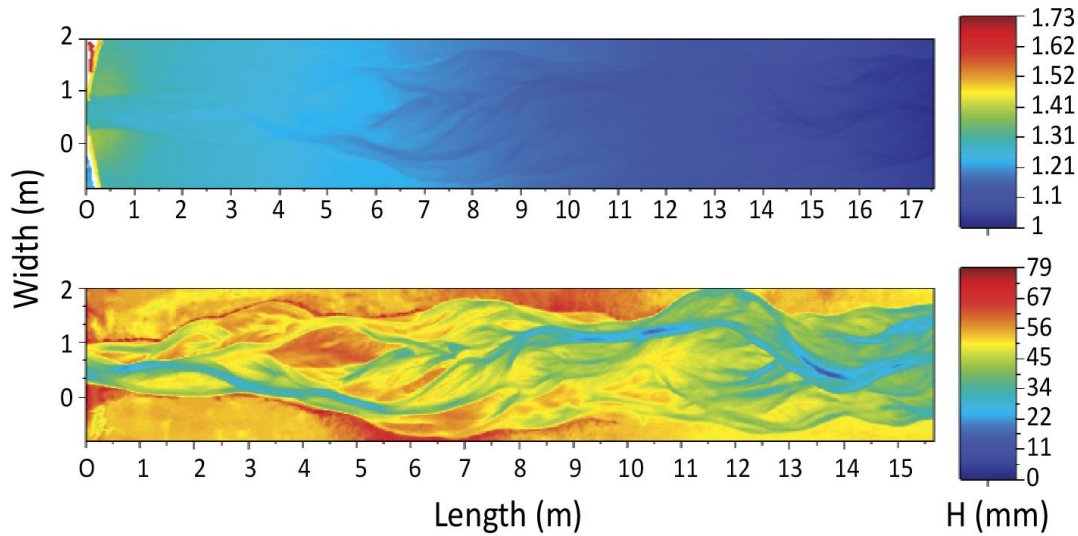
Figure 3.22 – DEM detrending using a correction matrix based on the model slope where the top image is a DEM before the flume slope is removed and the bottom is the detrended DEM.

3.6.3 DEM Error and Level of Detection

The uncertainty in each individual DEM can be represented by δz so that the uncertainty in the surface representation of a DEM can be described as:

$$Z_{Actual} = Z_{DEM} \pm \delta z \qquad (3.8)$$

Where Z_{actual} is the true elevation value, and the Z_{DEM} is the elevation value given in the DEM (Wheaton et al., 2009). This equation assumes that error in the horizontal components is negligible and independent of the vertical error (Wheaton et al., 2009).

For this research, the final mask created from the last DEM in an experiment was used to determine the standard deviation of the non-moving areas across all corrected-detrended DEMs (Table 3.7). This method assumes that any differences and therefore uncertainty found in non-moving flat areas will be similar to the uncertainty found in areas of change. The standard deviations of error (SDE) for each experiment were then used to define the threshold level of detection when creating DoDs and serve as an estimate of the vertical accuracy within the different experiments (James et al., 2012). The values in Table 3.7 are similar in magnitude to those found in other studies. Using similar digital photogrammetric

techniques for DEM extraction in a physical model of a drainage basin, Brasington & Smart (2003) reported standard deviation of errors of 1.2 mm.

Table 3.7 - Vertical error estimates for each experiment based on 1 standard deviation (σ) in the distribution of the elevations for the non-moving areas.

Experiment	σ (mm)
1	2.4
4	1.3
9	1.66
12	0.96
13	0.79
11	1.15

The standard deviations of error decreased with each sequential experiment (Table 3.7). In general, this is due to improved experimental procedures and photo quality over time. For example, out of focus photos were the main cause of the poor-quality DEMs in experiment 6 and 8, which resulted in those two experiments being excluded from data analysis. With the somewhat uniform appearance of the flume surface, this blurriness was not obvious while taking the photo surveys. In later experiments, small line drawings were added to flat areas of the flume surface at the upstream end as a check for focus. In addition, it was found that Agisoft performs better with a greater number of targets detected. In later experiments, targets that were being systematically omitted from detection were repositioned and resurveyed to increase overall target detection. Experiment 9 used 24 mm lenses rather than the 20 mm lenses used in all other experiments. This change and the reduction in surface overlap between photos might account for the relatively high error value Table 3.7 associated with that experiment.

3.6.4 DEMs of Difference

Once DEMs of each run were corrected, the aim was to quantify topographic change through DEM differencing, where successive DEMs are subtracted to reveal changes in

elevation (Figure 3.23). Two different methods were used to create DEMs of Difference (DoDs) and both methods were done using Scilab scripts written by Dr. Pauline Leduc.
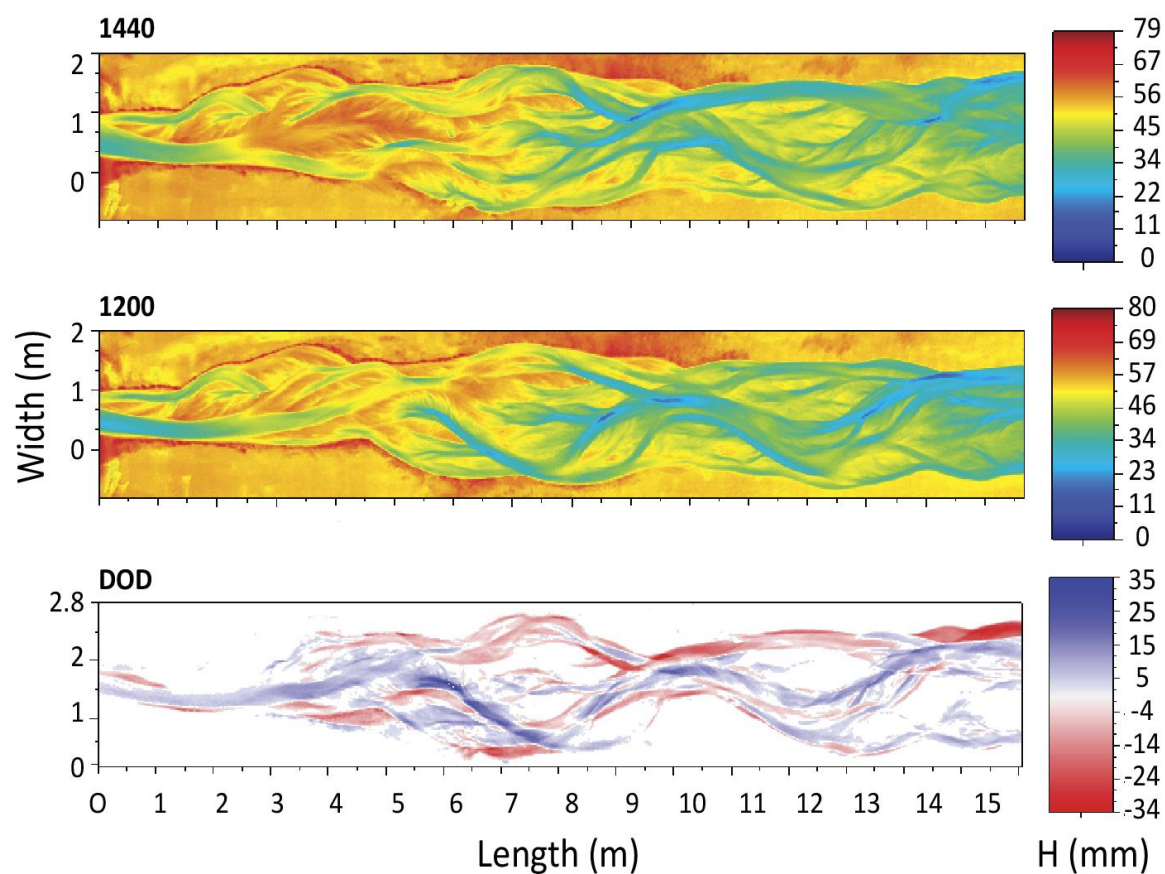
Figure 3.23 – Generation of a DEM of Difference using two consecutive DEMs. In this example, DEM$_2$ (time=1200 min) was subtracted from DEM$_1$ (time = 1400 min) to create a DEM of Difference where areas of erosion are red and areas of deposition are blue.

The first approach was the simple subtraction of two successive DEMs (DEM$_{t1}$ and DEM$_{t2}$), where all values less than the absolute threshold value ($<|\text{Th}|$) were removed:

$$DoD = DEM_{t2} - DEM_{t1} \qquad (3.9)$$

For this simple threshold method the absolute threshold value was based on the one standard deviation (σ) of the vertical error for each experiment (Table 3.8) (Rumsby et al., 2008). Further analysis found that these levels of detection still produced 'noisy' results in terms of areas and volumes of erosion and deposition. While geomorphic change detection

analysis will always have error associated with it, the quality of the final analysis will depend on the ratio between the signal (i.e., the changes in elevation) and the noise (i.e., the error) (James et al., 2012). To reduce the noise and increase the confidence in the elevation signals, thresholds of 2σ and 3σ of the error estimate were also applied to the DoDs (Table 3.8 and Figure 3.24). These additional thresholds serve to provide more confident, although conservative, estimate of areas and volumes of change. For these results, it is assumed that the error fits a normal distribution. These thresholds were applied directly to the DoDs so that any absolute z values below the threshold were removed from analysis. This method is referred to as the "simple method".

Table 3.8 - Absolute threshold values for 1, 2 and 3 standard deviations (σ) of the vertical error estimates used in the simple threshold method.

Experiment	1σ	2σ	3σ
	mm	mm	mm
1	2.4	4.8	7.2
4	1.3	2.6	3.9
9	1.66	3.32	4.98
12	0.96	1.92	2.88
13	0.79	1.58	2.37
11	1.15	2.3	3.45

For the second threshold approach, a dilation filter was used which considers the status (e.g., change or no-change) of surrounding cells. This method was used to help reduce noise and increase continuity between areas of change. First, a DoD was created from two successive DEMs but no thresholds were applied. From this DoD, a binary mask was made using the absolute 3σ threshold so that '1' represented all values above the threshold and '0' were all values below the threshold. On this mask, a dilation filter was applied so that any '0' cells neighbouring '1s' within the filter were converted to '1s.' While different sizes and shapes of filters were created, the final filter was a circle with a 15-cell radius corresponding to a radius of ~3.3 cm, which is the size of a small channel in the flume. The result was a second mask, where the '1' areas had been extended into neighbouring cells. This secondary mask was applied to the original raw DoD (i.e., the DoD without a

threshold), and a lower detection threshold of 1 mm was applied only to remaining areas (i.e., cells with a value of 1) to get the final DoD. This method will be referred to as the "dilation method" (Figure 3.24).

Elevation Change (mm)

Deposition   Erosion

1 σ   2 σ   3 σ

Simple Threshold Method   Dilation Method
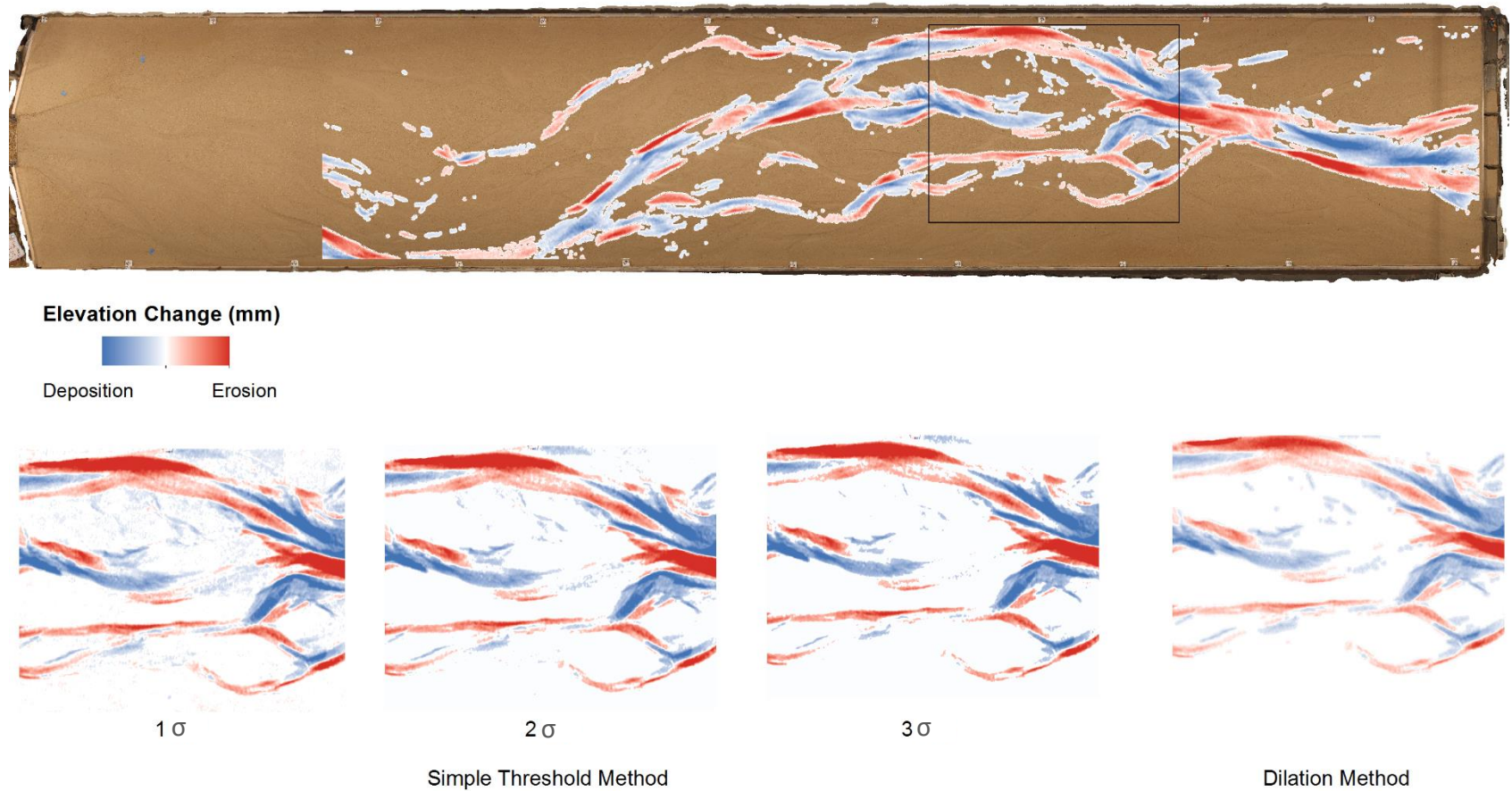
Figure 3.24 – Comparison of threshold methods used for change detection. **The top image shows the entire flume with an overlay of a DEM of difference from experiment 13. The bottom images show the different threshold methods as applied to the area in the black box of the full flume image. σ refers to standard deviation where the first three threshold images represent the simple threshold method at 1, 2, and 3 standard deviations of the vertical error estimate. The final threshold image is based on the dilation method.**

3.6.5 Sensitivity and Error Analysis

Figure 3.25 shows the active areas (i.e., areas of topographic change) for each of the threshold methods. As expected, the active area decreased with every increase in the simple threshold value. The dilation method lays between the thresholds of 1 and 2 standard deviations (Figure 3.25). Also, the thresholds for 2σ, 3σ, and the dilation method seem to follow a very similar pattern, but the lowest threshold (1σ) had a much more exaggerated and variable result (Figure 3.25). This sensitivity analysis, which was completed for each experiment, supports the use of two thresholds for further analysis. The simple 2σ threshold was chosen because it substantially reduced the amount of noise found at 1σ but was less conservative than 3σ, which had the potential to exclude significant areas of change. The dilation method was also used in the final analysis as a comparison between the two threshold methods (i.e., simple and dilation). Using only two thresholds rather than all four has the advantage of decreasing the amount of data analysis and script processing time. Therefore, analysis in subsequent chapters uses results from the simple method using the simple 2σ threshold and the dilation method.
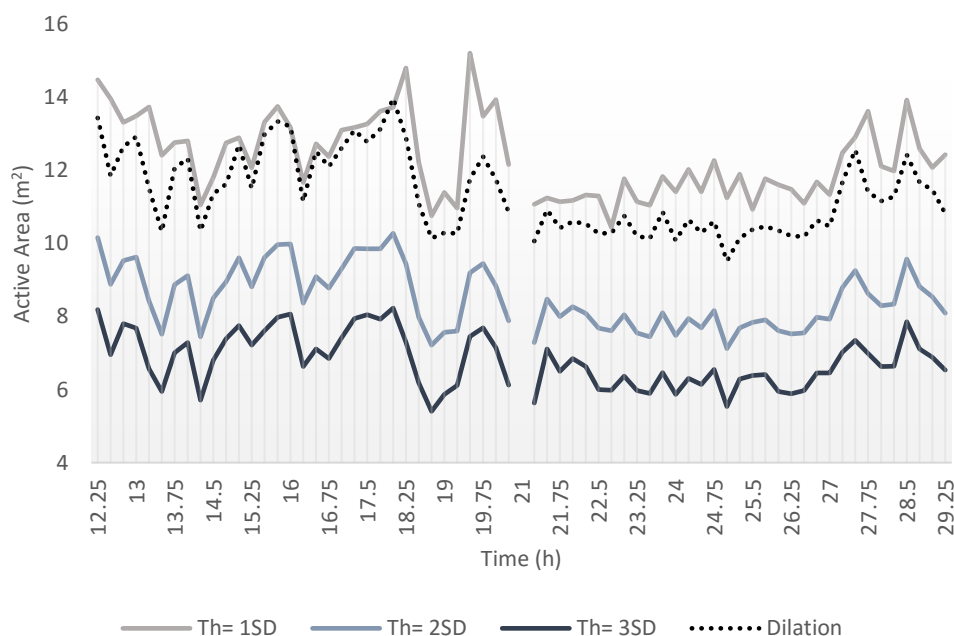
Figure 3.25 – Sensitivity analysis of the total active areas measured from a DoD based on the four different threshold methods. Results shown are from experiment 13.

Once the error for the individual DEMs has been determined, the error propagated into the DoD can be described as:

$$\delta U_{DoD} = \sqrt{(\delta Z_{new})^2 + (\delta Z_{old})^2}$$ (3.10)

Where δU is the propagated error in the DoD, and δZ_{new} and δZ_{old} represent the individual errors in the new DEM and old DEM respectively (Wheaton et al., 2009). Based on this equation, each experiment would have a propagated DoD error based on the standard DEM error (Table 3.9). The uncertainty values for the DoDs are of the same order of magnitude as the D_{50} of the bed sediment in the model (1.18 mm).

Table 3.9 - Estimated DoD error (δUDoD) based on the propagation of the standard deviation (σ) of the error in the experimental DEMs.

Experiment	DEM σ	δUDoD
	mm	mm
1	2.4	3.39
4	1.3	1.84
9	1.66	2.35
12	0.96	1.36
13	0.79	1.12
11	1.15	1.63

3.6.6 Visual Inspection

In addition to the methods of analysis already described, each of the DEMs and DoDs were visually inspected. With knowledge of the expected terrain, as well as photos from the Olympus cameras, it was possible to note inconsistencies and distortions between the photos and the surface representation (Rumsby et al., 2008). As a result, several DoDs were deemed to be of poor quality and removed from the final analysis. For example, one DoD from experiment 1 was found to have very large areas of erosion and deposition on the sides of the flume in areas that are known to be flat. For this reason, this DoD was removed from all additional analyses. A similar visual inspection resulted in 13 DoDs being removed from the final analysis (Table 3.10).

Table 3.10 - Final number of DEMs of Difference (DoD) used for each experiment.

Experiment	Removed	Final DoD Count
1	1	37
4	3	65
9	3	68
12	2	64
13	0	66
11	4	113
Total	13	413

3.7 Measurements

3.7.1 Active Areas and Volumes of Erosion and Deposition

The final DoDs were cropped to 14 m from the downstream end of the flume to reduce inlet effects from the upstream weir (Figure 3.26). The study area was also cropped to exclude the sides of the flume so that the flume edges and targets would not be included in the final calculations of active areas and volumes of change.
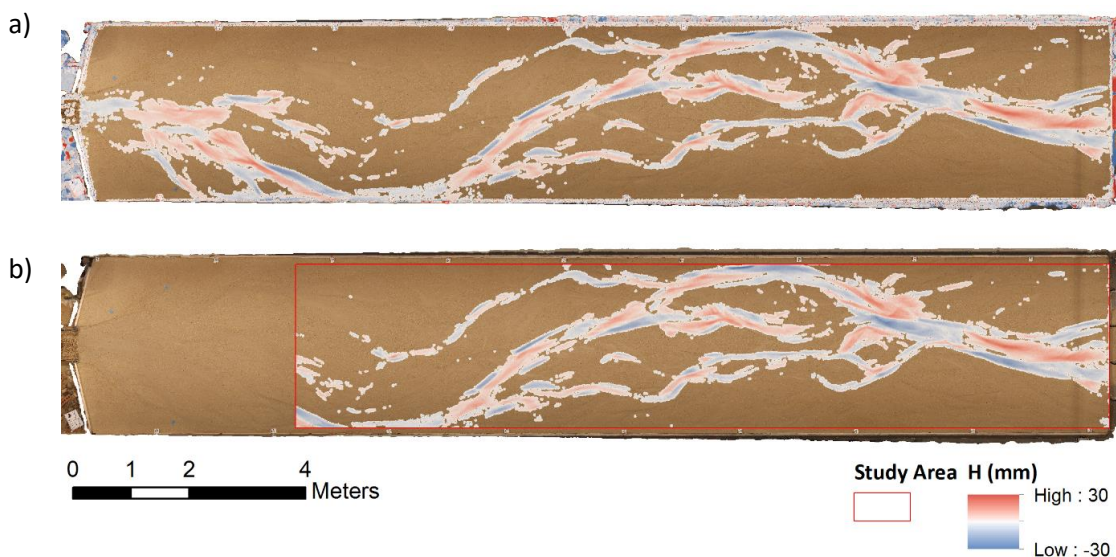
Figure 3.26 – The 14m downstream study area where image a) shows an overlay of the flume surface with a DEM of Difference from experiment 13, and b) shows the same DoD cropped to the 14 m downstream study area.

After the simple and dilation thresholds had been applied and the data had been cropped to the appropriate study area, an automated Scilab script was used to extract the active area. The total active area, defined as all areas of the flume that had topographic (i.e., morphological) change were quantified in the DoDs as the sum of all erosion and deposition cells multiplied by the cell size (0.0015 x 0.0015 m). The reach-averaged morphological active width (AW) was estimated for each experimental run by dividing the total active area (m^2) by the reach (i.e., 14 m) length (m):

$$Active\ width = \frac{Active\ area}{Reach\ length} \qquad (3.11)$$

By multiplying the elevations (sum of z values) in the active areas of deposition and active areas of erosion by the cell size (0.0015 x 0.0015 m) it was possible to calculate a volume of deposition (V_d) and erosion (V_e). The summed volumes of erosion represent all of the sediment moving from storage (i.e., eroding banks or bars) while the summed volumes of deposition represent additions to sediment storage (i.e., aggradation of bars) (Wheaton et al., 2013). The total volume (m^3) of morphological change, also known as the bulk change, was then calculated for each experimental run (Wheaton et al., 2013):

$$Bulk\ Change = \sum V_d + \sum V_e \qquad (3.12)$$

The active depth, a reach-averaged measure of the depth of change, was estimated by dividing the total bulk change by the total active area for each experimental run:

$$Active\ depth = \frac{Bulk\ change}{Total\ active\ area} \qquad (3.13)$$

Since the thresholds removed all values below the absolute threshold, any change in elevation (z) greater than 0 represented depositional areas and values less than 0 represented erosional areas. In this way, the active areas and bulk change, as well as the active width and depth, could be calculated in terms of their separate erosional and depositional components for additional analysis.

3.7.2 Sediment Budgeting

The volumetric net change in storage (δS) was determined from each DoD by summing all of the volumes of erosion and subtracting them from the summed volumes of deposition (Rumsby et al., 2008; Wheaton et al., 2013):

$$\delta S = \sum V_d - \sum V_e \qquad (3.14)$$

Integrating the net change in storage over a given time (Δt) expresses a sediment budget based on the conservation of mass:

$$Q_o = Q_i - \gamma_s \delta S / \Delta t \qquad (3.15)$$

where Q_o is the mass transport output from the reach, Q_i is the mass transport into the reach, γ_s is the sediment bulk density, δS is the volumetric net change in sediment storage and Δt is the time interval (Hoey & Sutherland, 1991; Martin & Church, 1995; Brasington & Smart, 2003; Brasington et al., 2003; Surian & Cisotto, 2007). In many cases it is impossible to know both the input and output into the reach which introduces uncertainties into the analysis (Lindsay & Ashmore, 2002; Brasington & Smart, 2003). In this research, the sediment output was known and measured from the downstream sediment baskets. With volumes of erosion and deposition, the time interval, and a known Q_o from the downstream baskets, it was possible to create sediment budgets for each experimental run using equation 3.15 to investigate spatial and temporal patterns of sediment transport (Brasington & Smart, 2003).

3.7.3 Wetted Width

The minimum, maximum, and average wetted width for each experiment was determined using a combination of wet bed orthophotos and the Olympus photos taken during the experimental runs. Like the dry bed photo surveys, the wet bed photo surveys were processed in Agisoft which resulted in a DEM and an orthophoto of the surface covering between 6-10 m of the flume surface (Figure 3.27).

Figure 3.27 – Example of a wet bed orthophoto created from a wet bed photo survey. This orthophoto was taken from experiment 11 and the arrow indicates flow direction.

Following the procedure described in Egozi and Ashmore (2008, 2009), the total wetted area and exposed bars were manually outlined in each orthophoto using ArcGIS (Figure 3.28). From here, the total wetted width was calculated by dividing the total wetted area (i.e., channel area and inundated area) by the reach length. In Figure 3.28, channel areas were defined by locations where water appeared to be flowing (i.e., ripples on the surface of the water), while inundated areas were areas darkened by water without obvious flowing water. This additional digitizing and classification was helpful for determining the braiding intensity from the orthophotos.

Given the large number of experimental runs, only a small subset of orthophotos were digitized for each experiment. For experiment 1, only 4 orthophotos were digitized. For experiments 4, 9, 12, and 13 one orthophoto was digitized every two hours of experimental time, evenly spaced out through the experiment. Therefore, a total of 8 orthophotos were digitized for those experiments for a total of 36 digitized images across all the constant discharge experiments. For experiment 11, one orthophoto was digitized at the end of each discharge step for all three hydrographs for a total of 28 digitized images.
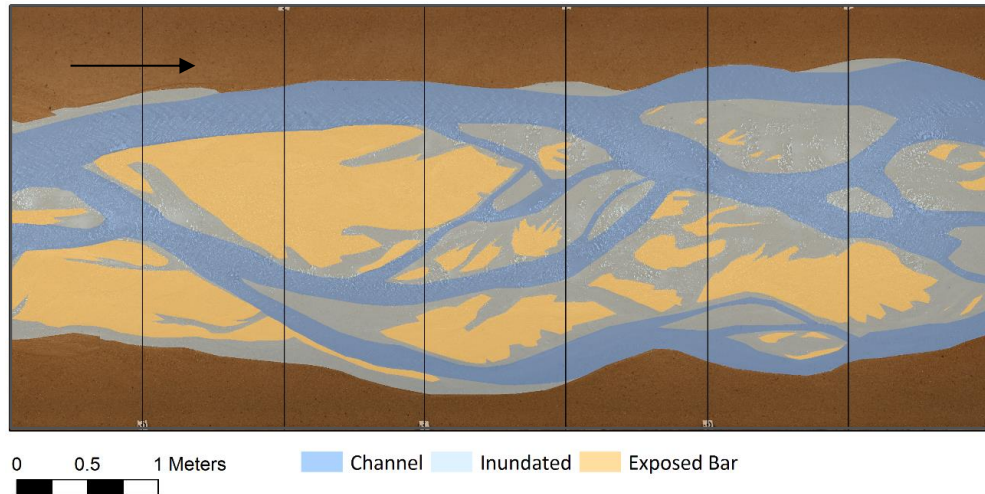
Figure 3.28 – Example of digitized orthophoto for measuring wetted width and braiding intensity. The black vertical lines represent the 1 m cross-section used for channel counts. Arrow indicates flow direction.

3.7.4 Braiding Intensity

The definitions of braiding intensity follow those provided by Egozi and Ashmore (2009) so that the total braiding intensity (BI) was the average number of wetted channels and the active braiding intensity (ABI) was the number of channels actively conveying sediment. Like the estimates of wetted width, measures of braiding intensity were based on the wet flume orthophotos complemented with images from the overhead Olympus cameras. Estimates of braiding intensity were completed using the channel count method at 1m cross-sections in ArcMap 10.4 and then averaged for the reach (Figure 3.28).

Average active braiding intensity (ABI) was determined using the DoDs from the experimental runs. In many cases a single channel may have multiple active areas, therefore a simple overlay of the dilation DoDs on the digitized orthophotos was used to distinguish channel boundaries (Figure 3.29). The active channel count was completed at the same cross-sections as braiding intensity and then averaged for the reach.
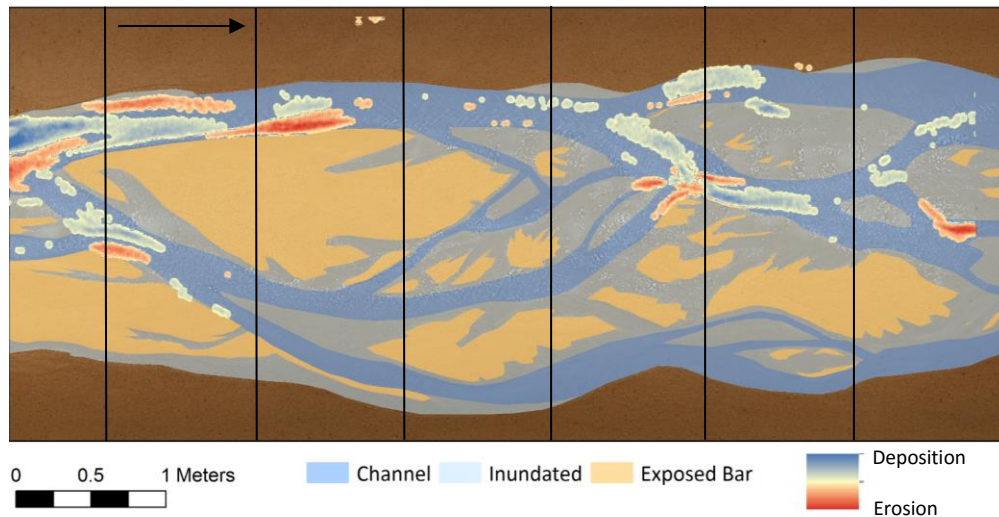
Figure 3.29 – Overlay of a DoD and digitized orthophoto for the estimation of active braiding intensity. Black vertical lines delineate the 1m cross-sections used for the channel count method. Arrow indicates flow direction.

3.7.5 Particle Size

Sediment samples from the sediment baskets were collected at irregular intervals for experiments 1- 9. For experiment 11, samples were collected for each experimental run while sampling from the baskets was done for every 4th experimental run during experiments 12 and 13 (Table 3.11).

Table 3.11 - Total number of sediment samples collected from the downstream sediment baskets.

Experiment	Samples
1	3
4	4
9	6
12	15
13	16
11	117
Total	161

The procedure used for determining the particle size distribution was a combination of simple dry sieving and composite sieving. Simple dry sieving is appropriate with clean samples that have negligible amounts of silt and clay particles (Head, 2006). Composite sieving is a means of reducing the size of a sample so that the resulting sample is more manageable when sieving (Head, 2006). Samples were sieved at intervals of 0.5 phi from -2.5 to 2 phi (5.6- 0.25 mm) corresponding with a coarse mesh 5.6 mm to a fine mesh of 0.25 mm (Additional details on sieving in Appendix G). Sediment samples were analyzed using the open-source grain-size distribution software program GRADISTAT (Blott, 2000).

3.7.6 Bulk Density

Estimates of the volumetric transport rate, which can be obtained from the volumes of erosion and deposition integrated over time, were converted into a mass transport rate by multiplying by an estimated bulk density (Goff & Ashmore, 1994). This is necessary for the direct comparison of the morphological method for estimating sediment transport and the observed sediment transport determined from the downstream sediment baskets. The results of 30 samples provided an average dry bulk density of 1.79 g ml^{-1}. Additional details of bulk density measurements can be found in Appendix H.

3.8 Summary

In total, six flume experiments at constant and varying discharge were completed between April 6, 2015 and January 4, 2016. Prior to this, the weir was calibrated and photogrammetric methods were refined and tested, resulting in one year of experimental work. The UWO flume provided the ideal location for the investigation of the research objectives by allowing for several experimental conditions, with unique discharge and slope combinations, to be tested. The use of digital photogrammetry and the software program Agisoft provided high-resolution (±1 mm) orthophotos and DEMs of the dry and wet flume surface. The orthophotos were used extensively for digitization to determine wetted width, braiding intensity and active braiding intensity. The DEMs were used to generate DEMs of Difference (DoDs) which allowed for the quantification of active areas and volumes of change. From here it was possible to investigate the role of the active width

and depth in gravel-bed braided rivers as well as produce morphological reach-averaged sediment budgets. The downstream sediment baskets allowed for the calculation of bedload transport rate, which served to develop sediment transport budgets and to investigate the relationships between changes in morphology, bedload transport, and bed mobility simultaneously. Overall, these methods helped collect one of the largest flume datasets on gravel-bed braided rivers to date with over a 1000 DEMs, 20 000 Olympus photos, 200 sieved sediment samples and ~500 direct measurements of bedload transport rate spanning a range of discharge, total stream power, and braiding morphologies.

Chapter 4

4 The Variability in the Morphological Active Width

4.1 Introduction

4.1.1 Chapter Introduction and Objectives

Braided rivers exhibit a complex multi-thread morphology with spatially and temporally variable bedload transport rates. Consequently, it has been difficult to measure and predict mean bedload fluxes in braided rivers due to challenges in collecting field data and producing reliable numerical models. Currently, our knowledge of braided river morphodynamics is incomplete, particularly with respect to the fundamental relationships between variable bedload transport and the dynamic morphological changes in these systems.

The focus of this chapter is to investigate the relationships between channel morphology and bedload transport in gravel-bed braided rivers by building on research related to the morphological active width. For example, while the active width is highly variable, both spatially and temporally, it is expected to increase with stream power, wetted width, and braiding intensity. Bertoldi et al. (2009a) and Ashmore, Bertoldi, & Gardner (2011) found that there may be a strong linear relationship between active width as a proportion of the wetted width and dimensionless stream power (ω^*):

$$\omega^* = \frac{QS}{b\sqrt{g\Delta D_{50}^3}} \tag{4.1}$$

where Q is discharge, S is slope, D_{50} is mean grain size, Δ is relative submerged density, b is the average wetted width and g is the acceleration due to gravity. This relationship could have meaningful practical implications as dimensionless stream power can be calculated with relatively little information on the channel geometry, unlike most bedload transport functions based on channel hydraulic calculations (Ashmore et al., 2011). In combination with simple relationships with the wetted width and braiding intensity, which are relatively easy to measure from aerial photos, it may be possible to characterize general relationships

between channel morphology, bedload transport and reach-averaged hydraulic parameters with minimal data.

The current knowledge of the active width and its role in driving bedload transport and braiding morphodynamics is based on limited field data and simplified numerical models. Similarly, while research has already found that braided rivers generally accommodate changes in discharge by adjusting their width, with smaller changes in depth, the importance of the active depth in braided rivers morphodynamics is unknown (Ashmore et al., 2011). To investigate these relationships further, reliable measurements of bedload transport flux and channel morphology are required over a range of discharge and stream power (Bertoldi et al., 2009a). Specifically, the predicted relationships between active width, wetted width, active braiding intensity, and stream power need to be investigated in a systematic way across a range of channel morphology, discharge, and stream power. By completing experiments at a constant channel-forming discharge as well as over a series of hydrographs, this research makes it possible to investigate the differences in these relationships in terms of 'downstream' and 'at-a-station' channel geometry. Therefore, one of the goals of this research, and the focus of this chapter, is to characterize these relationships to improve our understanding of the morphodynamics of braided rivers by addressing the following research objectives:

1. Quantify the morphological active width in a physical model over a range of gravel-bed river morphology.
2. Characterize the relationship between the active width and wetted width, braiding indices, and dimensionless stream power over a range of flow conditions.
3. Characterize the relationship between the active width and bedload transport flux under channel forming conditions and variable discharge conditions.

From these objectives it is possible to address the following specific questions about the nature of the active width and morphodynamics of braided river systems:

1. How does the morphological active width vary over a range of constant channel-forming discharges and over a series of event hydrographs?

2. Does the morphological active width increase linearly with dimensionless stream power and active braiding intensity under constant and variable discharge conditions?

3. Does the morphological active width have relationship with bedload transport rate?

4. Does the active depth have a relationship with channel morphology and bedload transport?

This research will build on work done by previous researchers outlining the possible importance of the morphological active width. In addition, reliable estimates of bedload flux in a braided rivers will have benefits for applied engineering, geomorphology and ecology. Furthermore, a greater understanding of the relationships between bedload transport and channel morphology in these complex river systems will inform future numerical models (Bertoldi et al., 2009a).

4.1.2 Chapter Structure

The results presented here are split into two main sections. The first section presents the results for experiments completed at a constant channel-forming discharge (Section 4.2), while the second section is based on the results from the hydrograph experiment (Section 4.3). In both cases, the section begins with a summary of the experimental conditions in terms of the braiding evolution, the wetted width, braiding indices and the general outcomes of the DEM and DoD processing (Sections 4.2.1 and 4.3.1). For details on the methods used for each result, refer to Chapter 3.

Next, each main section presents the average and range of experimental results in terms of bedload transport rates and measurements of morphological change including active width, active depth as well as volumes of erosion and deposition (Sections 4.2.2 and 4.3.2). Both sections end with an analysis of correlations and trends found across all the experimental runs. (Sections 4.2.3 and 4.3.3) Section 4 highlights the linkages between channel morphology, bedload transport and channel hydraulics by directly addressing the research questions in terms of the other research previously presented. The chapter concludes with an overall summary of the findings as well as the expected research significance and contributions (Section 4.4).

4.2 Constant Discharge Experiments

4.2.1 Experimental Conditions

4.2.1.1 Braiding Evolution

Each experiment started from an initially straight channel and was left to self-form at the imposed channel forming discharge until a stable morphology (i.e., consistent average wetted width) was achieved (Figure 4.1). Apart from experiment 9, which had an increase in wetted width during the second round of experimental runs, the rest of the experiments had a consistent average wetted width throughout the experiment (Figure 4.1).
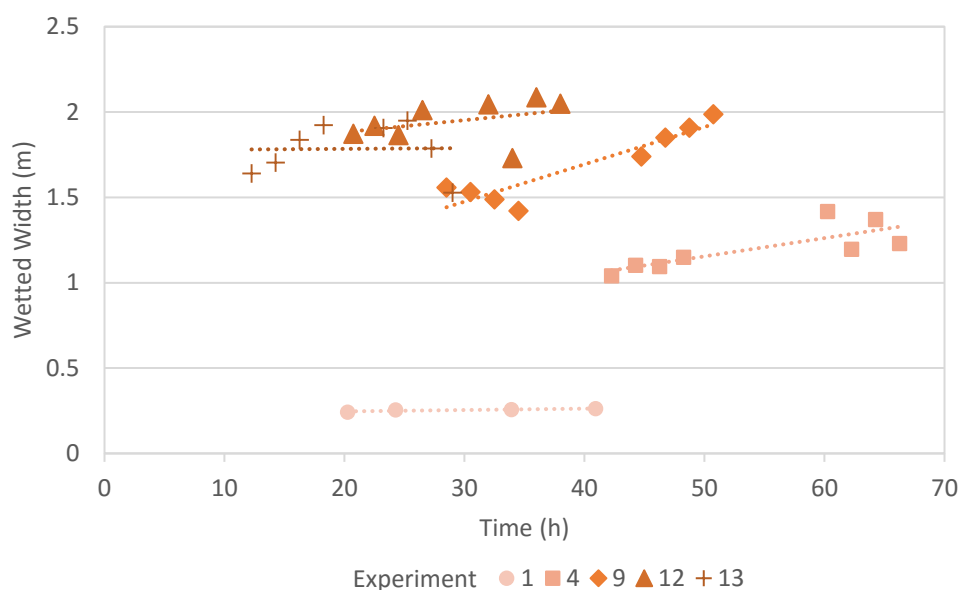
Figure 4.1 – Measured wetted widths for each constant discharge experiment as a function of time. Differences in time are a result of differences in initial evolution time.

During the evolution stage of all experiments, the initially straight channel eroded its banks and generated a series of regularly spaced alternate bars (Figure 4.2). While the final morphologies for each experiment were different, they all followed a similar evolutionary path from the initially straight channel to fixed alternating bars at regular intervals and then finally towards the development of channel bifurcations, confluences, and medial bars. The only exception to this evolutionary path was experiment 1 which maintained a single threaded channel throughout the length of the experiment.
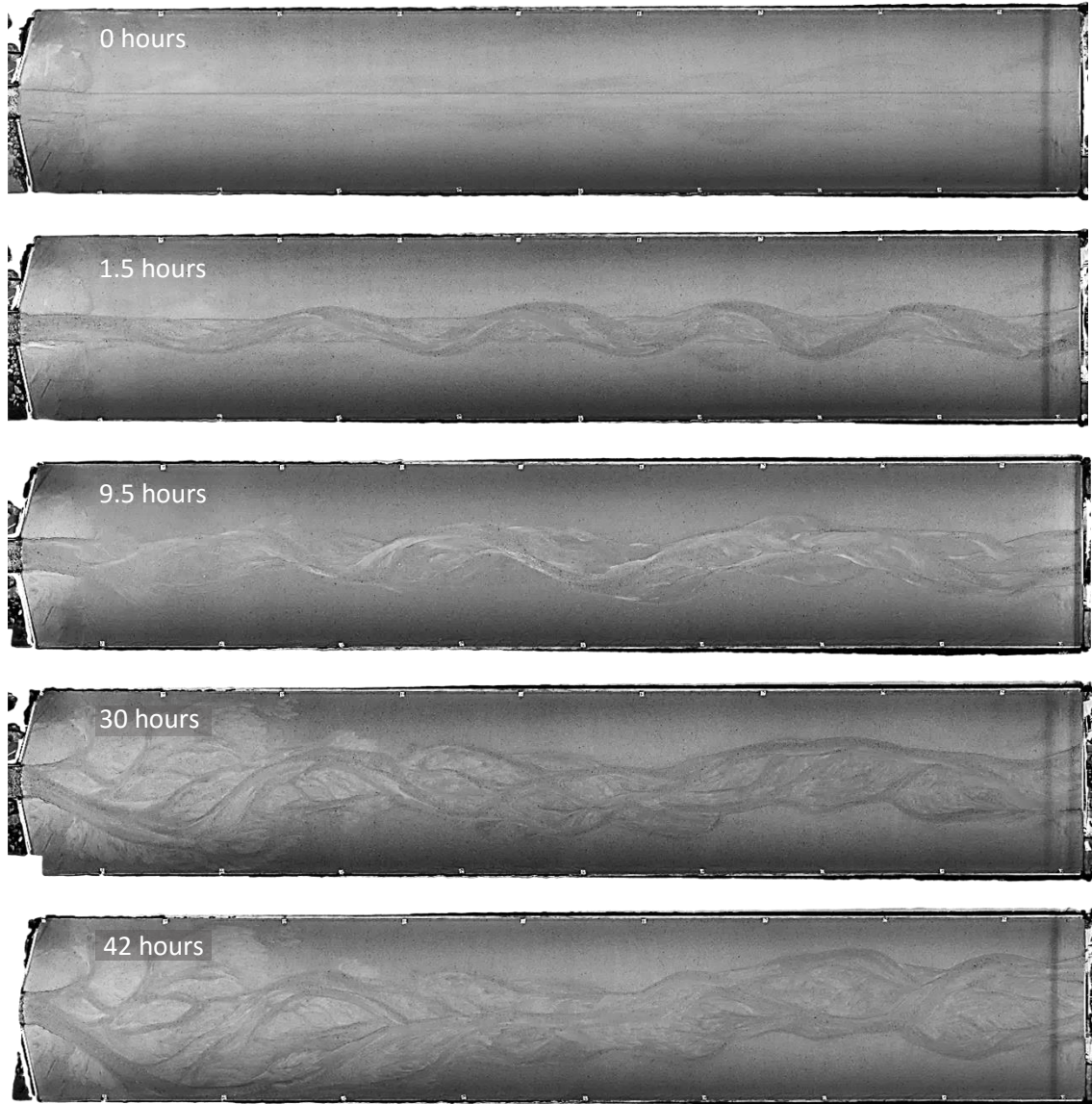
Figure 4.2 – Spontaneous evolution of a braided morphology in the physical model over time. The orthophotos were generated during the 42 hour initial evolution stage of experiment 4.

Figure 4.3 presents the final morphologies at the end of each evolution stage, before the experimental runs were started. After 16 hours of evolution, experiment 1 maintained a single threaded morphology with submerged alternate bars so that the wetted width was approximately the same as the channel width (Figure 4.3a). Experiment 4 evolved over 42 hours, which showed remnants of multiple channel switches and flooding (Figure 4.3b). Experiment 9 had a much greater wetted width than both experiment 1 and 4 and was the

first experiment to laterally develop to the flume edge (Figure 4.3c). Experiments 12 and 13 represented braided river morphologies at the higher end of the morphodynamic spectrum reworking most of the braidplain during the evolution stage of the experiment (Figure 4.3d and e).

After the extended period of initial evolution, each of the experimental channels continued to self-form into a variety of final morphologies after two rounds of experimental runs (Figure 4.4). Even after all 41 hours of run time, the morphology of experiment 1 maintained a stable single-threaded pattern, dominated by submerged alternating bars and little morphological change (Figure 4.4a). Experiment 4 was characterized by one primary channel and multiple smaller secondary channels divided by the classic braided river medial bars (Figure 4.4b). Experiment 9 was also dominated by a single primary channel which unfortunately ran along the flume edge for most of the study area (Figure 4.4c). Like experiment 4, experiment 9 had several smaller secondary channels that had acted as primary channels during earlier experimental runs. By the end of experiment 12, most of the flume surface had been reworked, especially in the downstream study area. It had multiple active primary channels and experiment 12 was the first experiment to laterally develop to both walls of the flume (Figure 4.4d). Finally, experiment 13, with the highest stream power, reworked all the flume surface with the exception of small areas near the upstream weir and minor areas on the sides of the flume (Figure 4.4e). In this experiment, there was extensive braiding and large changes in channel morphology with each 15-minute experimental run.
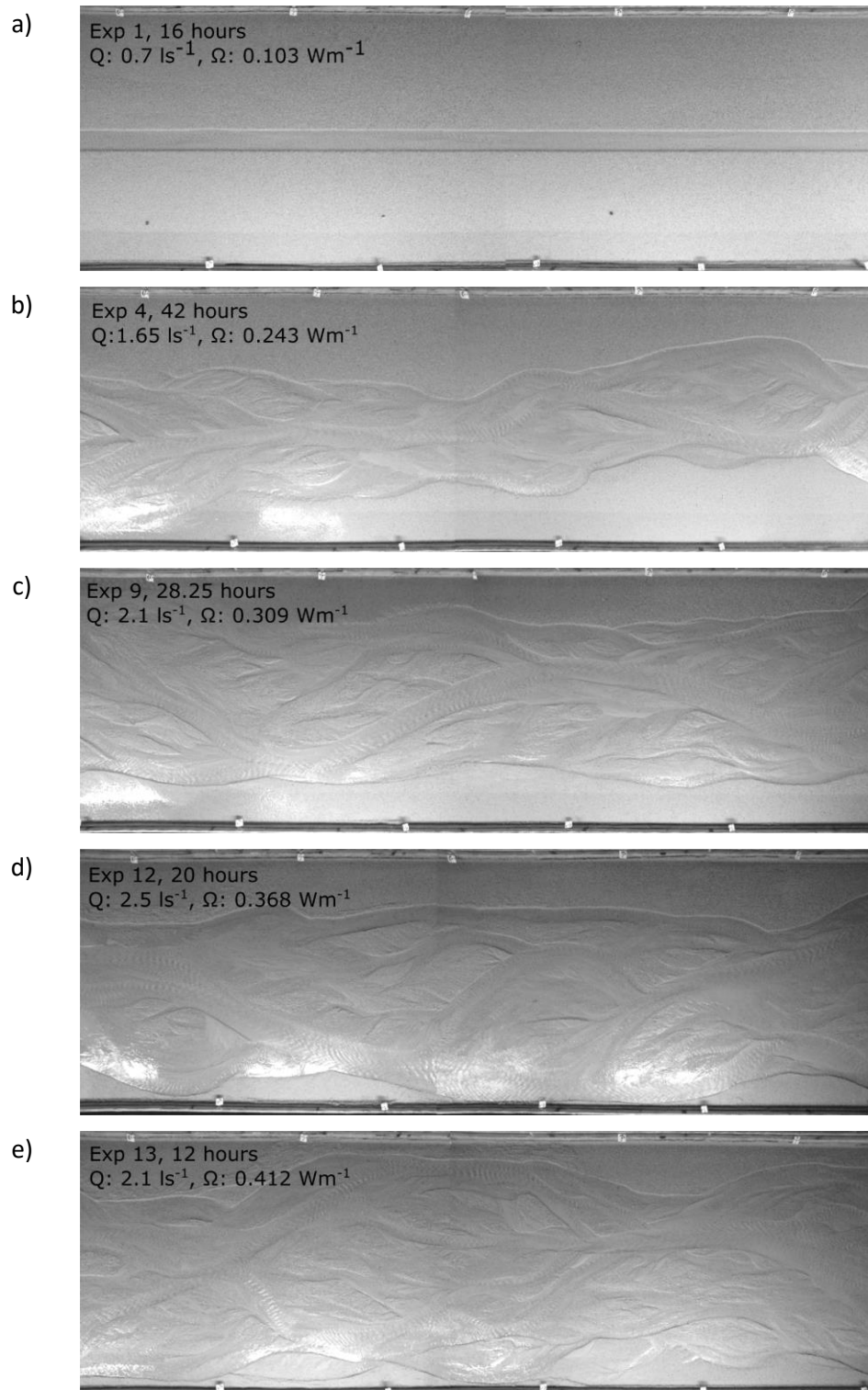
Figure 4.3 – Orthophotos of each experimental surface at the end evolution. Time refers to the total hours of initial evolution, Q is the imposed channel-forming discharge, and Ω is the total stream power for each experiment. Flow is from the left.

a) Exp 1, 41.17 hours
Q: 0.7 ls^{-1}, Ω: 0.103 Wm^{-1}

b) Exp 4, 68 hours
Q:1.65 ls^{-1}, Ω: 0.243 Wm^{-1}

c) Exp 9, 54.5 hours
Q: 2.1 ls^{-1}, Ω: 0.309 Wm^{-1}

d) Exp 12, 38.5 hours
Q: 2.5 ls^{-1}, Ω: 0.368 Wm^{-1}

e) Exp 13, 29.25 hours
Q: 2.1 ls^{-1}, Ω: 0.412 Wm^{-1}
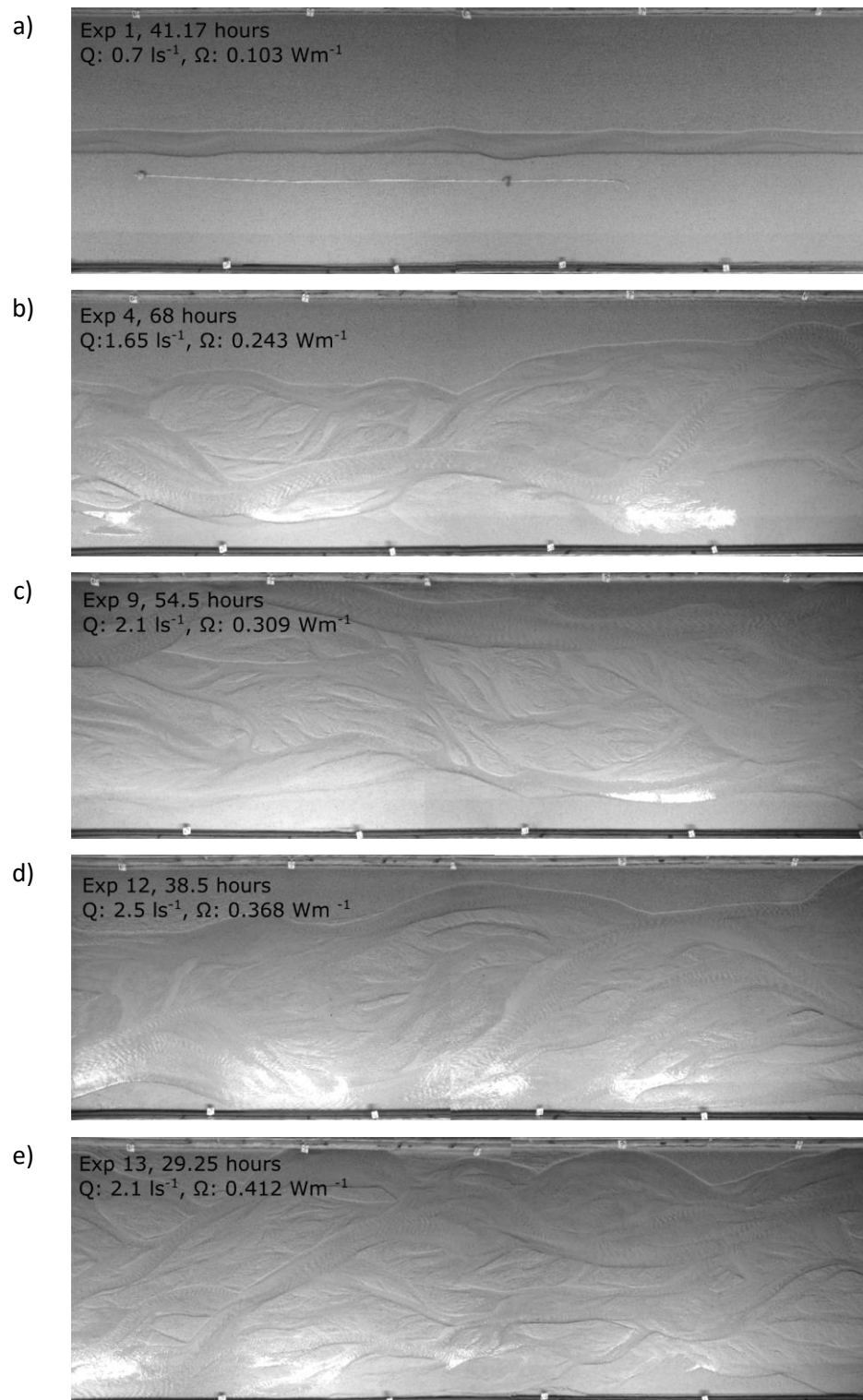
Figure 4.4 – Orthophotos of final channel morphology. Time refers to the total experimental time, Q is the discharge and Ω is the total stream power for each experiment. Flow is from the left.

4.2.1.2 Wetted Width and Braiding Intensity

Figure 4.5 shows the range in the wetted width across all 5 constant discharge experiments. As expected, experiment 1 has both the lowest and least variable wetted width since the channel was restricted to a single straight channel. Above this lower threshold of change, the wetted width increases positively with discharge. Interestingly, while experiment 13 had a greater stream power than experiment 12 (0.412 and 0.368 W m^{-1}, respectively), it had a lower mean wetted width. Therefore, it seems that wetted width may be more responsive to differences in discharge than in total stream power.
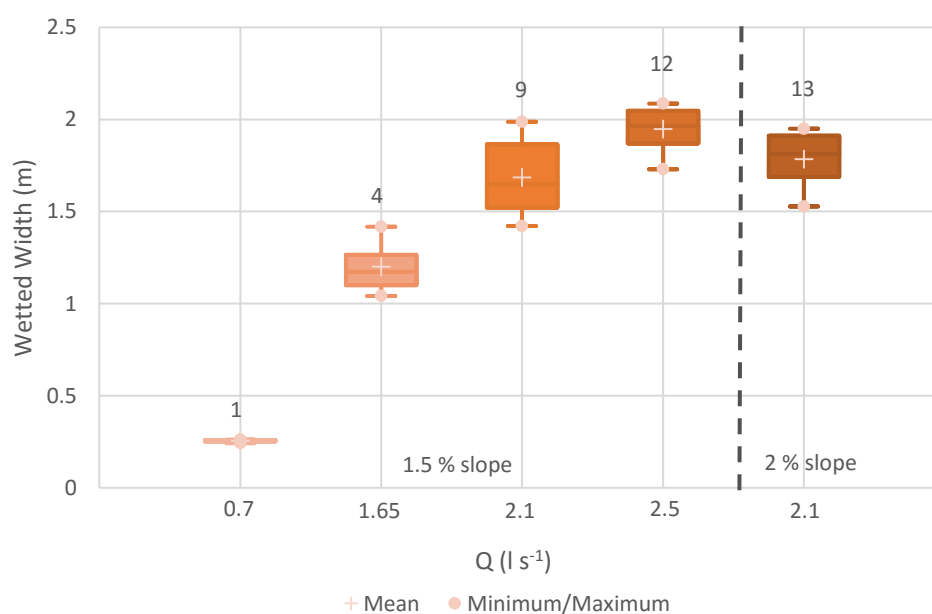
Figure 4.5 – Wetted width measurements for the constant discharge experiments, where Q is discharge. The upper and lower bounds of each box plot represent the 1st and 3rd quartile while the horizontal line dissecting the plot represents the median. The 'whiskers' extend 1.5 times the interquartile (IQ) range (e.g., 1.5(IQ$_3$-IQ$_1$)) from the first and third quartile. The values above the box plots refer to the experiment number and the dotted vertical line divides the 1.5 % from the 2 % slope experiments.

The temporal changes in wetted width are shown in Figure 4.1, which help explain the large variability in the wetted width of experiment 9. Unlike the other experiments which had consistent wetted width values across the entire length of the experiment, experiment 9 had a large increase in the wetted width during the second round of experimental runs.

This drastic change was the result of the downstream end of the flume becoming heavily inundated during the second round of experimental runs (Figure 4.6)
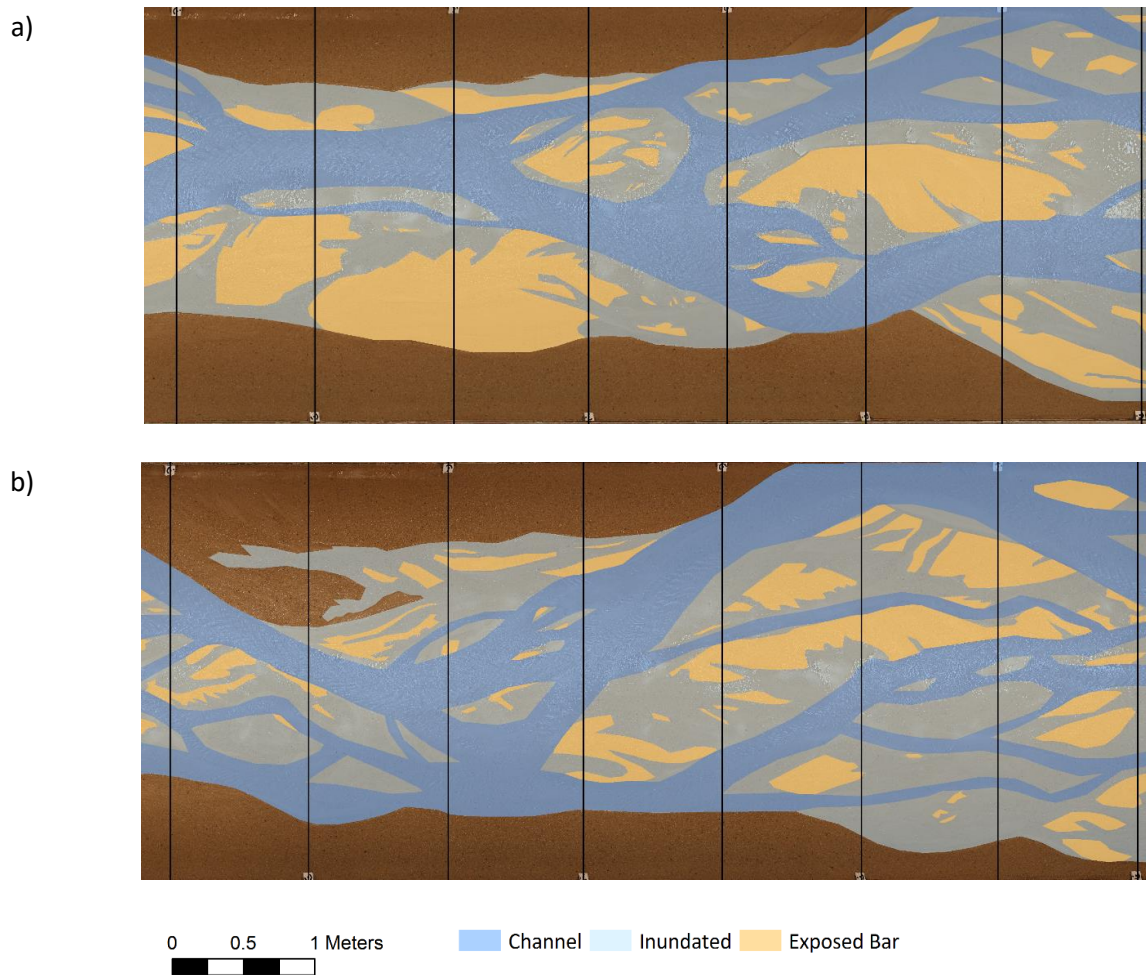
Figure 4.6 – Digitized orthophotos of experiment 9 illustrating the expansion of the wetted width between a) experimental round 1 taken 28.5 hours into the experiment and b) experimental round 2 taken 46.75 hours into the experiment.

Plotting the temporal changes in braiding intensity (BI) indicates that all the experiments except for experiment 9 had a stable BI over time (Figure 4.7). This reflects that, in general, as wetted width increases so does BI and therefore these trends mimic those in Figure 4.1 and those found in previous studies (Egozi & Ashmore, 2009).
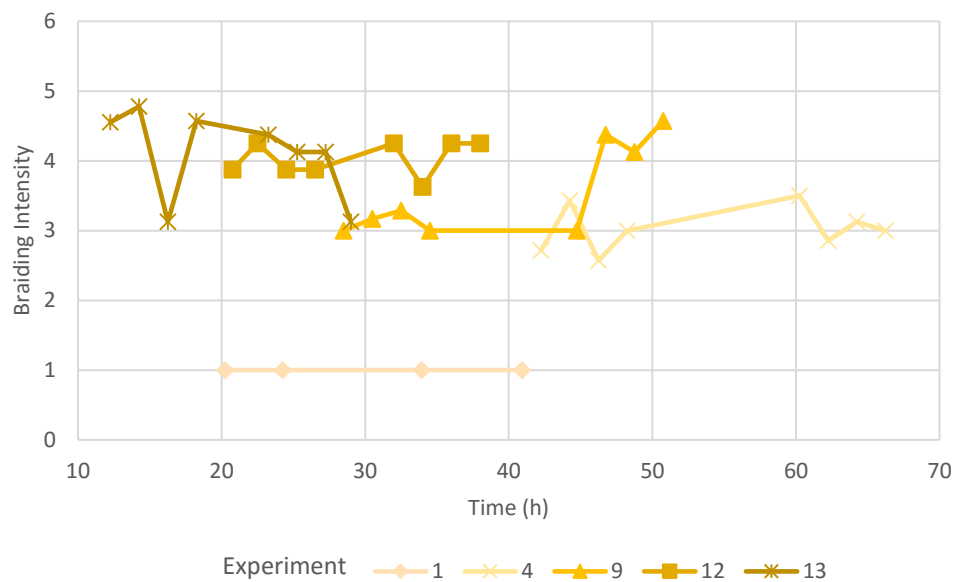
Figure 4.7 – Braiding intensity as a function of time for all constant discharge experiments. Different time spans for each experiment reflect differences in initial evolution time.

A comparison of means suggests that braiding intensity (BI) and active braiding intensity (ABI) tended to increase with discharge and total stream power (Figure 4.8).
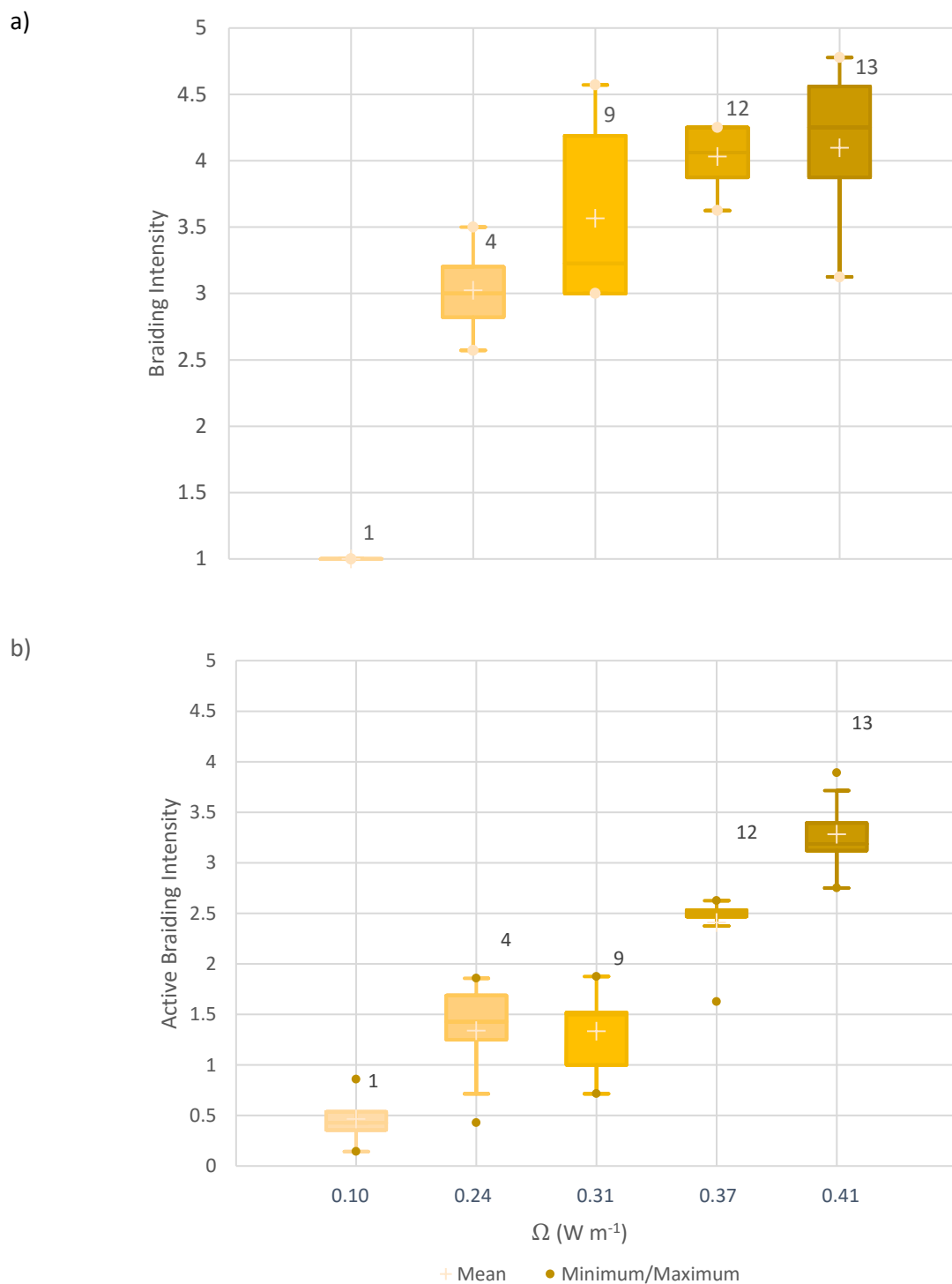
Figure 4.8 – a) Braiding intensity and b) active braiding intensity for constant discharge experiments as a function of total stream power (Ω). Values above the box plots refer to the experiment number.

Plotting ABI as a function of BI, there is an overall positive trend amongst the multi-thread braided rivers (Figure 4.9). As discharge and stream power increase, a greater proportion of the wetted channels are becoming active. Unlike the other experiments, experiment 1 had a single threaded morphology, resulting in a BI of 1 and a slightly variable ABI, ranging from 0.1- 0.8 (Figure 4.9).
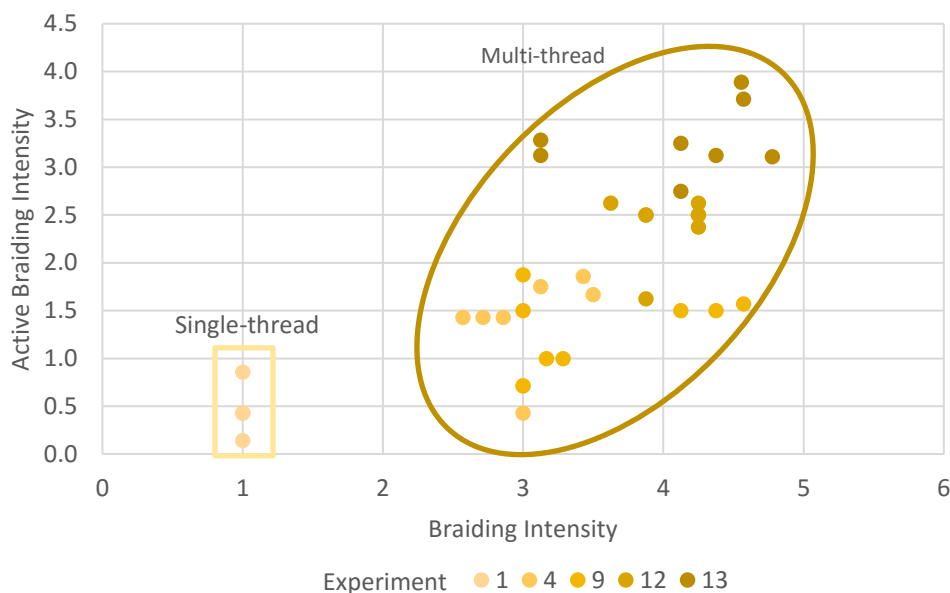
Figure 4.9 – Active braiding intensity as a function of braiding intensity. Results from the single thread experiment (i.e., experiment 1) are outlined by a box, while results from the multi-thread braided experiments (i.e., experiments 4, 9, 12 and 13) are outlined by an oval.

Figure 4.10 shows a plot of BI and ABI against wetted width for the multi-thread braided experiments. While both BI and ABI have a positive relationship with wetted width, a least-squares trendline of BI has a much higher R^2 value of 0.601 compared to the ABI with an R^2 of 0.286 (Figure 4.10). In some cases, the ABI is below 1 due to the nature of the measurement. The ABI represents the average number of times an active area was present at an observation cross-section in each DEM of difference. The active areas themselves are patchy, especially at low discharge, so the average for a given reach could be less than one due to discontinuous active areas along the reach and between cross-sections.
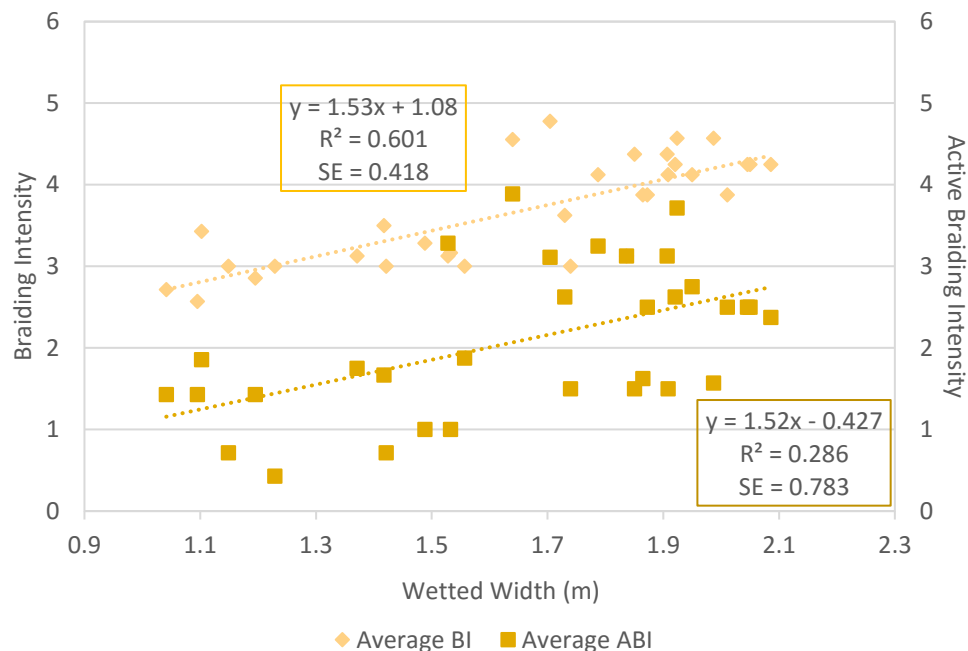
Figure 4.10 – Braiding intensity and active braiding intensity as a function of wetted width for the multi-thread constant discharge experiments (4, 9, 12 and 13). Dashed lines represent the best fit trendlines.

The ratio of ABI to BI varies between 0.14 and 1.05 and increases with increasing stream power (Figure 4.11). Experiment 13 with the highest stream power always has ABI/BI ratios above 0.6, compared to experiment 4 and 9 which range between 0.2 and 0.6 (Figure 4.11).
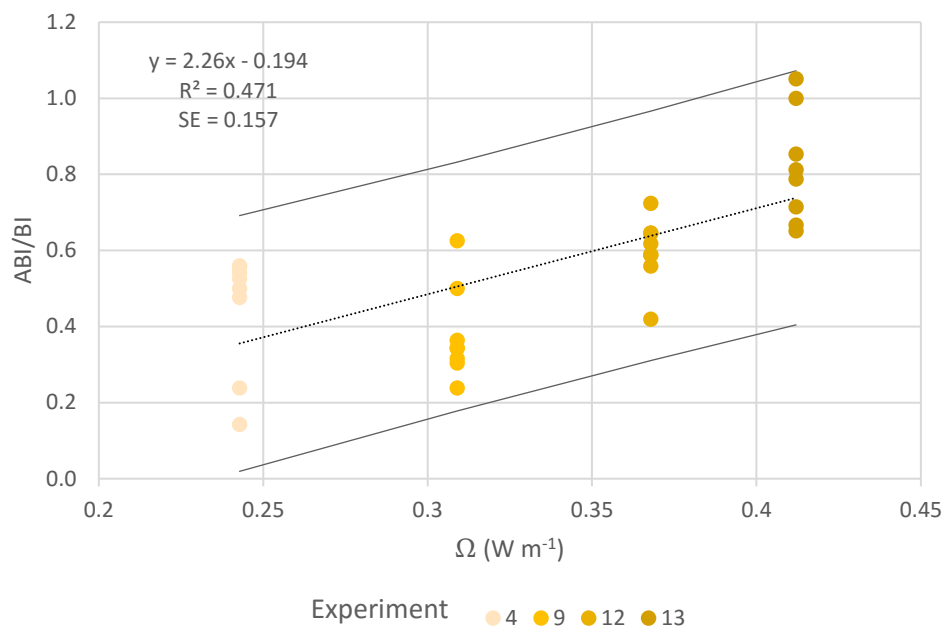
Figure 4.11 – Ratio of active braiding intensity (ABI) and braiding intensity (BI) as a function of total stream power (Ω) for the multi-thread constant discharge experiments. The dashed line represents the best fit trendline and the solid gray lines represent the 95 % prediction interval.

4.2.1.3 DEM and DoD Generation

Digital elevation models (DEMs) created from each dry surface of the flume were used to create DEMs of Difference (DoDs) from which the active areas, and therefore the active width and depth, could be derived.

Examples of DEMs for the final channel morphology of each experiment can be seen in Figure 4.12. Compared to the orthophotos in Figure 4.4, the DEMs make it much easier to see the final morphology of experiment 4 in the DEM because flooding on the sides evident in the Olympus photos is eliminated when taking DEMs of the dry flume surface. Based on a preliminary visual inspection the DEMs highlight that experiment 13 left very little flume surface untouched, apart from minor areas near the upstream weir and several small areas by the flume edges (Figure 4.12). Therefore, while it was possible to increase the total stream power in the flume via changes in slope, this would have likely resulted in more extreme, and undesirable, edge effects. The experiments used in this research

represent the practical extremes between low stream power (experiment 1, 0.10 Wm^{-1}) and high stream power (experiment 13, 0.41 W m^{-1}) available in the physical model used.

Exp. 1
Q: 0.7 l s^{-1}
Ω: 0.10 W m^{-1}

Exp. 4
Q: 1.65 l s^{-1}
Ω: 0.24 W m^{-1}

Exp. 9
Q: 2.1 l s^{-1}
Ω: 0.31 W m^{-1}

Exp. 12
Q: 2.5 l s^{-1}
Ω: 0.37 W m^{-1}

Exp. 13
Q: 2.1 l s^{-1}
Ω: 0.41 W m^{-1}
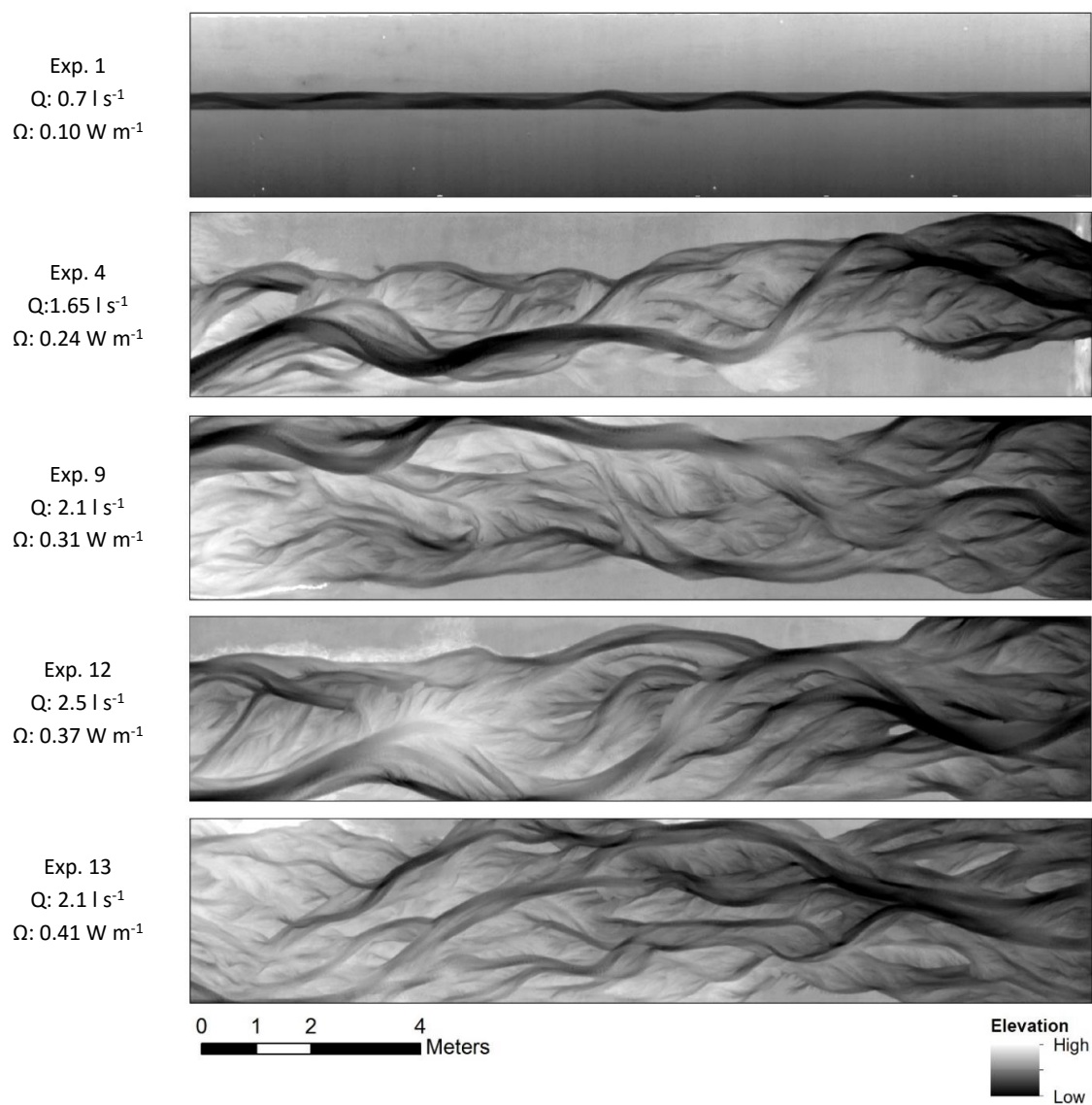
Figure 4.12 – DEMs of the final channel morphology for each of the constant discharge experiments. Q is the model discharge and Ω is the approximate total stream power.

Examples of DoDs from the end of each experiment are presented in Figure 4.13**.** The active area, defined as the number of coloured (i.e., red or blue) cells increases with increasing discharge and stream power.

Based on a preliminary visual inspection, experiment 1 had very little topographic change, even over 30 minutes of experimental run time (Figure 4.13). In experiment 1, erosion and deposition are restricted to a single main channel, with erosion on the outer banks of the channel and deposition on regularly spaced alternate bars. There also seem to be strong linkages between areas of erosion and areas of downstream deposition. Specifically, areas of erosion are followed closely (i.e., the next bar head) by areas of deposition. Experiment 4 and 9 show increased complexity compared to experiment 1, with some areas clearly showing at least two main active channels (Figure 4.13). In both DoDs, there are areas with erosion and deposition occurring side-by-side. Finally, experiments 12 and 13 show high levels of channel complexity, even after only l5 minutes of flow. In these DoDs, there are multiple active channels, adjacent areas of erosion and deposition, and overall greater depths of erosion and deposition compared to previous experiments (Figure 4.13). This selection of DoDs seems to support the trends found with ABI. Experiment 1 remains an outlier of sorts, with its unique single-thread morphology. Experiments 4 and 9, while they differ in active area, have similar ABI mainly restricted to one channel, with some cross-sections having a greater ABI of 2. Experiment 12 and 13, the most complex channels, have large active area and a greater number of active anabranches than the other constant-discharge experiments (Figure 4.13). Experiment 13, in particular, activates large areas of the flume, spanning almost the entire width of the model in some locations.

Looking at all the DoDs collectively it is possible to see how, as discharge and stream power increase, the areas of morphological change expand and become more continuous, both laterally and downstream. At low discharges, the areas of change are patchy and areas of erosion are separate from areas of deposition. At high discharges, it is possible to outline the entire form of the primary channels as well as multiple smaller channels solely based on the active areas represented in the DoDs. The areas of erosion and deposition, while still discrete, occur side-by-side within the channel and have a complex longitudinal pattern (Figure 4.13).
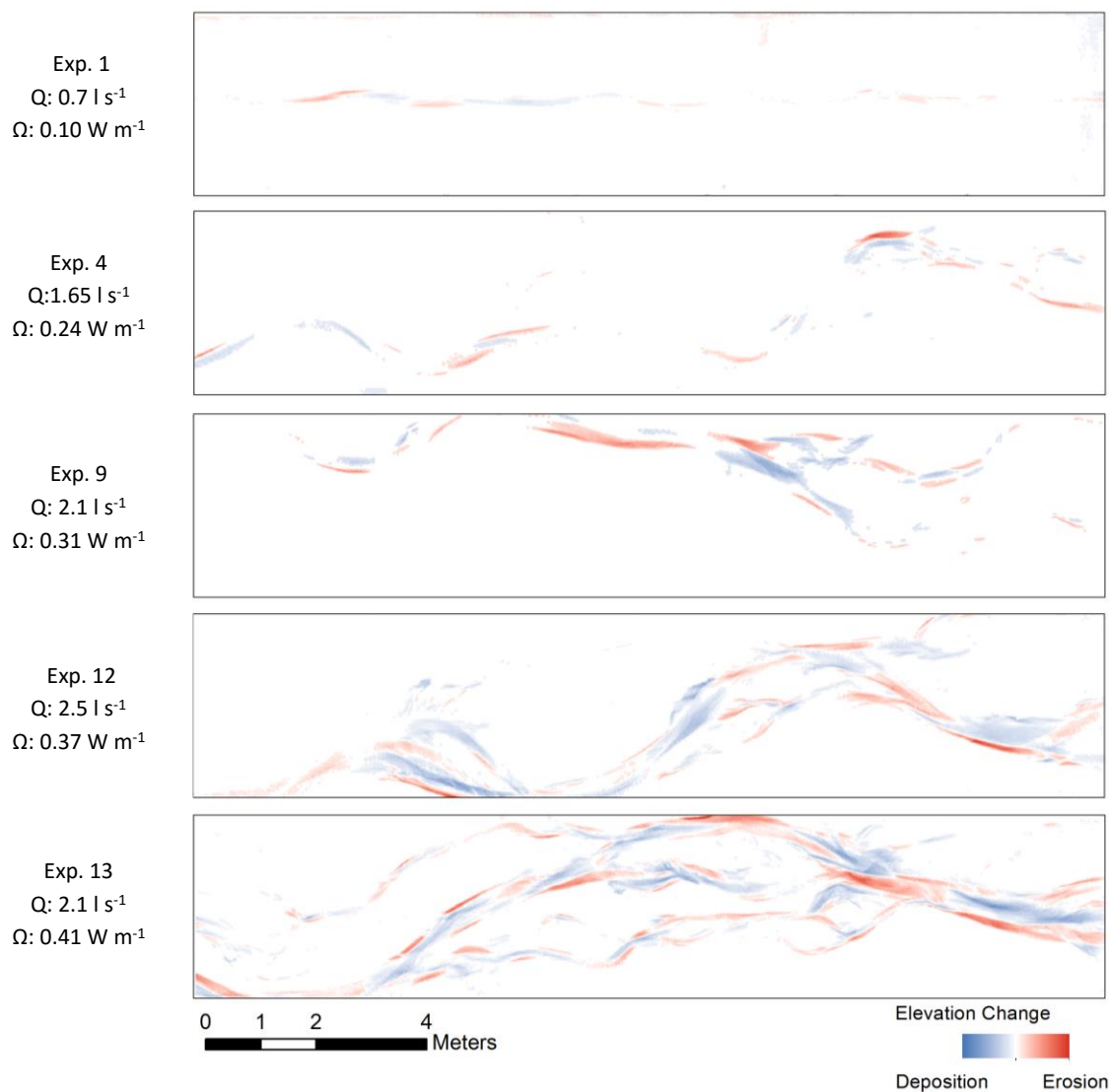
Figure 4.13 – Example DEMs of difference from each constant discharge experiment, where Q is the model discharge and Ω is the total stream power. Results shown are derived from the dilation threshold method.

4.2.2 Experimental Results

The next section presents the main results of the constant discharge experiments with respect to the bedload transport rates, active areas, and the volumes of erosion and deposition. Additional analysis follows in section 4.2.3.

4.2.2.1 Bedload Transport

Temporal variation in the bedload transport rate for each experiment is shown in Figure 4.14. While there is an increase in transport rate with stream power, there is also a lot of overlap in the ranges of bedload rates, particularly between experiments 12 and 13, despite their differences in total stream power (0.37 and 0.41 W m^{-1}, respectively).

A visual inspection indicated a greater variability in transport rate in the first round of experimental runs than the second in experiment 1. A two-sample t-test ($\alpha= 0.05$) between the bedload transport rates of round 1 ($\bar{x} = 0.79$ g s^{-1}, $\sigma = 0.31$ g s^{-1}) revealed that it was significantly different from the bedload transport rates in round 2 ($\bar{x} = 0.59$ g s^{-1}, $\sigma = 0.13$ g s^{-1}); t (35) = 2.44, p = 0.02. This could be due to the natural variability in sediment transport rate and the development of alternate bars. At this low discharge, once the alternate bars were developed, which began during evolution but continued through the experimental runs, the amount of unimpeded sediment transfer may have decreased.

Based on the results of experiment 1, an exploratory two-tailed Student's t-test was conducted on the bedload transport rates of the remaining experiments, comparing round 1 and round 2 of the experimental runs. Experiment 4 round 1 ($\bar{x} = 3.45$ g s^{-1}, $\sigma = 1.94$ g s^{-1}) and round 2 ($\bar{x} = 2.31$ g s^{-1}, $\sigma = 1.23$ g s^{-1}) were also found to be significantly different from each other; t (64) 2.87, p = 0.006. In addition to experiment 1 and 4, experiment 9 was also found to have a significant difference between the bedload transport rates in round 1 ($\bar{x} = 5.85$ g s^{-1}, $\sigma = 3.86$ g s^{-1}) and round 2 ($\bar{x} = 3.06$ g s^{-1}, $\sigma = 1.71$ g s^{-1}); t (71) = 4.12, p = 0.0001. In both experiment 4 and 9, the average bedload transport rates were much greater in the first round of runs then in the second. This highlights how the extended secondary evolution stage produced different channel morphologies, even at a constant discharge and relatively stable braiding intensities. Therefore, two rounds of experiment runs was helpful for capturing a large range of possible bedload transport rates for the constant discharge experiments. Based on a two-tailed Student's t-test, experiments 12 and 13 did not have significant differences in the bedload transport rates between rounds 1 and 2.
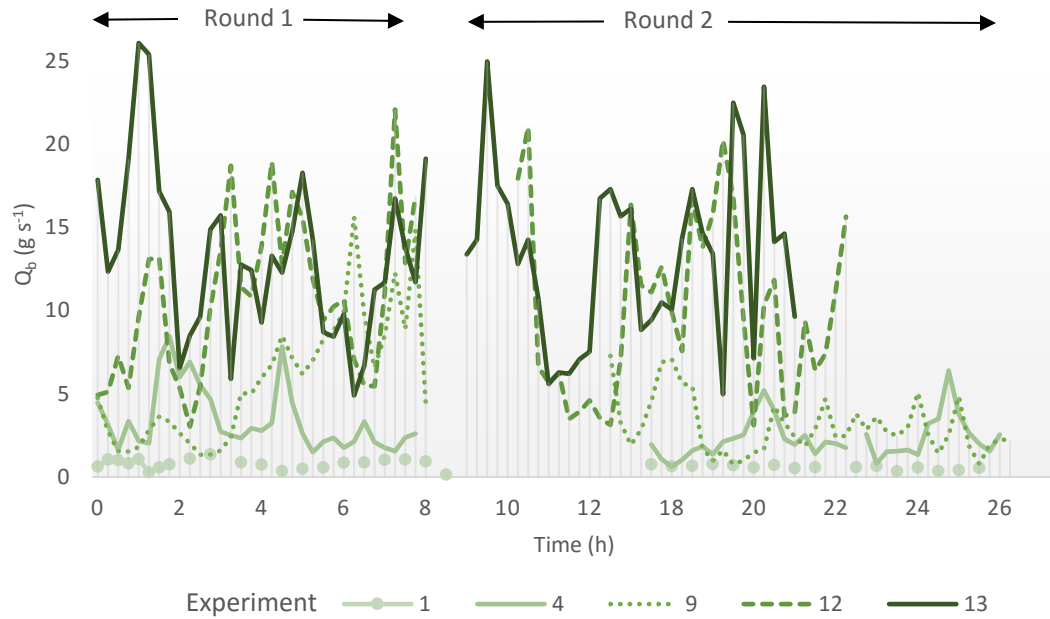
Figure 4.14 – Time series of bedload transport rate (Q_b) during the two rounds of experimental runs for the constant discharge experiments. Differences in total experiment time reflect differences in the duration of the second round of evolution.

Figure 4.15 shows the mean and ranges of values for the measured bedload transport rates across all the constant discharge experiments. Experiment 1 has both the lowest mean (n = 37, $\bar{x}$ = 0.71 g s^{-1}, σ = 0.26 g s^{-1}) and the lowest range of values. From there, increasing stream power results in an increase in the mean bedload transport rate as well as the relative variability. The average bedload transport rate for experiment 4 was 2.87 g s^{-1} (n = 66, σ = 1.70 g s^{-1}), while experiment 9 had an average of 4.32 g s^{-1} (n = 72, σ = 3.21 g s^{-1}). Experiments 12 and 13 had the highest averages with bedload transport rates of 10.28 g s^{-1} (n = 64, σ = 5.06 g s^{-1}) and 13.30 g s^{-1} (n = 66, σ = 5.09 g s^{-1}) respectively (Figure 4.15).
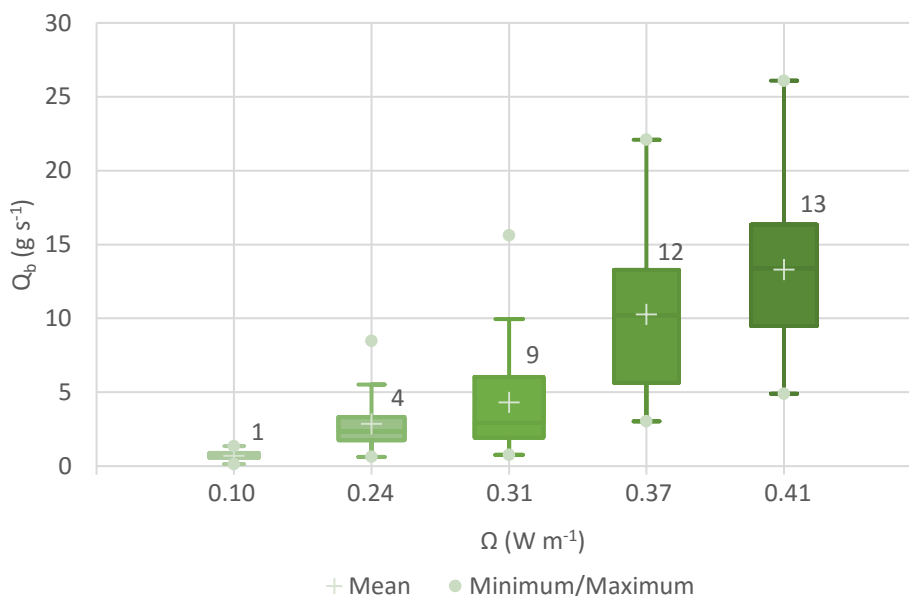
Figure 4.15 – Bedload transport rates (Q_b) as a function of total stream power (Ω) for each of the constant discharge experiments.

4.2.2.2 Active Width and Active Depth

The reach-averaged morphological active width, which could be divided into separate erosional and depositional components, was derived from DoDs. This is accomplished by first determining the active area (total, erosional, or depositional) and dividing by the reach (study area) length of 14 m (Figure 4.16).
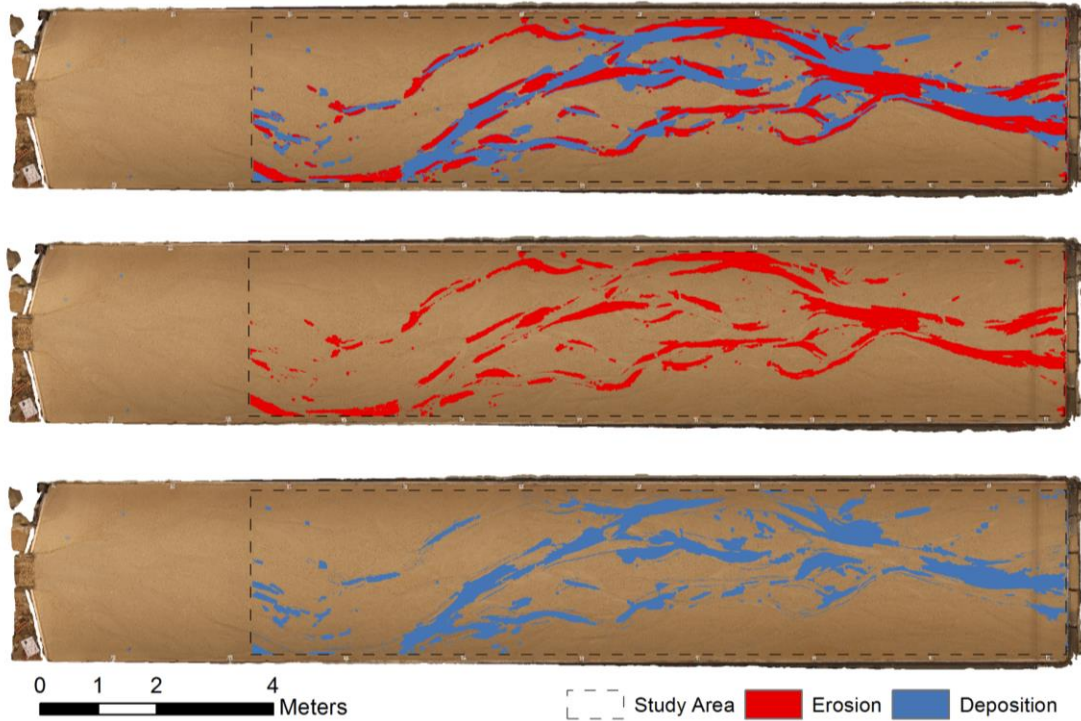
Figure 4.16 – DEM of Difference highlighting the total active area erosional area, and depositional area within the flume study area as an overlay on an orthophoto of the river model.

Given the complex nature of braided rivers with the tendency for variable bedload transport and dynamic morphology, it was expected that the active width would be variable, even at a constant discharge. The results revealed that while the average active width had an overall positive relationship with stream power it was highly variable at any given discharge (Figure 4.17a and b). Figure 4.17b highlights the differences between the two threshold methods in terms of change detection. Under all experimental conditions, except experiment 1, the dilation method produces a significantly greater active width than the simple 2σ threshold based on a two-tailed Student's t-test (α= 0.05) (See full results in Appendix I, Table I.1). This is expected because dilation incorporates a greater area of change than the more conservative simple threshold (See Section 3.6.5 for more details on threshold methods).

a)

b)
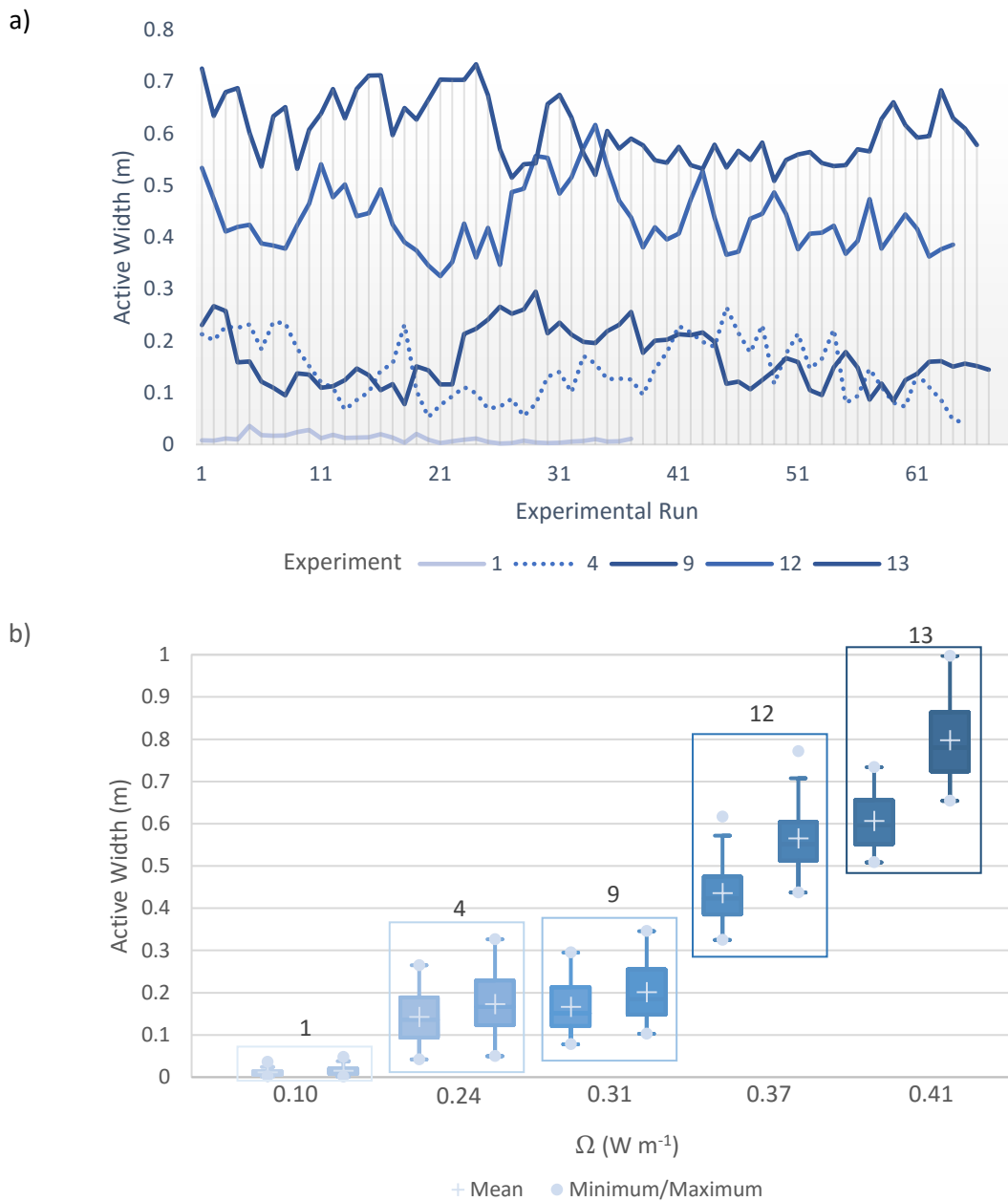
Figure 4.17 – Active width for the constant discharge experiments as a function of a) time (represented by experimental run) and b) total stream power (Ω) for all constant discharge experiments. 4.17a shows the average active width for each experimental run using the simple threshold method. In 4.17b each experiment has two box plots, the left plot represents the results of the simple 2σ threshold method and the right plot represents the results of the dilation method.

Focusing on the mean active width for each stream power, there is a strong positive power relationship based on least-squares regression using both the simple and dilation threshold methods (Figure 4.18). The methods were not significantly different based on a two-tailed Student's t-test on active width (t (8) =-0.432, p= 0.677).
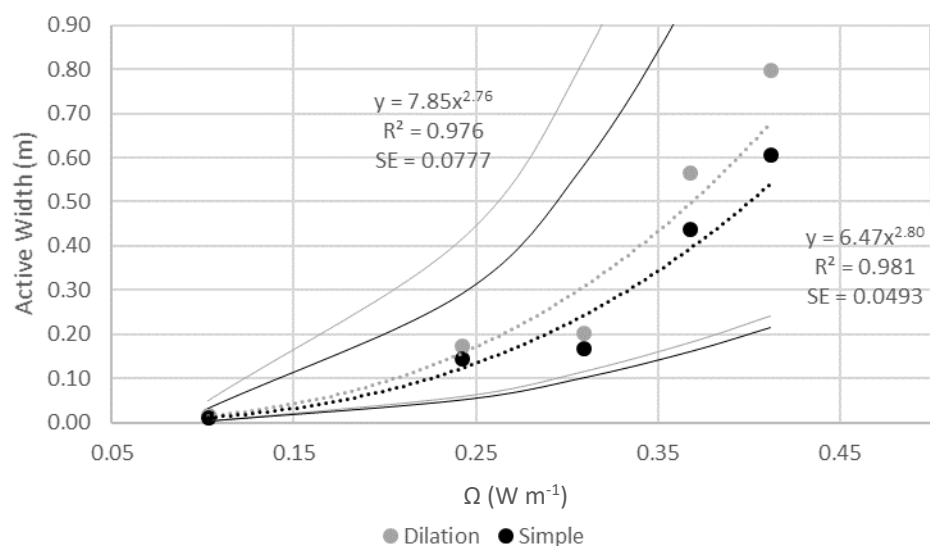
Figure 4.18 – Mean active width as a function of total stream power (Ω) for the constant discharge experiments based on both threshold methods. The dashed lines represent the best fit trendlines and the outer solid lines represent the 95 % prediction interval for the observations.

Splitting the active width into its erosional and depositional components, a two-tailed Student's t-test showed no significant difference between the width measurements in experiments 1, 4, and 9 ($\alpha = 0.05$) (Figure 4.19). In experiment 12, the depositional active widths ($\bar{x} = 0.24$ m, $\sigma = 0.04$ m) were significantly different from the erosional active widths ($\bar{x} = 0.20$ m, $\sigma = 0.03$ m) using the simple 2σ threshold; t (126) = -6.0, p = <0.0001. Experiment 13 also had a significant difference between the depositional active widths ($\bar{x} = 0.32$ m, $\sigma = 0.04$ m) and the erosional active widths ($\bar{x} = 0.28$ m, $\sigma = 0.03$ m) using the simple 2σ threshold (t (130) =-7.31, p = < 0.0001).
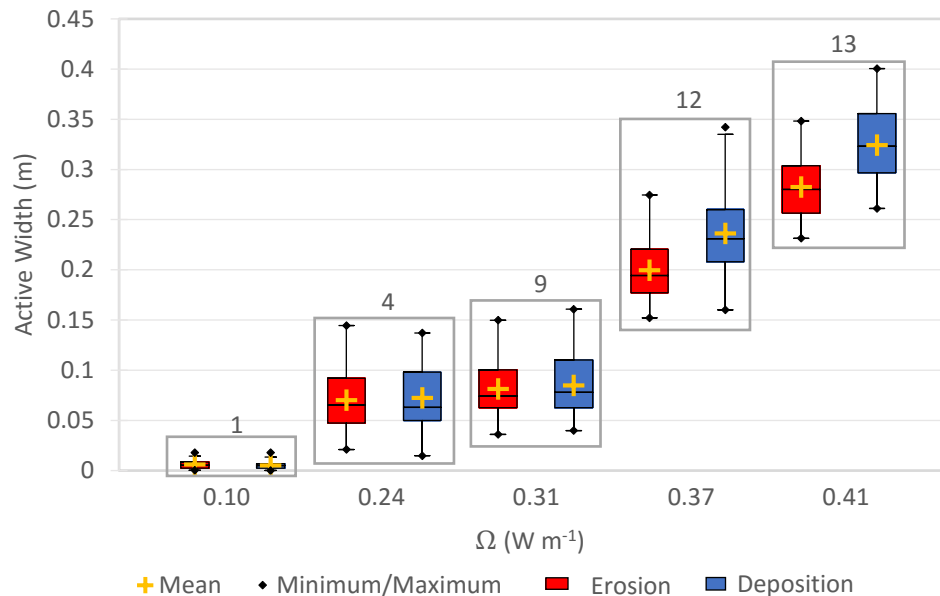
Figure 4.19 – Erosional and depositional active widths as a function of total stream power (Ω) for the simple 2σ threshold.

From the DoDs it is possible to extract not only the active areas, but also the volumes of erosion and deposition. These volumes will be discussed in the next chapter in more detail, but by dividing volumes by their corresponding active area (e.g., total volume of change/total active area) it is possible to calculate reach-averaged active depths, representing the average change in bed elevation in the reach. The graph of temporal changes in the average active depth indicates that the reach-averaged active depth is not very sensitive to changes in stream power because there is a lot of overlap in the range of active depths between the multi-threaded experiments (e.g., experiment 4, 9, 12, and 13) (Figure 4.20a). Looking at the box plots of active depth in Figure 4.20b, the mean active depths tend to increase under the first three experimental conditions (experiment 1, 4, and 9) before declining under the higher stream power conditions of experiment 12 and 13. This could be the result of more complex morphologies at high stream power, resulting in smaller primary channels and more extensive bar networks. Within each experiment, the active depth was always smaller under the dilation method than the simple threshold method although the differences were not statistically significant for any of the experiments based on a two-tailed Student's t-test (See full results in Appendix I, Table I.2). The slightly smaller active depths using the dilation method reflects the fact that the total volumes of

change, which are similar under both thresholds, were divided by greater areas of change under the dilation method.
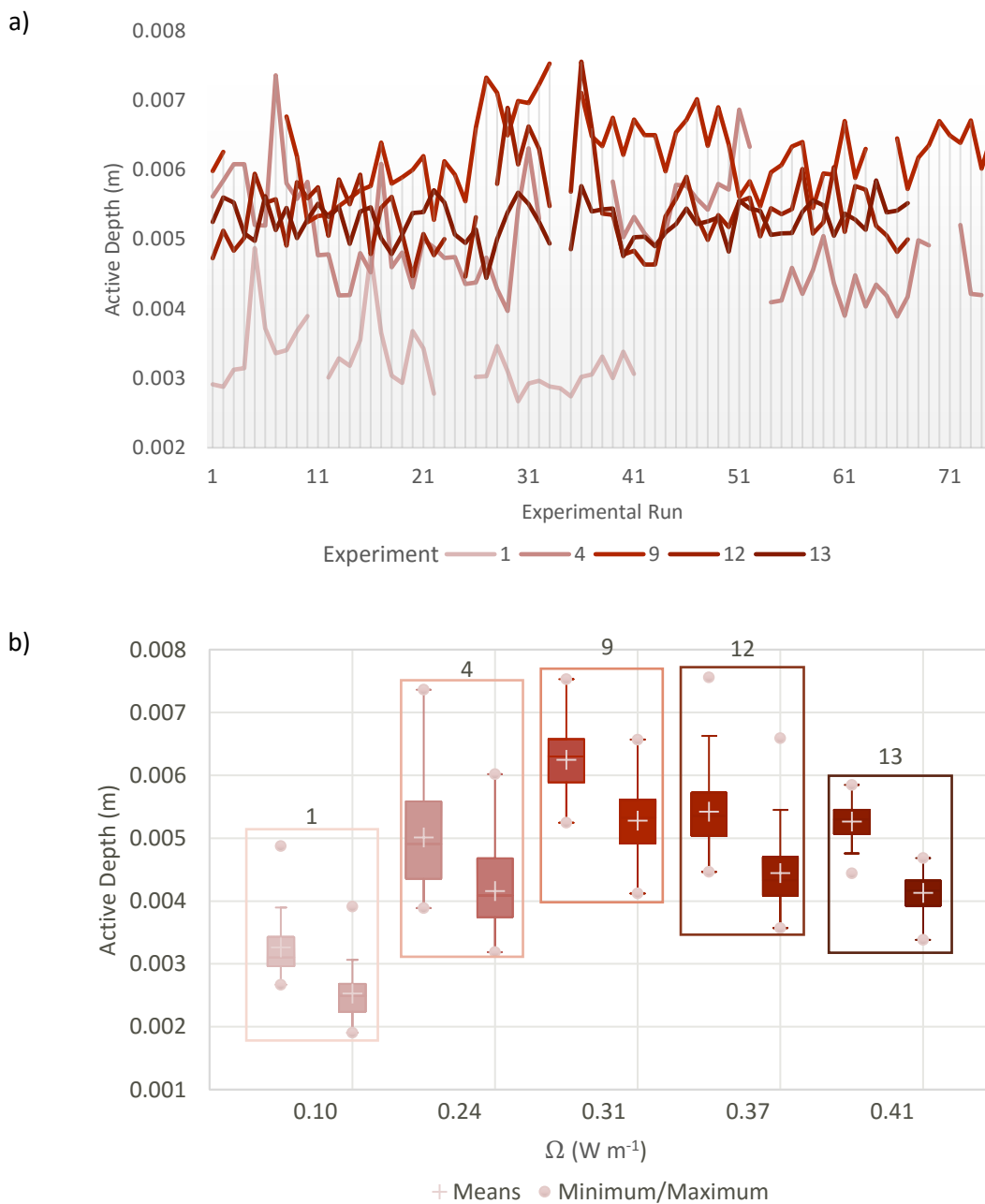
Figure 4.20 – Reach-averaged active depths for the constant discharge experiments as a function of a) time (represented by experimental run) and b) total stream power (Ω). 4.20a shows the results for the simple threshold method while 4.20b shows the results of the simple (left) and dilation (right) thresholds for each experiment.

When split into its erosional and depositional components there is much more overlap between the reach averaged active depths among experiments than there was for the active widths (Figure 4.21). Across all experiments, the active depths are greater for erosion than for deposition, which is the opposite of the trend found for the active widths (Figure 4.19 and Figure 4.21). This may reflect the relatively small elevation changes associated with accretion on bars compared to relatively large elevation changes associated with bed scour and bank erosion.
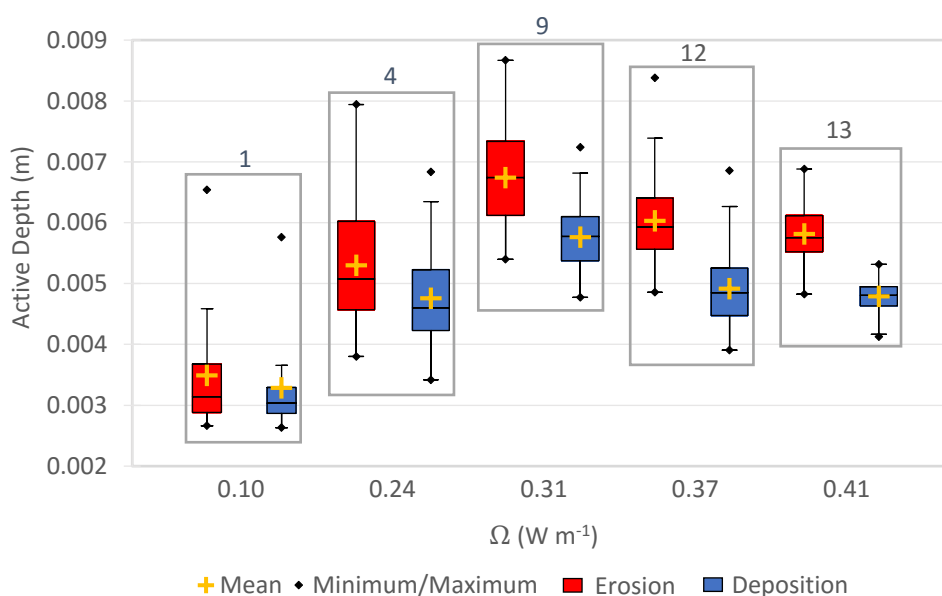
Figure 4.21 – Erosional and depositional active depths as a function of total stream power (Ω) for constant discharge experiments. Results shown were derived using the simple 2σ threshold method.

Bedload transport rates and the morphological active width were both found to be sensitive to changes in stream power (Figure 4.15 and Figure 4.18) The active depth, on the other hand, was not sensitive to changes in stream power as indicated by Figure 4.20 and Figure 4.21. These results indicate that bedload transport rate will likely be more strongly correlated with active width than active depth. This relationship is investigated in more detail below in section 4.2.3.

4.2.2.3 Volumes of Erosion and Deposition

From the DoDs it was possible to extract bulk change (total volumes of change) by multiplying the elevation (z) value of each cell by the cell size (0.0015 x 0.0015 m). Figure 4.22 demonstrates that the bulk change tends to increase with stream power, and as expected there is a temporal variability like that found with bedload transport rates.
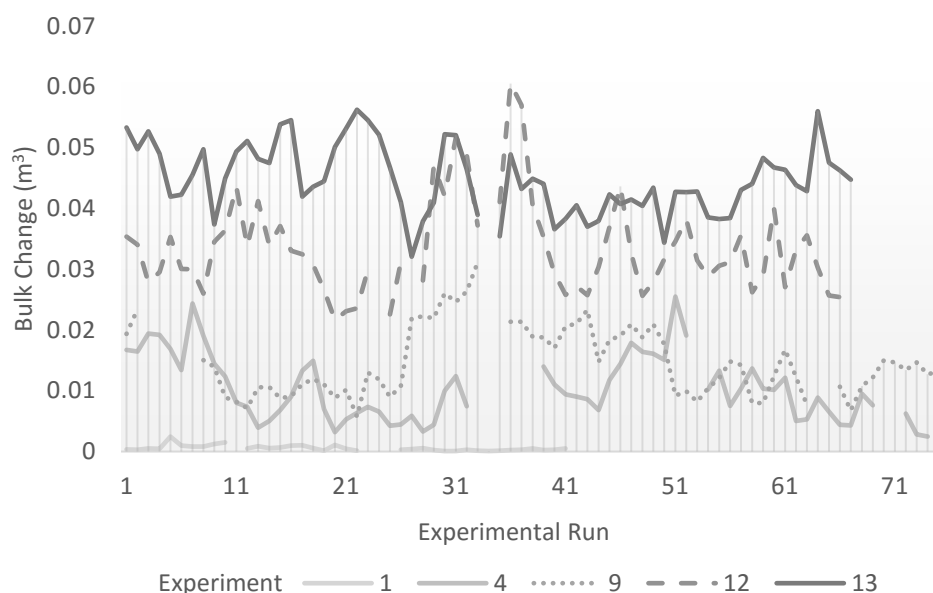
Figure 4.22 – Temporal variability in bulk change for all of the constant discharge experiments. Results shown were derived using the simple 2σ threshold method and time is represented as experimental runs.

The volumes of erosion and deposition both increase with stream power so that experiment 1 has the lowest volumes and experiment 13 has the highest (Figure 4.23). Although the differences were not significant based on a two-tailed Student's t-test ($\alpha = 0.05$), erosion volumes were greater than depositional volumes in all experiments, except experiment 1 where the average volumes of erosion and deposition are the same (0.0003 m^3) (See full results in Appendix I, Table I.3). Given that these results reflect the trends of the active depth, but not the active width, it seems that erosional areas are defined by greater active depths than depositional areas, while depositional areas are defined by greater active widths. Similar results were reported by Brasington et al. (2003) and Rumsby et al. (2008) who found that areas of erosion were generally localized but deeper than the more dispersed

and shallow areas of deposition. The trends found in Figure 4.22 and Figure 4.23 are presented for the simple 2σ threshold, which mimic the results of the dilation method.
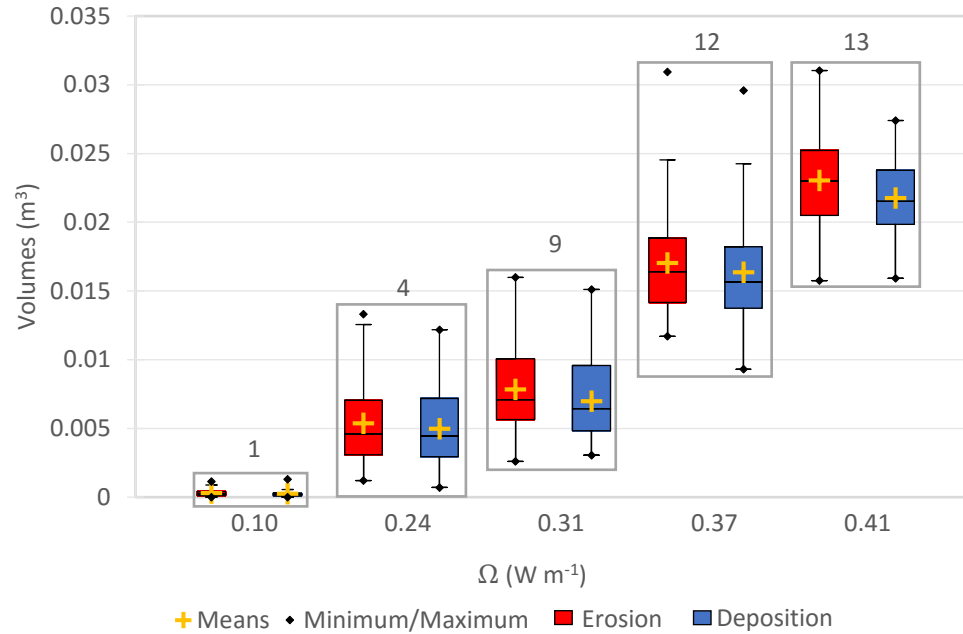
Figure 4.23 – Volumes of erosion and deposition as a function of total stream power (Ω). Results shown were derived using the simple 2σ threshold method.

4.2.3 Analysis of Constant Discharge Experiments

Following the work of Bertoldi et al. (2009a), the dimensionless bedload flux (qb*) was plotted against dimensionless stream power (w*) for the 32 multi-threaded experimental runs for which wetted width was measured (Figure 4.24) (See methods in Section 3.7.3). Dimensionless stream power was calculated using equation 4.1, and the dimensionless bedload flux is calculated using the following equation:

$$qb^* = \frac{Qs}{\gamma b \sqrt{g \Delta D_{50}^3}} \tag{4.2}$$

where Q_s is bedload flux in kgs⁻¹, γ is the water specific weight, b is the average wetted width, g is the acceleration due to gravity, Δ is relative submerged density, and D_{50} is mean grain size. By making the variables dimensionless, it is possible to compare results across

a range of datasets. The variability in bedload flux, even at a constant discharge, resulted in a relatively low linear R^2 value of 0.351 (α= 0.05, p-value = 0.000) (Figure 4.24).
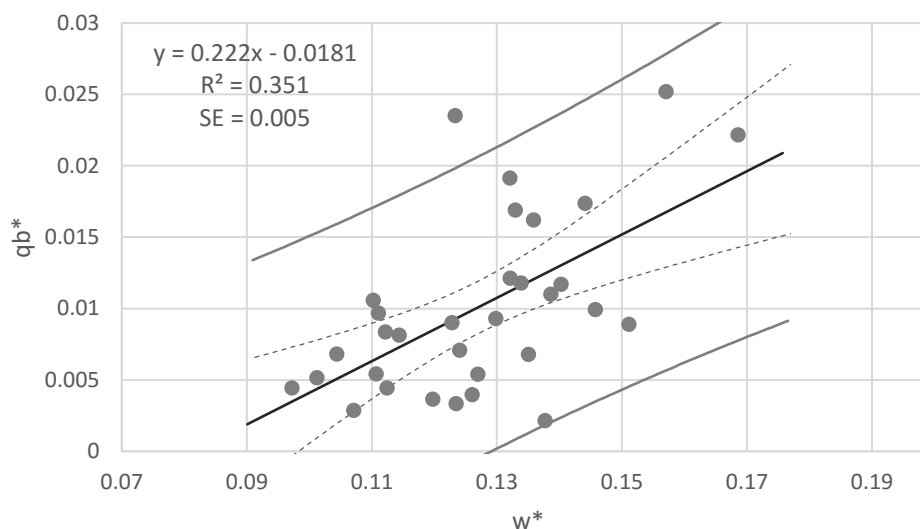
Figure 4.24 – Dimensionless bedload flux (qb*) plotted against dimensionless stream power (w*) for the multi-threaded experiments (i.e., experiments 4, 9, 12, and 13). The dashed lines represent the 95 % confidence interval around the mean of the regression line, and the outer solid lines represent the 95 % prediction interval for the observations.

Plotting the ratio of active width and wetted width against dimensionless stream power follows additional analysis by Bertoldi et al. (2009a) (Figure 4.25). Experiment 1, a single-thread channel, behaves very differently from the rest of the experiments, which all had a braided multi-thread morphology. For this reason, experiment 1 was removed from the analysis and a linear regression was completed (Figure 4.26). This linear regression model for the multi-threaded experiments produced an R^2 of 0.507 (n = 32, α= 0.05, p-value = <0.0001) (Figure 4.26).
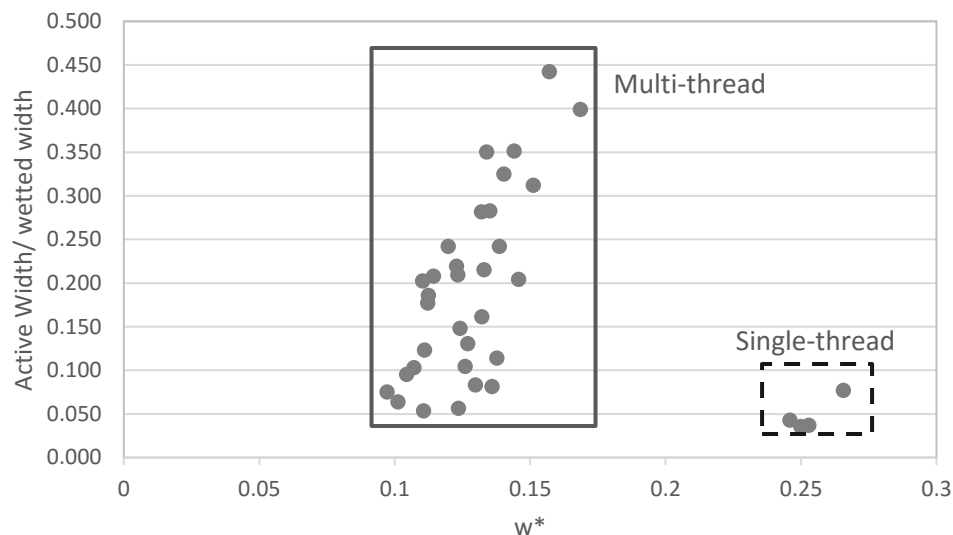
Figure 4.25 – Ratio of active width and wetted width plotted against dimensionless stream power (w*). Experiment 1, which had a single-thread morphology, is outlined by a dashed box and the multi-threaded experiments are outlined by the solid box.
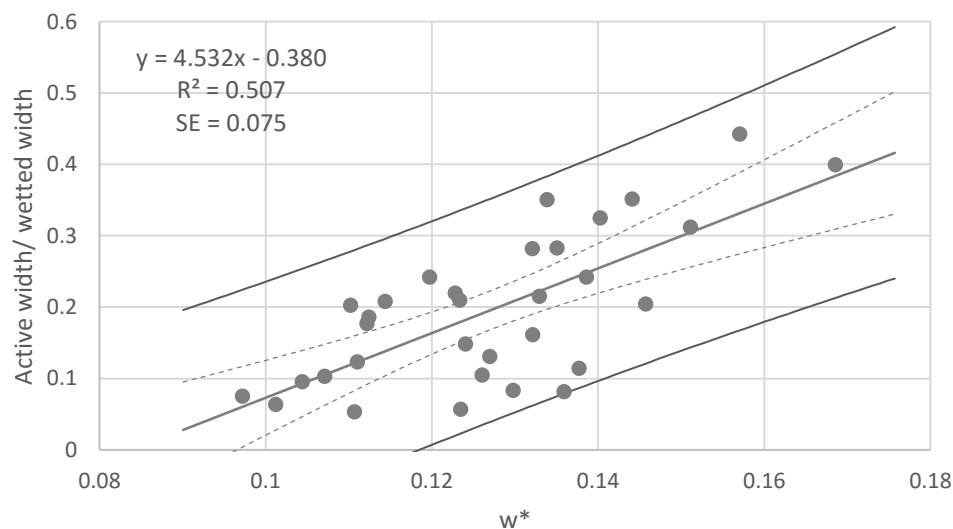
Figure 4.26 – Ratio of active width and wetted width as a function of dimensionless stream power for the braided experiments (i.e., experiments 4, 9, 12, and 13). Results are for the simple 2σ threshold where the dashed lines represent the 95% confidence interval around the mean of the regression line, and the outer solid lines represent the 95% prediction interval for the observations.

Plotting the ratio of the active width and wetted width against the active braiding intensity (ABI) for all the experiments there is a statistically significant positive relationship with a linear R^2 value of 0.745 (n= 32, α= 0.05, p-value = <0.0001) (Figure 4.27).
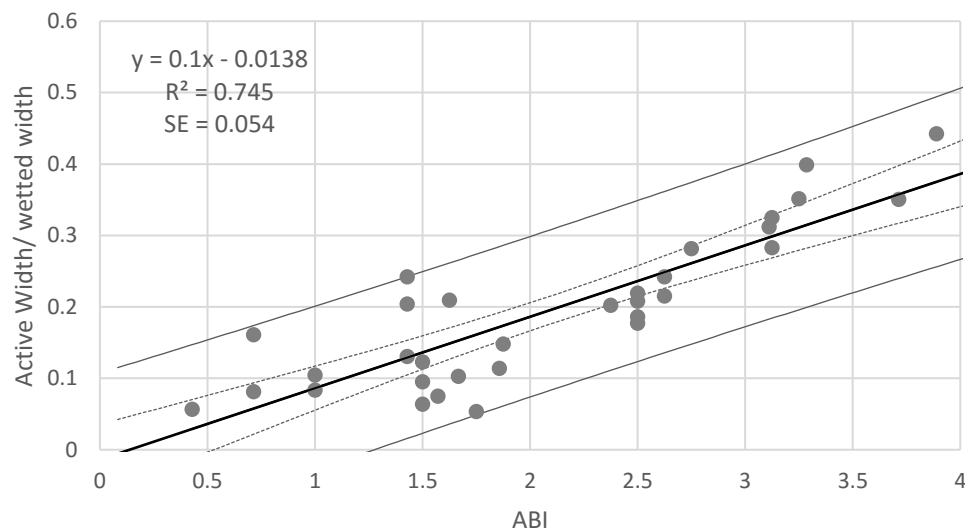
Figure 4.27 – Ratio of active width and wetted width as a function of active braiding intensity (ABI). Results are for the simple 2σ threshold and multi-threaded experiments (i.e., experiments 4, 9, 12, and 13). The dashed lines represent the 95% confidence interval around the mean of the regression line, and the outer solid lines represent the 95% prediction interval for the observations.

Looking at the linear regression of all the observations for the multi-thread experiments only, the active width and bulk change had an R^2 of 0.964 (n= 262, α = 0.05, p-value = <0.0001) (Figure 4.28a). This strong relationship suggests that even though there is a large amount of scatter in the active width for a given discharge, the active width could have predictive value in terms of the total volumes of erosion and deposition. Looking at the same relationship in terms of the active depth, there is no correlation with bulk change (R^2=0.001) (Figure 4.28b).

a)

b)
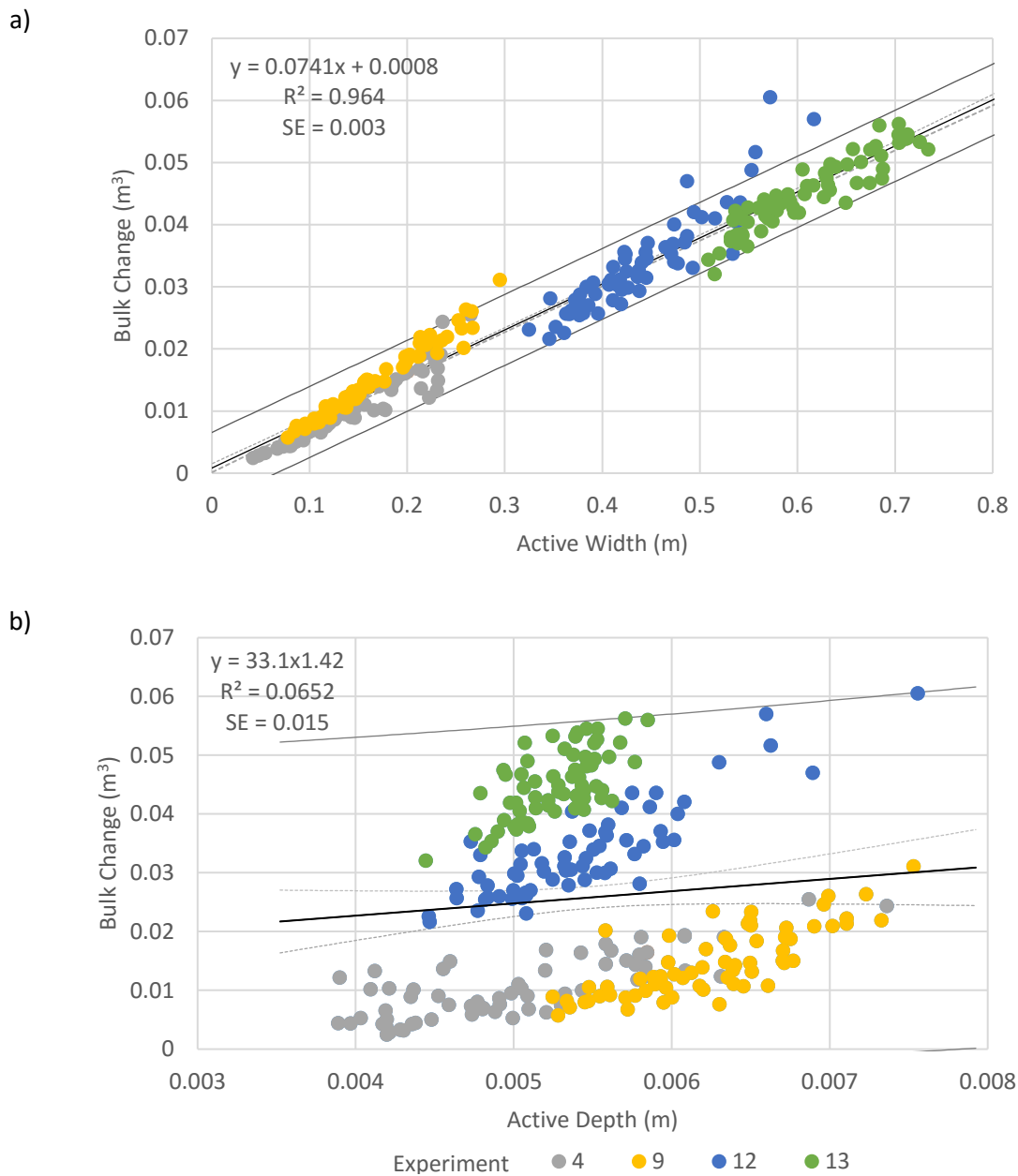
Figure 4.28 – Bulk change as a function of a) active width and b) active depth. Results are for the simple 2σ threshold and multi-threaded experiments (i.e., experiments 4, 9, 12, and 13). The dashed lines represent the 95% confidence interval around the mean of the regression line, and the outer solid lines represent the 95% prediction interval for the observations.

While there is no clear overall trend, or significance, between the average active depth and bulk change, plotting the least-squared trendline of the experiments individually does

provide stronger positive relationships, although still much weaker than those found for the active width (Figure 4.29).
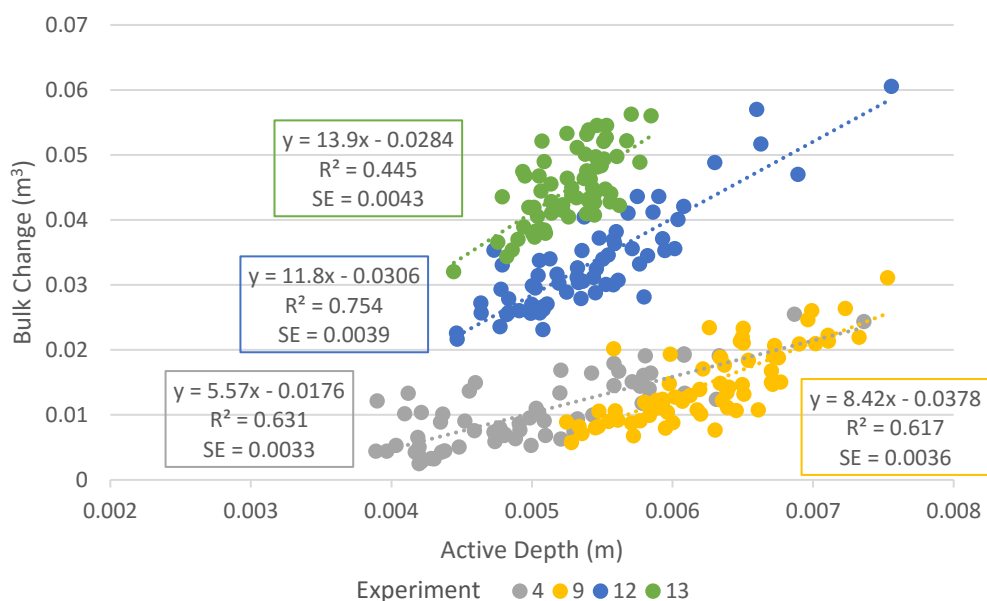
Figure 4.29 – Bulk change as a function of active depth for individual constant discharge experiments. Results are shown for the simple 2σ threshold method.

Active width and bedload transport rate had an overall positive relationship with an R^2 value of 0.515 (n= 259, α= 0.05, p-value = <0.0001) (Figure 4.30a). While there is an overall positive relationship between active width and bedload transport rate, there is considerable scatter for each stream power, highlighting the overall variability of gravel-bed river morphodynamics. Plotting the dimensionless versions of active width and bedload transport rate results in a slightly weaker R^2 of 0.420 (n= 32, α= 0.05, p-value = 0.0001) (Figure 4.30b). This weaker relationship is likely the result of less data observations since the wetted width was only calculated for a subset of experimental runs (See Section 3.7.3 for details).

a)

b)

Experiment   ● 4   ● 9   ● 12   ● 13
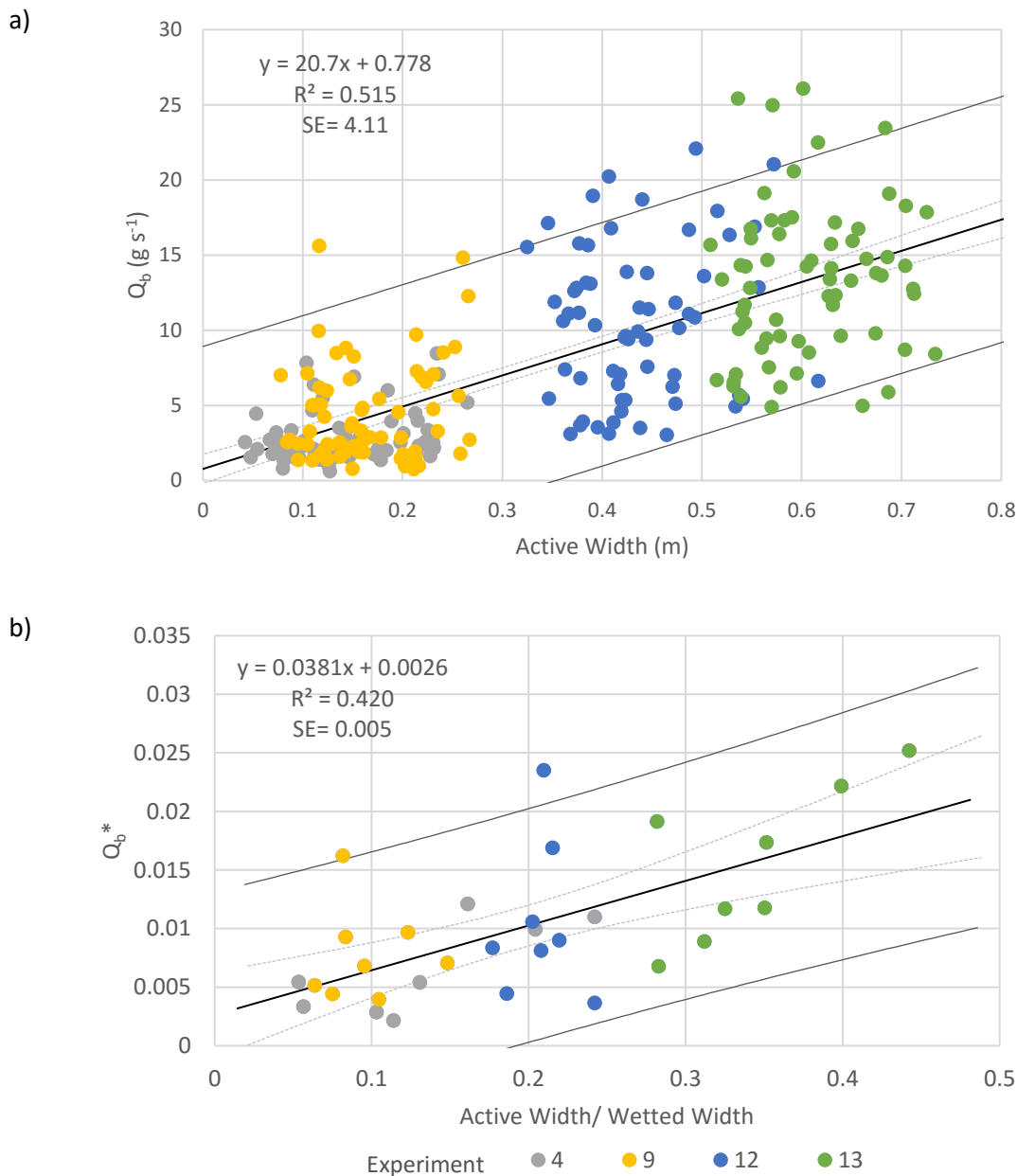
Figure 4.30 – Bedload transport rate (Q_b) as a function of active width where a) bedload transport rate as measured from the downstream sediment baskets is plotted as a function of active width and b) dimensionless bedload transport rate (q_b*) is plotted as a function of the ratio of active width to wetted width. Results are shown for the simple 2σ threshold and the multi-thread experiments (experiments 4, 9, 12, and 13). The dashed lines represent the 95% confidence interval around the mean of the regression line, and the outer solid lines represent the 95% prediction interval for the observations.

4.3 Hydrograph Experiment

4.3.1 Experimental Conditions

4.3.1.1 Braiding Evolution

The braided channel used in the hydrograph experiment, experiment 11, evolved from a straight channel at 2.1 l s^{-1}. Once the stable equilibrium morphology was reached, hydrographs A, B, and C were run sequentially without any intervening constant-flow. The hydrograph experiments were completed to see how the bedload transport rate, active width, active depth, and bulk change would respond to the varying discharge and stream power of the model event hydrographs of a braided channel. Since slope was held constant at 1.5 %, differences in stream power are due to differences in discharge alone. Each hydrograph began with a low discharge, either 0.7 or 0.83 l s^{-1} and then discharge was progressively increased to a maximum of 2.1 l s^{-1}. As expected, when discharge was increased, the total area of the wetted channel increased (Figure 4.31).
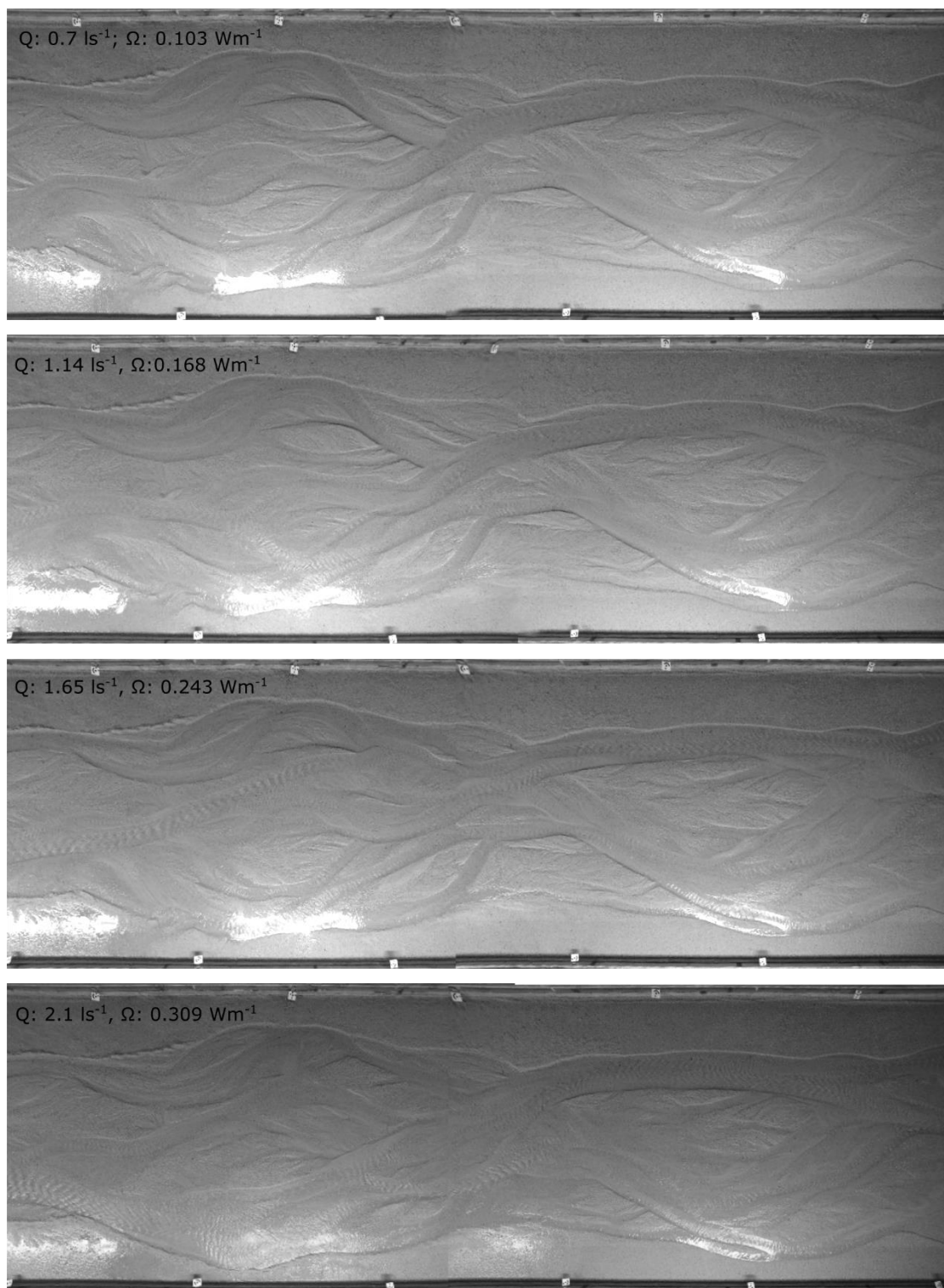
Figure 4.31 – Orthophotos from the rising limb of hydrograph A showing changes in wetted width with increasing discharge.

4.3.1.2 Wetted Width and Braiding Intensity

The wetted width in experiment 11 increased with increasing discharge, although there was variability for a given discharge (Figure 4.32). Note that each discharge has a different number of observations based on the number of times that discharge was used in the hydrographs.

a)

b)
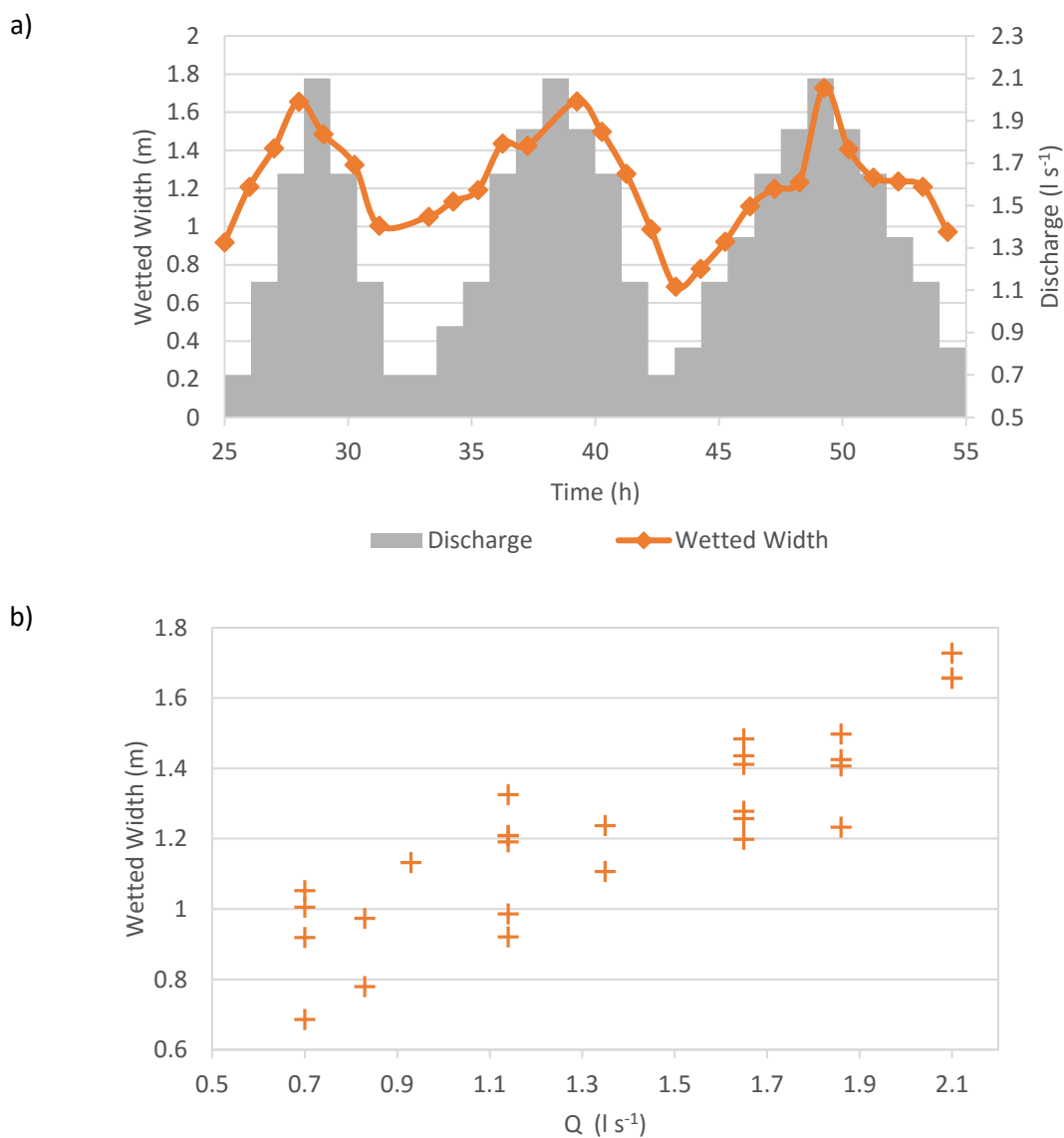
Figure 4.32 – Measured wetted width for the hydrograph experiment as a function of a) time and b) discharge (Q).

Plots of braiding intensity and active braiding intensity show that both indices increase with discharge (Figure 4.33). This is especially true for active braiding intensity, which not only increases with increasing discharge, but is reduced to zero under some low discharge conditions (Figure 4.34). This highlights the fact that at low discharges, detectable elevation change is reduced to zero or near zero.
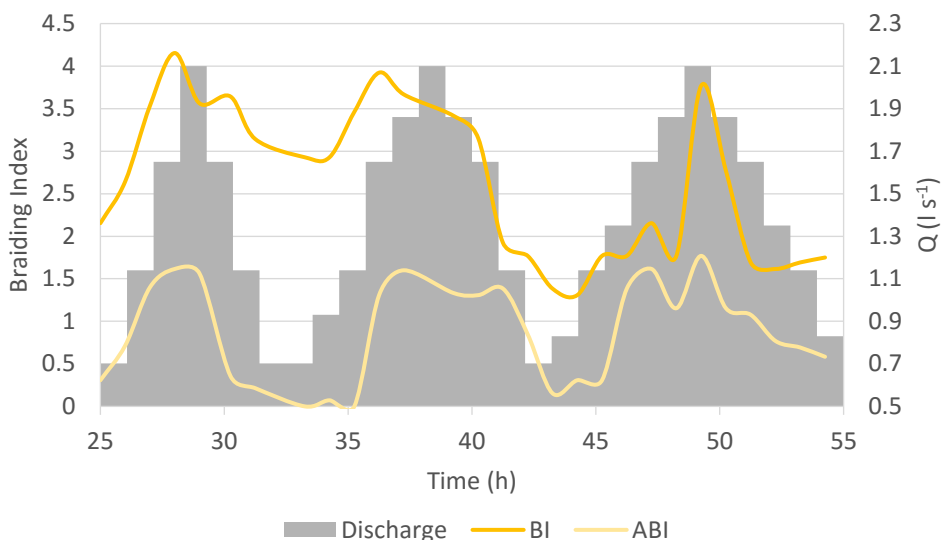
Figure 4.33 – Temporal variability in braiding and active braiding intensities (BI and ABI, respectively) across the three experimental hydrographs, where Q is discharge.

The braiding intensity was found to be highly variable for a given discharge in the hydrograph experiments (Figure 4.34). In general, the BI was greatest at high discharges and lowest at the low discharges, although there were differences between the three hydrographs. The trend of increasing BI with stream power (or in this case, discharge) is much less clear than it was for the constant discharges experiments. The ABI, however, does have a positive relationship with discharge (Figure 4.34). The exception is the experiment at $0.93\,l\,s^{-1}$, but as mentioned, this could be due to the relatively limited amount of data available at that discharge.

a)

b)
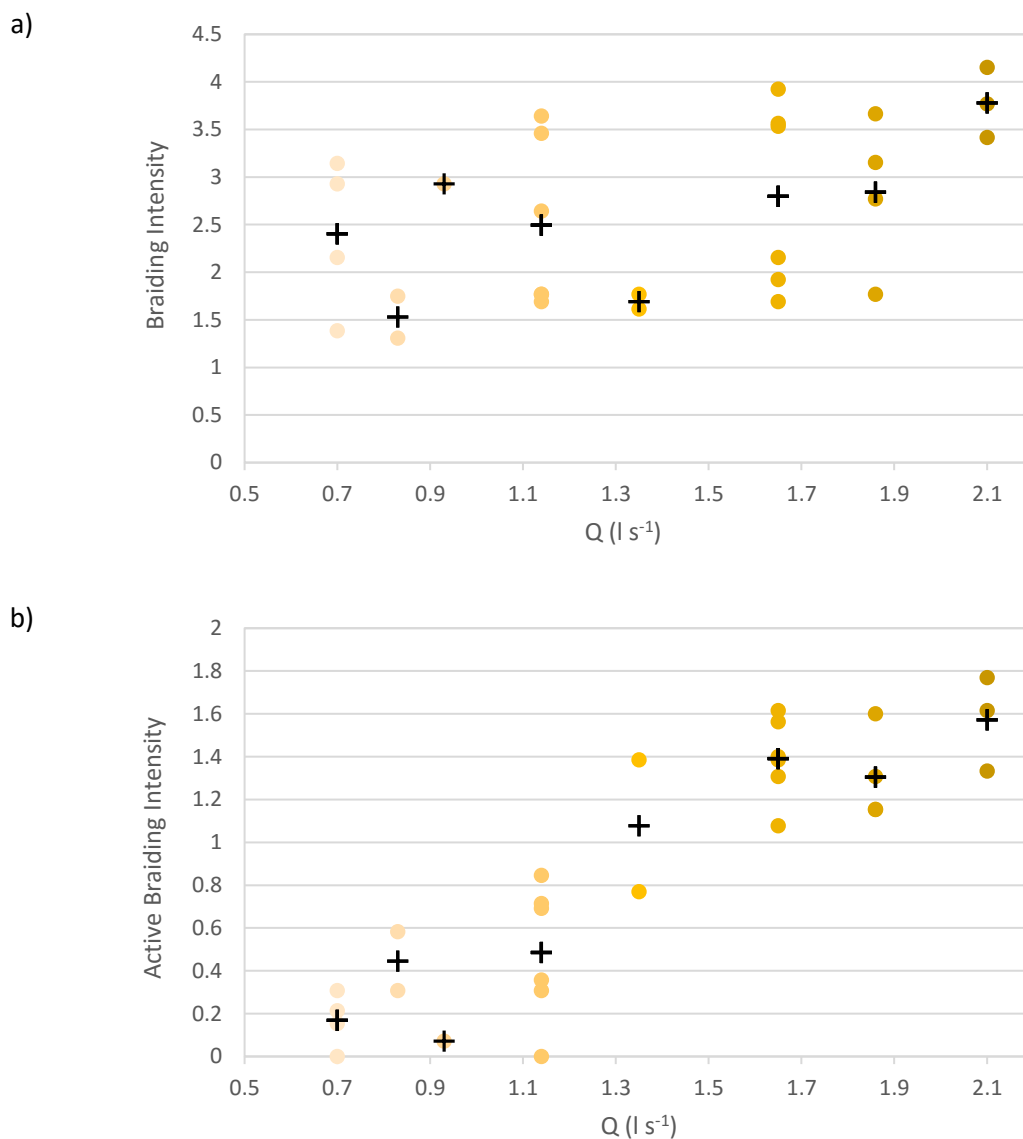
Figure 4.34 – a) Braiding intensity and b) active braiding intensity for the hydrograph experiment as a function of discharge (Q). Black crosses represent the mean for each discharge.

A plot of the active braiding intensity (ABI) as a function of the total braiding intensity (BI) is in Figure 4.35. There is an increase in ABI with discharge but there is substantial scatter in the BI for any given discharge. For example, there is a cluster of observations for 1.65 l s^{-1} with a BI of ~1.7 and another cluster with a BI > 3.5. This would reflect changes in morphology and channel switching as the hydrographs progressed. Only discharges

greater than 1.35 l s^{-1} achieved an ABI greater than one and all observations for discharges greater than 1.65 l s^{-1} have ABI's between 1-1.8 (Figure 4.35).
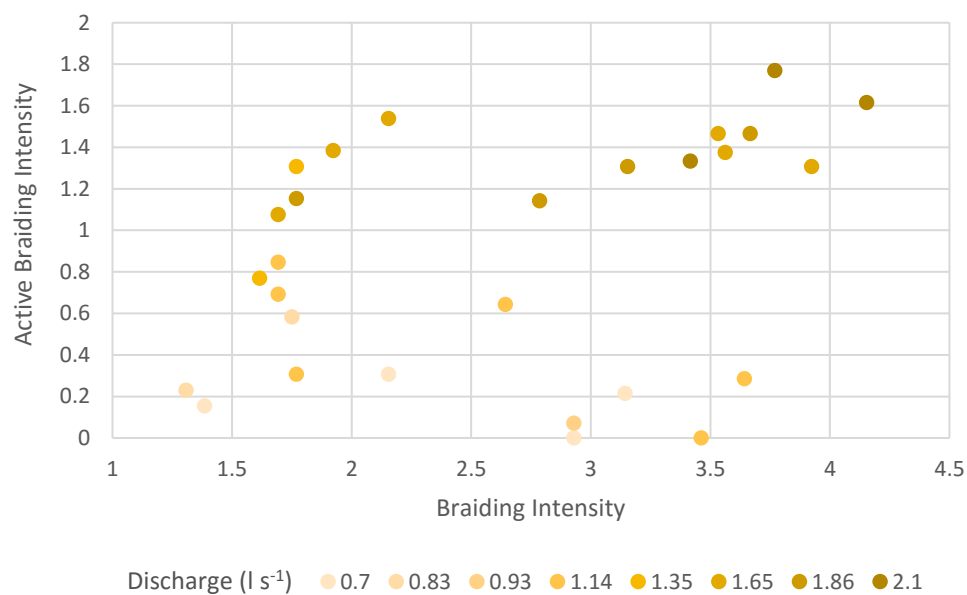
Figure 4.35 – Active braiding intensity plotted against braiding intensity for the different discharges used in the hydrograph experiment.

Plotting the braiding indexes against the wetted width there is a positive relationship (Figure 4.36). Both BI and ABI have a similar R^2 value with 0.540 and 0.566, respectively.
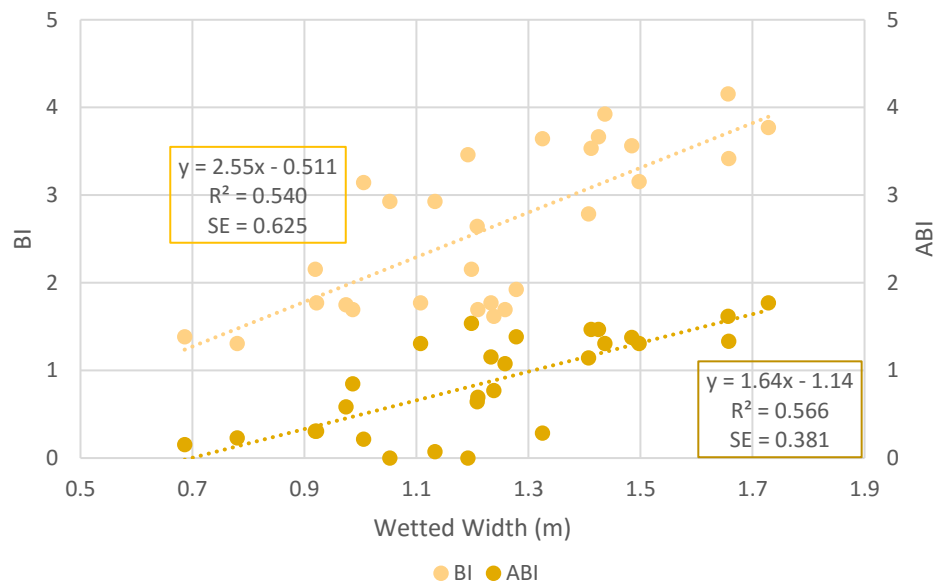
Figure 4.36 – Braiding intensity (BI) and active braiding intensity (ABI) as a function of wetted width. The dashed lines represent the best fit trendlines.

The ratio of ABI and BI has a mean of 0.35 ($\sigma = 0.22$) but a range from 0 to 0.78 (Figure 4.37). In general, the ratio of ABI to BI does increase with discharge, reflecting that a larger proportion of wetted channels are active at high discharge.
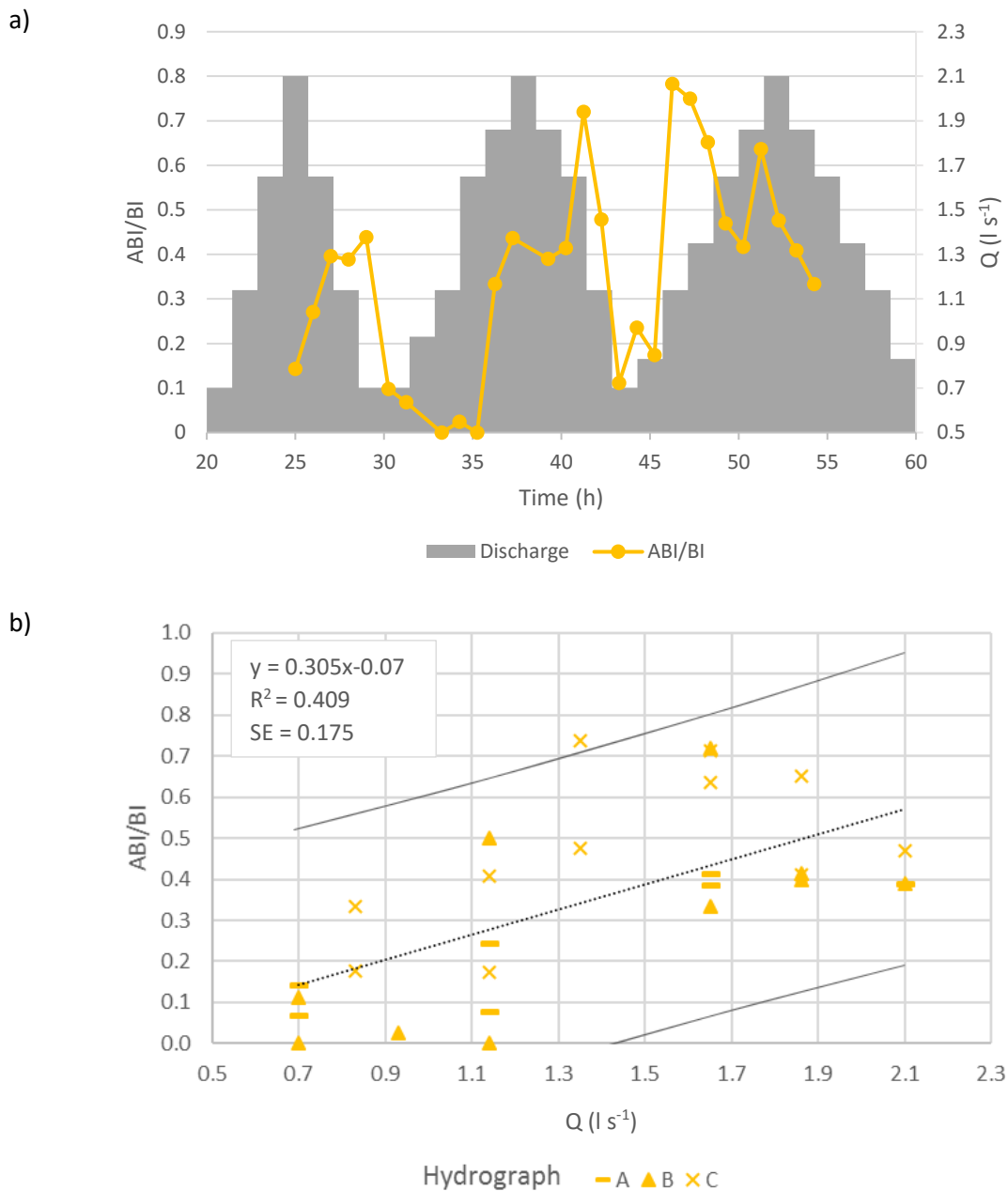
Figure 4.37 – Ratio of active braiding intensity (ABI) to total braiding intensity (BI) as a function of a) time and b) discharge (Q). The dashed line in b) represents the best fit trendlines and the outer solid lines represent the 95 % prediction interval for the observations.

4.3.1.3 DEMs and DoDs

Figure 4.38 shows an example DEM from the rising limb of hydrograph A as well as the final DEM at the end of hydrograph C. There are multiple primary and secondary anabranch channels and braid bars that had developed over the course of the experiment. Also, while most of the channel boundaries remained unchanged, there was one laterally migrating channel that reached the flume sides by the end of the experiment visually indicating that there was still a lot of change over the three hydrographs (Figure 4.38).
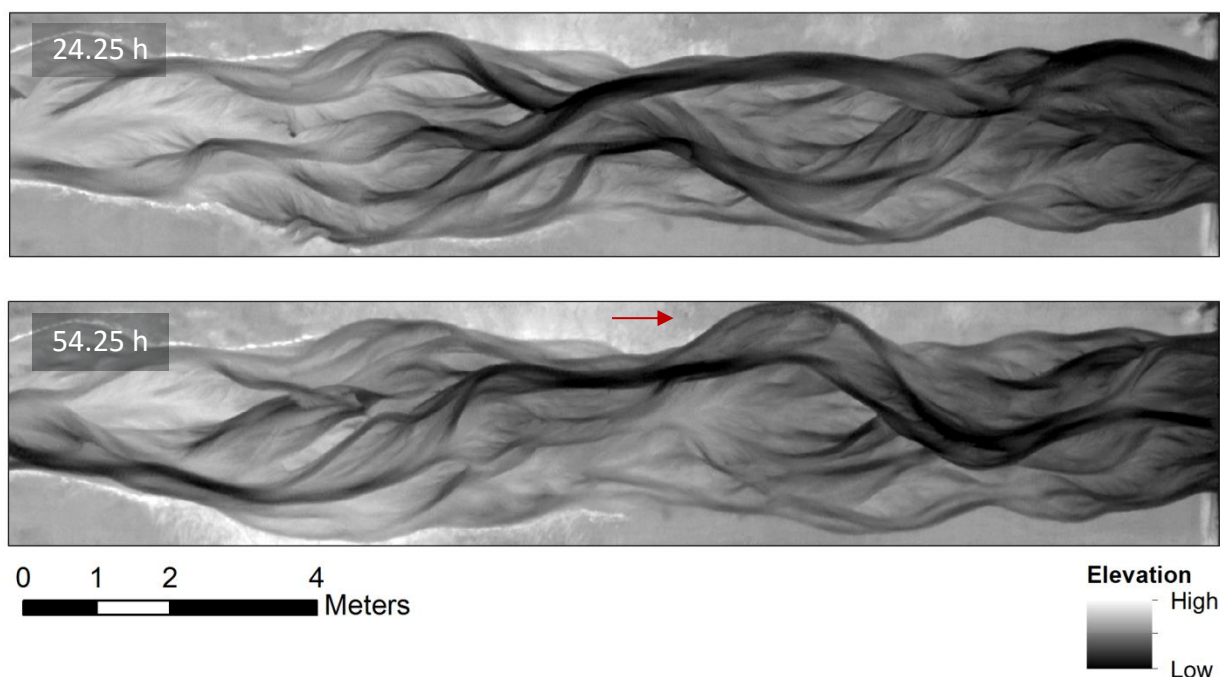
Figure 4.38 – Example DEMs from Experiment 11. The top DEM is from the beginning of the experiment runs and the bottom DEM is from the last experimental run of the hydrographs. The red arrow in the bottom DEM shows a location of strong lateral migration. Flow is from left to right.

Figure 4.39 shows DoDs from each step of the rising limb of hydrograph A. Based on a preliminary visual analysis, these DoDs show that as discharge increases the areas of erosion and deposition increase as well. Furthermore, the areas of change become more continuous and the depth of change becomes greater with increasing discharge, consistent with the results of the constant discharge experiments (Figure 4.39).

Q = 0.7 l s⁻¹
Ω = 0.10 W m⁻¹

Q = 1.14 l s⁻¹
Ω = 0.17 W m⁻¹

Q = 1.65 l s⁻¹
Ω = 0.24 W m⁻¹

Q = 2.1 l s⁻¹
Ω = 0.31 W m⁻¹
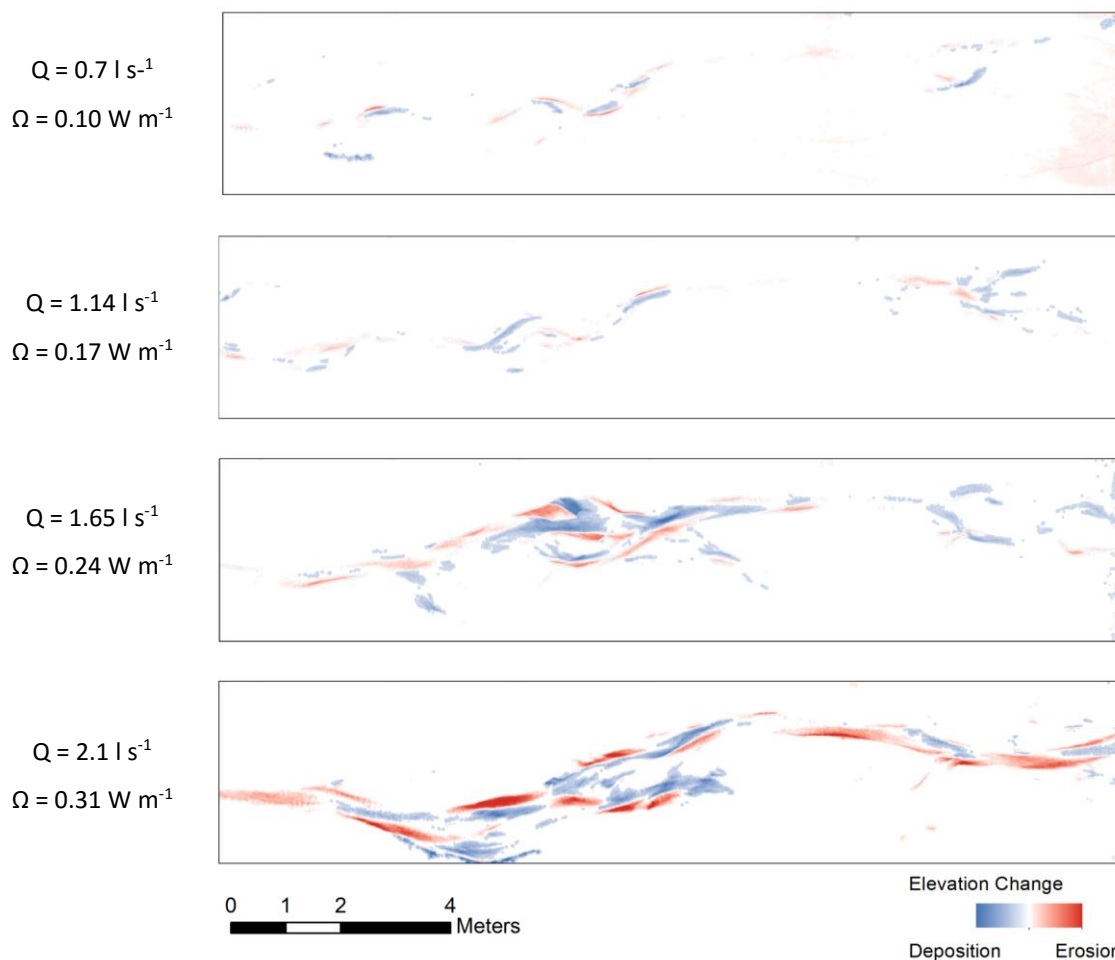
Figure 4.39 – DoDs from the rising limb of hydrograph A showing increasing area and depth of elevation changes with increasing discharge. Flow is from left to right, where Q is discharge and Ω is total stream power. Results shown were derived using the dilation method.

4.3.2 Experimental Results

4.3.2.1 Bedload transport

To investigate the linkages between bedload transport and the active width over the experimental hydrographs, all the sediment collected at the downstream end was weighed at the end of each run. Temporally, bedload transport is highly variable, both across the hydrographs and at the same discharges between hydrographs (Figure 4.40). Looking at the variability at each discharge in a box plot, the mean bedload transport rate and range increased above a lower threshold of 1.14 l s⁻¹ and then continued to increase positively

with discharge and stream power (Figure 4.40). Below 1.14 l s^{-1}, measured bedload transport rates were negligible (Figure 4.40).

a)

b)
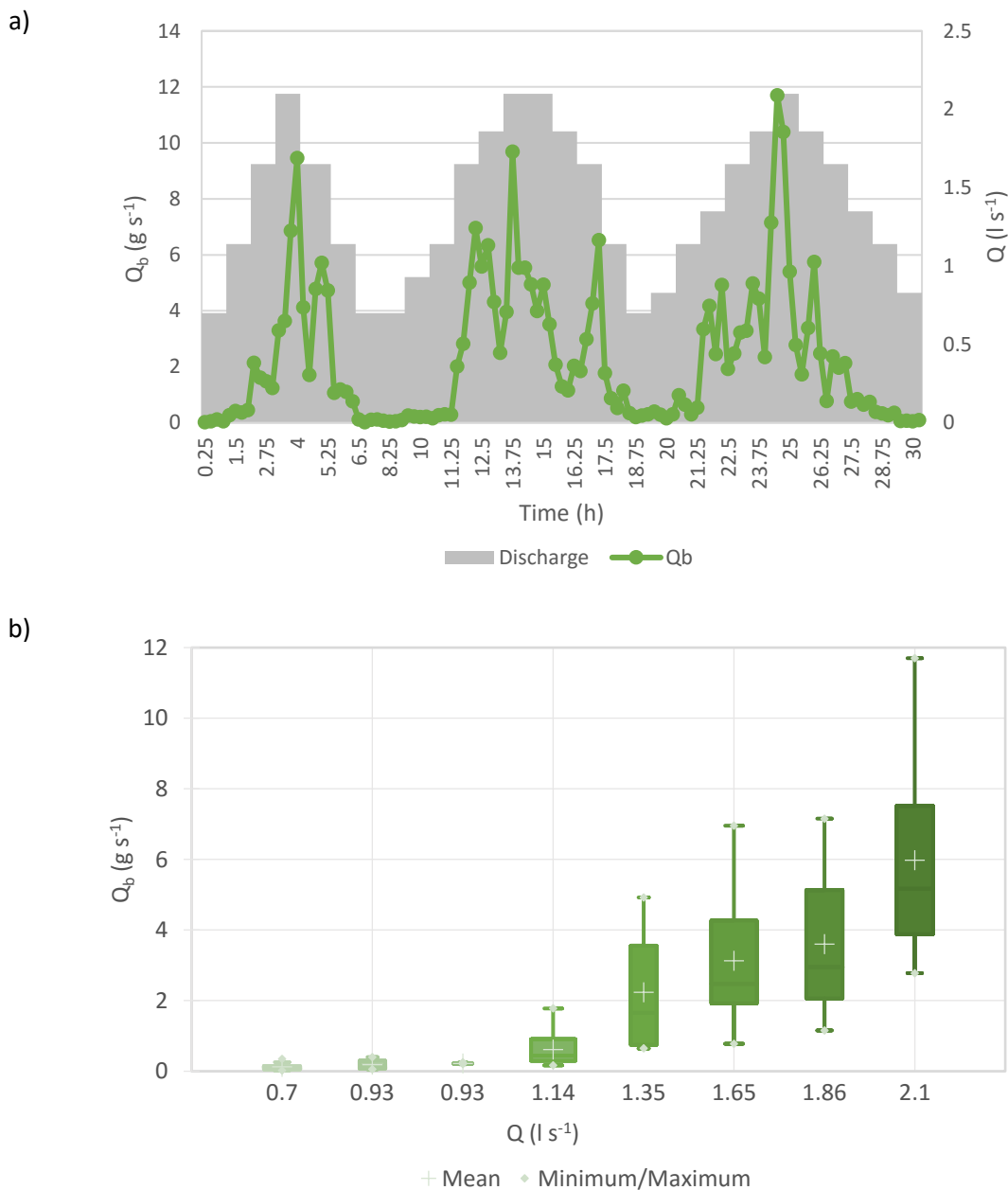
Figure 4.40 – Bedload transport (Q$_b$) as a function of a) time and b) discharge (Q), over the range of discharges from the hydrograph experiment, experiment 11.

4.3.2.2 Active Width and Active Depth

As with the constant discharge experiments, the active width in the hydrograph experiment varied with increasing discharge over time (Figure 4.41). From both the temporal and box

plot graphs it appears that below discharges of ~ 1.14 l s^{-1} there is very little detectable morphological change (average < 0.03 m). Above 1.14 l s^{-1}, the mean active width increases with increasing discharge, although there is also greater range in active width at greater discharges. In addition, the active width seems to increase faster with the rising limb of the hydrograph than on the falling limb, which is most noticeable in hydrograph B. Like the constant channel-forming discharge experiments, the dilation method produces greater values of active width, reflecting the slight increase in active area created using this method (See Section 3.6.5 for more information on threshold methods). The differences in the simple 2σ threshold and the dilation were not significant for any of the discharges below 1.65 l s^{-1} based on a standard two-tailed Student's t-test (See full results in Appendix I, Table I.4). The values of active width for 1.65 l s^{-1} measured with the simple threshold ($\bar{x}$ = 0.16 m, σ = 0.04 m) were statistically different from the dilation threshold results ($\bar{x}$ = 0.21 m, σ = 0.05 m) (t (48) = -4.64, p = <0.0001). Similarly, the results were significantly different for both the 1.86 l s^{-1} (t (28) =-2.70; p = 0.01) and 2.1 l s^{-1} (t (28) = -2.47, p = 0.020) (Appendix I, Table I.4).
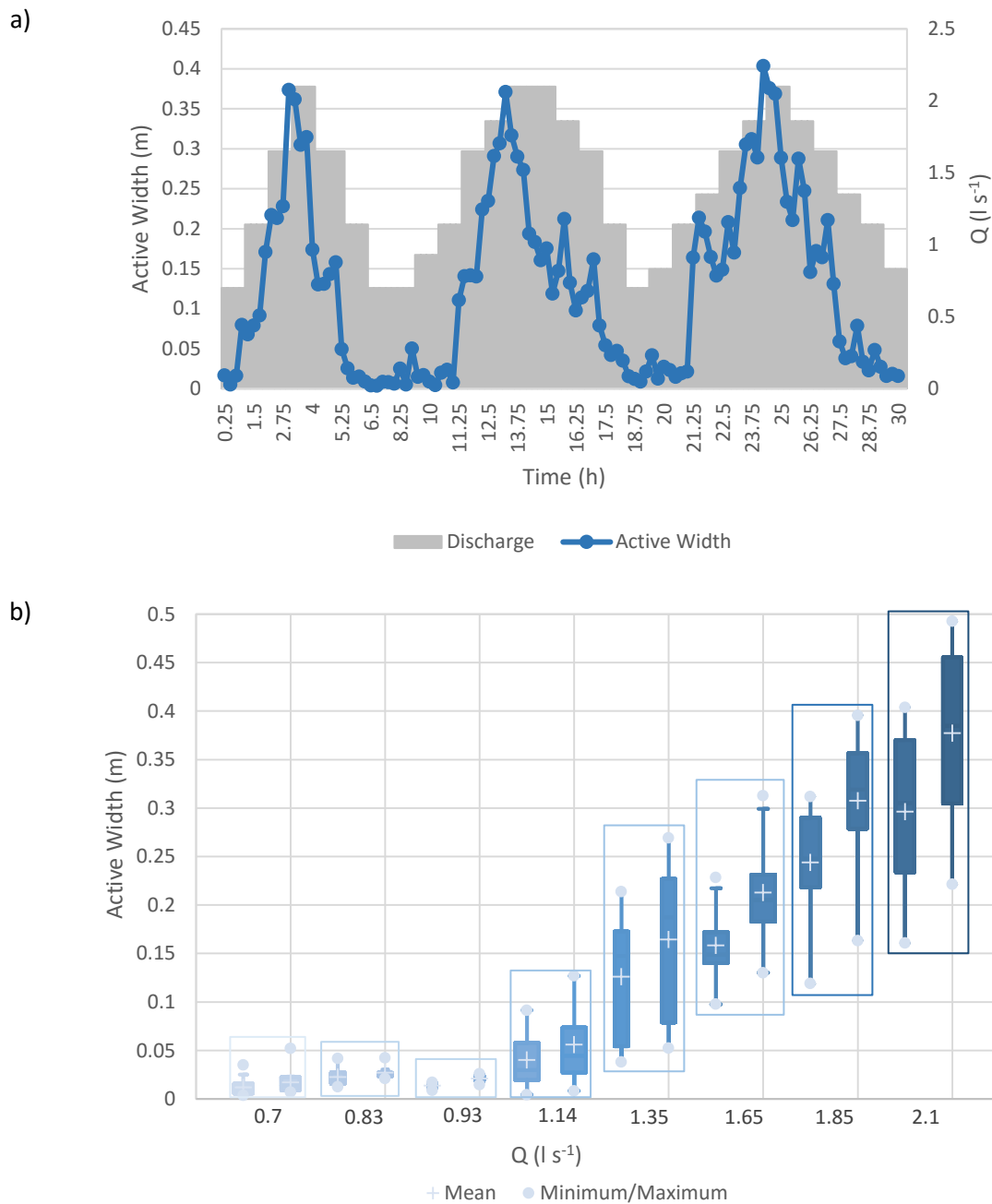
Figure 4.41 – Active width as a function of a) time and b) discharge (Q) across the hydrograph experiments. The top graph shows the temporal results using the simple 2σ threshold. The box plot shows results from both the simple (left) and dilation (right) threshold methods in each discharge box.

When plotting the average values for active width using both thresholds and stream power, there is a strong positive power relationship (Figure 4.42). Based on a simple two-tailed Student's t-test, there was no significant difference between the two threshold methods (t (14) =-0.533, α= 0.05, p= 0.603).
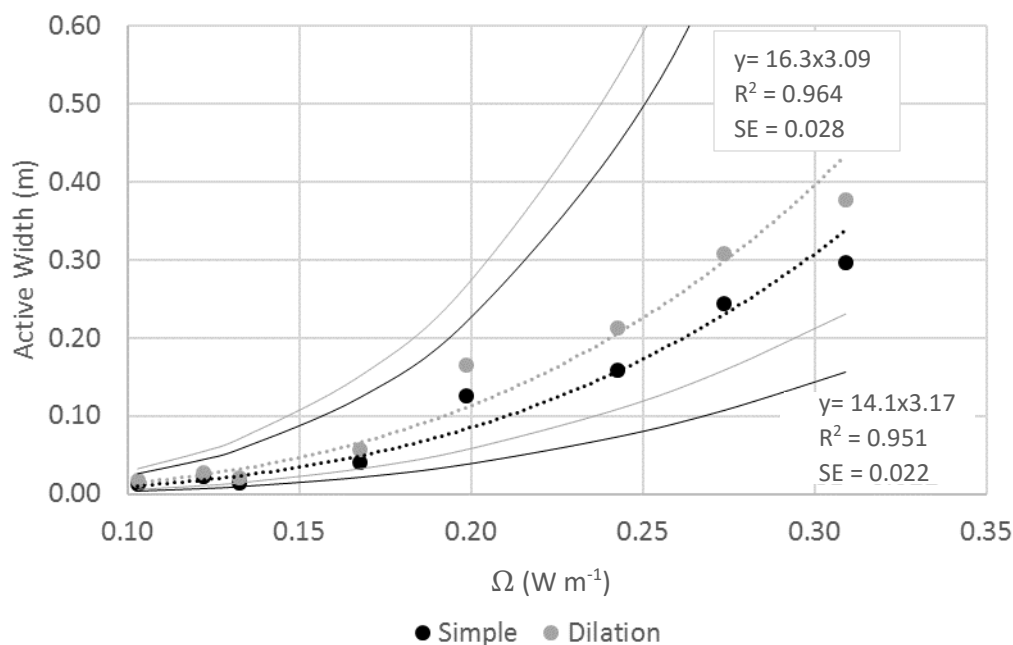
Figure 4.42 – Active width as a function of total stream power (Ω). The dashed lines represent the best fit trendlines and the outer solid lines represent the 95% prediction interval for the observations.

Like the constant discharge experiments, the active erosional and depositional widths both increased with increasing discharge and therefore stream power, although there is considerable variation at high discharges (Figure 4.43). Similarly, the hydrograph results support the trend found in the constant discharge experiments, where the widths of deposition are consistently larger than the erosional widths under all discharges, apart from experiments done at a discharge of 0.83 l s^{-1}. Like the total active width, values of active width for erosion and deposition are generally very low below 1.14 l s^{-1} (average < 0.015 m) and increase steadily above this lower threshold.
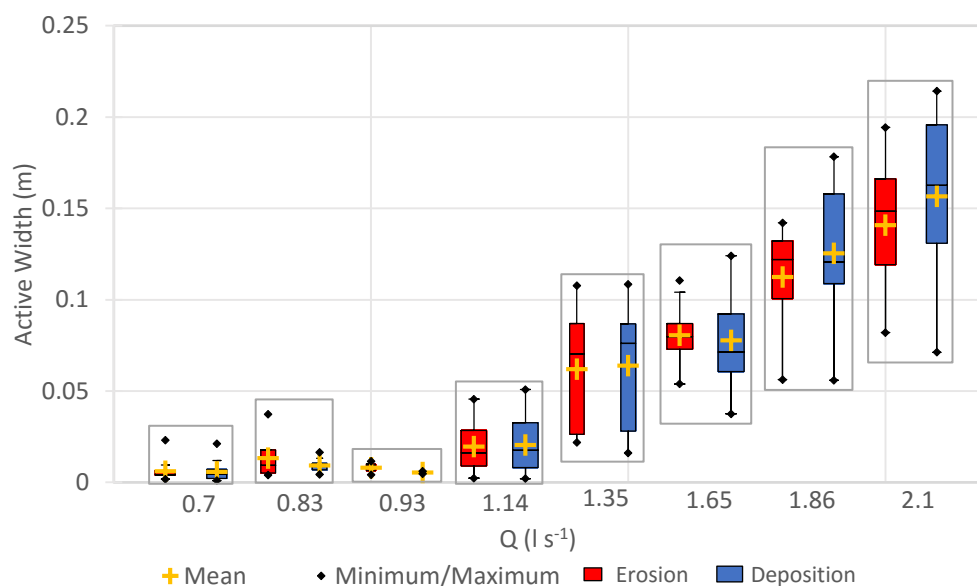
Figure 4.43 – Erosion and deposition active widths for the hydrograph experiments using the simple 2σ threshold, where Q is discharge.

The relationship between active depth and discharge appeared much stronger for the hydrograph experiments than it was for the constant discharge experiments (Figure 4.20 and Figure 4.44). Here, there was a positive trend with stream power, especially at discharges greater than $1.14 \, \text{l s}^{-1}$. As expected, the values of average active depth are larger using the simple 2σ threshold than the dilation threshold and the differences were found to be statistically significant for all discharges apart from those at $1.35 \, \text{l s}^{-1}$ (See full results in Appendix I, Table I.5).

a)

b)
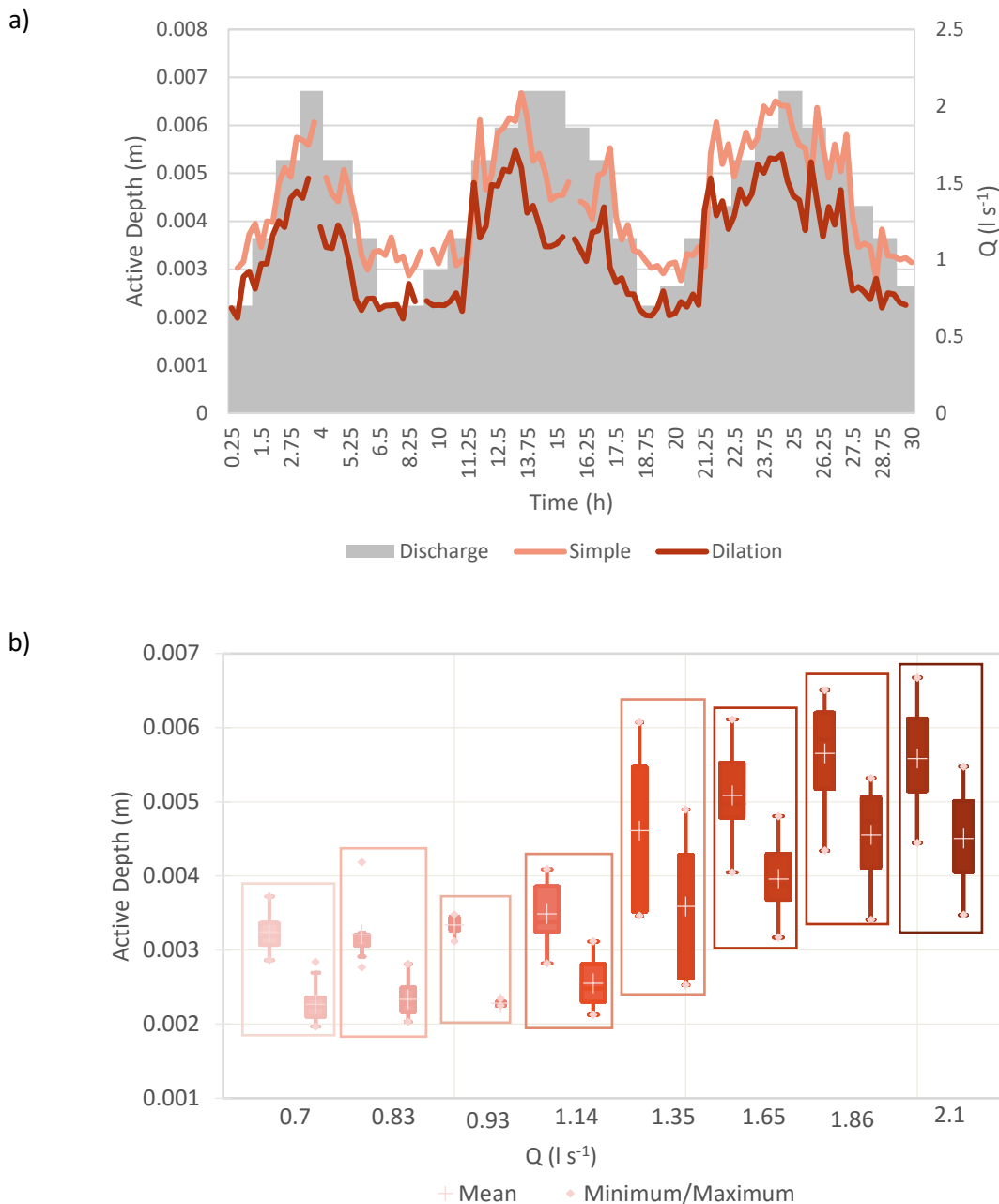
Figure 4.44 – Active depths as a function of a) time and b) discharge (Q) for the 3 hydrographs. Results are shown for both the simple 2σ threshold (left in box plot) and the dilation threshold (right in box plot) for each discharge.

Figure 4.45 shows the active depth divided into its erosional and depositional components. Like the active width, depths of erosion and deposition increase with discharge and stream power above the threshold of 1.14 l s^{-1} or 0.17 W m^{-1}, below which the values are largely undetectable. At low discharges ($0.7 - 0.93 \text{ l s}^{-1}$) depths of erosion are greater than depths

of deposition, while at higher discharges the depth of deposition is generally greater. The exception to this trend is 1.65 l s^{-1} which has a slightly higher erosional depth of 0.081 m compared to its depositional depth of 0.078 m (Figure 4.45). Based on a simple two-tailed Student's t-test, the differences between depths of erosion and deposition were not significant (See full results in Appendix I, I.5). This outcome is much different than those found for the constant discharge experiments which showed a much less clear correlation with stream power and had greater erosional depths than depositional depths under all experimental conditions (Figure 4.21).
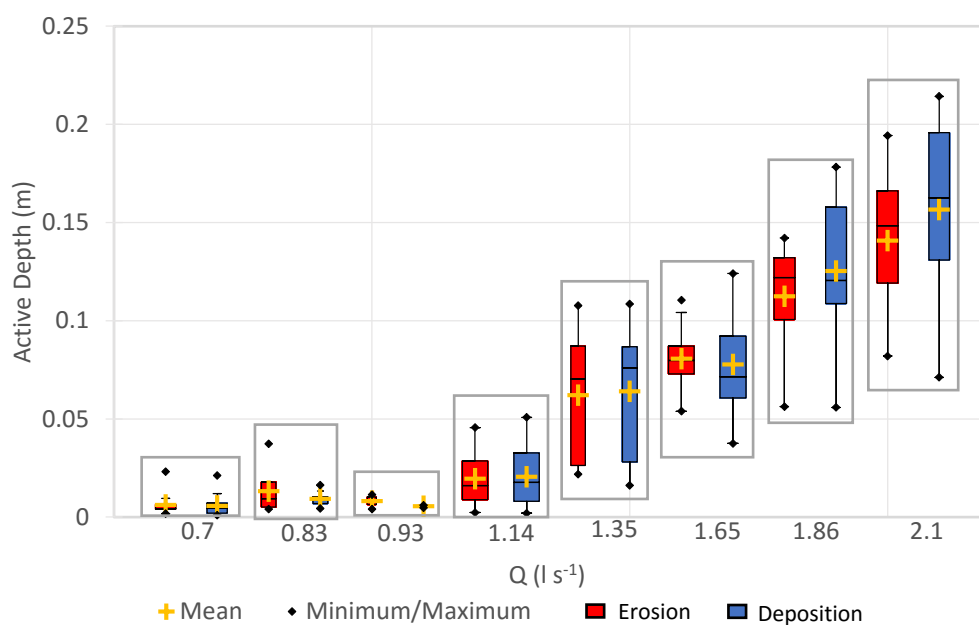
Figure 4.45 – Variability in erosional and depositional depths of all hydrograph discharges. Results shown are for the simple 2σ threshold and where Q is discharge.

4.3.2.3 Volumes of Erosion and Deposition

Plotting the erosional and depositional volumes of change temporally along with the bulk change, it is clear how all three correspond with discharge over all three hydrographs (Figure 4.46). Yet, although all three hydrographs had the same peak discharge of 2.1 l s^{-1}, the mean bulk change for each peak was different. Hydrograph C had the greatest values for both volumes of erosion and deposition, followed by hydrograph A, and finally hydrograph B. The exact reason for this is unknown but hydrograph B had 8 consecutive runs at 2.1 l s^{-1} while A and C each only had 4. The interesting thing is that the first 4 runs at 2.1 l s^{-1} for hydrograph B have very similar volumes of change as hydrograph A and C.

In the second 4 runs, however, the volumes of change are almost half of the first four runs. This variability within a given hydrograph and between hydrographs may highlight the importance of antecedent conditions and morphology in determining volumes of change, and ultimately bedload transport rates.
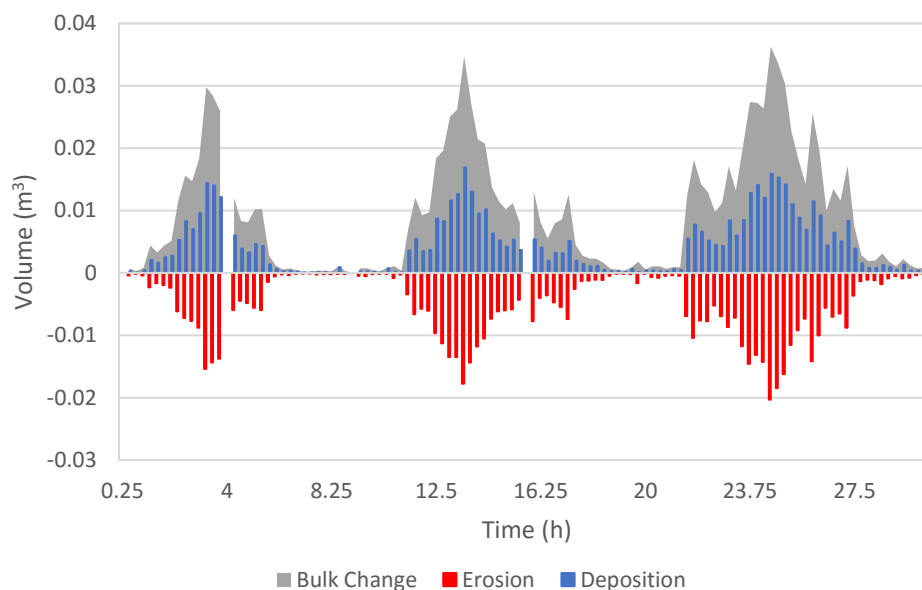
Figure 4.46 – Temporal variability in the volumes of erosion and deposition overlying bulk change.

Looking at the box plots for the erosion and deposition volumes, all discharges below 1.14 l s^{-1} show very small volumes of change (average < 0.001 m^3) (Figure 4.47). Above this lower threshold of change, the volumes increase with increasing stream power towards the maximum volumes of change at the peak discharge of 2.1 l s^{-1}. Comparing the volumes of erosion and deposition, volumes of erosion are consistently greater than those of deposition and the difference of means seems to increase with greater discharge. In other words, at greater discharges a greater proportion of the total volume change was attributed to erosional features. This could be an artifact of the measurement techniques, which may also explain why this trend is different than for the erosional and depositional components of the active width and active depth. The volumes are calculated as a product of the z values (i.e., the estimated change in elevation) and the number of active cells, while both the active width and depth are average estimates for the 14 m study reach. The results in Figure 4.47

suggest that even though the average active widths and depths are greater for depositional areas, locally, erosion accounts for a greater proportion of the measured bulk change.
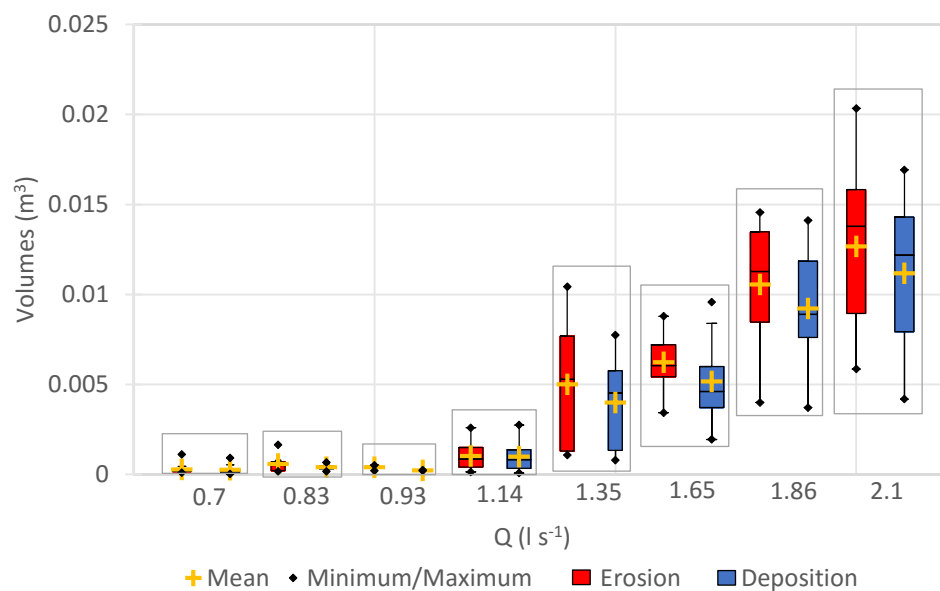
Figure 4.47 – Box plots of the volumes of erosion and deposition for the simple threshold method, where Q is discharge.

4.3.3 Analysis and Comparison with Constant Discharge Experiments

To fulfill the main research objective of this chapter, it important to look at how the active width corresponds with hydraulic and morphological parameters. In addition, the data allows for the comparison of the constant channel-forming discharge experiments and the hydrograph experiments, which is essentially a comparison of downstream verses at-a-station responses. While the hydrograph experiments did not achieve the stream powers of experiment 12 and 13, all the other constant discharge experiments were represented in multiple steps of the hydrograph experiments.

First, dimensionless bedload transport rate (qb*) and dimensionless stream power (w*) have a much stronger positive relationship in the hydrograph experiments than the constant discharge experiments, which had a poor linear relationship defined by an R^2 of 0.351 (Figure 4.24). Here, the results are best represented by a power relationship with an R^2 value of 0.730 (Figure 4.48). There were 5 observations that plotted away from the best fit

trendline and each of these observations had a relatively high bedload transport rate compared to other measurements for the same discharge. Therefore, these observations reflect some of the variability in bedload transport rate for a given discharge.

The plot shows qb^* (y-axis) versus w^* (x-axis), with the annotation:

$$y = 431x^{5.31}$$
$$R^2 = 0.730$$
$$SE = 0.003$$
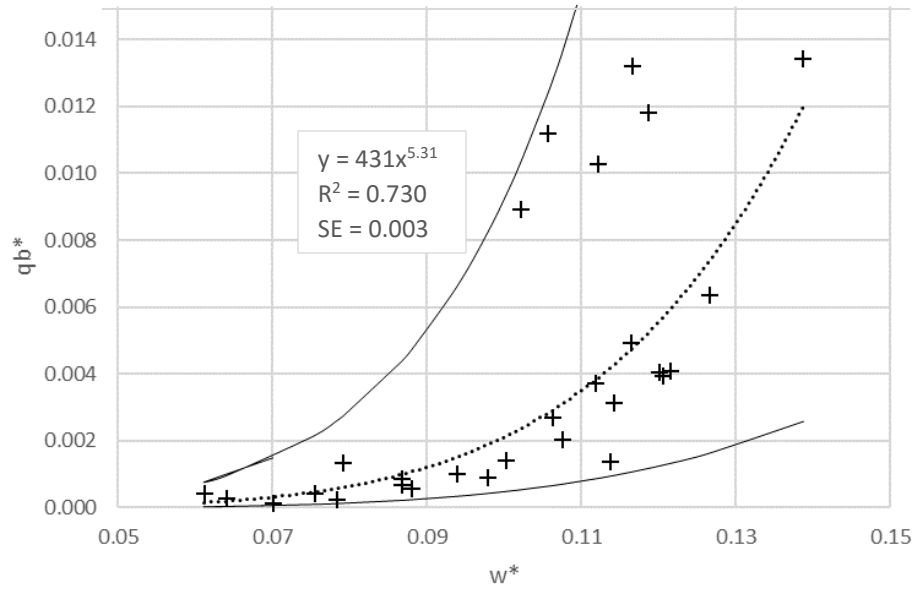
Figure 4.48 – Dimensionless bedload transport rate (qb*) as a function of dimensionless stream power (w*) for the hydrograph experiments. The dashed lines represent the best fit trendlines and the outer solid lines represent the 95% prediction interval for the observations.

The non-dimensional active width plotted against dimensionless stream power for 27 data points from the hydrograph experiments demonstrated a positive linear relationship with an R^2 of 0.679 (Figure 4.49). This appears to be a stronger relationship than what was found with the constant discharge experiments, which had an R^2 of 0.507 (Figure 4.26). Similarly, by plotting the ratio of the active width and wetted width against ABI, there is a strong positive linear relationship with an R^2 of 0.709.

a)

b)
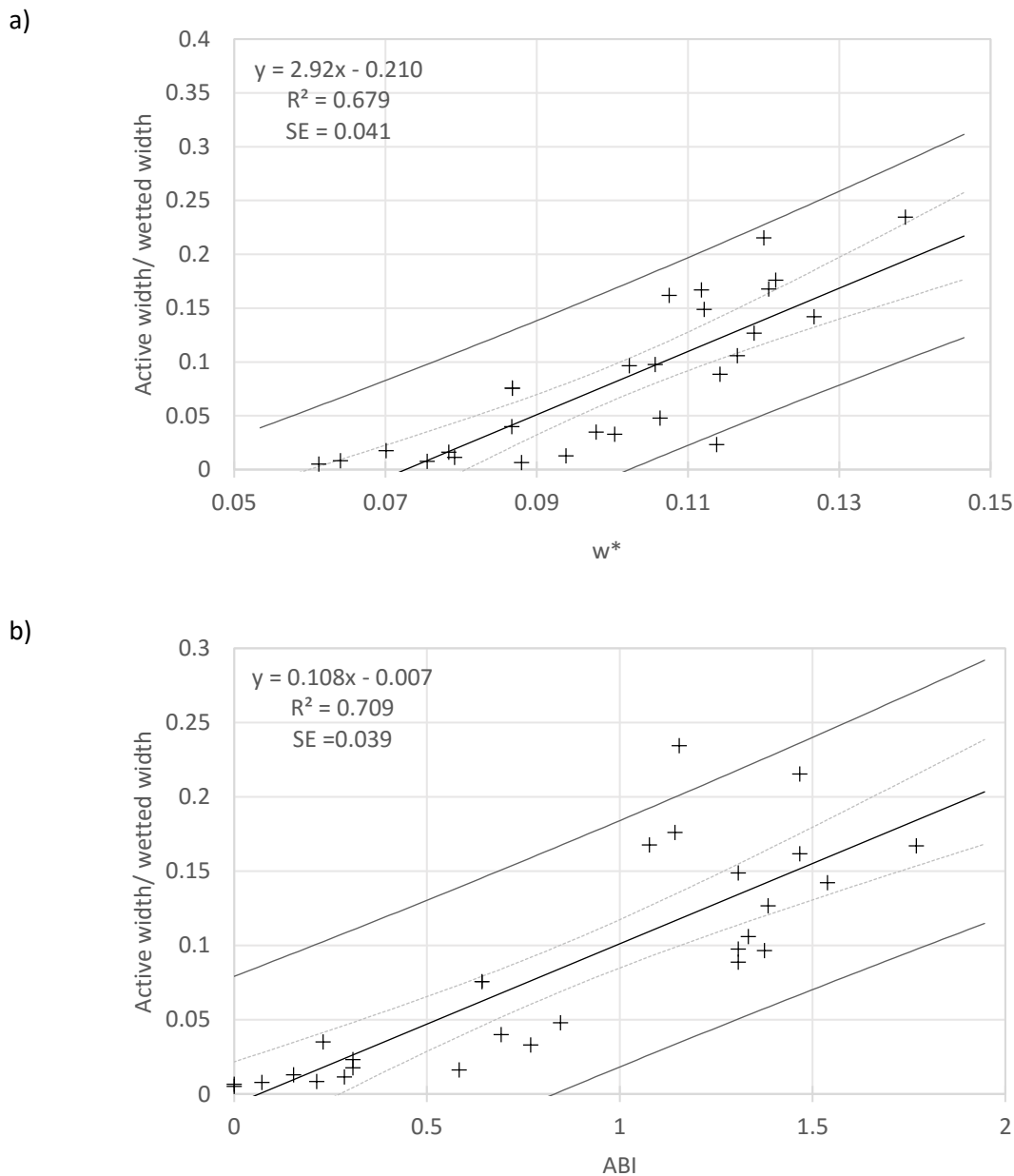
Figure 4.49 – Ratio of the active to wetted width as a function of a) dimensionless stream power (w*) and b) active braiding intensity (ABI) for the hydrograph experiments. The dashed lines represent the 95 % confidence interval around the mean of the regression line, and the outer solid lines represent the 95 % prediction interval for the observations.

The bulk change in the hydrograph experiments exhibited a strong positive, linear, relationship with active width and active depth (Figure 4.50). This is a stronger trend than

the active depth and bulk change relationships found with the constant discharge experiments.

a)

b)
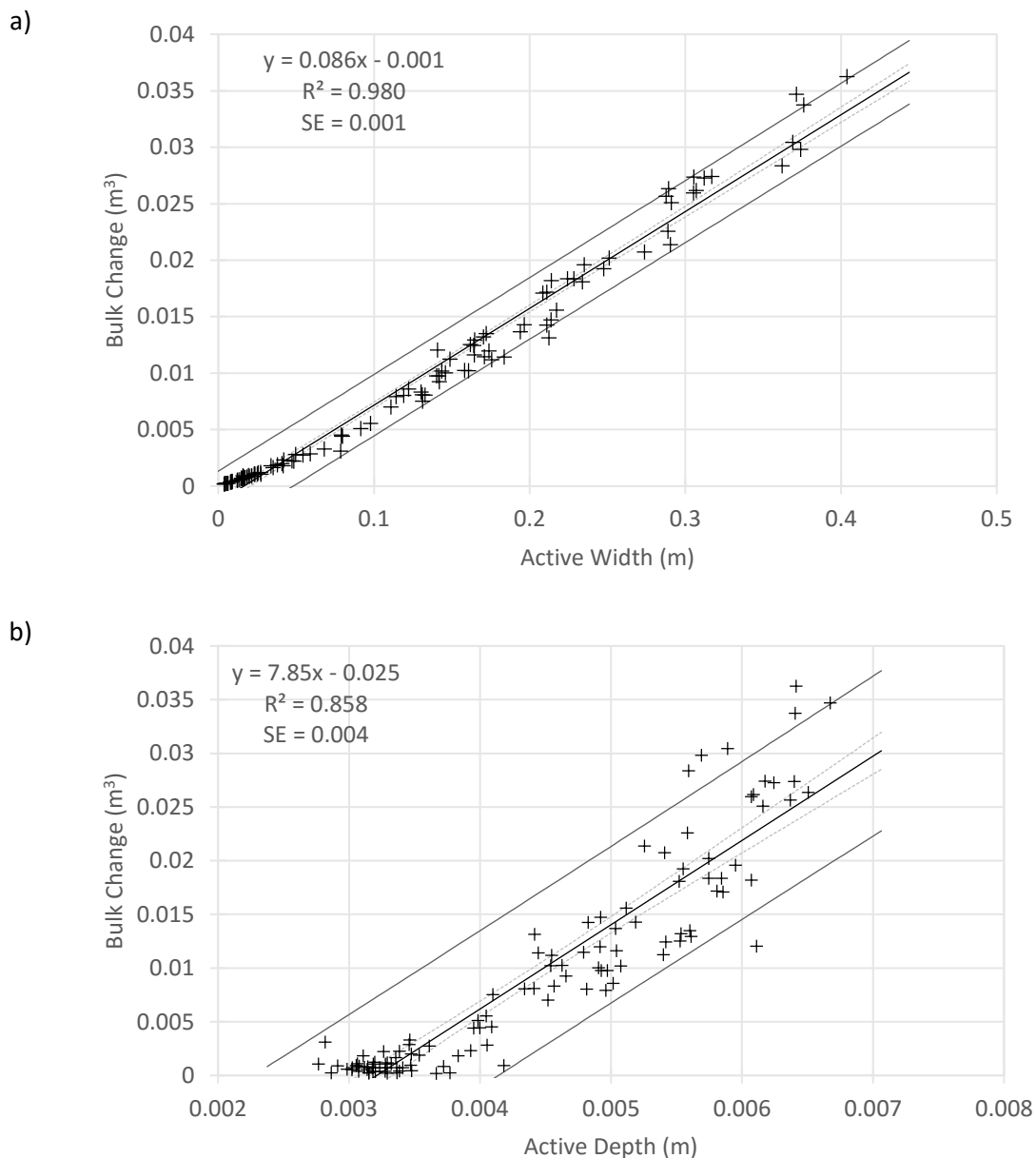
Figure 4.50 – Bulk change as a function of the a) active width and b) active depth for the hydrograph experiments. The dashed lines represent the 95 % confidence interval around the mean of the regression line, and the outer solid lines represent the 95 % prediction interval for the observations. Results are for the simple 2σ threshold.

Plotted together with the results from the constant discharge experiment, the hydrograph experiment covered a similar range of active widths and depths found in the constant discharge experiments 1, 4, and 9 (Figure 4.51). In terms of the active depth, while the hydrograph experiment covered most of the range of the constant discharge experiments, the values are generally higher than those found in experiments 4 and 9. This result is interesting because while the morphologies were different given their self-forming evolution, both the hydrograph experiment and experiment 9 evolved from the same initial discharge of 2.1 l s^{-1}.
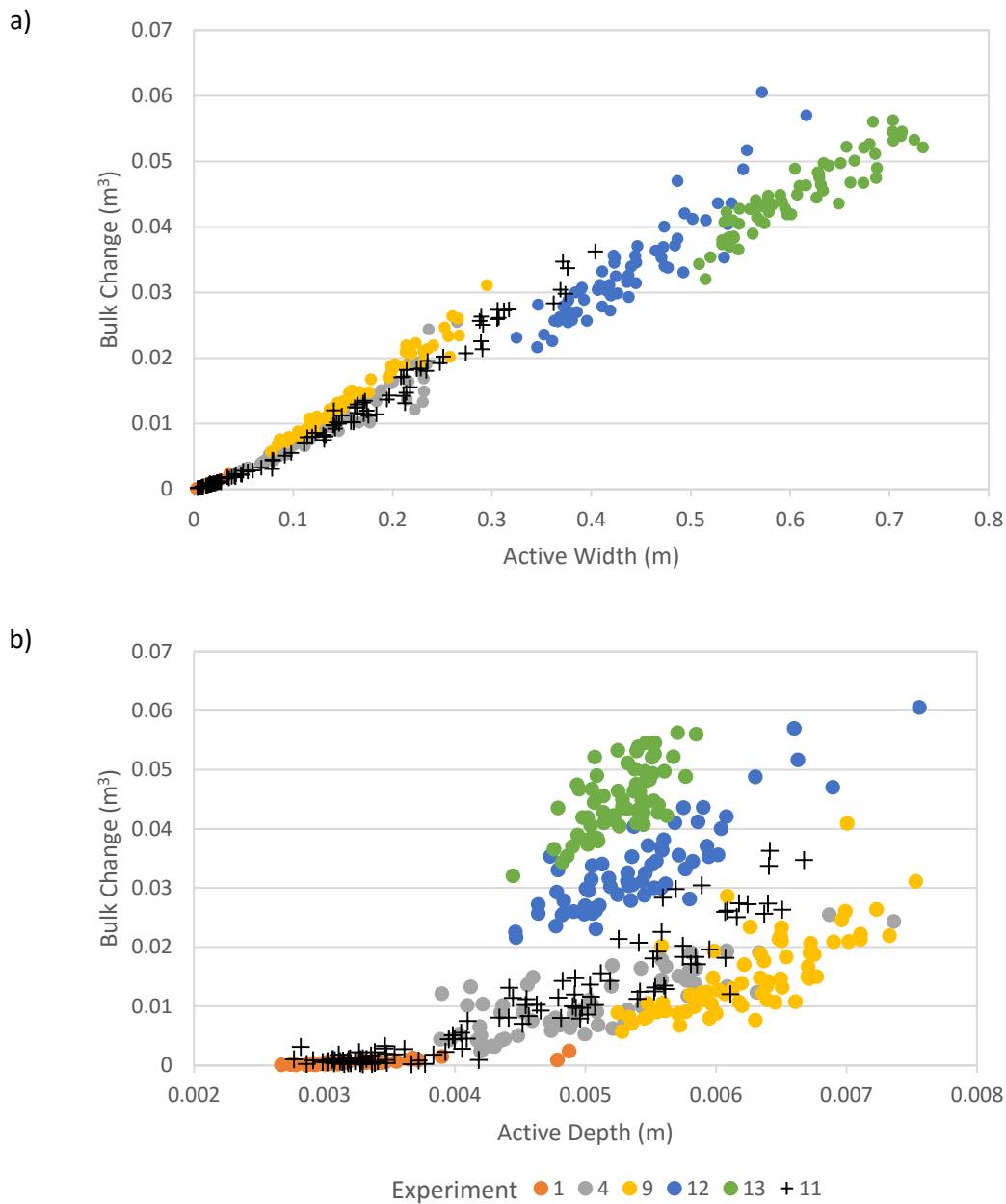
Figure 4.51 – Bulk change as a function of the a) active width and b) active depth for the constant discharge and hydrograph experiments (i.e., experiment 11).

Reach-averaged active depth and reach-averaged active width for the hydrograph experiments have a strong positive relationship (Figure 4.52). This suggests that for a given river, or given discharge in a river, an average measure of active width could provide an estimate of average active depth for a prediction of bedload flux.
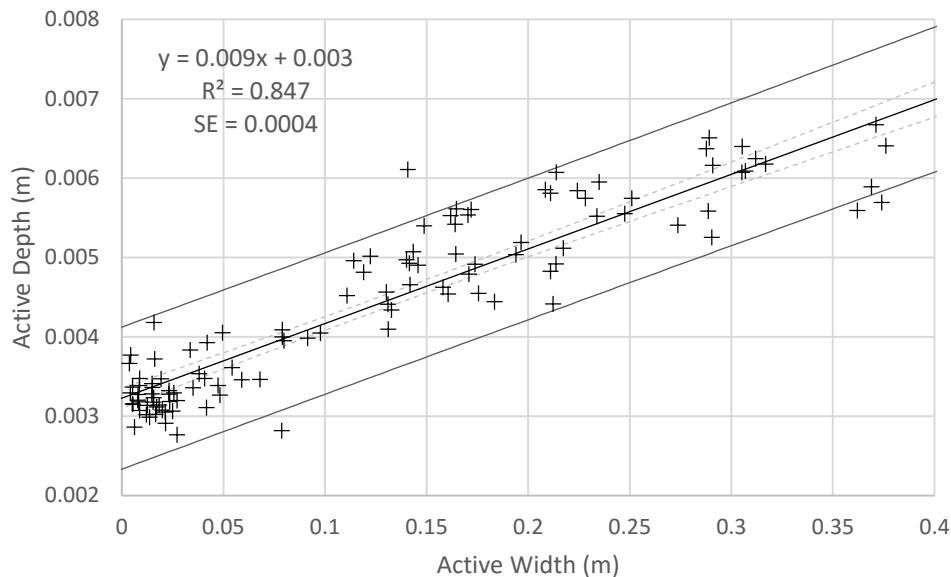
Figure 4.52 – Active depth as a function of active width for the hydrograph experiments. The dashed lines represent the 95 % confidence interval around the mean of the regression line, and the outer solid lines represent the 95 % prediction interval for the observations. Results shown were derived using the simple 2σ threshold.

Plotting the bedload transport rate as measured from the downstream sediment baskets with the active width for the hydrograph experiments produced a positive relationship. Like the constant discharge experiments, this relationship can be well described with a power relationship (Figure 4.53). In Figure 4.53a, the results for both the simple and dilation methods are presented. As expected, the dilation method provides slightly greater active width values than the simple threshold method. Given the nature of the procedure, and the fact that only elevation changes greater than the 3σ are dilated, the result also provided a higher R^2 value of 0.797 (Figure 4.53) (Additional details on the dilation method can be found in Section 3.6.3). Plotting this relationship with the constant discharge experiments for the simple threshold method, the hydrograph experiment again had similar values to the constant discharge experiments 1, 4, and 9 with experiments 12 and 13 extending beyond the range of the hydrograph experiments (Figure 4.53b).
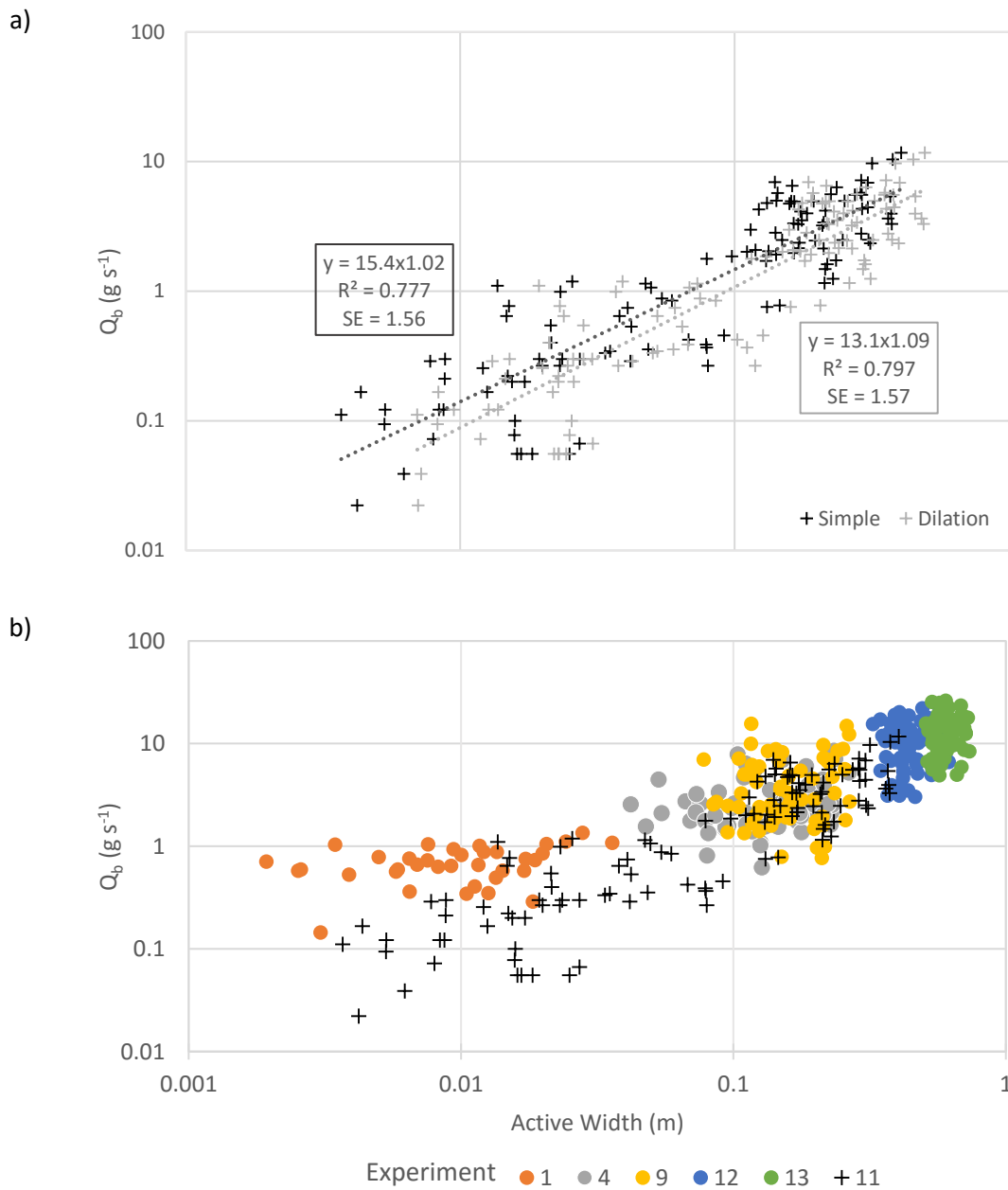
Figure 4.53 – Bedload transport rate (Q_b) determined from sediment baskets as a function of the morphologically-derived active width where a) shows all observations from the hydrograph experiment for both the simple and dilation thresholds and b) shows the results of the simple 2σ threshold for both the hydrograph and constant discharge experiments.

4.4 Discussion

The results of this research can now be compared to previous literature in order to expand on knowledge of braided river morphodynamics. For instance, the wetted width increased with discharge for both the constant discharge and hydrograph experiments. This increase in wetted width with discharge was expected and is supported by other field and flume observations (Ashmore & Sauks, 2006; Bertoldi et al., 2009a).

In a similar way, braiding intensity increased with discharge and stream power for both the constant discharge and hydrograph experiments. For the constant discharge experiments, the results followed previous studies that found that BI increased with changes in channel-forming discharge to a stable equilibrium for a given discharge (Egozi & Ashmore, 2009). In terms of the hydrograph, the ABI was more sensitive to changes in discharge than BI, which followed results by Egozi & Ashmore, (2009), who found that ABI responded to changes in discharge faster than BI. The difference in response rates could explain the apparent convergence of BI and ABI for the hydrograph experiments (Figure 4.36), where the ABI responded to changes in wetted width (i.e., discharge) faster than the BI.

The ratio of ABI to BI for the constant discharge experiments showed that the ratio generally increases with stream power, but was still highly variable within a given experiment. As with previous results, ABI was always less than the BI so that average ABI/BI ratio was 0.559 for the constant discharge experiments (excluding experiment 1, which had a single-thread morphology), and 0.350 for the hydrograph experiments. The differences in the mean ratios are likely due to the differences in stream power between the two experiment types. Based on the results of the hydrograph experiments, morphological change and bedload transport rates were minor below the lower threshold discharge of 1.14 l s^{-1}, or a dimensionless stream power of ~0.08. All the braided constant discharge experiments exceeded this lower threshold, with experiment 4 having the lowest discharge (1.65 l s^{-1}) and dimensionless stream power ($\bar{x}=$ 0.128). The hydrograph experiments, however, had several runs with an ABI value of 0, which were associated with dimensionless stream power close to or below the lower dimensionless stream power threshold of 0.08. The result was a lower overall mean ratio of ABI to BI for the hydrograph experiments. In addition, the range of values of ABI/BI for both the constant discharge

experiments (0.1-1) and the hydrographs (0-0.7) were larger than in previous studies by Egozi and Ashmore (2009) and Bertoldi et al. (2009b), who found that ABI/BI typically stabilized between 0.3 and 0.8. The differences in the lower bounds are related to differences in measurement techniques. In this research, the ABI was measured from cross-sections of DoDs, so any topographical change, which was used as a surrogate for direct observations of bedload transport, below the level of change detection would have resulted in an underestimation of ABI.

Bedload transport rates in the constant discharge experiments followed trends from previous studies that suggest bedload transport rates increase with discharge and stream power, but can be highly variable temporally (Ashmore, 1982, 1988; Bertoldi et al., 2009a). This variability is often associated with the increased bedload activity (e.g., movement of bedload sheets, bar migration and erosion, bank erosion etc.) that occurs under greater stream powers and therefore shear stress. The rates of bedload transport can be compared to those results found during flume experiments reported in Bertoldi et al. (2009a). Plotting the data together, the range of total stream power is similar between all of the experiments, except for one run that completed with a discharge of 4.5 l s^{-1} and slope of 1.5 % (Figure 4.54). Plotting a least-squares trendline indicates a positive relationship and produces an R^2 of 0.682 across all of the experimental observations.
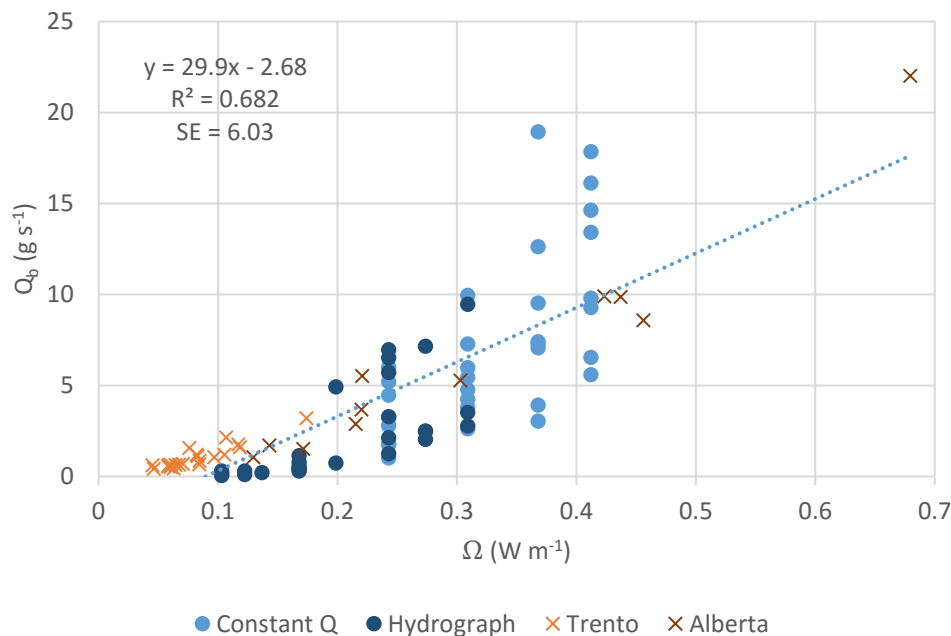
Figure 4.54 – Bedload transport rate (Q_b) as a function of total stream power (Ω) for 4 experimental conditions. The constant Q and hydrograph results represent the constant discharge and hydrograph experiments, respectively. The Trento and Alberta results were published in Bertoldi et al. (2009a).

Using the dimensionless values for bedload flux (qb*) and stream power (w*), the data from the current braided UWO experiments (e.g., excluding experiment 1) and Bertoldi et al. (2009a) results in an overall power relationship with a R^2 value of 0.575 (Figure 4.55). This is different than the power relationship Bertoldi et al. (2009a) originally defined, which had an R^2 of 0.916 (Figure 4.55). The results of the constant discharge and hydrograph experiments cover the low end of the dimensionless stream powers found in the Bertoldi et al. (2009a) experiments, but have a greater range of qb* values. Differences between the two datasets could be the result of differences in data collection methods. For example, while the UWO experiments and Alberta experiments had empirical measurements of wetted width, the wetted widths for the Trento experiments were estimated using a 1D numerical model. In addition, the Trento experiments were completed on a bed of uniform sand with a D_{50} of 0.63 mm. Although it was not included in the calculation of the power trendline, it is interesting to note the location of experiment 1 in Figure 4.55. Experiment 1 had a single-threaded morphology with a relatively high

dimensionless stream power, but a relatively low dimensionless bedload transport rate (Figure 4.55). This difference between braided and single-thread rivers requires more investigation to see if there is in fact a distinct threshold between the different channel morphologies.
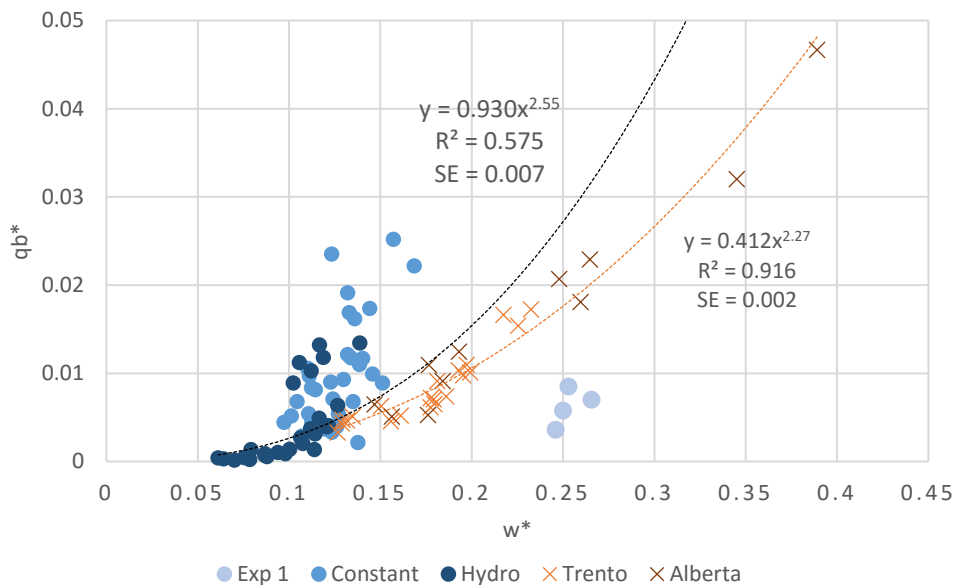
Figure 4.55 – Dimensionless bedload flux (qb*) as a function of dimensionless stream power (w*) for 4 different flume experiments. The black dashed line represents the updated best fit trendline for all of the multi-thread observations while the orange dashed lines represents the original power function defined by Bertoldi et al. (2009a). Experiment 1 was not included in the determination of the trendlines.

In the current research, the active width increased positively with stream power, but was largely undetectable below a threshold discharge (e.g., $1.14\,l\,s^{-1}$) and dimensionless stream power (~0.08) in the hydrograph experiments. In both the constant and hydrograph experiments, the depositional active width was slightly greater than the erosional active width, which suggests that on average, areas of deposition are greater in spatial extent than areas of erosion. Furthermore, the active depth was not particularly sensitive to changes in stream power across the constant discharge experiments, but remained in a relatively narrow range from of values from 0.003-0.007 m for the four multi-threaded experiments (i.e., experiments 4, 9, 12, and 13). This suggests that changes in stream power between experiments was accommodated by increases in the active area (i.e., active width) and

braiding intensity, with relatively little change in active depth. Similar results have been found by Ashmore & Sauks (2006) and Redolfi et al. (2016) in the field and flume, respectively. During the hydrograph experiments, there was a stronger relationship between active depth and stream power (i.e., discharge). Unlike the constant discharge experiments, this suggests that changes in stream power resulted in an increased active area as well as an increased depth of the active layer. In the hydrograph experiments, active width and active depth were strongly and positively correlated. Consequently, a measure of active width could be used as a general predictor of active depth under similar circumstances. Splitting the active depth into its erosional and depositional components, it was found that erosional depths were generally greater than depositional depths for the constant discharge experiments. This, in combination with the results from the active width, suggests that areas of erosion may be more localized but deep, and areas of deposition are shallow and dispersed. Linking these findings to channel morphology indicates that erosion of banks, bars, and scour holes results in greater changes in elevation than scour fill and deposition on bars (Brasington et al., 2003; Rumsby et al., 2008; Kasprak et al., 2015).

Bertoldi et al. (2009a) and Ashmore et al. (2011) found a linear relationship when plotting the active width as a proportion of the wetted width against dimensionless stream power. Focusing on just the results that were measured, and not those that were computed in a numerical model, the findings from this research plot between the results previously found (Figure 4.56a) (Ashmore et al., 2011). The exception is experiment 1, which plots away from the rest of the braided rivers, with a very high dimensionless stream power (~0.25), but a low ratio of active width to wetted width (~0.05) (Figure 4.56a). Differences between the results in this research and those from previous UWO experiments are likely related to differences in methods for measurements of the wetted width. The results from the current experiment are consistent with estimates from the Sunwapta River, especially in terms of the hydrograph experiments (Figure 4.56a).

The same observations were used to plot the active width as a proportion of the wetted width against ABI (Figure 4.56b). The results are relatively similar to results found by Ashmore et al. (2011), particularly with regard to results from the Sunwapta River (Figure

4.56b). This not only indicates that the active braiding intensity could be used to predict a measure of the active width, but supports the use of physical models, as this model corresponds well with its field prototype.
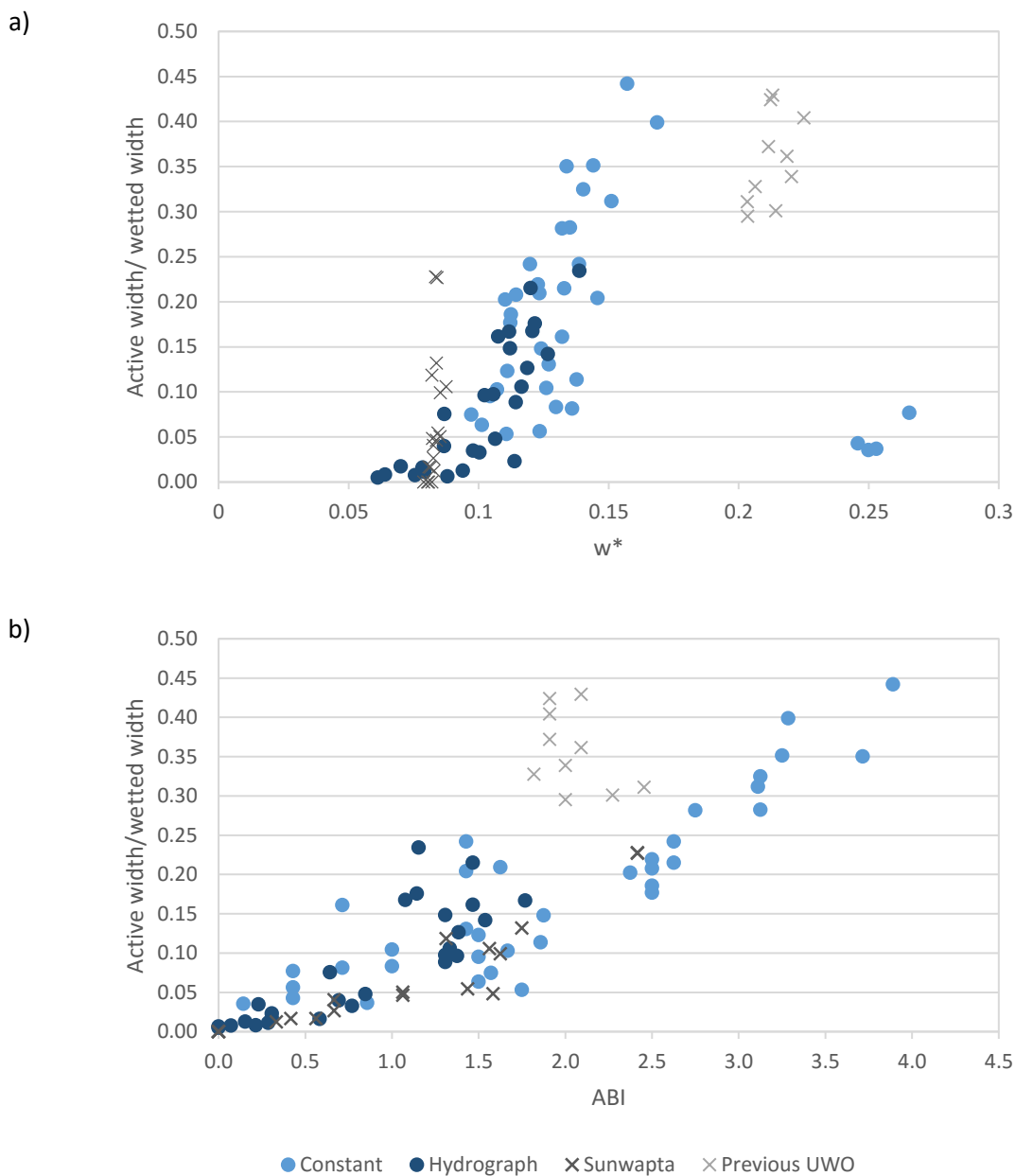
Figure 4.56 – Active width as a proportion of wetted width plotted as a function of a) dimensionless stream power (w*) and b) active braiding intensity (ABI) combined results with Ashmore et al. (2011).

In addition to the results that can be compared to previous literature, this research expands on current knowledge about braided river morphodynamics. For instance, it was found that bulk change had a very strong positive and linear relationship with active width, and a weaker but still positive relationship with active depth in the constant discharge experiments. The relationship between active depth and bulk change was stronger when viewing experiments individually (rather than across all experiments). This suggests that active depth as a measure of morphological change may more meaningful for a given river morphology or stream power than as a global predictor. This idea is supported by the results from the hydrograph experiment, which showed a stronger relationship between active depth and bulk change than the constant discharge experiments.

The results also indicated that bedload transport rates measured from the downstream sediment baskets were positively correlated to morphological measures of the active width. No previous study has reported measured values for the morphological active width and bedload transport simultaneously or over such a large dataset. Finally, morphological measures of channel change (i.e., active width, active depth, and bulk change) as well as bedload transport rates, were largely undetectable below the same lower threshold of 1.14 l s^{-1} or a dimensionless stream power of 0.08. These results have not been characterized before but suggest that there is a strong relationship between form and process in gravel-bed braided rivers.

4.5 Summary and Conclusions

This part of the thesis investigated linkages between morphology, bedload transport, and stream power across a range of channel morphologies both at temporally constant discharge as well as varying discharge. Overall, the findings support and extend previous work in terms of the wetted width, braiding intensity, active braiding intensity, and active width all increasing with increasing discharge and stream power. Each of these parameters is highly variable both temporally and over a constant discharge because of the intrinsic variability in braided river morphodynamics.

Focusing on the morphological active width, it was found to have a strong power relationship with total stream power, under both constant channel-forming and varying

discharge conditions. During the constant discharge experiments, active depth showed no clear trend with stream power and was generally restricted to a small range of values but showed a stronger positive relationship during the hydrograph experiments. This suggests that active depth may be strongly dependent on channel morphology rather than just channel hydraulics. The active width had extremely strong positive relationships with bulk change within and between the experiments, suggesting that it could be used as a general predictor of bulk change with high confidence and precision. In addition, the reach-averaged active depth had a strong positive relationship with active width in the hydrograph experiments, suggesting that the active width could be used as a general predictor of bulk change and active depth for a given gravel-bed braided river.

Comparing the results of this research with those of previous research, there was a less obvious positive linear relationship between the active widths as a proportion of the wetted widths against dimensionless stream power (w*) than was found by Bertoldi et al. (2009a) and subsequently by Ashmore et al (2011). These differences could be related to differences in data collection, sample size, and the conditions modelled. For example, the Trento experiments were completed on uniform sand and wetted widths were generally estimated using a 1D computational model.

In addition to the trends found, it was notable that in the hydrograph experiments that ABI, bedload transport, active width, active depth, and bulk change were largely undetectable below a dimensionless stream power of 0.08 (i.e., discharge of 1.14 l s^{-1}). This suggests that while all the parameters are variable, even for the same discharges, they are clearly connected. Therefore, since there was no measured bed material movement without detectable morphological change and vice versa, this dimensionless stream power acts as a lower threshold for morphological and bedload activity.

From this research the following main conclusions can be made:

1. The morphological active width is variable spatially and temporally, even at a constant discharge, but increases with discharge across both constant channel-forming discharge and event hydrograph experiments.

2. The active width has a very strong positive and linear relationship with bulk change under constant discharge and varying discharge conditions as well as over a range of braiding river morphology.

3. The morphological active width has a positive linear relationship with both total stream power and active braiding intensity under constant and varying discharge conditions.

4. While variable, the morphological active width has a positive relationship with bedload transport rate under constant discharge and varying discharge conditions.

5. The active depth seems less sensitive to changes in total stream power and discharge than the active width, suggesting that the active width may be more important in terms of channel geometry, and the correlation of morphology with bedload.

6. Morphological change and bedload transport rate both experience the same lower threshold of detection around a dimensionless stream power of 0.08.

Chapter 5

5 Morphometric Estimates of Bedload Transport Rate

5.1 Introduction

5.1.1 Chapter Introduction and Objectives

The morphological method, also known as the inverse method, infers information on bedload transport rates from changes in channel topography over time (Ashmore & Church, 1998). This method evolved out of the growing recognition that channel form and topography are fundamentally linked to bedload transport in gravel-bed rivers, both spatially and temporally.

There are several reasons why the morphological method is useful in gravel-bed braided rivers. First, calculating bedload transport rates from traditional formulae and field samplers has proved inefficient and in some cases, impossible (McLean & Church, 1999; Metivier & Meunier, 2003). Secondly, the high dynamism of braided river morphology makes it possible to detect topography changes over relatively short spatial and temporal scales. In addition, recent improvements in data collection and processing techniques, such as digital photogrammetry and automated stereo-matching of images, are able to provide detailed topographic data at spatial and temporal resolutions never before possible. These technologies have made the morphological method a reasonable alternative to bedload formulae and direct sampling in gravel-bed braided rivers (Brasington & Smart, 2003). Finally, given the complex morphology of braided rivers it is clear that these systems are not strictly driven by hydraulic principles, but also morphodynamics. For example, Wickert et al. (2013) found that all bedload material transported in an experimental braided river was incorporated into downstream bars. In addition, tracer studies in gravel-bed rivers and braided rivers also suggest that much of the transported bedload in these systems is deposited on downstream bars (Pyrce & Ashmore, 2003a; Kasprak et al., 2015). Therefore, any reliable measure of bedload transport rates in these rivers must consider changes in morphology. Therefore, by placing less emphasis on hydraulic parameters alone, the morphological method allows for insights into the relationships between channel form and

process including the spatial and temporal patterns of channel morphodynamics and bedload transport rates (Ashmore & Church, 1998; McLean & Church, 1999).

One common application of the morphological method is the estimation of bedload transport rates from changes in topography using the reach-budget method. The reach-budget equation can be expressed as a time-integrated transport rate by converting the volumes to a mass as a product of bulk density, and integrating it over the time interval to give:

$$Q_o = Q_i - \gamma s \delta S / \delta t \tag{5.1}$$

where Q_o is the mass transport output from the reach, Q_i is the mass transport into the reach, γ_s is the sediment bulk density, δS is the volumetric net change in sediment storage (i.e., volume of deposition – volume of erosion) and δt is the time interval (Hoey & Sutherland, 1991; Martin & Church, 1995; Ashmore & Church, 1998; Brasington & Smart, 2003; Brasington et al., 2003; Surian & Cisotto, 2007). In braided rivers, the volumes of erosion will be determined by the amount of lateral migration, bar erosion, and evolution of bed scour holes. Volumes of deposition will be the product of bar and floodplain aggradation as well as channel fill (Hoey & Sutherland, 1991; McLean & Church, 1999). Measures of net change were traditionally based on interpolation of repeat surveys of cross-sections but more recently it is common to use aerial photography, differential GPS, digital photogrammetry, or terrestrial scanners to create a series of continuous topographical surveys, or DEMs, of the area of interest (Brasington et al., 2003; Surian & Cisotto, 2007).

While propagation of the reach-budget method necessitates knowing the bedload transport rate at a specific channel cross-section, due to the challenges in measuring bedload transport fluxes in braided rivers, few field studies have a known flux boundary condition (i.e., a known input or output). Therefore, they must rely on the 'minimum' budget in which the sediment input is either assumed to be zero or adjusted so that the resulting downstream budget remains positive (McLean & Church, 1999; Surian & Cisotto, 2007). Although this approach introduces a strong negative bias, it can provide minimum estimates of bedload transport rates, which are useful for engineering applications. In situations where it is

possible to estimate the negative bias, it may be possible to adjust the minimum budget ad hoc.

Another approach to estimate the bedload transport rate with limited data is based on an estimated path length, which is the distance travelled by a grain of sediment from initial entrainment to final deposition (Haschenburger & Church, 1998; Church, 2006):

$$Q_b = V_e(L_t/L_r)/t \tag{5.2}$$

where V_e is the volume of mobilized bedload (i.e., volume of eroded sediment), L_t is the transfer distance, L_r is the reach length, and t is the interval between surveys (Ashmore & Church, 1998). This equation is built on the idea that there must be a strong relationship between path length and channel morphology because the movement of individual grains fundamentally controls channel morphology (Pyrce & Ashmore, 2003a; Kasprak et al., 2015). Therefore, it is expected that the distance of particle displacement must reflect some morphological length scale, such as pool-bar spacing or the distance between confluences and bifurcations (Pyrce & Ashmore, 2005). As a result, by rearranging the equation it should be possible to estimate an average reach path length:

$$L_t = Q_b \alpha/V_e \tag{5.3}$$

where $\alpha = L_r*t$, so that for a given reach and time interval, α is constant. If reasonable estimates of path length are possible using equation 5.3, in terms of the scale of morphological features, it further confirms the fundamental linkages between sediment transport rates and river morphodynamics (Church, 2006) and provides a method for estimating path length without the use of tracer particles.

This chapter will focus on the application of the morphological method to estimate sediment budget and path lengths in gravel bed braided rivers. Specifically, this chapter will look at the spatial and temporal variability in estimates of bedload transport and morphology over a range of constant channel-forming discharges, for the entire study reach as well as smaller subreaches. This research will improve our understanding of the fundamental relationships between channel morphology and bedload transport by addressing the following objectives:

1. Quantify the spatial variability in the areas and volumes of erosion and deposition as well as net change and bulk change for a range of river morphologies.

2. Calculate the morphological sediment budget for models of multi-thread gravel-bed rivers over a range of discharge and stream power conditions based on a known bedload output.

3. Calculate the morphological sediment budget for models of multi-thread gravel bed rivers over the same range of channel conditions, with the assumptions of a minimum budget.

4. Estimate the path length from measures of topographic change and bedload transport flux.

5. Examine the spatial and temporal dynamics of sediment transport in experimental gravel-bed braided rivers.

By completing these objectives, it will be possible to answer the following questions about braided river morphodynamics and the relationships between channel change and the variability in bedload transport rates:

- What are the frequency distributions of bedload transport rates as measured from different cross-sections using the morphological reach-budget method and how do they compare to the measured flux from the downstream sediment baskets?

- What are the differences between the bedload transport rates estimated from a known boundary condition (i.e., the downstream bedload flux) and those estimated from the minimum budget method?

- Does an estimate of path length based on morphological change relate to the length scale of channel topography?

- Is there a strong spatial correlation between sections within a reach in terms of morphological change or bedload transport rate?

5.1.2 Chapter Structure

This chapter will focus on the results from the constant discharge experiments with a multi-braided morphology (Experiments 4, 9, 12, and 13). Section 5.2 presents the results for the variability in bedload transport rates for those experiments, this time having converted the sediment masses into dry sediment masses for use the reach-budget method. Section 5.3

quantifies differences in channel morphology between the four experiments in terms of net change, and percentage of the total change due to erosion and deposition for the entire 14 m study reach. Section 5.4 presents and compares the results from the 2 morphologically-derived sediment budgets, the bedload budget, with a known sediment output, and the minimum budget. Section 5.5 looks at the spatial differences in the 1m subsections of the study area. Section 5.6 places the results of this research with previous research and analysis, while discussing the implications of the findings. The chapter concludes with a summary of the main findings (Section 5.7).

5.2 Bedload Transport Rates

For the purposes of this chapter, the bedload transport rates were converted to a dry mass using the conversion coefficient of 1.22 (Figure 5.1) (See Methods and Appendix F for details). As mentioned before, while bedload transport rates measured at the downstream baskets tend to increase with stream power, there is substantial overlap in the range of transport rates, particularly between experiments 12 and 13.
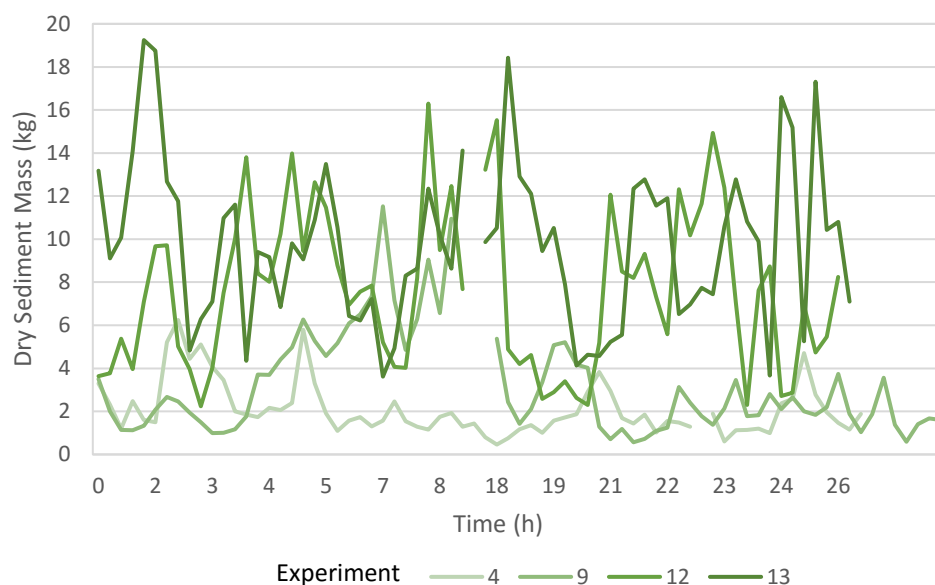
Figure 5.1 – Temporal variation in dry sediment mass at the downstream baskets for the constant multi-thread discharge experiments.

5.3 Rates of Morphological Change

5.3.1 Volumes of Erosion and Deposition

Volumes of erosion tended to be slightly larger than volumes of deposition, and both volumes increased with discharge and stream power across the multi-threaded experiments (i.e., experiments 4, 9, 12, and 13) (Figure 5.2).
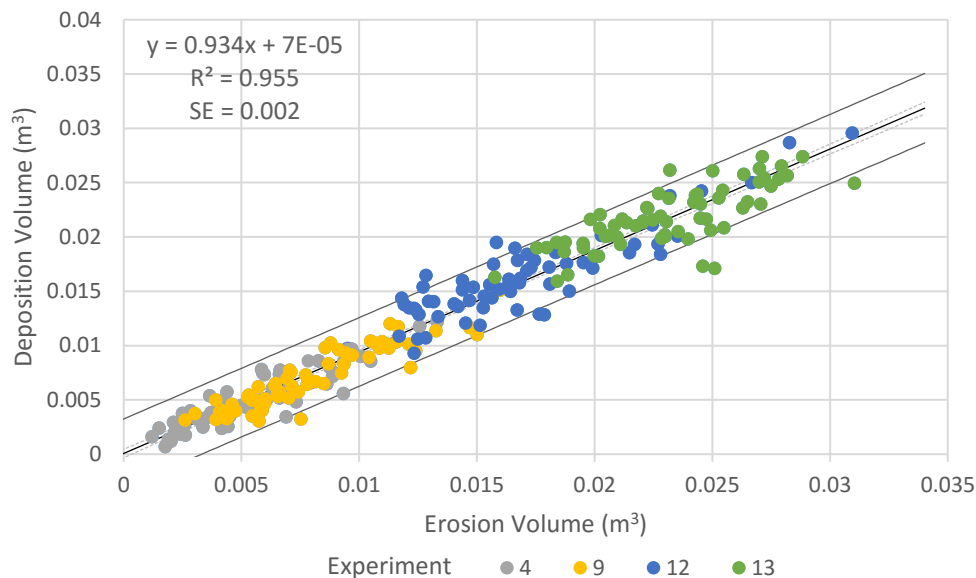
Figure 5.2 – Deposition volume against erosion volume for the multi-threaded experiments. The dashed lines represent the 95% confidence interval around the mean of the regression line, and the outer solid lines represent the 95% prediction interval for the observations. Results shown were derived using the simple 2σ threshold.

By dividing the volumes of erosion and deposition for each experimental run by the total bulk change for that run, it was possible to calculate a percent erosion and percent deposition for each run. On average, erosion accounted for 51.6 % of the bulk change in experiment 4, 53 % in experiment 9, 50.9 % in experiment 12 and finally 51.4 % in experiment 13 (Figure 5.3). While the mean values for percent erosion were similar for all of the experiments, the range of values decreased with stream power so that the percent erosion varied from 38-71 % in experiment 4, 43-56 % in experiment 12 and 47-59 % in experiment 13 (Figure 5.3).
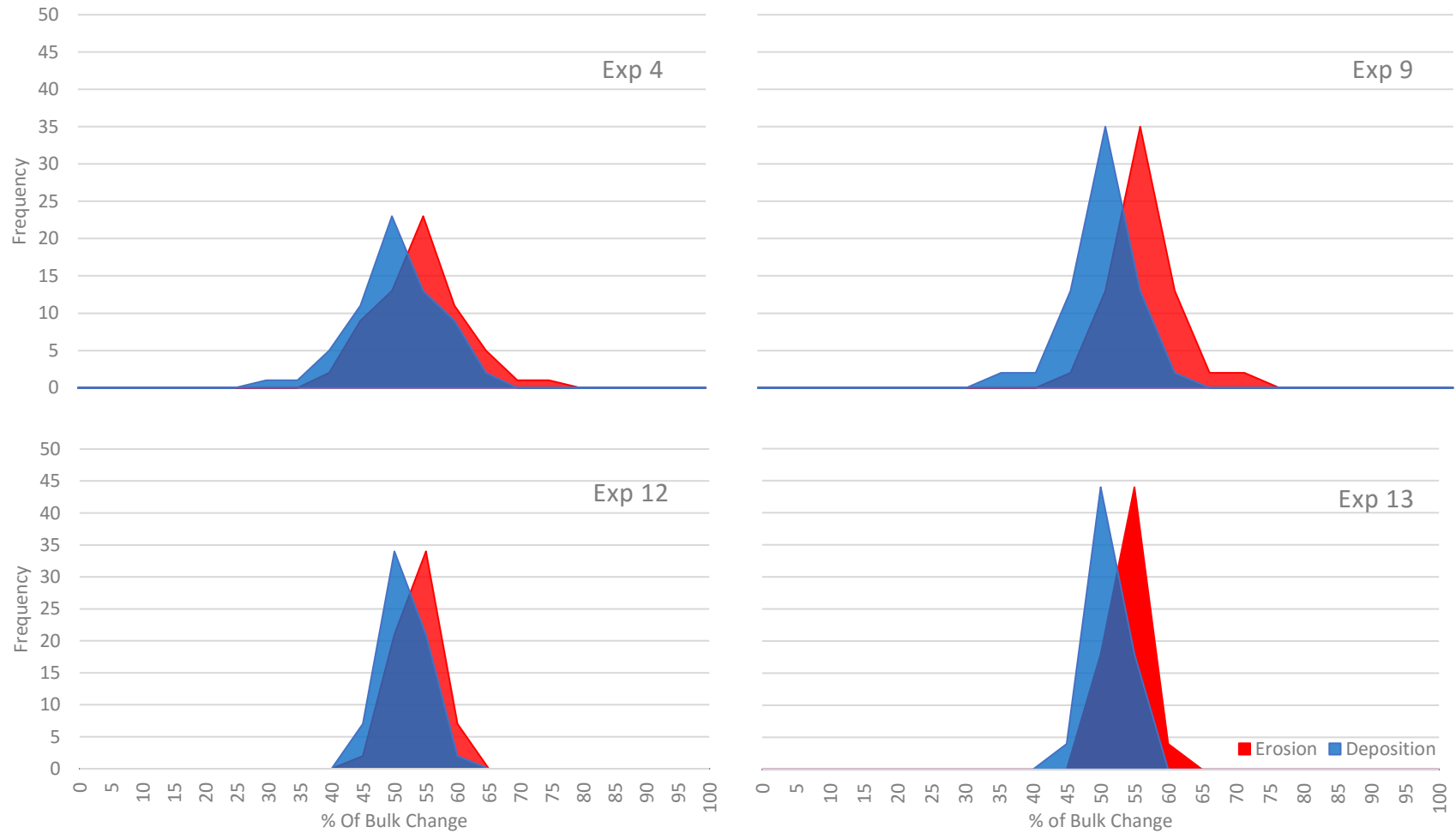
Figure 5.3 – Distributions of erosion and deposition volumes as a percentage of the total bulk change for all of the experimental runs in the multi-thread braided experiments.

5.3.2 Net Change

Net change refers to the difference in the total volume of deposition and total volume of erosion. For each experiment, the net change calculated for the entire 14 m study area was temporally variable (Figure 5.4). Experiment 4 had more erosional runs (i.e., net change < 0 m^3), and in general the results of the simple and dilation threshold methods closely coincide. In experiment 9, most runs had a net erosional change, with less than 20 % of the runs having a net positive value. It is also clear from the experiment 9 graph in Figure 5.4 that the simple and dilation methods strongly agree with the direction of change but that the simple method has slightly higher values of net change overall. Experiment 12 has one of the most sporadic results, both in terms of the switching between net erosional and net depositional, and in terms of the differences between the two threshold methods (Figure 5.4). There are several runs where the simple threshold method found a net erosional change and the dilation method found a net positive change. This occurs when the net change via the simple threshold method is close to zero, so likely reflects the differences between the methods in classifying elevation change near the threshold of detection. Experiment 13 had the greatest magnitude of net change and had strong agreement between the two threshold methods in terms of the direction and magnitude of change (Figure 5.4). This supports the idea that the differences between the two methods are least noticeable when the changes in morphology are much greater than the minimum level of detection. Across all experiments, the number of runs that had a net erosional change is always greater than net depositional.
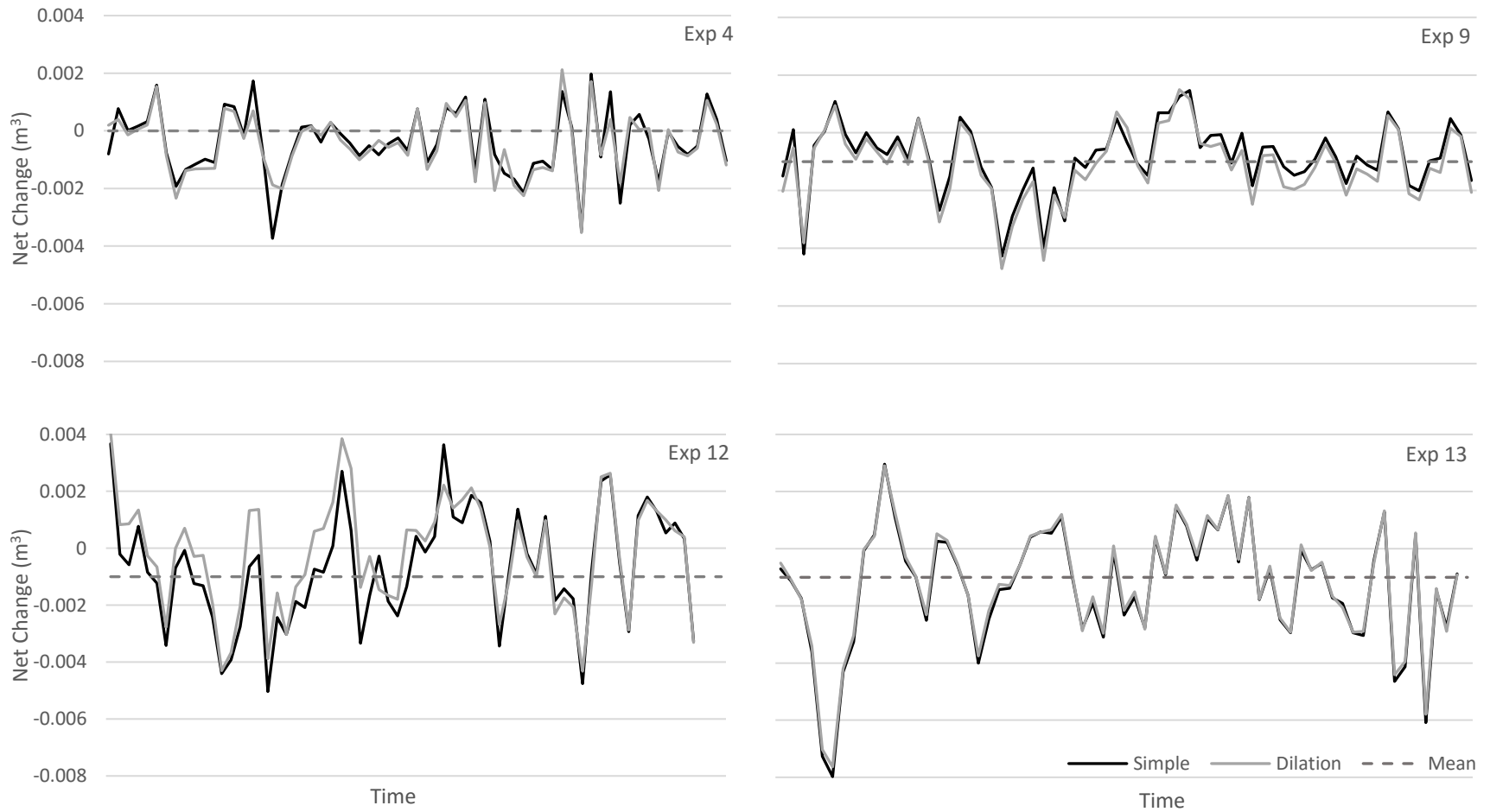
Figure 5.4 – Temporal variability of net change for all experimental runs in the multi-threaded constant discharge experiments. Results are shown for both the simple 2σ threshold and dilation methods. Dashed lines represent the mean net change for each experiment.

The average net change was generally low (-0.0001 - -0.0013 m^3) and was slightly negative across all experiments (Figure 5.5). Figure 5.5 indicates the general agreement between the simple and dilation threshold methods in terms of the net change, which were not significantly different based on a two-tailed Student's t-test (t (6) =-0.188, p=0.857). The variability in the net change increases with stream power, so that experiment 12 and 13 have a much greater range of net change values than experiments 1, 4, and 9 (Figure 5.5). This emphasizes that experiments 12 and 13 had much greater amplitudes of topographic change than the lower stream power experiments of 4 and 9.
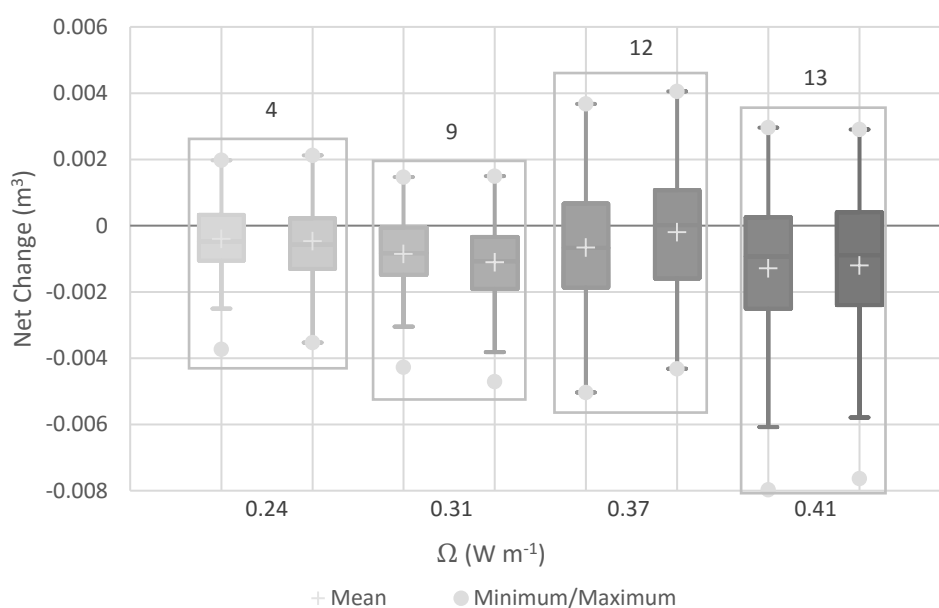
Figure 5.5 – Variability in net change for the multi-thread constant discharge experiments (i.e., experiments 4, 9, 12, and 13) in terms of total stream power (Ω). The results for each experiment represent the simple (left) and dilation (right) threshold methods.

Measurements presented in Figure 5.5 coincide with measures of bedload transport rates from the downstream baskets, where experiments 12 and 13 had the greatest mass of sediment in the downstream baskets, but also the greatest variability (Figure 5.1). Figure 5.6 shows a plot of the bedload transport rate as a function of the net change for each of the multi-thread constant discharge experiments. As expected, greater values of bedload transport are associated with greater negative values of net change. As the system erodes

(i.e., negative net change), more sediment is being mobilized and transported to the downstream baskets. Figure 5.6 also suggests that the greatest bedload transport rates and volumes of net change occur at higher stream power (e.g., experiment 12 and 13).
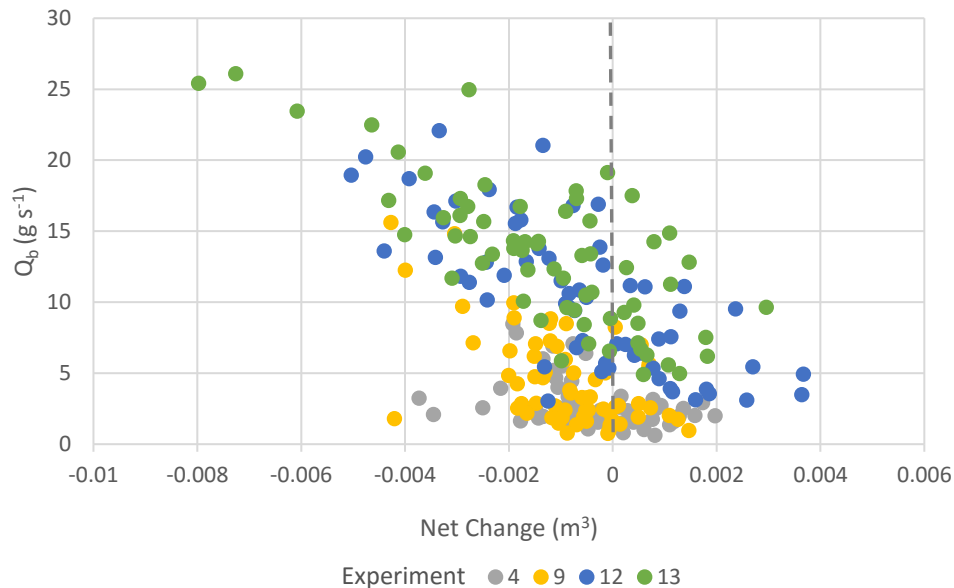
Figure 5.6 – Bedload transport rate (Q_b) from the downstream baskets as a function of net change (simple 2σ threshold) for the multi-thread constant discharge experiments.

5.3.3 Path Length

Equation 5.3 was used to estimate a mean path length from the volumes of erosion in the flume. As part of this calculation, the estimated volume of erosion was first compared to the dry sediment mass captured in the sediment baskets (Figure 5.7).
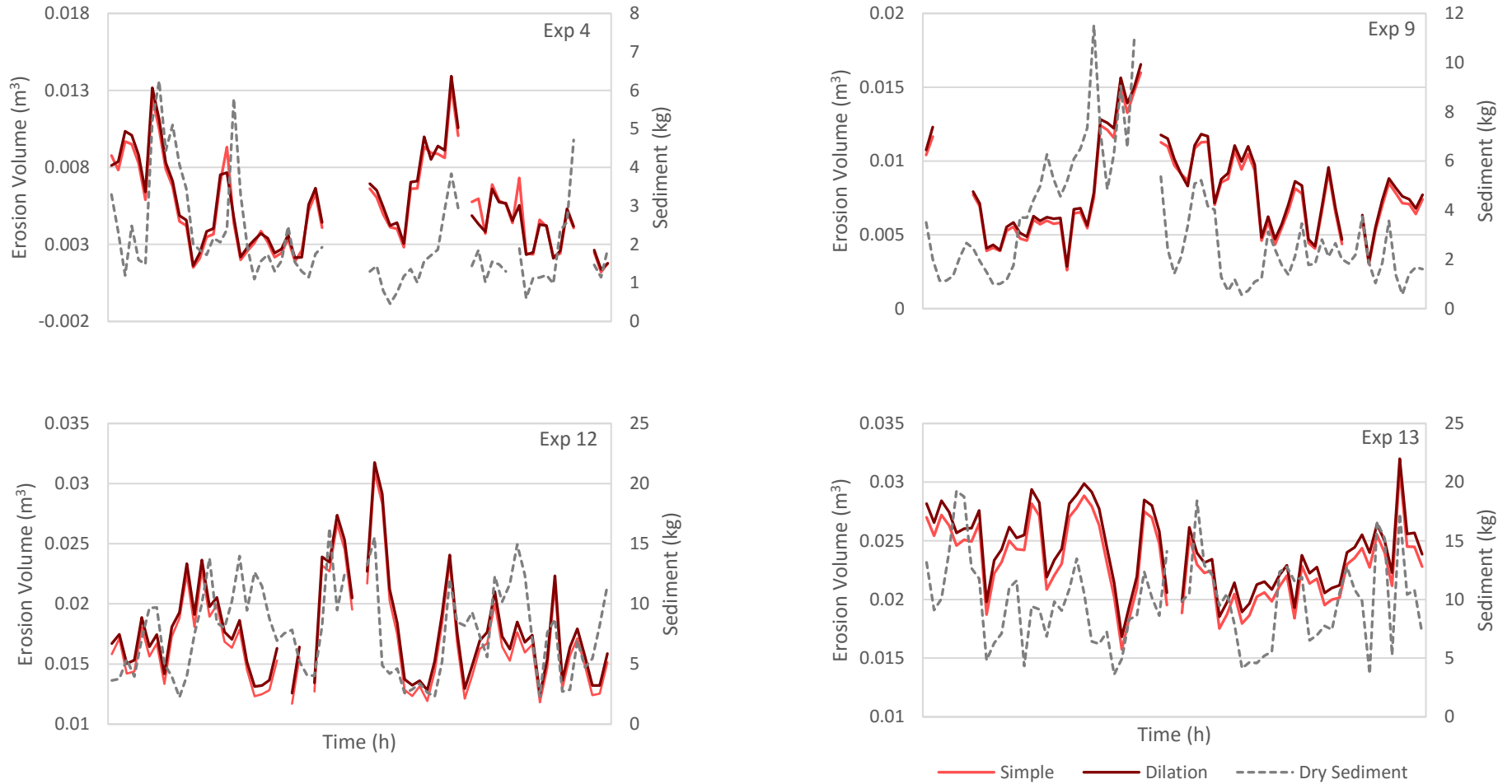
Figure 5.7 – Temporal variability in erosion volumes and bedload sediment mass as a function of time for the multi-threaded constant discharge experiments. Erosion volumes are shown for both the simple 2σ threshold and dilation method. Note differences in axes.

Visually, there seems to be a strong agreement between volumes of erosion and bedload mass temporally for all experiments except for experiment 9, which has some large deviations in the second round of experimental runs (Figure 5.7). Plotting the linear regression of the above graphs, there is a positive trend between the volume of erosion as measured from the DoDs and the mass of sediment collected at the downstream end of the flume (Figure 5.8). The linear function in Figure 5.8 would generally underestimate the volumes of erosion for experiment 13. This is because as stream power increases there is an increase in the varaibility of bedload transport flux for a relatively small range of erosion volumes, possibly reflecting the increased rates of lateral migration, passage of bedload sheets, and bar erosion at higher stream power.
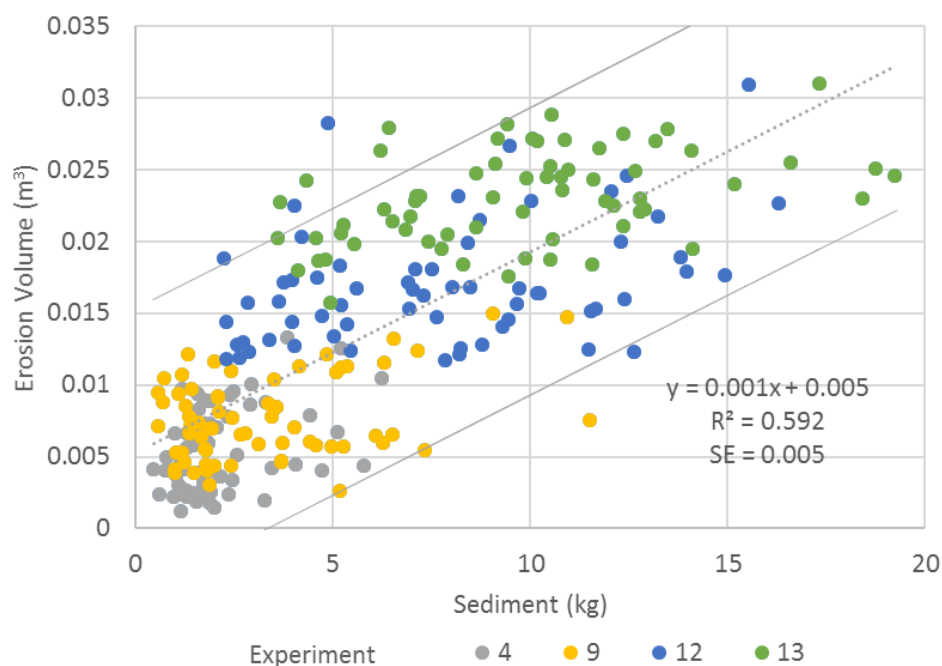
Figure 5.8 – Erosion volumes as a function of bedload sediment mass measured at the downstream baskets. These results are for the simple 2σ threshold method and multi-thread experiments (experiments 4, 9, 12, and 13). The dashed lines represent the best fit trendlines and the outer solid lines represent the 95 % prediction interval for the observations.

Path length estimates are shown in Figure 5.9. The mean values range from 3.1- 3.7 m across all 4 experiments and decrease with increasing stream power. In addition, variability in the estimated path length decreased with increasing stream power (Figure 5.9). Given

the outliers are strongly influencing the mean values for each experiment, it is more meaningful to consider the median values. The median path lengths using the simple threshold for each experiment are 2.72 m, 3.08 m, 3.31 m and 3.20 m for experiments 4, 9, 12, and 13 respectively. Given that experiment 12 had a greater median path length than experiment 13, the results suggest that the path length might be more sensitive to discharge than stream power (Figure 5.9). As expected, the dilation values provided slightly lower estimates of path length because the dilation yields slightly higher volumes of erosion for the same sediment output, but the means are not significantly different (t (6) = -0.037, p = 0.972).
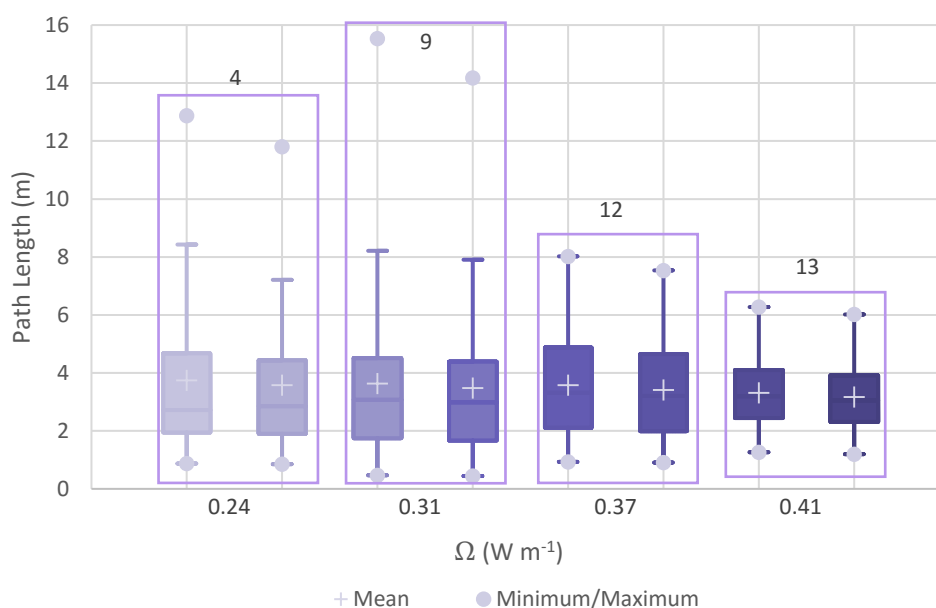
Figure 5.9 – Estimated morphological path lengths as a function of total stream power (Ω). Results are shown for the simple 2σ threshold (right box plot) and dilation threshold method (left box plot) for each experiment.

The distributions and summary statistics of estimated path lengths can be seen in Figure 5.10 and Table 5.1. In addition to the summary statistics, Table 5.1 shows the skewness, which reflects the asymmetry of the distribution, and the kurtosis, which reflects the form of the tails, for each of the distributions. A positive skewness value reflects a distribution skewed to the right (i.e., more lower values). In this case, all the experiments have a positive skewness, with experiments 4 and 9 having a strong positive skewness (Figure 5.10 and Table 5.1). This suggests that in general, most bedload particles move relatively

short distances. In terms of kurtosis, a positive value indicates a distribution with more outliers (Leptokurtic) than the standard normal distribution. Experiments 4 and 9 had a positive kurtosis value (i.e., the tails are more extreme than would be found in the normal distribution), while experiments 12 and 13, had negative kurtosis values (Table 5.1).
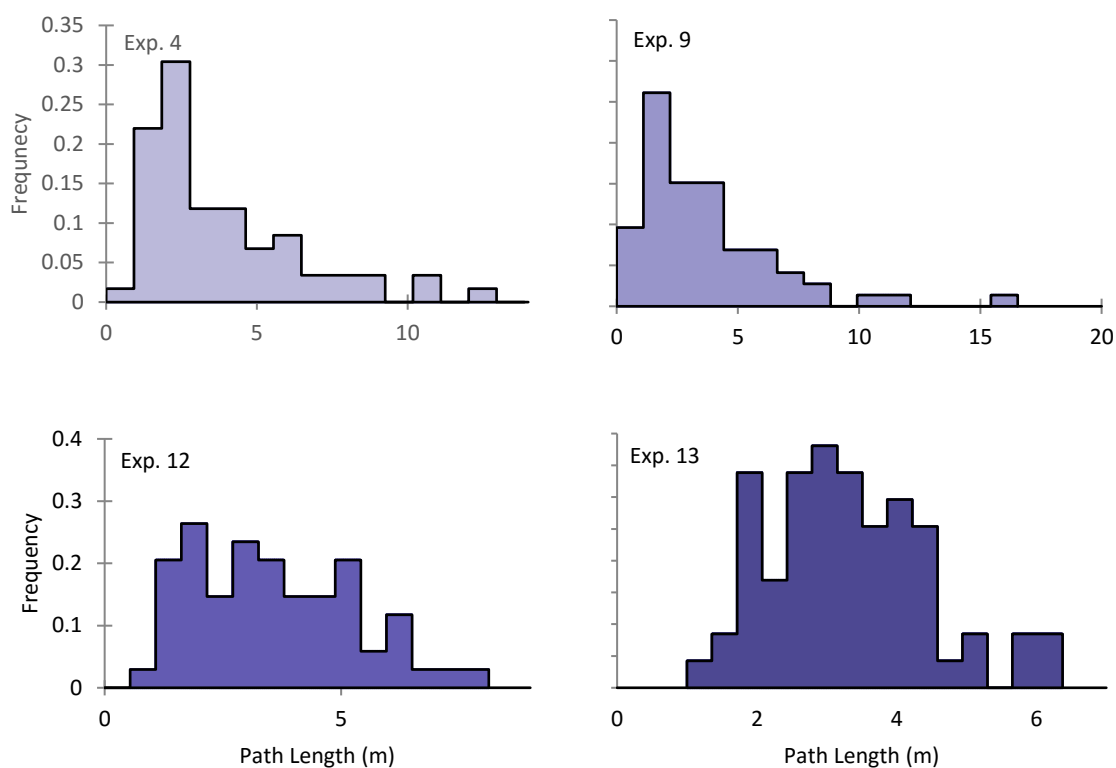
Figure 5.10 – Frequency distributions of estimated path lengths for the multi-thread constant discharge experiments.

Table 5.1 - Summary statistics for path length, where n is the number of observations, the mean is the average path length, and σ is the standard deviation.

Experiment	n	Mean (m)	σ (m)	Skewness	Kurtosis
4	74	3.75	2.61	1.40	1.53
9	75	3.64	2.80	1.83	4.30
12	67	3.59	1.68	0.44	-0.68
13	67	3.32	1.17	0.48	-0.27

5.4 Morphological Sediment Budgets

To investigate spatial variation in bedload the study reach was divided into 14, 1 m slices, for which a Scilab script was used to extract the active areas (erosion and deposition) as well as volumes of erosion and deposition for the simple 2σ threshold and the dilation method (Figure 5.11). The 14 subsections were labelled 1 to 14, with 1 being the downstream-most slice because the budget was propagated from the known basket output at the end of slice 1 (Figure 5.11).

Figure 5.11 – The flume study area divided into 14 x 1 m slices for sediment budgeting.

From this dataset, two complete sediment budgets were calculated for each 1 m slice of each DoD: 1) the budget estimated from the bedload output in the sediment baskets, herein called the 'bedload budget' and 2) the minimum budget, which will be discussed in more detail in Section 5.4.1. In the bedload budget, the bedload transport rate output (Q_o) from section 1 was known from the downstream baskets and the changes in storage (i.e., net change) were calculated from the volumes of erosion and deposition in each 1 m slice. Following the procedure in Martin and Church (1995) and Brasington and Smart (2003) it was possible to calculate the Q_i for the section 1 using equation 5.1. The Q_i for section 1 then served as Q_o for section 2. In this way, the sediment budget was propagated upstream to include all 14 slices of the study area. For each experiment, these calculations yielded at least 64 measurements of bedload flux for each 1 m slice, making it possible to capture the overall variation in bedload transport along the entire reach, spatially and temporally. An example of a sediment budget completed for a single run from experiment 13 is shown below (Figure 5.12). In this example, the upstream sections were net depositional (positive values of net change), while the downstream sections were net erosional. The reach-averaged net change was slightly negative at -0.15 g s^{-1}.

a)

b)

c)
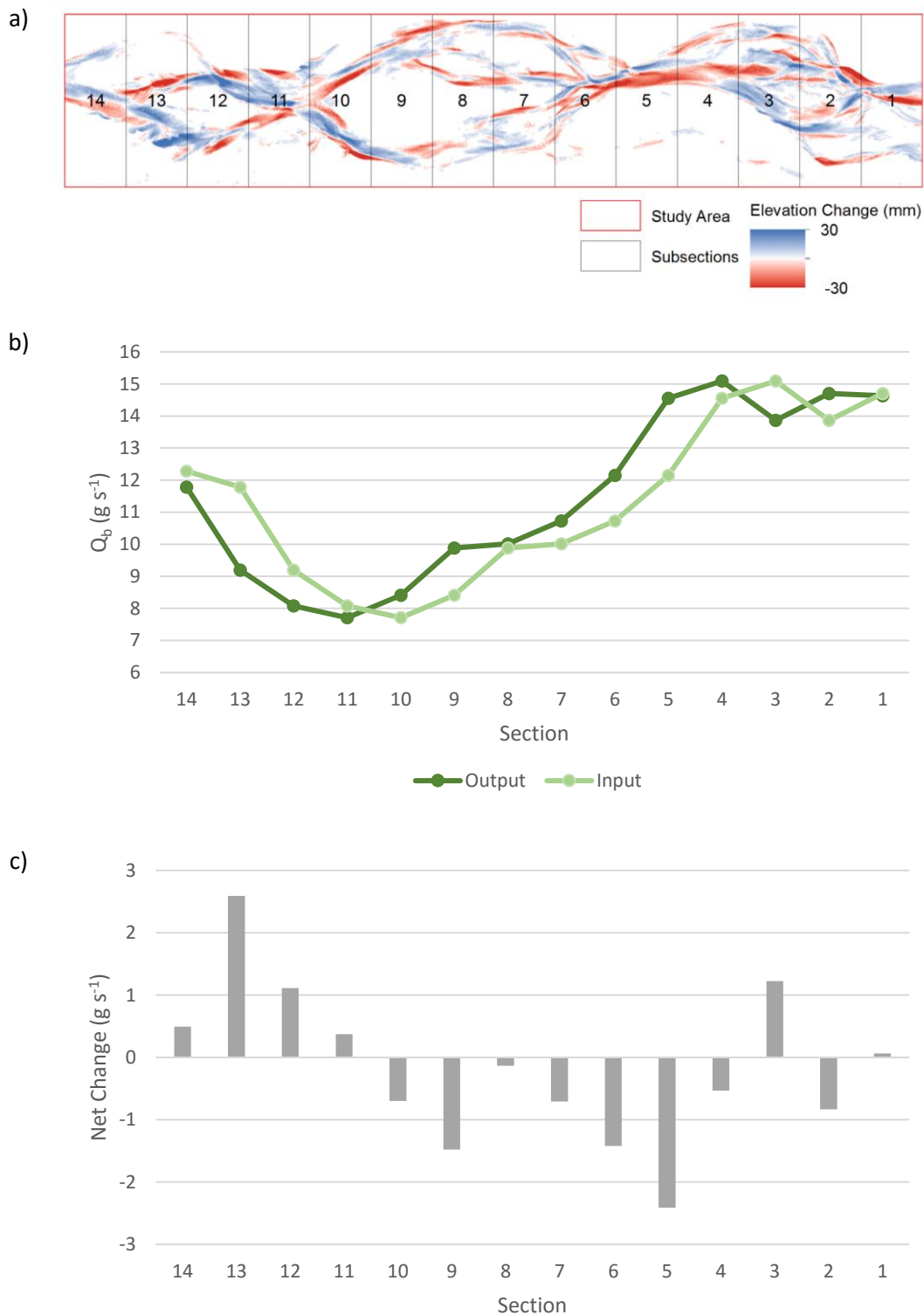
Figure 5.12 – Example sediment budget from experiment 13 where a) shows the DoD, b) shows the corresponding spatial changes in bedload transport rate (Q_b) from upstream to downstream and b) shows the spatial changes in terms of net change.

The variability in the morphological sediment transport rate (Q_o) from each section is plotted for each experiment in Figure 5.13. As expected, there was a lot of variability in the sediment transport rate for each experiment but also a general positive trend with increasing stream power. The mean rate of transport increases from ~2 g s^{-1} for experiment 4 to 3 g s^{-1} for experiment 9, 7.2 g s^{-1} for experiment 12 and finally 9 g s^{-1} for experiment 13. Similarly, the standard deviations for these estimates also increase with stream power from 1.3 g s^{-1} for experiment 4 to 2.8 g s^{-1} in experiment 13 (Figure 5.13 and Table 5.2).
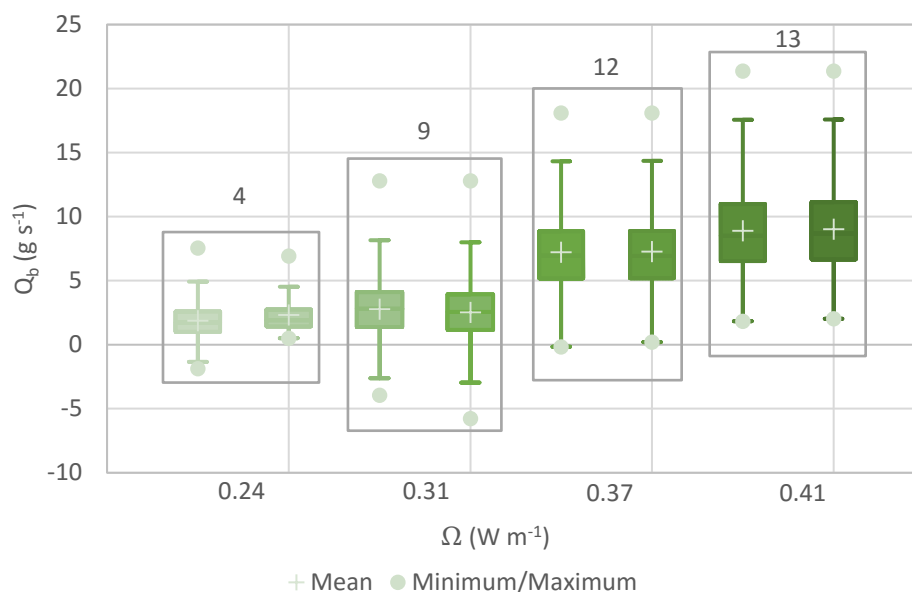
Figure 5.13 – Variation in morphological bedload transport flux (Q_b) as a function of total stream power (Ω). Results are shown for the simple 2σ threshold (right box plot) and dilation threshold method (left box plot) for each experiment.

The differences between the estimates of the simple and dilation threshold are relatively small, and not statistically different (t (6) = 0.037, p = 0.972), in terms of the estimated bedload transport rates (Table 5.2). In addition, the differences between the two methods decreases with quantity of morphological change and stream power. This supports the idea that greater values of morphological change provide more precise and less biased results, whereas change close to the lower threshold of detection may impact the final morphological estimates.

Table 5.2 - Summary statistics for estimated morphological transport rates for both the simple 2σ threshold and dilation method, where the mean is the average value and σ is the standard deviation.

	Threshold Method	Mean	σ
		$g\ s^{-1}$	$g\ s^{-1}$
4	Simple	1.88	1.39
	Dilation	2.34	1.38
9	Simple	2.79	2.18
	Dilation	2.52	2.32
12	Simple	7.24	3.05
	Dilation	7.27	3.07
13	Simple	8.90	3.21
	Dilation	9.04	3.22

To expand on the box plots in Figure 5.13, which show the variation in Q_o across all sections, the frequency distributions of Q_o for each 1 m section are presented in Figure 5.14. This includes the known bedload transport rate from the downstream sediment baskets represented by section 1.

Experiment 4 had the smallest range of transport rates, with a minimum of -1.8 $g\ s^{-1}$ and a maximum of 7.55 $g\ s^{-1}$ (Figure 5.14 and Figure 5.15). The negative minimum value corresponds with a section where the morphological net change in the section was depositional (i.e., positive) and greater than the estimated input into the section. In general, the distributions of each section are symmetrical with peaks very close to the average transport rate of 1.88 $g\ s^{-1}$. There is an increase in transport rate in the downstream direction, indicated by the shifting of distributions in Figure 5.14, so that section 14 had a mean of 1.71 $g\ s^{-1}$ and section 1 had a mean of 2.34 $g\ s^{-1}$ (Figure 5.15).

Experiment 9 had a greater range of transport rates than experiment 4 spanning from -3.9 to 12 $g\ s^{-1}$ (Figure 5.14). Experiment 9 had the greatest number of negative transport values indicating that the estimated sediment input was often insufficient to compensate for the erosion that occurred in a particular section. This could indicate an error in the estimate of the net change or be a function of propagating the budget with only a single boundary condition (i.e., only the Q_o is known, not the Q_i). Unlike experiment 4, the transport rates

in experiment 9 seem to decrease in the downstream direction, resulting in a slightly bimodal pattern overall. As a result, the upstream sections have a slightly negative skew and the downstream sections have a slightly positive skew. Experiment 12 had a greater range of transport rates than both experiment 4 and 9, this time with a minimum of -.0.15 and a maximum of 18 g s^{-1} (Figure 5.15). Like experiment 4, the individual sections in experiment 12 tend towards the same distribution. The only exception is section 1, the most downstream section, which showed a bimodal distribution (Figure 5.14). In addition, experiment 12 is positively skewed given the several extremely high transport rates being estimated throughout the reach. Finally, experiment 13 had the greatest range in sediment transport rates, spanning from 1.84 to 21.3 g s^{-1} making it the only experiment to not have a negative sediment output (Figure 5.15). This means that all the estimated sediment inputs for each section satisfy any net change that occurred in the section. The distributions for sections in experiment 13 covered a larger range of transport rates than the other experiments, showing a positive skew in the upstream sections and a bimodal pattern in the downstream sections (Figure 5.14). Experiment 13 also showed increasing transport rates moving longitudinally downstream (Figure 5.15).

To see if the differences in the bedload transport rates between the 14 sections was significant, an Analysis of Variance (ANOVA) followed by the multiple comparisons Tukey Honest significant difference (HSD) was completed for each experiment. Tukey HSD is one of the most common procedures in pairwise multiple comparisons and it provides a p-value for each pair of sections to determine if they are significantly different from each other. Experiment 4 had no significant differences between any of the 14 subsections ($F_{(13,924)} = 1.775$, $p = 0.043$). In experiment 9 the downstream sections 1-6 were found to be significantly different than the upstream sections 12-14 ($F_{(13,966)} = 7.937$, $p = <0.0001$). Experiment 12 only had two significant differences, with subsection 1 being significantly different than upstream sections 10 and 14 ($F_{(13,896)} = 2.934$, $p =0.000$). Finally, experiment 13, like experiment 9 has several significant differences between downstream sections 1-5 being significantly different than subsections 11-14 ($F_{(13,910)} = 11.445$, $p = <0.0001$) (Full results of Tukey HSD presented in Appendix J).
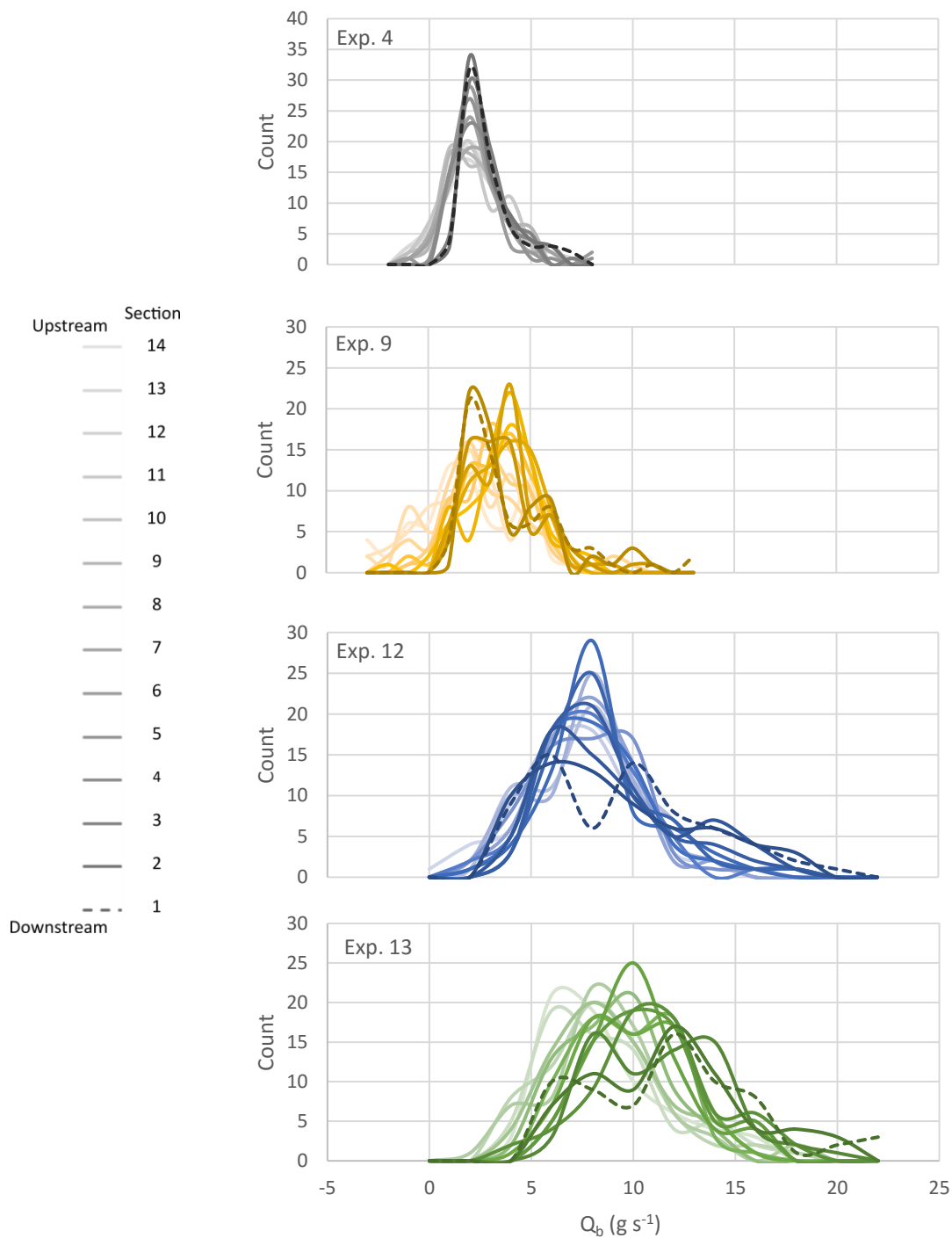
Figure 5.14 – Distributions of morphological bedload transport rate (Q_b) estimates for each 1 m section for each multi-thread constant discharge experiment. Results shown were derived using the simple 2σ threshold method. Section 1 (dashed line) represents the measured output from the downstream sediment baskets.
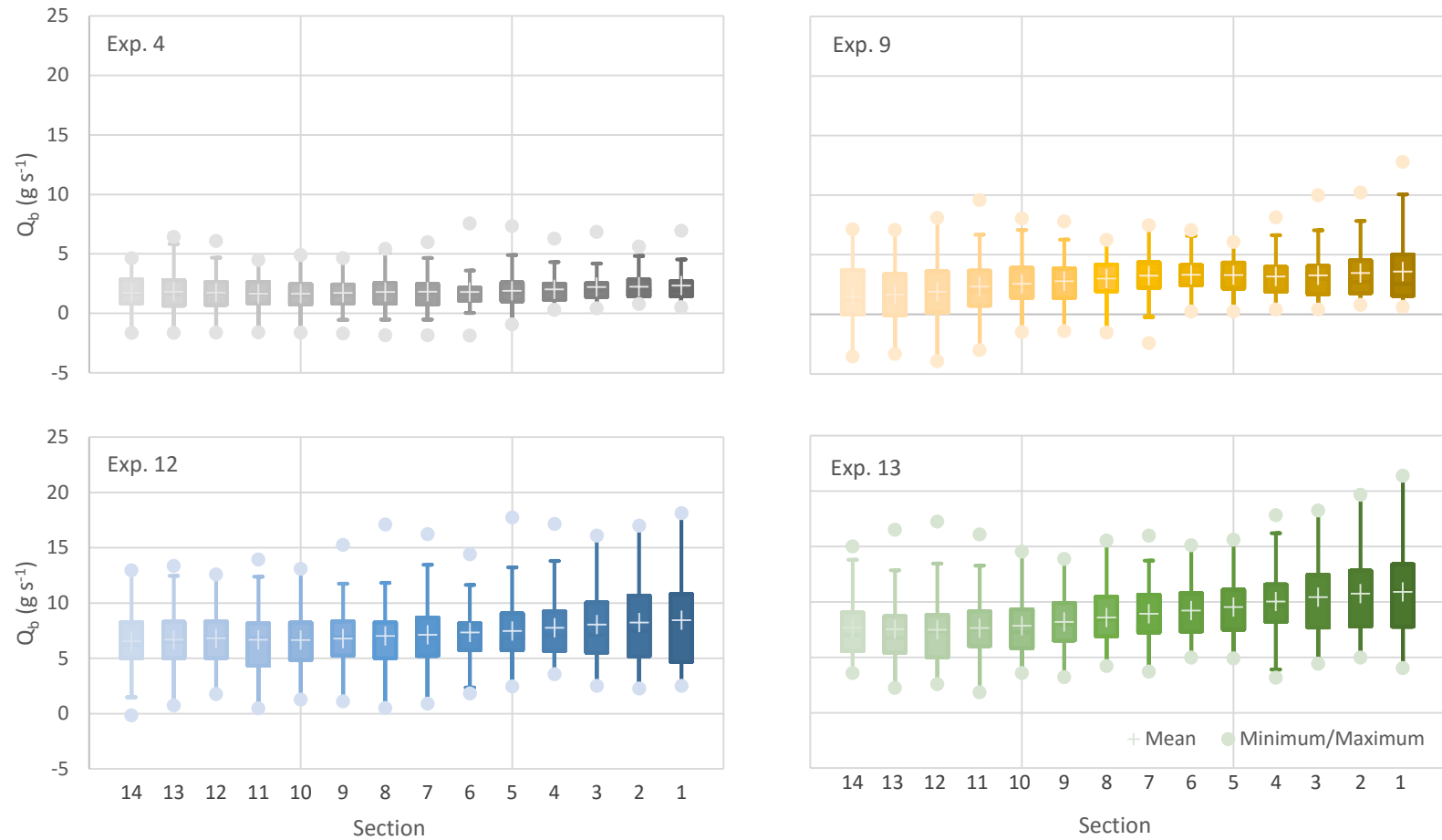
Figure 5.15 – Distribution of morphological bedload transport rates (Q$_b$) for each 1 m section of the multi-thread constant discharge experiments. Results are for the simple 2σ threshold method.

The bimodal trends found in some sections of experiments 9, 12, and 13 could be related to edge effects in the flume. All three experiments had a primary channel interact with the edge of the flume sometime during the length of the experiment. When this happens, the channel begins to act like a chute, transporting material quickly downstream without any interference from bars. For example, in experiment 9, while one anabranch met the side of the flume early in the experiment, it didn't become well developed until the second round of experimental runs. Looking at Figure 5.16, the increase in sediment in the basket downstream of the edge interaction is clear during the second round of experimental runs. Similar trends can be found in the baskets of experiment 12 and 13 downstream of edge chutes.
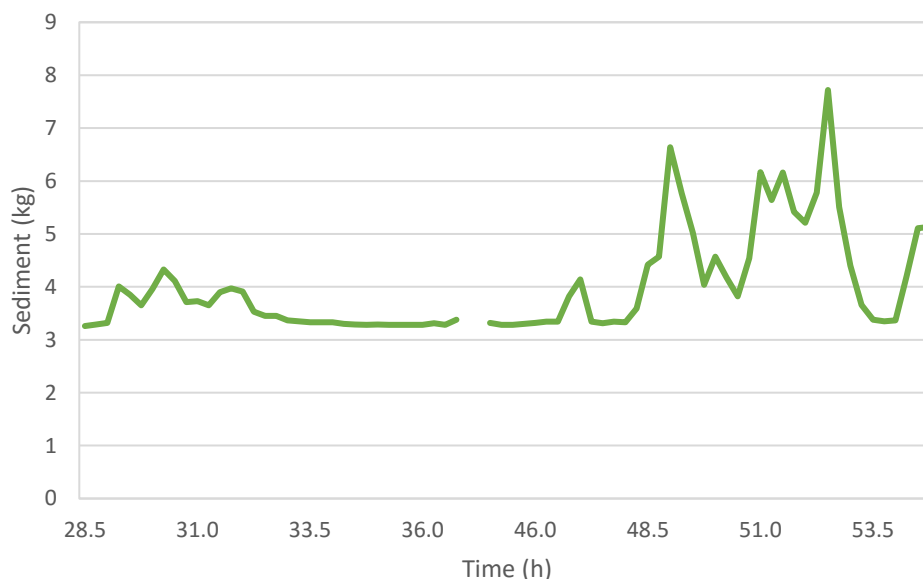
Figure 5.16 – Sediment mass in basket by the flume edge during experiment 9.

With a Q_o value for each section of each run for each experiment, there was sufficient data to determine the distributions of bedload transport rates in multi-thread gravel- bed rivers. Using XLSTAT, each dataset was paired with the distribution curve providing the best statistical description of the frequency plots according to the Kolmogorov-Smirnov test for comparing distributions (Figure 5.17) (XLSTAT, 2017). Experiment 4, 9, and 12 were each paired with the logistic distribution, while experiment 13 was defined by a Beta4 distribution. The fit of experiment 4 was not statistically significant (p-value = 0.005, α = 0.05), even with 938 observations. Experiment 9 had a stronger p-value of 0.545 with the

logistic distribution using 980 observations. Experiment 12 had statistically significant but poor fit with the logistic distribution (p-value = 0.262). Finally, experiment 13 was very well defined by the Beta4 distribution, with a p-value of 0.94 over 924 observations.

Table 5.3 shows the values for skewness and the kurtosis for each of the distributions. In this case, all the experiments have a positive skewness, with experiments 4, 12, and 13 having a strong positive skewness (Figure 5.17 and Table 5.3). This represents a distribution skewed to the right, reflecting a greater number of low transport rates. In terms of kurtosis, all the distributions have more extreme values (i.e., outliers) than would be expected with a normal distribution, but the values for experiment 12 and 13 are much lower than 4 and 9 (Figure 5.17 and Table 5.3).

Table 5.3 - Skewness and kurtosis of bedload transport rate distributions, where n is the total number of calculations for all 14 cross-sections within each experiment.

Experiment	4	9	12	13
n	938	980	910	924
Skewness	0.62	0.23	0.72	0.60
Kurtosis	1.31	1.32	0.67	0.38
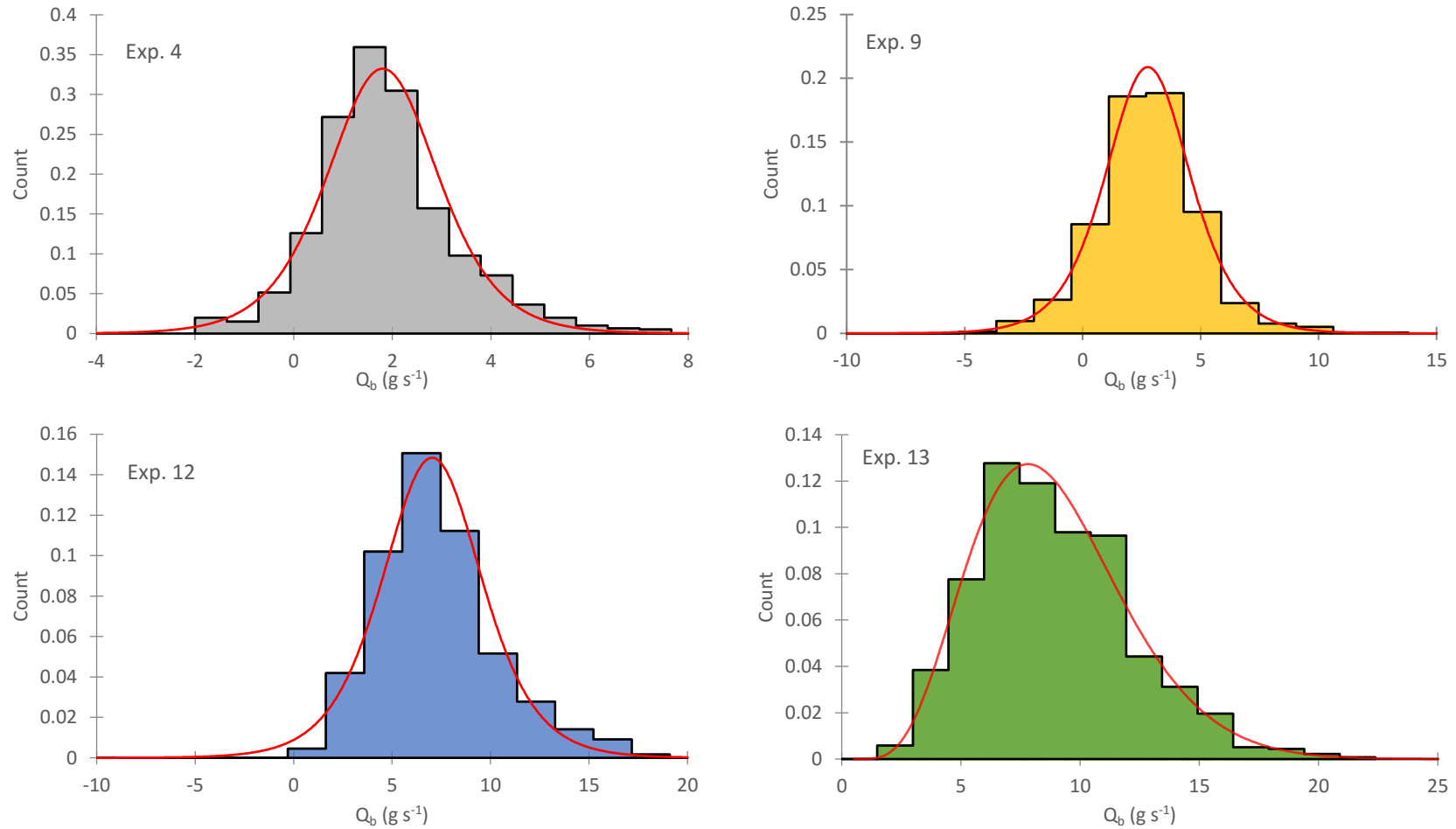
Figure 5.17 – Distribution of morphological bedload transport rate (Q_b) estimates for all 14 sections of the flume across all experimental runs. Results are for estimates from the simple threshold method. Note the differences in axis values.

5.4.1 Minimum Budget

Many morphological reach-budgets do not have a known boundary condition like the downstream sediment baskets used in this study. Therefore, many studies rely on assumptions about the boundary conditions, for example that the upstream input is zero. For this research, the minimum budget was completed so that the downstream boundary condition was unknown and the upstream boundary condition was initially set to zero. From here, the upstream sediment input was adjusted to satisfy the downstream sections so that there was no negative flux (i.e., negative Q_i or Q_o) in any section. Figure 5.18 shows the same sediment budget from Figure 5.12 but this time plotted with the minimum budget as well. In this case, the minimum input into section 14 was adjusted from 0 g s^{-1} to 4.11 g s^{-1} so that the output from section 11 would not be negative.
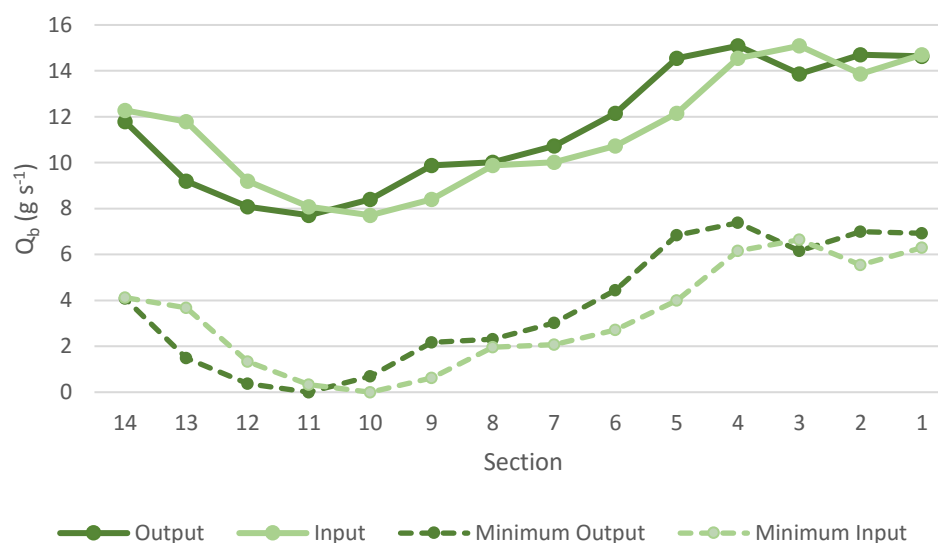
Figure 5.18 – Comparison of the bedload and minimum budget for a run during experiment 13. Results are shown for the simple 2σ threshold.

Across all experiments, the minimum budget significantly underestimated the known bedload transport rates (Figure 5.19 and Table 5.4) Comparing the mean estimates of transport rates, the minimum budget underestimates by a factor of 1.2 - 2.7, with the greatest propagated discrepancies occurring for experiment 13 (Table 5.4).
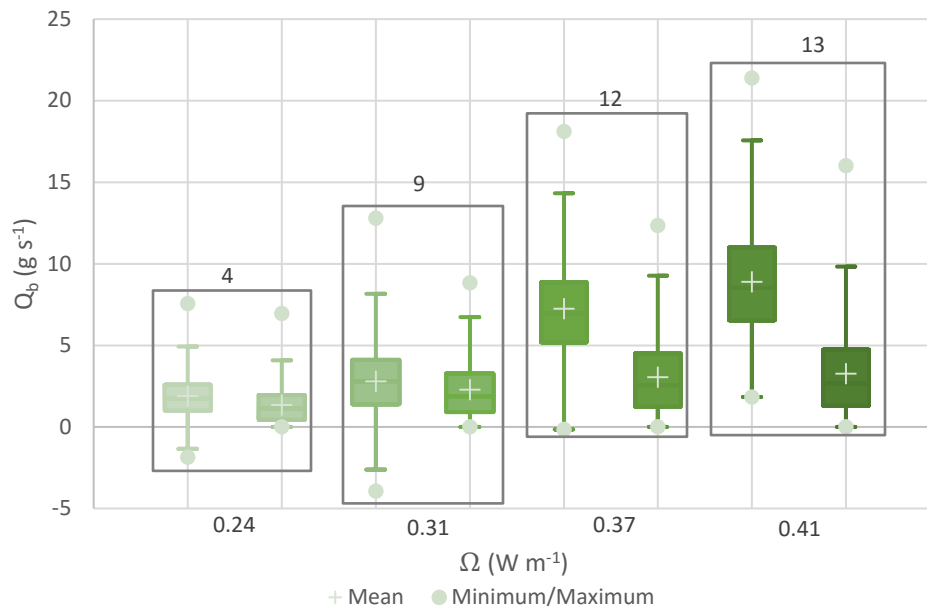
Figure 5.19 – Morphological bedload transport rate (Q_b) as a function of total stream power (Ω) for the known bedload boundary condition (left) and minimum budget (right). Results are for estimates from the simple 2σ threshold method.

Table 5.4 - Statistical comparison of the bedload and minimum budgets, where n is the number of observations, mean is the average value, σ represents the standard deviation, and the t-value and p-value represent the output from a two-tailed Student's t-test.

	Budget Method	n	Mean	σ	t-value	p-value
			g s^{-1}	g s^{-1}		
4	Bedload	938	1.88	1.39	9.067	<0.0001
	Minimum	938	1.35	1.17		
9	Bedload	980	2.79	2.18	5.631	<0.0001
	Minimum	980	2.28	1.77		
12	Bedload	910	7.24	3.05	32.827	<0.0001
	Minimum	910	3.05	2.35		
13	Bedload	924	8.90	3.21	41.518	<0.0001
	Minimum	924	3.27	2.58		

5.5 Spatial and Temporal Correlations

To investigate the spatial and temporal relationships between morphology and bedload transport rates further, the morphological changes and bedload transport rates in each section (1-14) were examined individually as they changed through time. For example, the temporal variation in section 1 for all of experiment 13 in terms of net change, bulk change, and masses of erosion and deposition are shown in Figure 5.20.
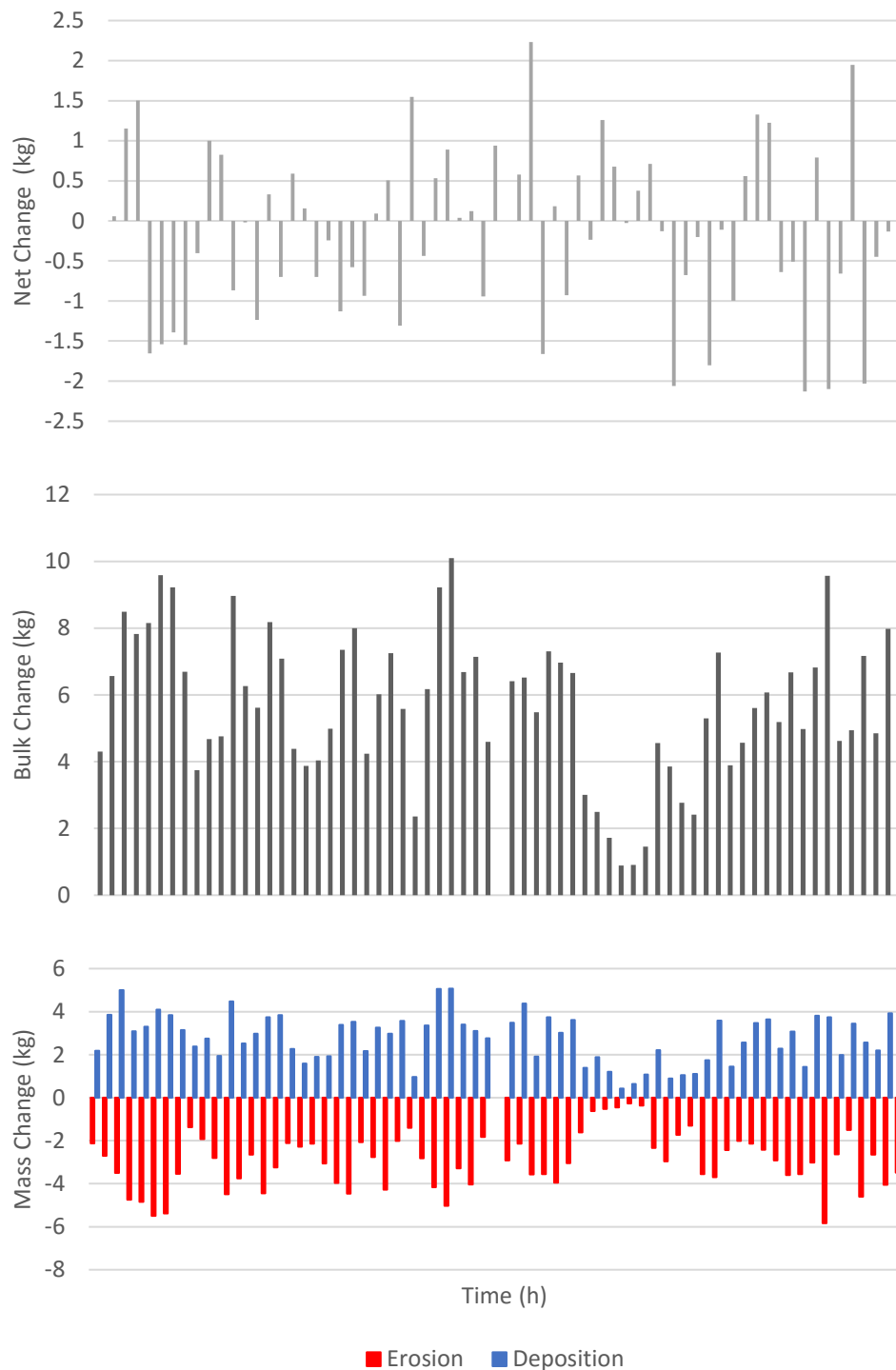
Figure 5.20 – Temporal variability in the masses of net change, bulk change, and erosion and deposition for section 1 of experiment 13.

Given the high amount of variability within each section over time, the subsections were averaged in terms of net change and bulk change (Figure 5.21). From these results, it was

possible to see how each experiment evolved, spatially and temporally. Most sections in experiment 4 were net erosional (i.e., negative net change) but sections 6, 11, and 12 had, on average, a net depositional regime. Interestingly, experiment 12 followed a very similar trend as experiment 4, with only section 11 having a net depositional regime while the rest of the sections were net erosional. Unlike experiment 4 and 12, experiment 9 is net erosional at the upstream end and transitions to a net depositional regime in section 4 and 5 before becoming erosional again the downstream 2 m of the flume. Experiment 13 had the greatest range of net changes with an average depositional regime for the upstream 3 m (sections 12-14), before plummeting towards net erosion for the rest of the study reach (Figure 5.21). Overall, the average net change does not seem to be sensitive to stream power, nor do there seem to be strong spatial trends beyond the fact that most sections were net erosional.

Looking at the average bulk change for each section, the trends within and between experiments follow more clear patterns. First, the bulk change is much more sensitive than net change to stream power, increasing from experiment 4 to experiment 13 at all cross-sections. Secondly, the spatial trends are similar for all experiments. Starting from a low bulk change in section 14, there was a general increase in bulk change longitudinally through each downstream section although experiments 9, 12, and 13 all experienced a final decrease in the average bulk change in section 1. It is possible that the lower values of bulk change at the upstream and downstream most sections reflect inlet and outlet effects. While the flume was cropped to 14 m to minimize these effects, the maximum extent of braiding generally occurred between ~2 and 12 m from the downstream end (sections 2-12). Outlet effects could not be avoided because it was necessary to know the downstream sediment output for the estimation of the known sediment budgets.

a)

b)
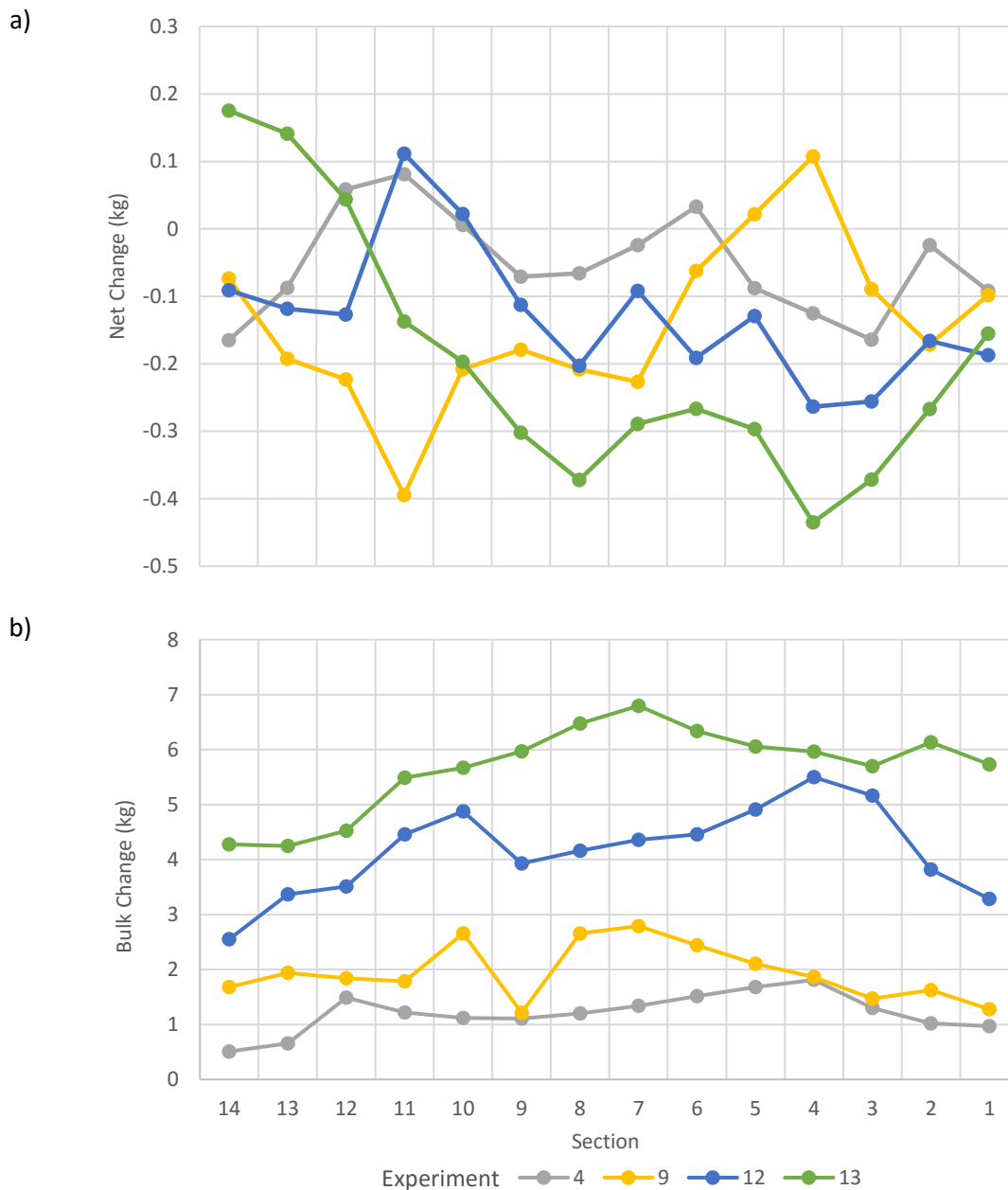
Figure 5.21 – Temporally averaged a) net change and b) bulk change plotted for each 1 m section, where section 1 is the downstream-most section of the flume.

The above graphs suggest that while there may be local changes in sediment storage (i.e., net change), the total amount of sediment being transferred within the system (i.e., bulk change) may be much more consistent on average for a given stream power. The average estimates for bedload transport rate for each section from Figure 5.15 were plotted together for all four experiments in Figure 5.22. A positive slope indicates an increase in sediment

mobilization with distance downstream, while a negative slope would be indicative of sediment deposition. The positive slope found for all experiments supports the overall erosional trends found in Figure 5.21 with respect to the net change. In addition, while all four experiments had a similar positive slope, there was an increase in bedload transport rate with increasing total stream power. These results also reflect the trends in Figure 5.21. The net changes were greatest for experiments 12 and 13, especially with large negative net changes in the downstream reaches where the channel were most active. Therefore, in these areas of high braiding complexity there was likely the greatest amount erosion in terms of lateral migration and bank erosion.
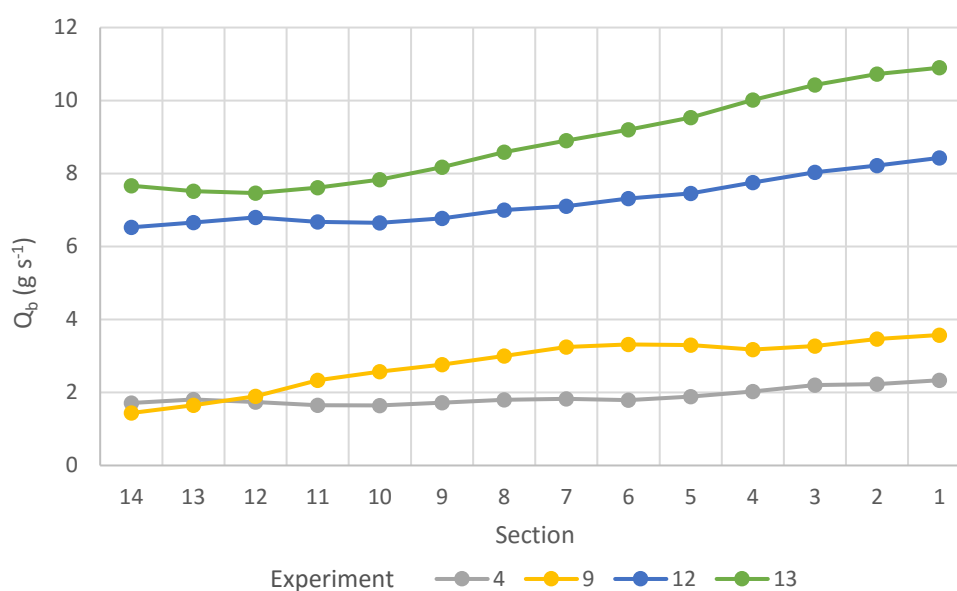
Figure 5.22 – Average morphological estimates of bedload transport rate (Q_b) plotted for each 1 m section of the flume, where section 1 is the downstream-most section. Results shown were derived using the simple 2σ for the multi-threaded constant discharge experiments (i.e., experiments 4, 9, 12, and 13).

An important consideration when propagating a morphological sediment budget is the propagation of error associated with the volume estimates from the DoDs. While not the focus on the current research, following the procedure in Brasington et al. (2003), an example of the propagated errors for morphological bedload transport rates for experiment 13 are shown in Figure 5.23. As expected, the amount of possible error increases with distance from the known bedload transport rate. The error on the morphological bedload

transport rates for each of the experiments, which is fundamentally based on the error in the active areas of each section, is plotted in Figure 5.24. As expected, the estimated error increases with the increased volume of change at higher stream powers and with distance from the known boundary condition at section 1.
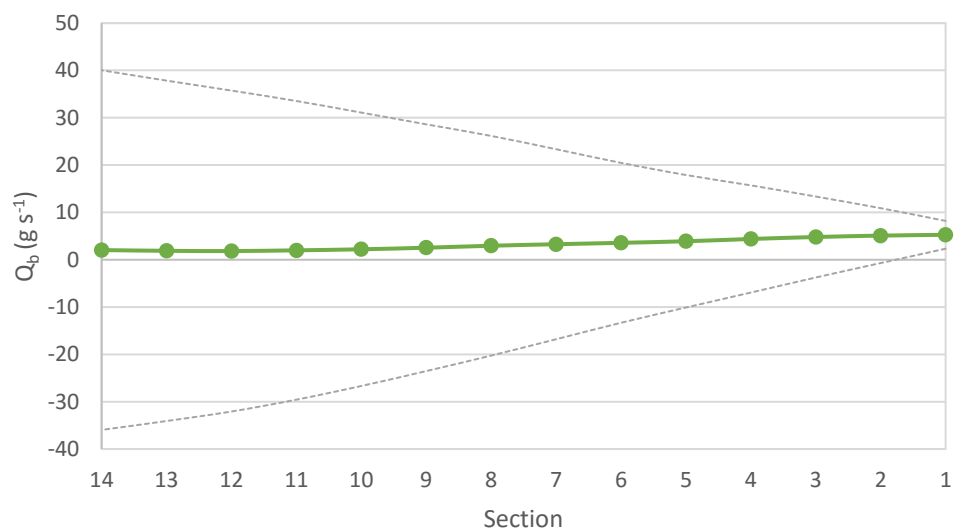
Figure 5.23 – Estimated error on the morphological mean estimates of bedload transport rate (Q_b) across all 14 sections for experiment 13where the dashed gray lines represent 95% confidence intervals.
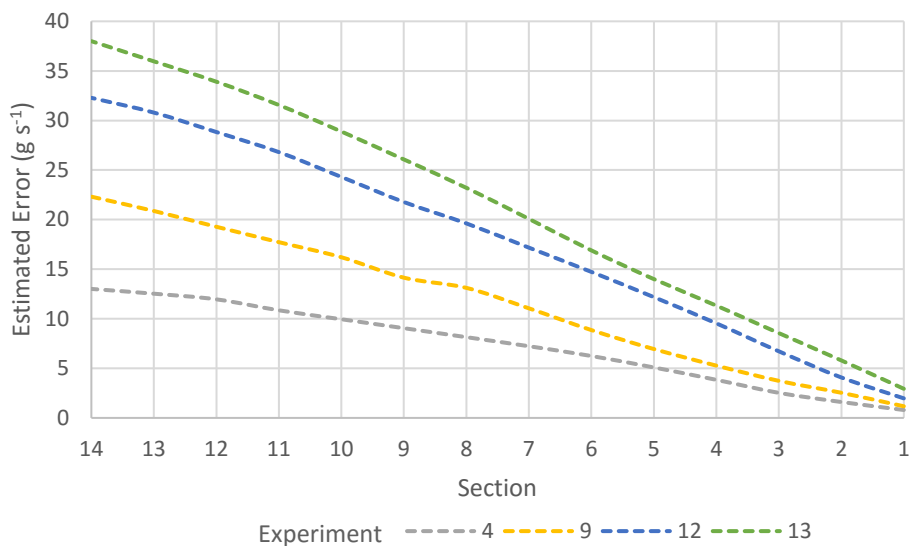
Figure 5.24 – Estimated error on the average morphological bedload transport rate in each section for each of the multi-threaded constant discharge experiments. Results shown are based on the simple 2σ threshold.

While both bulk change and bedload transport rate were sensitive to increasing stream power, given the large possible uncertainty on the transport rates due to error propagation, additional spatial analysis focused on the bulk change only. Figure 5.25 shows Pearson correlation maps of bulk change between each of the 14 sections. The Pearson correlation test measures the degree of linear correlation between two variables, where the coefficient values range from -1 to 1 so that -1 represents a perfect negative linear relationship and 1 represents a perfect positive linear relationship. A value of 0 indicates no linear relationship between the variables. Here, each section in the study reach was correlated with every other section within each experiment (Figure 5.25). In terms of the bulk change, there seems to be an adjacency effect such that each section has a significant positive relationship with its upstream and downstream neighbors and that in general, this correlational relationship decreases with distance from the section. Secondly, as stream power increased from experiment 4 through experiment 13, the number of sections with a significant correlation decreases (Figure 5.25 and Appendix K). Furthermore, as stream power increases and distance between sections increase, there is a greater likelihood of a slightly negative correlation between sections (Figure 5.25).
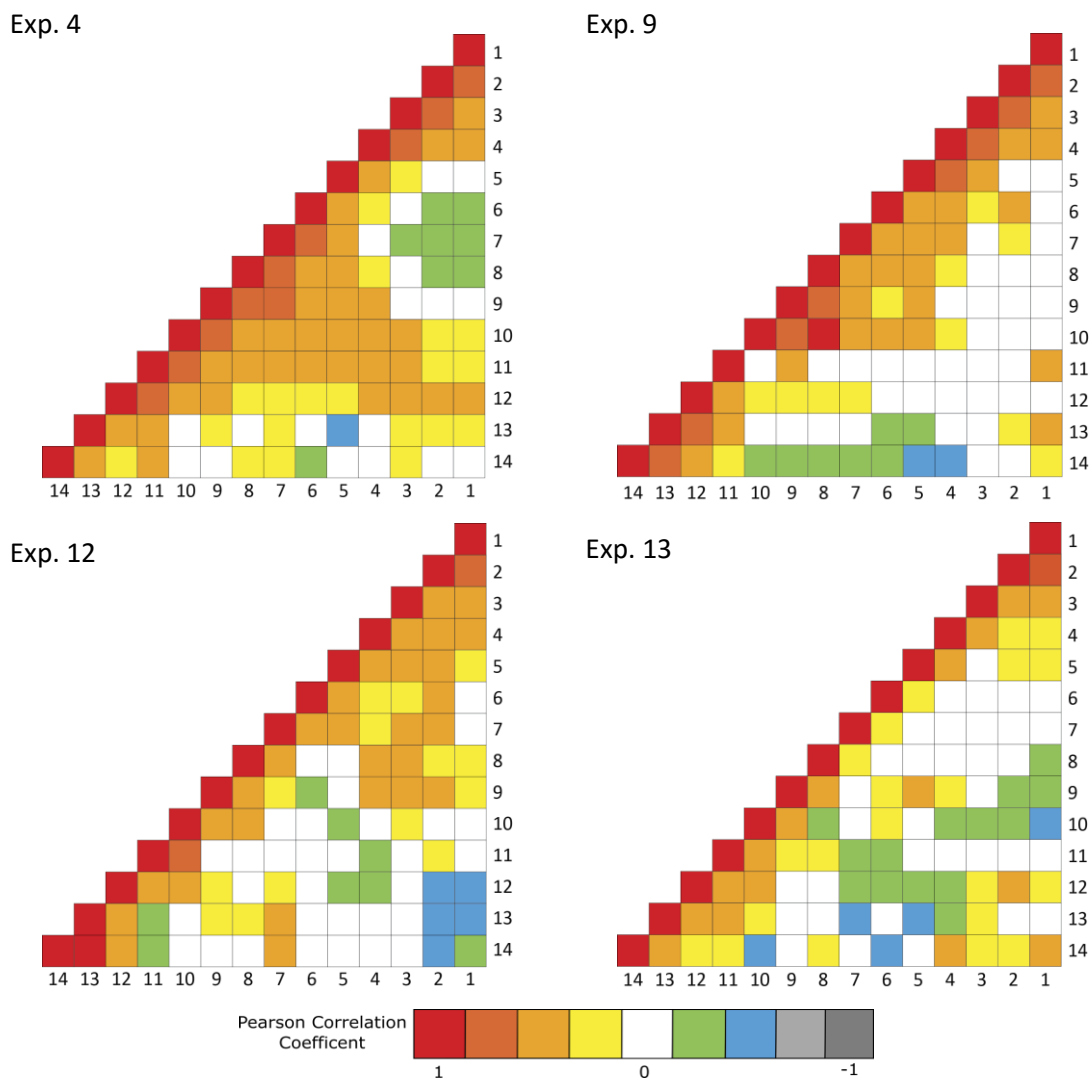
Figure 5.25 – Pearson correlation maps for bulk change (kg) between each 1 m section in the study area for each of the multi-thread constant discharge experiments.

5.6 Discussion

It was clear from Chapter 5 that bedload transport rates measured from downstream sediment baskets are highly variable temporally, even at constant discharge. These results are supported by many other authors who have found similar variability (Ashmore, 1991a; Hoey & Sutherland, 1991; Hoey, 1992; Bertoldi et al., 2009a). Breaking down this variability into its erosional and depositional components, it was found that erosion generally accounts for greater than 50 % of the total bulk change, regardless of stream power. As stream power increased, however, the range of percent erosion decreased, indicating that erosion consistently accounted for ~50 % of the bulk change in every run.

This trend could indicate that under high stream power conditions, more of the bed is being reworked so there are less extreme local examples of erosion and deposition. Therefore, these results reflect the 'patchiness' of the DEMs of Difference (DoDs) at low discharges, and the continuity of morphological change as stream power is increased. Another possible explanation is that as stream power increases the amount of time each run represents in the prototype also increases. It is likely that over longer periods of time more of the bed is reworked and therefore the amount of erosion and deposition would even out as a result of compensating scour and fill. Additional research should investigate the role of different time intervals on the rates of erosion and deposition (McLean & Church, 1999). As mentioned, the volumes of erosion were generally higher than volumes of deposition under all the experimental conditions tested. There are several possible reasons for this, related to both morphodynamics and experimental methods. In their research, Rumsby et al., (2008) found that in the Feshie River areas of erosion were generally local but deep in terms of elevation change, whereas areas of deposition were more likely to be diffuse and shallow. Similar results were found by McLean & Church (1999) on the Fraser River, where although the areal extent of erosional and depositional zones was similar, the volumes of erosion were greater than the volumes of deposition. If this is true, it is more likely that volumes of deposition will be underestimated because they fall below the minimum level of detection for morphological change, or the change detected is reduced/removed when applying a detection threshold to DoDs. Wheaton et al. (2010) compared volumes of erosion and deposition from raw DoD (i.e., no threshold applied) with three different threshold methods and found that on average, volumes of deposition are more greatly affected by thresholding than volumes of erosion. For example, when applying a simple 10 cm threshold to the DoDs, the volumes of erosion were reduced an average of 25 % from the raw DoD, while the volumes of deposition were reduced by 29 %. In addition, while the flume itself is assumed to be a closed system with a neutral sediment balance, the study area considered only the downstream 14 m of the model. In general, over the course of an experiment, the upstream end of the flume near the weir would aggrade and the downstream end would degrade. Therefore, the choice of study area could be another reason that most experimental runs resulted in a net erosional sediment balance.

While there was temporal variability in the net change during each experiment, the average net change for all four braided constant-discharge experiments was between -0.001 and 0 m^3. This suggests that over time volumes of erosion and deposition are relatively equal, although erosion was often slightly greater. This is especially interesting because the average net change was not sensitive to stream power even though the range of net changes did increase with stream power. This suggests that spatially and over time, changes in erosion and deposition are balanced regardless of stream power so that rivers are in equilibrium with respect to mass balance. Plotting the net change with the bedload transport rates from the downstream baskets, large negative values of net change were associated with the greatest bedload transport rates. This indicates that runs with the largest negative net change (i.e., strongly erosional) were associated with the greatest bedload transport rates. Extending this analysis found that volumes of erosion were positively, and linearly, correlated with measurements of bedload transport rates. Similar results were found by Hoey and Sutherland (1991) and Pryor et al. (2011) who stated that measurements of sediment output from their flume experiments would peak in response to channel erosion and troughed in response to channel aggradation or channel splitting. In the field, McLean & Church (1999) found that bedload transport rates were highly variable due to changes in channel stability. Specifically, lateral erosion and channel shifting were associated with high bedload transport rates. In addition, Hoey and Sutherland (1991) suggest that there could be a feedback loop between channel degradation and sediment output. As a channel erodes it will be able to capture more discharge and therefore continue to maintain a relatively high stream power and bedload transport rate.

Estimates of path length, as calculated from volumes of erosion, averaged between 3.1 - 3.7 m, with median values between 2.7-3.3 m across all four braided constant-discharge experiments. These results directly correspond with more detailed tracer measurements of path length completed by Kasprak et al. (2015) in the same river modelling flume. For five experimental runs completed at 2.1 l s^{-1} and 1.5 % slope, Kasprak et al. (2015) found an average path length of 2.5 m on a braided morphology, although some tracers were recovered as far as 10 m from the seed site. Kasprak et al. (2015) found that the majority (81 %) of recovered tracers were deposited on bar heads and bar margins. While the path lengths estimated in the current research were longer than those averaged from tracers there

are several possible reasons for this difference. The study by Kasprak et al. (2015) used coarse grains as tracers (D_{50}= 2.4 mm compared to the flume D_{50} = 1.2 mm) so that the grains would be large enough to recover at the end of the run. As a result, the estimated path lengths from the tracers are likely to underestimate the average path length of the bedload as they represent the larger size fractions which in general would have shorter path lengths (Pyrce & Ashmore, 2003b). In addition, a variety of seed sites were used during the experiment, and while this had little impact on the location of tracer deposition, it could account for differences in where a particle would be naturally entrained and where the tracers were seeded. Finally, Kasprak et al. (2015) only investigated path lengths for one experimental condition (2.1 l s^{-1}, 1.5 %) and found that path length could vary between 0.5-10 m over just five experimental runs, even at constant discharge. The current research estimates path lengths for over 250 experimental runs, under different experimental conditions, and the average values fall within a similar range found by Kasprak et al. (2015). In fact, excluding outliers, the range of path lengths estimated from volumes of erosion, across all experimental conditions, was between 0.5-8 m.

The distributions of path lengths found here coincide with general findings by Pyrce & Ashmore (2003b). They found that by looking at the distributions from field and flume tracer studies in straight and meandering gravel-bed rivers that path lengths fall into three categories: 1) positively skewed, 2) bimodal, or 3) symmetrical. The authors postulate that as particle mobility increases (i.e., more grains are being transported) the distributions will shift from 1 towards 3. A positively skewed distribution, like found in experiment 4 and 9, represents low particle mobility, where most grains are transported relatively short distances with few grains moving longer distances. This idea is supported again by the generally 'patchiness' of the DoDs for the lower discharge experiments. A bimodal distribution was common in tracer studies and was associated with some tracers not moving from the seed site, and others moving a characteristic length. Bimodal distributions were not found in this research because the path lengths were strictly based on particles that did move. Finally, the symmetrical distribution was linked to high particle mobility where most grains are being transported some characteristic distance downstream. Although their findings did not address braided rivers specifically, Pyrce & Ashmore (2003a) found that this characteristic length was associated with the average pool-bar spacing. Combined with

the tracer work on braided rivers by Kasprak et al. (2015) both research groups found that the majority of tracers (55-75 %, and 81 % respectively) were deposited on local downstream bars, indicating that path length is likely, at least in part, morphologically based. In addition, a higher proportion of tracers deposited on bars in the braided case (81 %) may suggest that morphology more strongly influences path length in those systems. Experiment 13 was defined by a more symmetrical distribution than the other experiments, which can be easily linked to greater sediment mobility given the higher bedload transport rates in that experiment. It is also interesting that the variability in the path length was lowest in experiment 13, possibly suggesting that path lengths in that system were strongly influenced by morphology (i.e., restricted) to local downstream bars. These results all indicate that path lengths are strongly related to channel morphology and as such, measures of channel morphology (i.e., volumes of erosion) could provide reasonable estimates of path length without the use of tracers. Although more research would be required, especially on braided rivers, this would be especially useful in the field where the use of tracers may be impractical.

For this chapter, two different morphologically based sediment budgets were created, the bedload budget and the minimum budget. Overall the results show that the morphological reach-budget method provided reasonable estimates of bedload transport rates at multiple channel cross-sections when propagated upstream from a known boundary condition. The distribution of these outputs, ~900 measures for each experiment, showed that the distribution of bedload transport rates was highly variable. This confirms what has been found many times in the past, that bedload transport rate is variable and that this is likely due to the passage of bedload sheets, scouring, and local erosion of bars and banks. This study, however, defined the distributions, which has rarely been done in the past. Following the work of Warburton and Davis (1994), the distributions of bedload transport rates in both studies resulted in either symmetrical or slightly positively skewed distributions.

Spatially there was little difference between the 14 subsections in terms of time-averaged bedload transport rates in experiments 4 and 12. Experiments 9 and 13, on the other hand, had significant differences between upstream and downstream reaches. The exact reason for this is not known but could reflect the changes in morphology over time in the

downstream reaches of both of those experiments. Experiments 9, 12, and 13 also had sections with a bimodal transport rates. There are two possible explanations: 1) the presence of the flume edge acted like a chute, locally increasing transport rates in the downstream reaches; 2) the morphology of the sections with the bimodal distribution drastically changed over time. For example, while it was shown that experiment 9 did have an edge chute, from Chapter 3 it was also shown that the wetted width in experiment 9 was vastly different from the first round of experiments to the second. It is possible that this change in morphology could also result in drastically different bedload transport signals over time and the significant differences in the upstream and downstream sections. Across all four constant discharge experiments, most of the morphologically-derived distributions for bedload transport rates (i.e., section 2-14) were not significantly different from the distribution or magnitude of the known bedload output (i.e., section 1). This suggests that the temporally variability in the known bedload transport rate is morphologically-driven.

Following the bedload budget, the same values of net change were used to calculate a minimum budget, where the output was assumed to be unknown and the input was adjusted to allow only positive bedload transport rates. While it was expected that the minimum budget would have a negative bias, the bias was significantly large and the discrepancies between the two budgets increased with stream power. These significant underestimates suggest that there may be a lot of sediment exchange at increased stream power. This explanation comes from images of DoDs that show active areas become larger and much more continuous with stream power. The minimum budget also does not account for any sediment throughput or chute-like channels where sediment is being transported but not causing morphological change. While still negatively biased, the minimum budget is useful for providing a lower boundary of sediment transport. Also, if the sediment input or output could be estimated, it would be possible to adjust the minimum budget to more realistic values. For example, using the same general method for estimating a morphological sediment budget Surian and Cisotto (2007) applied the minimum budget to the Brenta River in Italy. After finding that a bedload transport rate input of zero resulted in negative estimates of bedload transport rate at some cross-sections, the authors estimated possible bedload inputs from a nearby gauging station. As result, they could estimate feasible

bedload transport rates using the morphological method on a series of aerial photographs by mapping bank erosion.

As expected, it was found that within a single section the net change, bulk change and volumes of erosion and deposition were highly variable over time. This reflects the high dynamism of these systems and is linked to the highly variable bedload transport rates found in gravel-bed rivers. The average net change for each 1 m section reflects the trends for the entire reach so most 1 m sections were erosional, and overall net change was not sensitive to stream power. The bulk change, on the other hand, was sensitive to stream power and spatially variable. Finally, taking just the average bedload transport rate for each section there is a clear positive trend from upstream to downstream. This supports all the findings so far suggesting that the downstream reaches are more erosional and therefore transporting more material than upstream sections. Comparing these trends with those found in other studies, Ham and Church (2000) created morphological sediment budgets for the Chilliwack River, a gravel-bed river characterized by braided and meandering morphology. In their study, they found that the Chilliwack River became more active with distance downstream (i.e., greater volumes of change) and that there was significant variability in volumes of change over four study periods investigated. In their study, the largest increases in volumes of change were associated with flood events and subsequent bank erosion.

Lastly, this chapter looked at the correlations between different morphological signals at the different subsections. Bulk change seems to have some spatial persistence, which decreases with increasing stream power and channel complexity (i.e., braiding intensity). The exact reason for this is not known but it could be related to the morphological signatures of the experiments. Based on fluvial hydraulics, it would be expected that in the absence of morphological signatures (i.e., two-phase flow through a pipe) that the bedload transport rate at any cross-section would be equal to all others under steady flow conditions. As morphology is introduced, however, there are local changes in the spatial and temporal movements of sediment due to the passage of bedload sheets, breakdown of armour, erosion of the banks and bars etc. Therefore, it is possible that we are moving along a morphodynamic spectrum where under low stream power conditions, and therefore lower

braiding complexity, the movement of sediment is still strongly driven by a combination of morphology and hydraulics. From Chapter 4 we know that as stream power is increased, braiding intensity and active braiding intensity are also increasing. In addition, active areas are more continuous and the active width is greater as stream power is increased. Therefore, morphology will have a greater impact on the movement of sediment, possibly resulting in sections acting more independently of each other, like is seen in experiment 13 (Figure 5.25). In addition, the spatial decay in correlations is similar to the estimated path lengths in Figure 5.9 and those found by Kasprak et al. (2015). This further suggests that the spatial correlations between sections is likely linked to morphology at the scale of channel bar spacing.

5.7 Chapter Summary and Conclusions

This chapter highlighted the spatial and temporally variability in bedload transport rates and morphological change for the entire 14 m study reach as well as smaller 1 m subsections. Overall, it was found that erosion and deposition volumes were strongly positively related but that in general, erosion volumes were greater than deposition volumes. This was reflected in the slightly negative net changes found for all experiments. As expected, the volumes of erosion were positively correlated to sediment collected in the downstream baskets, which both increased with stream power.

Path length, as estimated from morphological change, provided reasonable estimates that correspond well with previous tracer studies and estimates of characteristic morphological lengths. Interestingly, estimates of path length decreased with stream power which may reflect stronger morphological influences with increasing morphological complexity.

Morphological estimates of bedload transport rates were similar in distribution and magnitude to independent measures of bedload transport at the downstream baskets. This suggests that much of the temporal variability in bedload transport rates reflects differences in morphology. Morphological budgets created with a known sediment output and the minimum budget assumptions provided significantly different estimates of bedload transport rates at a series of channel cross-sections. While the exact reason for the large differences is not known, it is likely partially related to sediment throughput and high levels

of sediment exchange. Since both are expected to be underestimates of the actual rates due to the limitations of volumetric analysis, they should be used with caution in practical applications but both can still be used to inform us about spatial and temporal differences in morphological change.

Finally, this chapter found that net change, bulk change, and estimates of sediment transport rates are spatially and temporally variable, but that bulk change and bedload transport rates were sensitive to changes in stream power. In addition, bulk change seems to have a spatial signal that decays after several metres, which corresponds with morphological signatures and estimates of path length and bar scale topography.

From this chapter the following conclusions are made:

- In general, rates of bedload transport, bulk change, and volumes of erosion and deposition all increase with increasing stream power.
- Net change is relatively insensitive to stream power, suggesting that even as volumes of erosion increase the volumes of deposition increase at a similar rate.
- Net change is generally slightly negative, indicating that all the experiments were net erosional. This could reflect the character of erosional and depositional features or be an artifact of methods (i.e., DoD thresholding and use of a physical model)
- Path lengths estimated from volumes of erosion provide reasonable estimates that are similar for the small range of stream power and discharge tested here.
- Morphological estimates of bedload transport rates provide similar distributions as measured flux rates, suggesting temporally variability in bedload transport rates is morphologically-driven.
- The minimum budget is negatively biased and significantly different from the bedload budget but provides important insights into volumes of sediment exchange and/or sediment throughput.
- Bulk change, and therefore the active width, has a spatial signal at the scale of the path length.

Chapter 6

6 Grain Size Evolution and Bed Mobility in Gravel-Bed Braided Rivers

6.1 Introduction

6.1.1 Chapter Introduction and Objectives

The grain size distribution of sediment being transported as bedload at any given time in a gravel-bed river will be a function of the grain sizes available, the mobility of the individual size fractions, and the bed configuration (Wilcock & Southard, 1989). The flow is only able to transport material in the exposed surface and the active subsurface when those grains become exposed during flow (Haschenburger, 2013). In general, the amount of bedload transported in gravel-bed rivers and the size of the grains mobilized will increase with flow as a result of selective sorting in which grains are differentially transported as a function of size (Wilcock & Southard, 1989; Rice & Church, 1998; Powell et al., 2001; Haschenburger, 2013). Finally, the bed configuration can modify local flow characteristics. As a result, the grain size distribution of the bedload is often finer than that of the bed surface, except under high discharge conditions when the largest grain size fractions can be mobilized (Powell et al., 2001).

The variability in transport rate in gravel-bed rivers, as well as the variability in the size of the grains being transported, has previously been described in terms of phases. During Phase I, transport rate is low and consists mostly of remobilized fine grains moving over a stable bed surface (Ryan et al., 2002). Phase II involves the mobilization of coarser grains from the surface. This mobilization of coarse grains causes finer grains from the subsurface to be exposed and entrained. The result is that Phase II has a significantly greater bedload transport rate and grain size range than Phase I transport (Ryan et al., 2002). Phase I and II are thought to be separated by a threshold flow, likely close to bankfull discharge, known as the breakpoint (Ryan et al., 2002). Defining the breakpoint is considered important in gravel-bed rivers because it quantifies the flow magnitudes needed to transport both large amounts of material as well as large grains. The nature of the Phase I to Phase II transition

can be poorly defined and complicated by factors such as the presence of bedforms, armouring, and grain shape. Unfortunately, data sets that can characterize the transition from Phase I to Phase II are lacking because of the challenges in collecting direct sediment measures in the field, particularly at high flow. This is especially true for larger rivers, and braided rives with complex and dynamic channel patterns.

Ryan et al. (2002) attempted to define the character of the breakpoint discharge in stable single-thread gravel-bed channels, with D_{50} ranging from 38 to 146 mm. In their study, they found that the surface was as much as 11 times coarser than the subsurface, indicating strong armouring, and that the breakpoint discharge was approximately 80 % of the bankfull discharge. Above these breakpoint flows, there was a substantial increase in grain size and transport rate. The authors suggest that there may be a second breakpoint at discharges higher than bankfull, where the local shear stress is reduced as the flow inundates the floodplain. Unfortunately, the flows required to confirm this hypothesis did not occur during the study. Ryan et al. (2002) suggest that their finding of the breakpoint discharge represents a fundamental link between channel form and process. With an annual return period, the bed roughness and morphology might represent the channel's adjustment to the imposed breakpoint discharge.

The variable bedload transport rate is also a function of sediment supply and bed structure. Previous research by Eaton and Church (2009) found that changes in the structure of the channel bed, specifically the degree of armouring (i.e., coursing of the bed surface), could created a fourfold range in sediment supply. Their results highlighted that under conditions of high sediment supply, the grain size distribution of the surface and subsurface would begin to converge as armouring was removed, resulting in a fining of the surface and a coarsening of the bedload (Pryor et al., 2011; Mueller & Pitlick, 2013; Venditti et al., 2017). The role of sediment supply in braided rivers may be less important because these systems are generally not supply limited. In fact, a large sediment supply is considered one of the defining features of these kinds of river systems. Yet, the relationship between sediment supply and the capacity of the river to transport sediment could be an indicator of both bed mobility and the size of the active width. Areas of the bed that are armoured

will generally be less available for transport, and therefore will not contribute to the active width or bedload transport rate of the river (Venditti et al., 2017).

It is also possible to investigate the role of fractional transport in channel mobility and channel morphology. Fractional transport, defined by the proportion of each grain size fraction in the total transport, can be classified into partial and full transport. For example, fine grains are mobilized under low flow conditions and therefore can be considered fully mobilized. Coarse grains, on the other hand, may never be mobilized (i.e., immobile) or only in a state of partial transport where some grains are moving but not in proportion to the availability of that size fraction on the bed (Haschenburger & Wilcock, 2003). Therefore, while the transport rate of all size fractions increases with discharge and stream power, the total bedload may be disproportionately composed of finer particles from the bed. Understanding these conditions is important for understanding channel dynamics and predicting bedload transport rates.

With knowledge of the bedload transport rate, grain size distributions, and the structure of the bed surface it is possible to classify the general bed mobility condition of a river. For example, Parker (2008) and later Venditti et al. (2015), provided four general bed mobility conditions that can exist in gravel-bed rivers including partial mobility, selective mobility, and equal mobility. Partial mobility occurs when the grain size distribution of the bedload is finer than the underlying surface, due to armouring or competency. Selective mobility occurs when the all the grain sizes in the surface are found in the bedload, but the distributions are different so that the bedload is still finer than the surface. Equal mobility occurs when the grain size distributions of the bedload and the surface are the same (i.e., all fractions are full mobilized). The final class was called a special case of selective mobility in which the bedload and subsurface were equal, although both still finer than the surface.

Venditti et al. (2015) defined the bounds of these classifications based on a ratio of bedload (pi) and surface (fi) against grain size, so that a pi/fi of one for all grain sizes represents equal mobility. Venditti et al., (2015) suggested that most gravel-bed rivers are dominated by a condition of partial mobility, but could reach selective mobility under high discharge conditions. These classifications have not been directly investigated in terms of gravel-bed

braided rivers, although a recent paper by Mueller and Pitlick (2013), found that braided rivers in the field were most likely to have similar bedload and subsurface grain size distributions compared to their less complex single-threaded counterparts. This is consistent with limited armouring in braided rivers due to their high rates of morphological change and depth of scour-fill (i.e., active layer depth) at high discharges. As a result, bedload transport in braided rivers is likely closer to equal mobility and therefore distinctly different from stable single-thread gravel-bed rivers with lower sediment supply.

Aside from contributing to the overall understanding of the morphodynamics of these complex river systems, there are several practical applications for understanding grain size and bed mobility evolution in gravel-bed rivers. For example, how the grain size distribution responds to increases in stream power has implications for the bedload sediment yield, which in turn is useful information for channel and reservoir design (Powell et al., 2001; Ryan et al., 2002). Venditti et al. (2015) characterized the existence of bed features, including bedload sheets and gravel dunes, in terms of mobility, which could have implications of channel design or river classifications. In addition, in locations where sediment size plays an important role in maintaining ecological functions, knowledge of fractional transport rates and bed mobility can help determine the disturbance regimes for fine grains which have implications for benthic organisms (Haschenburger & Wilcock, 2003). Similarly, information on changes to the bedload transport rates and grain sizes could have implications for infrastructure, such as bridges and roads (Powell et al., 2001). Overall, this information provides insights into the overall stability of the bed material and surface under a range of flow conditions. Finally, and perhaps most importantly in the braided case, understanding the relationship between grain size evolution and bed mobility can help classify channels as transporting at 'full capacity' or 'subcapacity.' This ability to predict river channel behaviour across a range of discharges will be especially useful in locations where no transport data is available (Powell et al., 2001).

Therefore, this third and final chapter of results will investigate grain size evolution and the role of bed mobility in a gravel-bed braided river. Specifically, this chapter will look at how grain size and bed mobility are related to channel morphology and bedload transport rates in gravel-bed braided rivers by addressing the following research objectives:

1. Quantify the grain size distribution of sediment collected from a gravel-bed braided river over a range of stream power conditions at constant, channel-forming discharge.

2. Characterize the evolution of grain size distributions across three experimental hydrographs, including fractional transport rates.

3. Characterize the range of bed mobility conditions in terms of partial, selective or equal mobility for a range of stream power conditions.

4. Describe the relationship between grain size evolution and bed-material mobility to the variability in the morphological active width, active depth, and bedload transport rate in gravel-bed braided rivers.

The aim of these objectives is to answer some new questions on bed mobility in complex rivers. Therefore, this chapter aims to answer the following research questions:

- How does the grain size distribution of the bedload change over a range of stream power and discharge conditions?

- Are braided rivers restricted to partial mobility like other gravel-bed rivers or do they also show selective or equal mobility?

- How does the variability in grain size distribution and bed mobility relate to channel morphology (i.e., the active width and active depth)?

6.1.2 Chapter Structure

This chapter will focus on results based primarily on sediment collected in the downstream sediment baskets. The chapter begins with details on the grain size distribution of the constant discharge experiments with focus on experiments 12 and 13 (Section 6.3). Section 6.4 outlines the grain size distributions of the hydrograph experiments, as they change temporally, as a function of discharge, and as a proportion of the total transport rate. The chapter finishes with a discussion (Section 6.5) and summary of the findings as well as the main conclusions (Section 6.6).

6.2 Constant Discharge Experiments

6.2.1 Grain Size Distribution

Sediment from the downstream baskets was collected after initial weighing of the wet sediment and was later sieved for several of the runs during the constant discharge experiments. Sieving allowed for the determination of grain size distribution curves. While few samples were taken for experiments 1, 4, and 9 in both experiment 12 and 13 sediment was collected approximately every fourth experimental run (Table 6.1). Given the high stream power of experiment 12 and 13 (0.37 and 0.41 W m^{-1}, respectively) it is expected that they are the most likely of the constant discharge experiments to transition to selective or equal mobility.

Table 6.1 - Summary of sediment sample counts collected from the constant discharge experiments, where Ω is total stream power.

Experiment	Ω (W m^{-1})	Samples collected
1	0.10	1
4	0.24	1
9	0.31	2
12	0.37	15
13	0.41	16
Total		35

This section will focus on the results from experiment 12 and 13 because the other experiments have too few samples to draw conclusions from. By plotting all the grain size distribution curves it is possible to see that there is a lot of overlap between the distributions of experiment 12 and 13 (Figure 6.1). Comparing the observations to the average grain size from the flume, most samples are finer than the flume subsurface. This could be an indication of armouring as the model subsurface was coarser than the bedload. Looking closely at Figure 6.1 it is possible to see that while experiment 13 had several runs that mimic the overall distribution of the model subsurface, experiment 12 was generally finer. These results were supported when looking at the average values of the D_{10}, D_{50} and D_{90} of each experiment (Table 6.2). Experiment 12 had finer D_{50} and D_{90} than both experiment

13 and the model but the differences were not significantly different based on a Student's t-test (t (29) = -0.712, p-value = 0.482, α = 0.05).
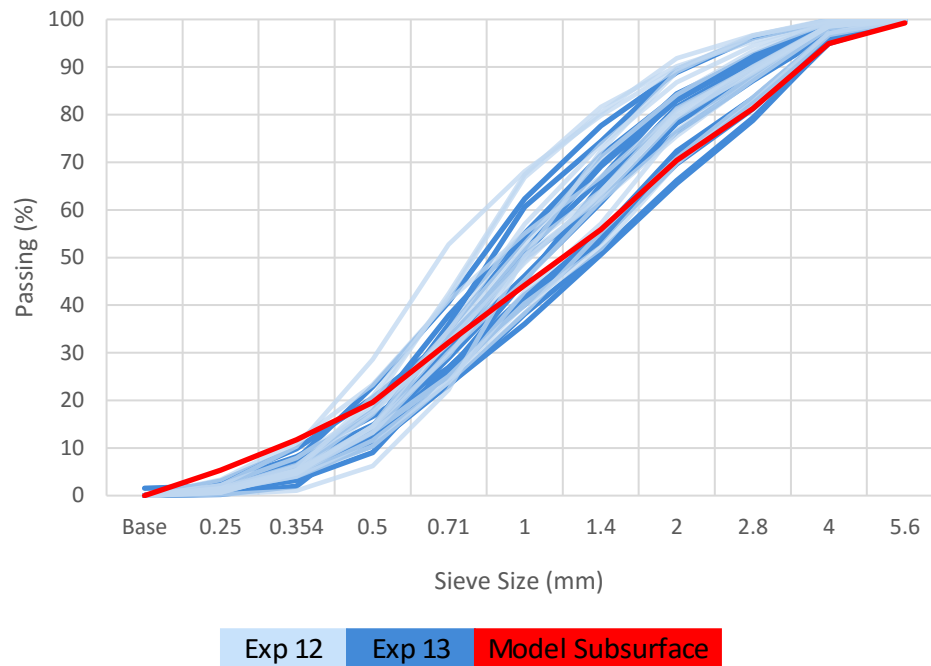
Figure 6.1 – Grain size distribution curves for experiment 12 and 13 and the subsurface of the model

Table 6.2 – Average D_{10}, D_{50} and D_{90} for experiment 12 and 13 as well as the bulk flume samples.

	n	D_{10}	D_{50}	D_{90}
Experiment 12	15	0.42	0.99	2.65
Experiment 13	16	0.44	1.10	2.99
Bulk Samples	7	0.32	1.18	3.52

Looking at the temporal changes in the grain size distribution is it clear to that that it is highly variable, even over constant discharge (Figure 6.2). This is especially true for coarser grain sizes, like the D_{50} and especially D_{90}. Overall, the D_{10} is essentially constant temporally and for two different stream powers (Figure 6.2).
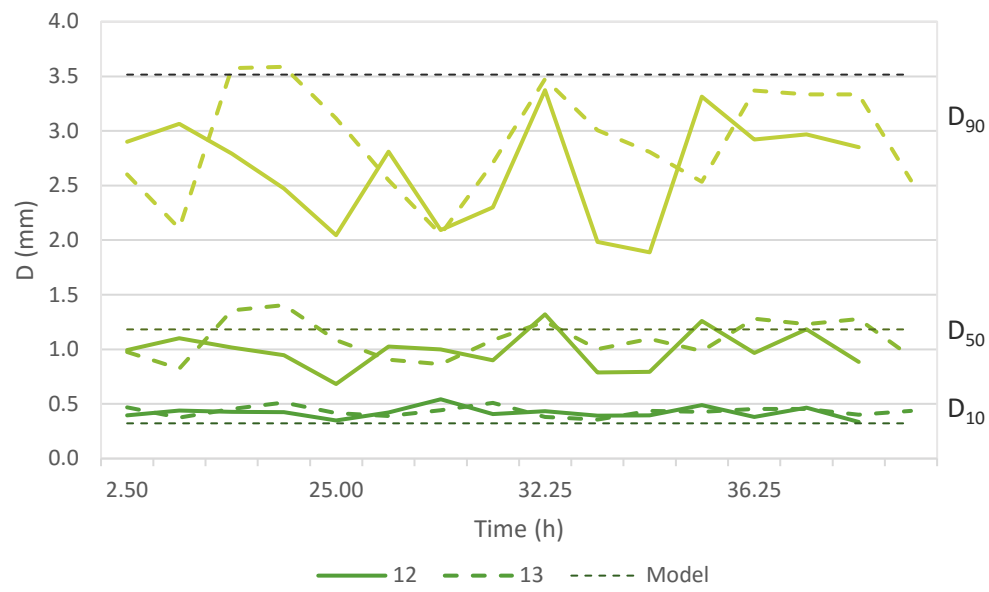
Figure 6.2 – Temporal variation in D_{10}, D_{50}, and D_{90} for experiment 12 and 13.

Figure 6.3 demonstrates that there is no clear trend when all D_{10}, D_{50} and D_{90} observations from experiment 12 and 13 are plotted with the bedload transport rate as measured from the downstream sediment baskets. As was also indicated in Figure 6.2, the overall range of grain sizes transported is much greater for the coarser size fractions (i.e., D_{90}) (Figure 6.3).
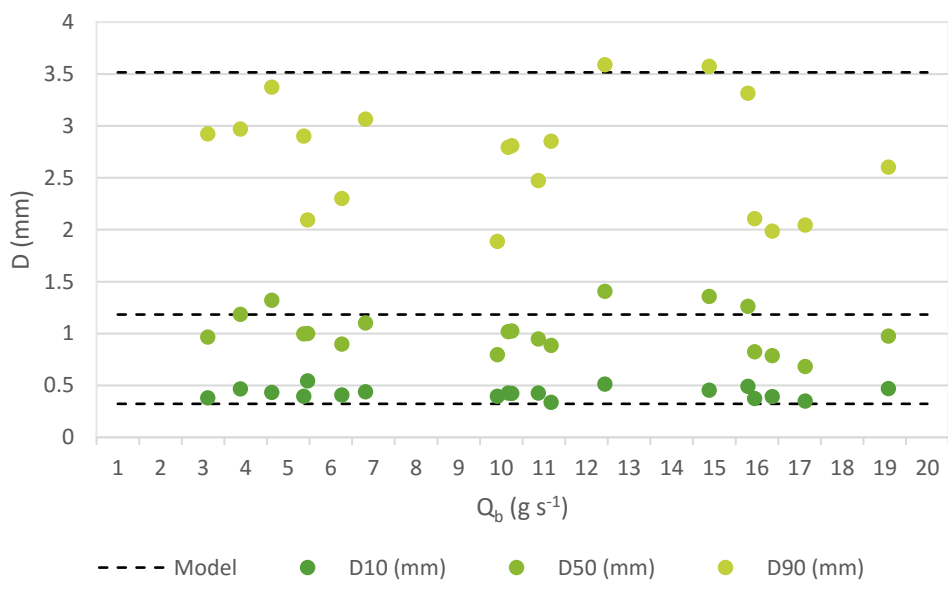
Figure 6.3 – D_{10}, D_{50}, and D_{90} as a function of bedload transport rate (Q_b) for experiments 12 and 13.

6.3 Hydrograph Experiment

6.3.1 Grain Size Distribution

117 particle size samples were collected during experiment 11. Across all discharges D_{10} ranged from 0.07- 0.57 mm, D_{50} ranged from 0.48-1.41 mm and D_{90} ranged from 1.15 - 3.57 mm (Figure 6.4 and Figure 6.5). Overall, D_{10} was relatively constant across all discharges and hydrographs except for 0.7 l s^{-1}, which had a mean D_{10} lower than all the other discharges (Figure 6.4 and Figure 6.5). D_{50} seems to increase slightly with discharge but generally plateaus above 1.35 l s^{-1} (Figure 6.5). Temporally, D_{50} is generally constant but seems to follow the general shape of the hydrograph, particularly at low discharges and during hydrograph A (Figure 6.4). Unlike the other two metrics, D_{90} clearly increases with increasing discharge (Figure 6.5). This positive trend is also obvious when looking at how D_{90} changes over the hydrographs, especially in hydrographs A and C (Figure 6.4).
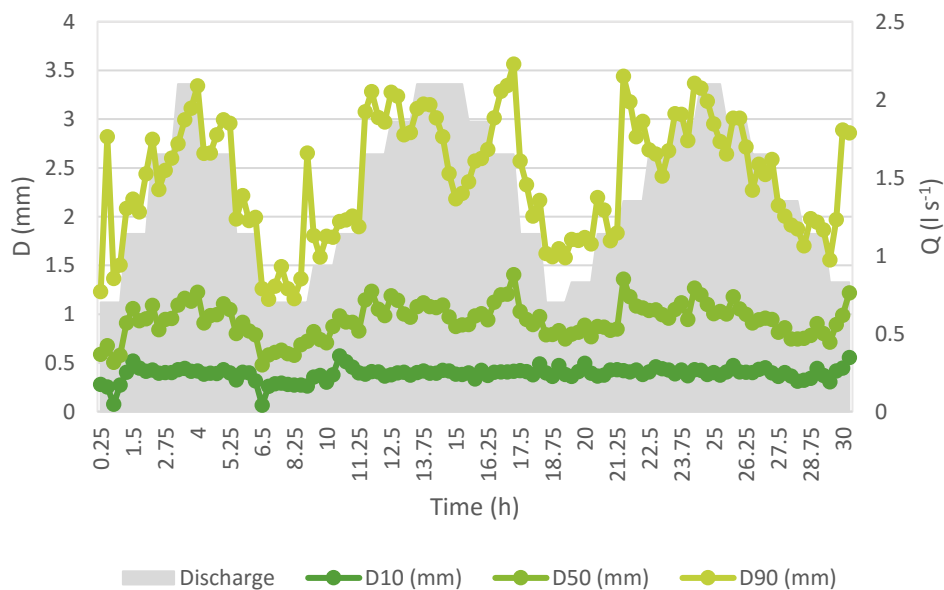
Figure 6.4 – Temporal variability in D_{10}, D_{50}, and D_{90} for the hydrograph experiments, where Q is discharge.
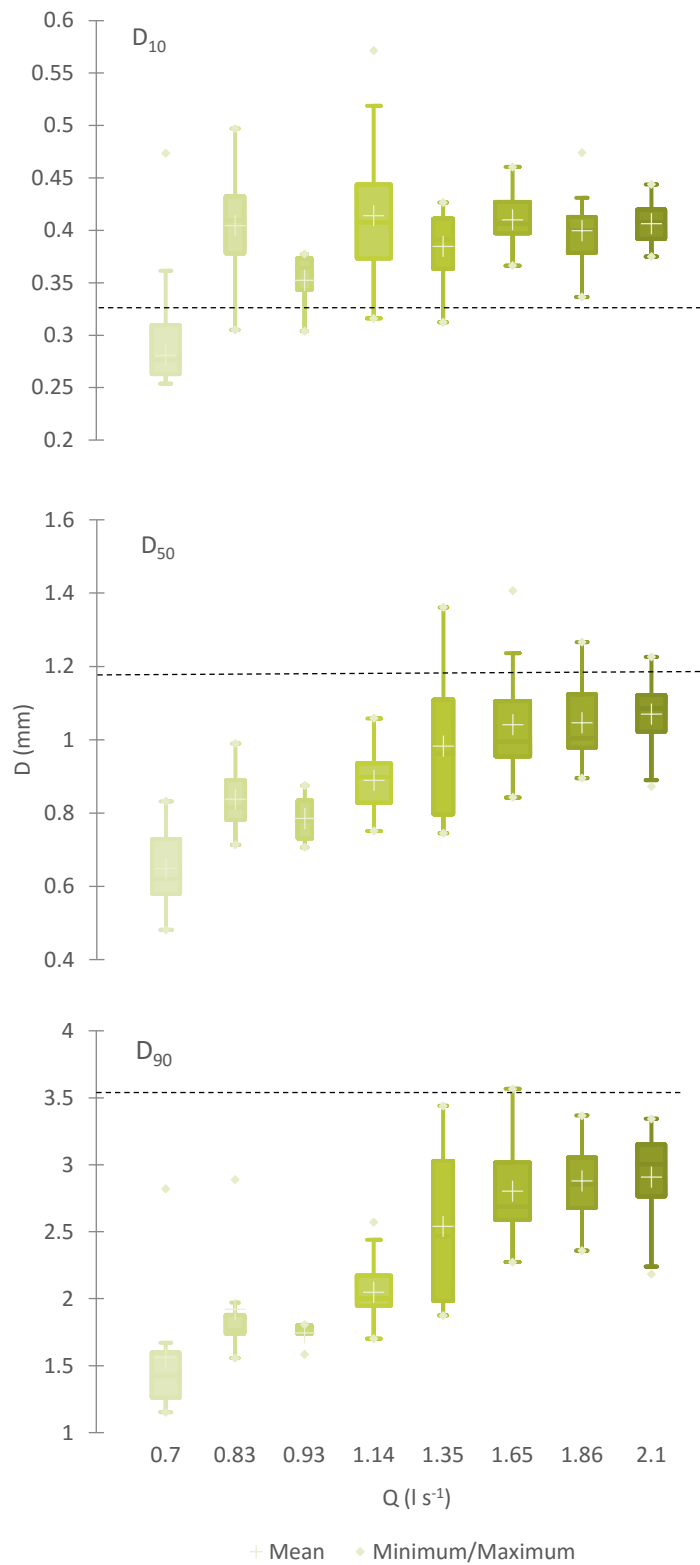
Figure 6.5 – Box plots of D_{10}, D_{50}, and D_{90} plotted against discharge (Q) over the 3 hydrograph experiments. The dashed lines represent the flume bulk samples.

Plotting the grain size distribution curve for each hydrograph clearly shows the progression of the bedload from a finer grain size distribution to a coarser one with increasing discharge (Figure 6.6). This trend is especially clear in hydrograph A, where the grain size distribution of the bedload begins to approach the grain size distribution of the model subsurface, but only at high discharge. Experiment B had more individual discharge steps so the trend seems slightly less clear because of the overlaps in the middle discharges. Hydrograph B also had the lowest average D_{90} of the experiments with a value of 2.76 mm compared to the 3.04 mm and 3.05 mm for hydrograph A and C, respectively. This may be the result of running 8 experimental runs at the peak discharge for hydrograph B rather than just 4 as in the other two experiments. While the first 4 runs at peak discharge in hydrograph had an average D_{90} of 3.10 mm, the second 4 runs had an average D_{90} of only 2.41 mm. Overall, the trend for hydrograph B mimics that of hydrograph A so that with increasing discharge the grain size distribution begins to reach unity with the grain size distribution of the model subsurface (Figure 6.6). Finally, unlike the other two hydrographs, the trend of the grain size distribution becoming coarser with discharge is less clear for hydrograph C. In a similar way to hydrograph B, this complexity could be the result of using more discharges throughout the course of hydrograph C, therefore this graph might reflect the general variability found at each discharge rather than showing the more discrete transitions found in hydrograph A which only used half the number of discharge steps. The differences in the three hydrographs highlights the importance of sampling multiple hydrographs, even over a similar morphology, to capture the variability in grain size distributions.
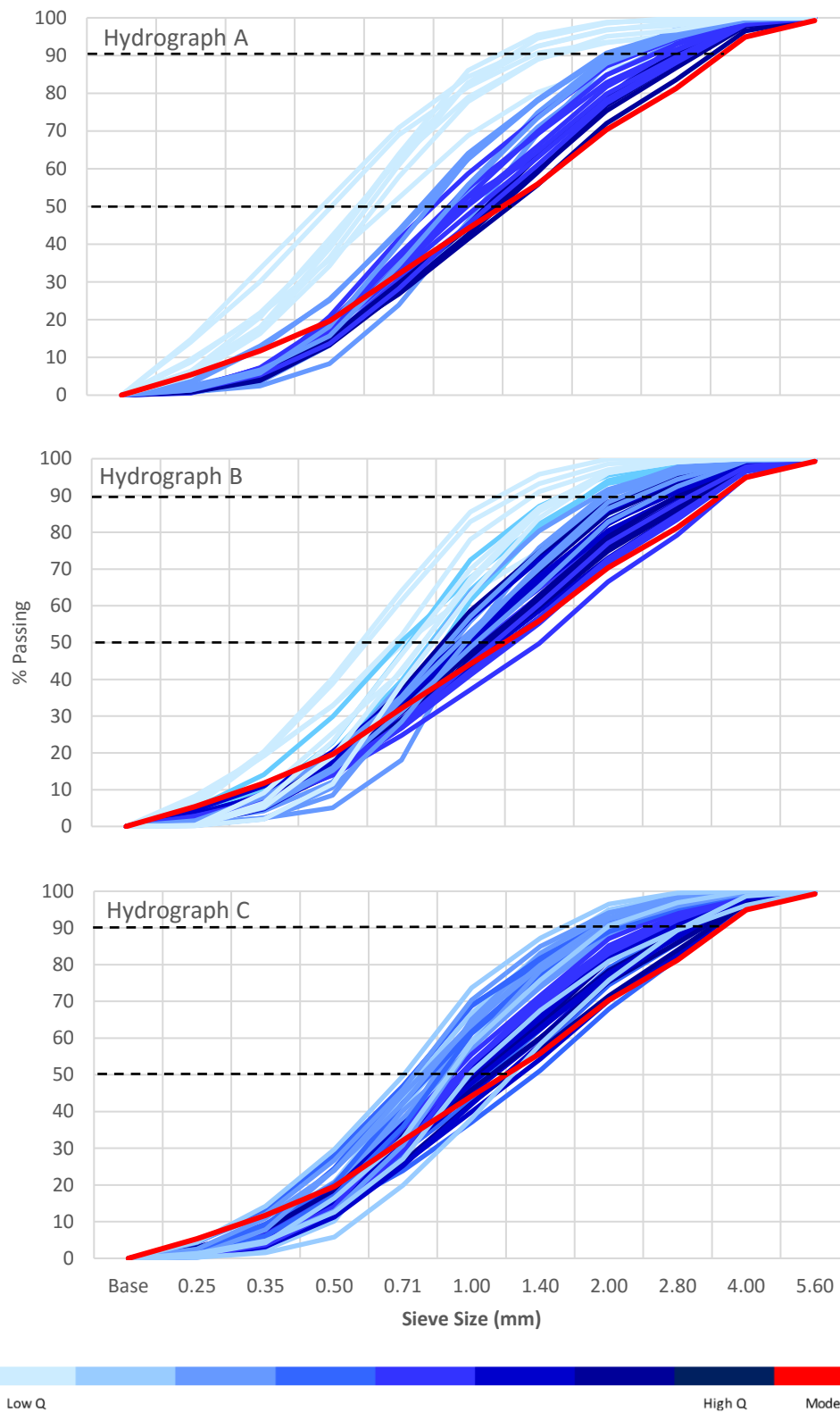
Figure 6.6 – Grain size distribution curves for hydrograph A, B, and C. The dashed lines indicate D_{50} and D_{90}.

Plotting all 117 samples together with the model distribution it is even clearer that there is a steady progression from a D_{50} around 0.5 mm to 1.4 mm as discharge is increased from $0.7\,l\,s^{-1}$ to $2.1\,l\,s^{-1}$ (Figure 6.7). Some discrepancy between the high discharge curves and the model curve could be due to the fact that the model curve was based on a bulk sample rather than a surface sample. This graph highlights that the distribution of the model subsurface is rarely reached and the only discharges that come close are the channel-forming discharges of $2.1\,l\,s^{-1}$.
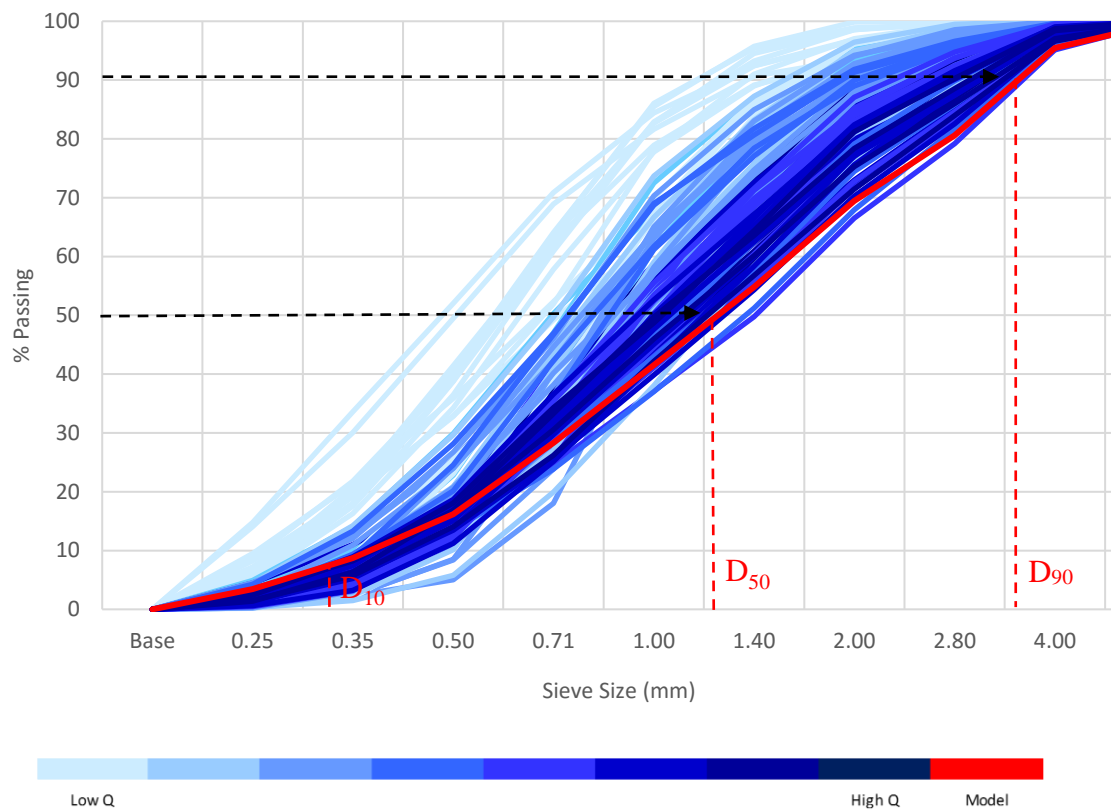
Figure 6.7 – Grain size distribution for all 117 hydrograph samples. Red dashed lines indicate the locations of the D_{10}, D_{50}, and D_{90} with respect to the bulk samples from the model. The black dashed arrows show the progression of D_{50} and D_{90} from low discharge (light blue) to high discharge (dark blue).

6.3.2 Fractional Transport Rate

Grain size distribution of bedload can also be analyzed in terms of bedload transport rate (Figure 6.8). Unlike the constant discharge experiments, which had no obvious trends, both D_{50} and D_{90} have a strong relationship with the bedload transport rate, approaching the bulk sediment D_{50} and D_{90} at the highest transport rates. As expected, the D_{10} has a very low R^2 value of 0.150 because it was essentially transported constant under all discharge conditions and therefore bedload transport conditions.

The figure shows scatter data with the following fits:

$y = 0.328\ln(x) + 2.402$, $R^2 = 0.681$

$y = 0.090\ln(x) + 0.939$, $R^2 = 0.604$

$y = 0.018\ln(x) + 0.389$, $R^2 = 0.150$

Axes: D (mm) versus Q_b (g s^{-1}). Legend: D10, D50, D90.
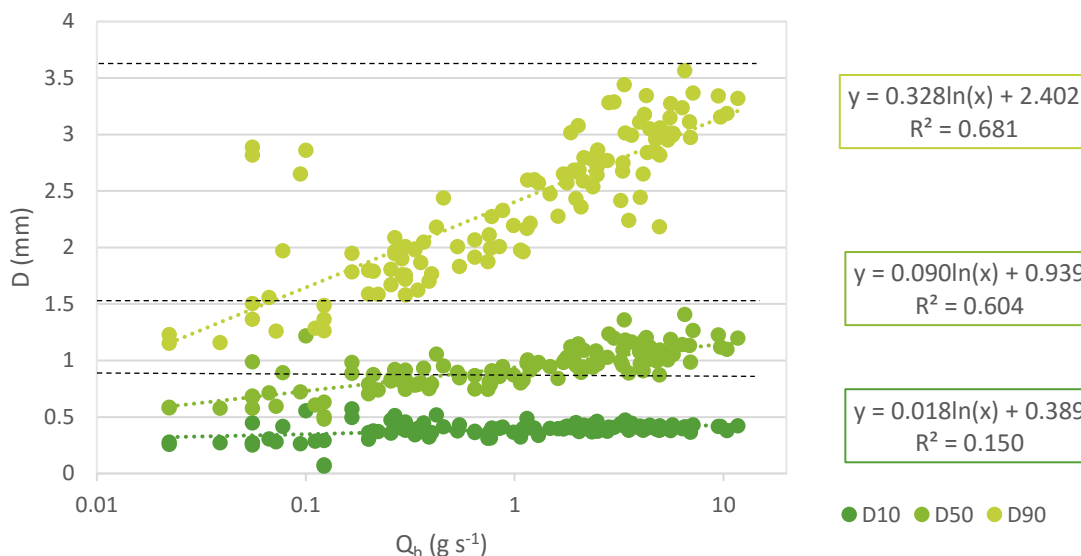
Figure 6.8 – D_{10}, D_{50}, and D_{90} as a function of bedload transport rate (Q_b). The horizontal dashed lines represent D_{10}, D_{50}, and D_{90} of the bulk samples from the model.

In addition, the total bedload transport rate can be analyzed for each particle size range to yield a fractional transport rate. Following the procedure of Ryan et al. (2002) the fractional transport rate for each 0.5 phi size was calculated as a proportion of the total transport rate. Across all discharges, the grain size fractions of 0.5-0.71 mm and 1-1.4 mm account for the greatest proportion of the total transport rate (Figure 6.9). Conversely, the smallest fraction (<0.25 mm) and the largest (>4 mm) always account for the smallest proportion of the total transport rate. In addition, the largest fraction only becomes detectable in discharges greater than 1.14 l s^{-1}, suggesting a possible breakpoint discharge between Phase I and Phase II flow.

a)

b)
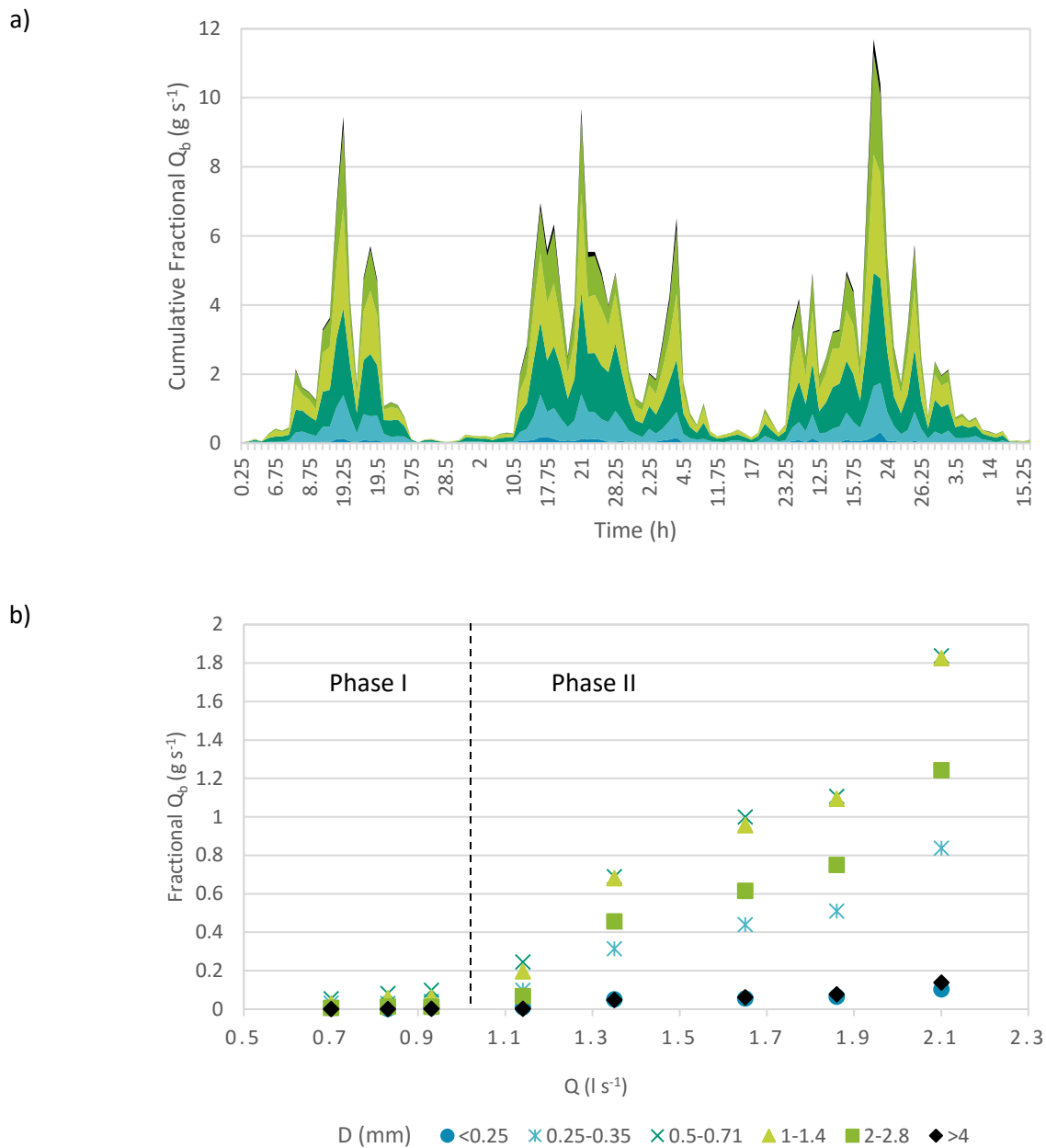
Figure 6.9 – Fractional transport rate (Q$_b$) plotted against a) time and b) discharge (Q). The dashed vertical line separates Phase I flow from Phase II flow. Colours in legend apply to both graphs.

It is possible to look at how the different size fractions change as a function of the total bedload transport rate, measured from the downstream baskets (Figure 6.10). Most of the observations have total bedload transport rates below 7.5 g s^{-1} with only four observations (all from runs at the peak discharge of 2.1 l s^{-1}) ranging between 9.5 – 11.7 g s^{-1}. Not

surprisingly, the largest grains (>4 mm) only appear above a lower transport rate threshold of ~1 g s^{-1}.
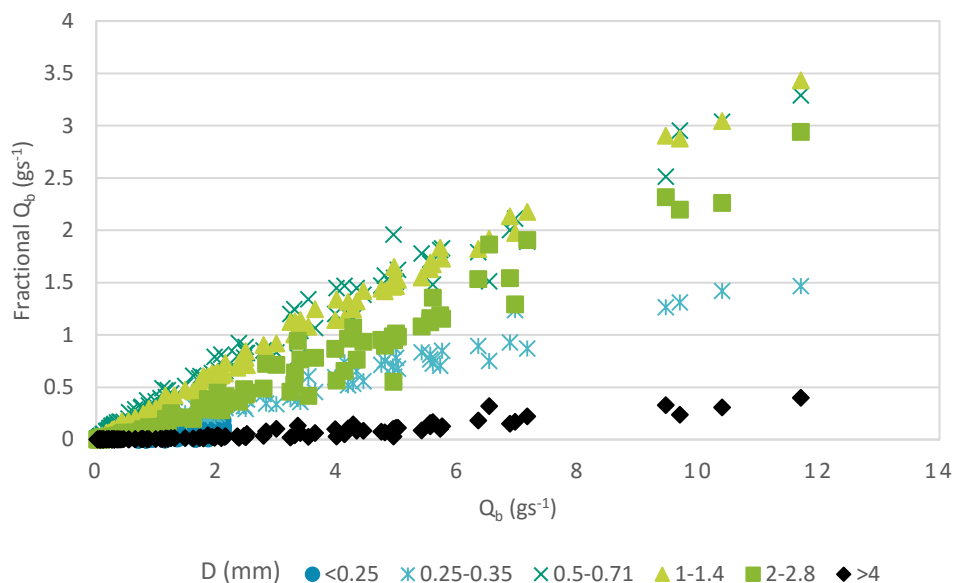
Figure 6.10 – Fractional transport rate as a function of the total transport rate (Q_b) for all of the runs in experiment 11.

6.3.3 Analysis of Bed-Material Mobility

Bed-material mobility can be defined based on the grain size distribution of the bedload compared to the grain size distribution of the channel surface or subsurface. The closer the two distributions are to each other, the closer the bedload transport rate is to equal mobility. It is clear from the results above that as discharge is increased from 0.7 l s^{-1} to the channel-forming discharge of 2.1 l s^{-1} that mobility was also transitioning. At low discharges, D_{50} and D_{90} are much lower than that of the flume subsurface, based on the bulk samples. This would be considered partial mobility, which Venditti et al. (2015) suggests is the usual condition for single-thread, stable, gravel-bed rivers. As discharge is increased, however, the grain size distribution of the bedload begins to transition towards equal mobility. Since the grain size distributions presented here are based on the model subsurface, under the classifications outlined by Parker (2008) and Venditti et al. (2015), at discharges above which bedload transport and morphological change are largely detectable (i.e., > 1.14 l s^{-1} in this case), the system would be classified as a special case of selective mobility. This means that the bedload and subsurface are equal but are likely still finer than the surface.

It is expected, however, that the surface and subsurface are essentially the same in this case because of the absence of armouring (Mueller & Pitlick, 2013; Leduc et al., 2015). As a result, the channel may be reaching a condition of true equal mobility as the discharge approaches channel-forming values.

To investigate this trend further, a modified version of *pi/fi* ratio was used. Based on the classification system outlined in Venditti et al. (2015), the *pi/fi* curve is expected to be at zero for large grains under partial mobility conditions. Under selective mobility conditions the *pi/fi* curve will decrease with grain size but remain above zero even at larger grain sizes. For 'true' equal mobility, each size fraction must exist in the same proportion in the bed and the total bedload so that *pi= fi* or *pi/fi* =1, where *fi* is the frequency of size *i* in the bed surface by weight and *pi* is the frequency of size *i* in the total bedload (Ashworth et al., 1992). Therefore, true equal mobility is achieved when the *pi/fi* curve is constant at 1. In the modified version, the *fi* values reflect the grain size fractions of the physical model subsurface, rather than the surface, which is normally used for armoured beds. The results of this analysis, including all 117 samples from the hydrograph experiment, can be seen in Figure 6.11. Figure 6.11 shows that as discharge increases, the system moves from a state of marginal partial mobility, through a state of selective mobility at higher discharges, to a state that is close to equal mobility (*pi/fi* =1 for all grain sizes).
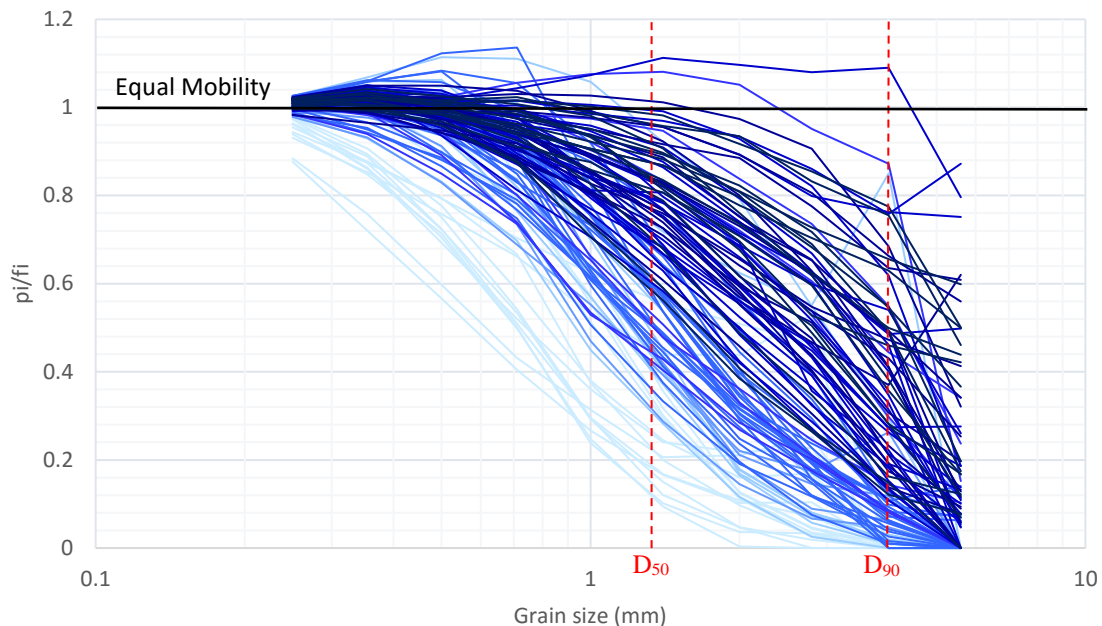
Figure 6.11 – Modified *pi/fi* ratio relationship with grain size for all the samples in the hydrograph experiment. Where *pi* represents the bedload and *fi* the model subsurface. Red dashed lines represent the D_{50} and D_{90} of the model subsurface.

A simple index for equal mobility is the D_{90} ratio between the subsurface and bedload. Figure 6.12a shows that this ratio decreases with increasing stream power. This supports the idea that at higher discharges the subsurface and bedload particle size distributions converge (i.e., *pi/fi* ratio closer to 1). Similarly, the ratio of D_{90} in the subsurface and bedload has a very strong power relationship with bedload transport rate with a mean value of about 1.2 at the highest stream power and transport rates (Figure 6.12b).
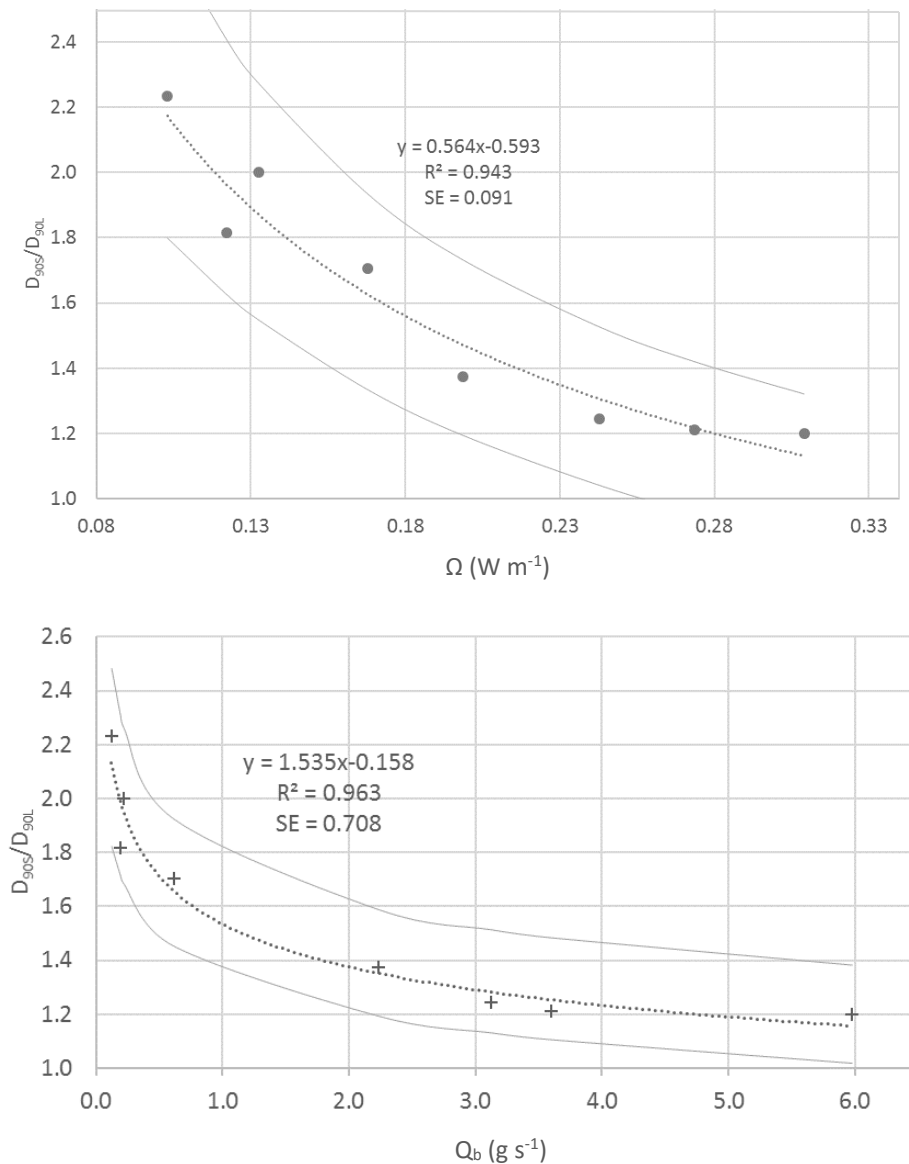
Figure 6.12 – D_{90} subsurface to bedload ratio as a function of a) total stream power (Ω) and b) bedload transport rate (Q_b). The dashed lines represent the best fit trendlines and the outer solid lines represent the 95 % prediction interval for the observations.

The D_{90} subsurface to bedload ratio also correlated with morphological parameters including active width, active depth, bulk change, and the areas of erosion and deposition (Figure 6.13). In response to these increases in morphological change, more of the surface and subsurface (i.e., the active layer) are being activated, allowing the bedload and bed-material grain size distributions to become more similar (i.e., $D_{90s}/D_{90l} \sim 1$).
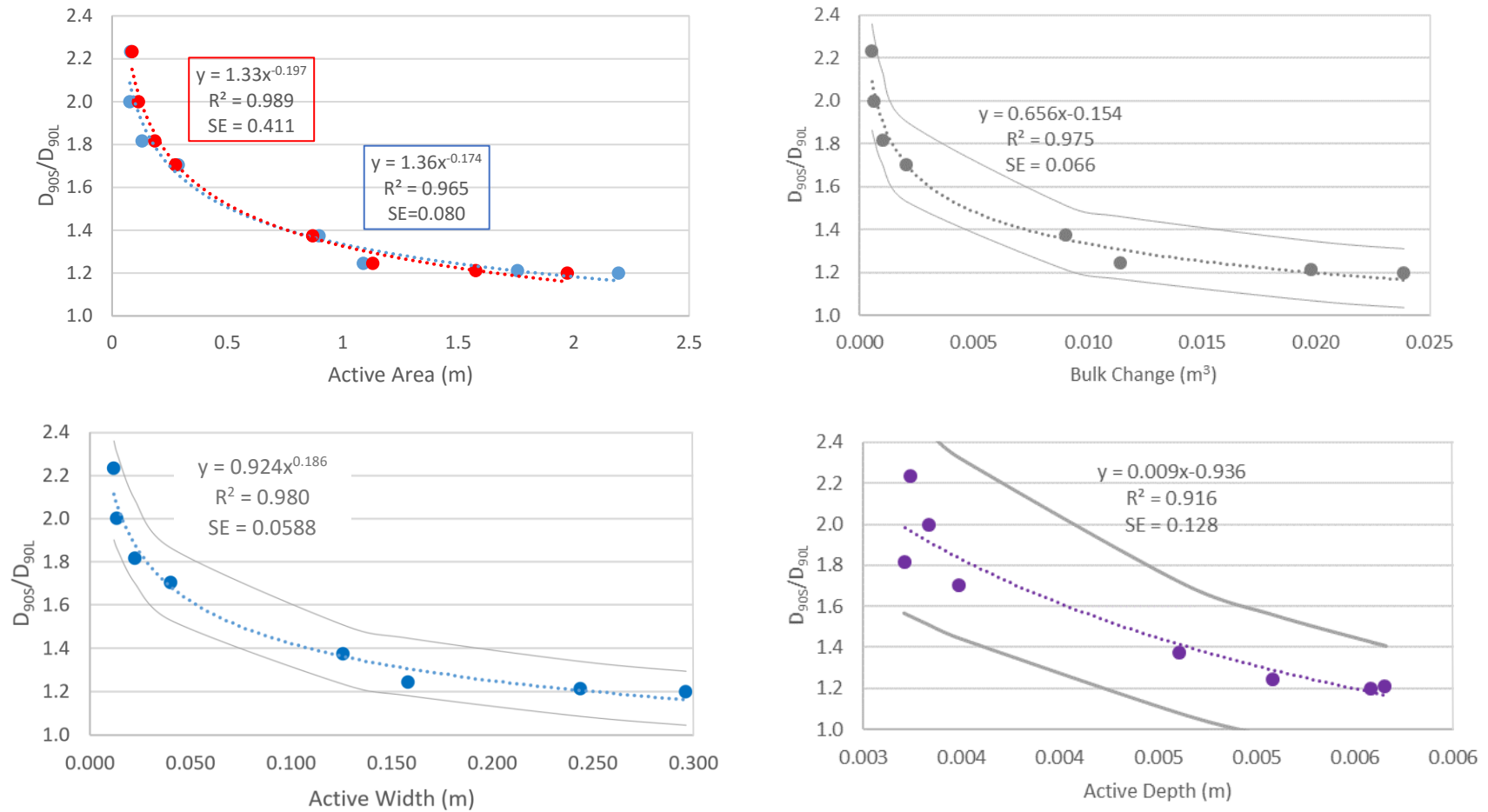
Figure 6.13 –D₉₀ subsurface to bedload ratio plotted against morphological parameters including the total active area, the bulk change, the morphological active width, and the active depth. The dashed lines represent the best fit trendlines and the outer solid lines represent the 95% prediction interval for the observations.

In addition to Figure 6.13, it is possible to relate D_{10}, D_{50} and D_{90} to morphological parameters. As expected, the D_{10} is equally mobile across all measures of active width, active depths, and bulk change (Figure 6.14). D_{50} and D_{90} both increase with all three morphological parameters, showing that as morphological change increases, so does the mobility of grains larger than D_{50} and D_{90}.
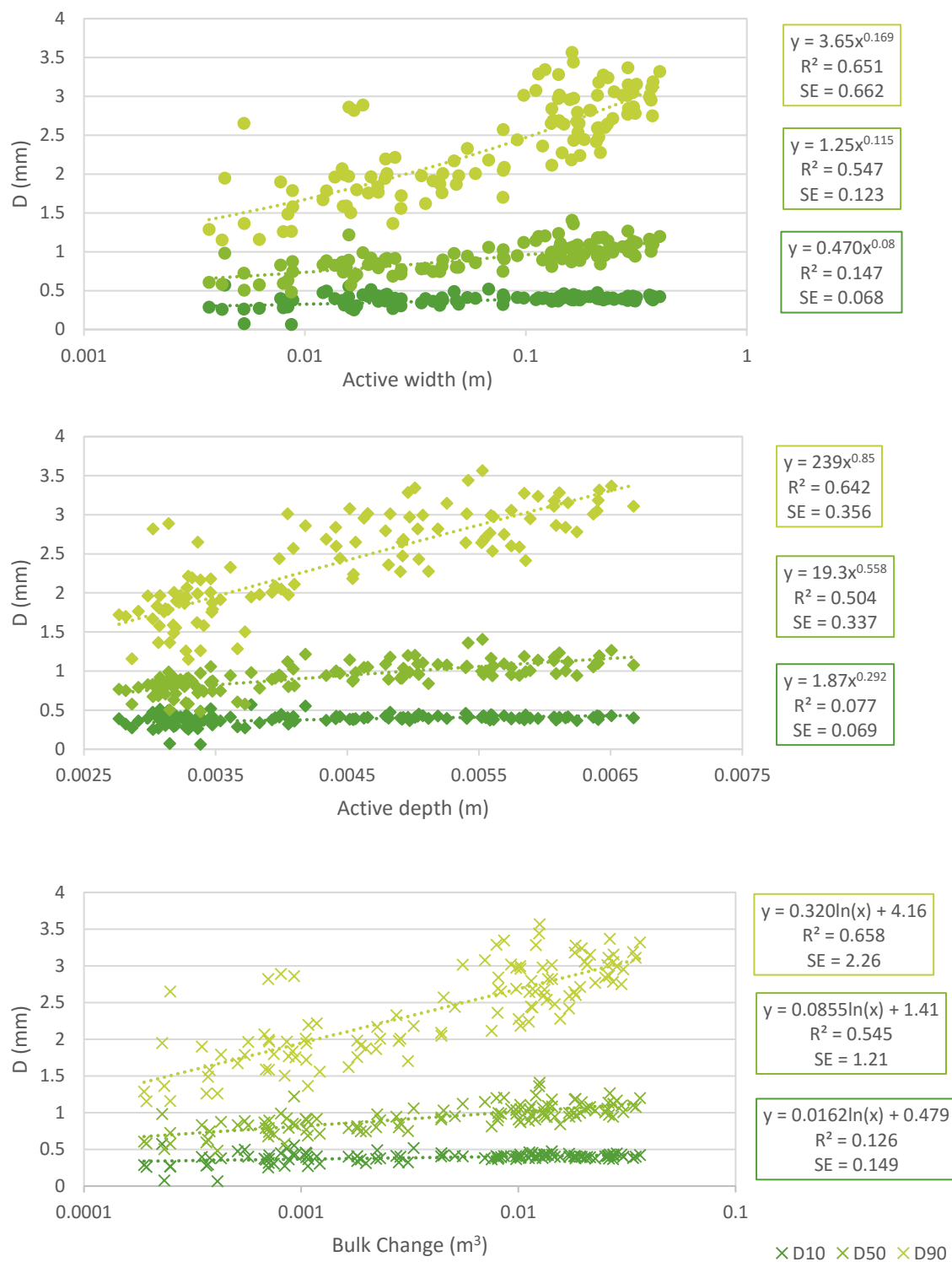
Figure 6.14 – D$_{10}$, D$_{50}$, and D$_{90}$ as a function of the active width, active depth, and bulk change in the hydrograph experiments.

6.4 Discussion

Results from the constant discharge experiments suggest that grain size distributions can be variable, even under constant channel-forming discharges. This is likely the result of local changes in bed shear stress and the active width. In general, experiment 12 had finer grain size distributions than experiment 13 and the model subsurface. This highlights the dependence of bedload transport and grain size on total stream power, rather than strictly discharge. In addition, while both experiments had full mobilized fine grains (i.e., D_{10}), D_{50} and D_{90} rarely reached unity with the model subsurface, suggesting that coarse grains were immobile or only partially mobilized during specific experimental runs. As a result, while experiment 13 had several runs approaching equal mobility, it seems that both constant discharge experiments were selectively mobile (i.e., all available grains sizes were being transported, but not in proportion to availability). Venditti et al. (2015) suggested that most gravel-bed rivers are partial mobile, expect under high bankfull discharges when selective mobility can be achieved. The constant discharge experiments were run at channel-forming discharge which could explain why selective mobility was more common than might be expected in a natural gravel-bed river, where most flows are below channel-forming or bankfull discharges. An alternative explanation is that armouring may be less important under high stream power conditions (e.g., experiment 13), allowing for a greater area of the bed and active layer to be activated and for more grain sizes to be mobilized (Ashworth et al., 1992; Mueller & Pitlick, 2013).

Some of these trends were clearer during the hydrograph experiment, where D_{50} and D_{90} noticeably increased with increasing discharge and stream power. In a similar study done on a straight gravel-bed river in an ephemeral stream Powell et al. (2001) found that the grain size distribution of the bedload became coarser with increasing shear stress above the threshold for entrainment. In their study, however, which looked at D_{16}, D_{50} and D_{84}, they found that the grain size of all fractions increased with increasing shear stress before leveling off under high shear stress conditions, which was not found in the current study. The results from both the constant discharge and hydrograph experiments suggest that D_{10} is essentially constant (i.e., fully mobile at all discharges) while D_{50} and D_{90} both increase with discharge. In the hydrograph experiments, the increase in D_{50} with discharge levels

off at high discharges, but still shows a positive trend while approaching D_{50} of the model. This levelling off could indicate full mobilization of those fractions at high discharge (i.e., all grains in those size fractions are moving). D_{90} increased with discharge and did not level off, even at the channel-forming discharge of 2.1 l s^{-1}, although it approaches the model D_{90} in a few cases. This likely means that at low discharges the coarsest grains were immobile, and then became partially mobilized with increasing discharge but did not reach full mobility. It is possible that with discharges greater than 2.1 l s^{-1} that the coarse grains would become full mobilized, but those conditions were not addressed in this study.

Looking at the differences in the evolution of grain size distributions across the three hydrographs, it seems that a transition of bed mobility from partial mobility towards equal mobility was most clear in hydrograph A, but less clear in both hydrograph B and hydrograph C. This could reflect the increased number of discharge steps in hydrograph B and C, which allowed for more intermediate discharges and therefore more overlap in the already variable grain size distributions. Also, with more discharge steps and longer experimental run time, the morphology on the rising and falling limb of hydrograph B and C may have been substantially different enough to capture some of the variability in grain size distributions for the same discharge. Similarly, it was found that hydrograph B had the lowest average D_{90} of the three hydrographs, but that this could have been related to running 8 experimental runs at peak discharge rather than just the four of the other hydrographs. While there are currently not enough data to confirm this, it is possible that these results from hydrograph B reflect changes in morphology and antecedent conditions of the river. For example, as discharge was increased the sediment sizes available for transport also increased. Once the large surface grains were made mobile, however, there may have been less coarse grains immediately available for transport in the active areas of the bed. Therefore, these results could reflect temporal and/or spatial changes in sediment supply (Lane & Richards, 1997). By the time hydrograph C reached peak discharge hours later, the active areas of the channel had changed location. Alternatively, the surface texture and therefore the sediment supply would have been changed by the falling limb of hydrograph B and the subsequent rising limb of hydrograph C. The differences in the three hydrographs highlights the importance of sampling multiple hydrographs, even over a

similar morphology, to capture the variability in grain size distributions and antecedent conditions of flow and channel morphology.

To look more closely at the transition from partial through equal mobility, the total bedload transport rate was separated into the fractional transport rates for the different grain sizes. The largest grain sizes only became noticeable above the lower threshold of $1.14\,l\,s^{-1}$. This lower discharge threshold was also found in terms of detectable morphological change in Chapter 4. Therefore, it could represent the breakpoint discharge for this system, and indicate the shift from Phase I (full mobility of fine grains only) towards Phase II (coarse grains mobilized and bedload transport rates increase). Unlike Ryan et al. (2002) who found that breakpoint discharge could happen at discharges as high as 80 % of the bankfull discharge, $1.14\,l\,s^{-1}$ corresponds with ~54 % of the channel-forming discharge of $2.1\,l\,s^{-1}$. These results suggest that the modelled braided river existed in Phase II for the majority of the hydrograph discharges tested, and that the transition to Phase II corresponds with the lower threshold found for detectable morphological change. This type of investigation has not been clearly done for gravel-bed braided rivers, but highlights that they may behave differently than their single-thread counterparts in terms of fractional transport rates and bed mobility.

Investigating the mobility of the bed in terms of a *pi/fi* ratio, the results showed again that increasing discharge and stream power causes a transition from a general state of partial mobility (*pi/fi*=0), towards equal mobility (*pi/fi* = 1), although most of the experimental runs existed somewhere in-between in a state of selective mobility. Comparing the *pi/fi* graph to others from gravel-bed rivers, the overall trends are similar. Powell et al. (2001) found that the differences between the bedload grain size and that of the bed material decreased with increases in shear stress, but that the D_{84} did not change much beyond 4_X critical shear stress. They suggest that this result confirms size selective transport under low shear stress conditions and a shift towards equal mobility at high shear stresses.

While the relationships between bed mobility and morphological change have not been well researched in the past, there are a couple of notable exceptions. For example, Haschenburger & Wilcock (2003) tie changes in fractional transport rates, which are strongly linked to overall bed mobility, with what is essentially the expansion and

contraction of the active width. In a relatively straight gravel-bed channel, they found that fine grains were fully mobile, but that coarse grains were generally immobile or only partial mobile (i.e., some grains moving but not in proportion to their availability on the bed). In terms of channel morphology and bed mobility, Haschenburger & Wilcock (2003) found that areas associated with the thalweg would often be fully mobilized, while the surrounding area would be partially mobilized. In addition, in areas near the channel margins coarse grains were most likely to be immobile. As flow increased, the fully mobilized zone would expand from the thalweg into the partially mobile zones, while the partial mobile zone would expand to the channel margins. When flow reached bankfull discharges, Haschenburger & Wilcock, (2003) found that zones of partial transport were almost completely replaced with zones of full mobilization. In other terms, Haschenburger & Wilcock (2003) seem to be describing the expansion of the active width and deepening of the active depth with increasing discharge and stream power and the transition from partial to selective mobility of the bed. In their study, Haschenburger & Wilcock (2003) found that areas covered by immobile grains or areas with only partial transport could persist over time and for multiple years, indicating that true equal mobility would be rare. This is likely where the braided case is very different from straight and meandering channels. While Haschenburger & Wilcock (2003) suggest that this persistence of immobile grains has implications for the development of armouring, this research has already suggested that armouring may be less important in braided rivers and under high stream power conditions. Furthermore, research by Leduc et al. (2015) on the same flume used in this research found that the surface layer was similar to bulk distributions, supporting the idea that braided rivers lack strong armouring. In addition, examination of the DoDs from previous chapters shows that not only does the active area become more continuous with increasing stream power, but that braided morphology is constantly changing and therefore it is unlikely that large portions of the wetted area would remain immobile for long periods of time. Linking this back to bedload transport rates, Haschenburger & Wilcock (2003) found that bedload transport rates can be large, even under conditions of partial transport but that transport rates would still increase during full surface mobilization. Similar results were found in this research, where increasing discharge caused more grains and larger grains are being activated into the bedload.

In another study, Lisle (1995) looked at 13 gravel-bed rivers in the field covering a range of channel morphologies including a braided river. Plotting the ratio of D_{50} in the subsurface with the D_{50} of the bedload (D^*) against dimensionless stream power (here w^* is used) Lisle (1995) found a negative relationship, so that at higher stream power the bed was closer to equal mobility. The results of the current study show a similar trend defined by a strong negative power relationship (Figure 6.15). These results highlight that while equal mobility is not perfectly achieved in the hydrograph experiments (where $D^* = 1$), at higher discharges and therefore dimensionless stream powers, the system does approach equal mobility (~1.1) (Figure 6.15). Lisle (1995) suggested that in many cases, true equal mobility may not be achieved until several times the bankfull discharge has been achieved, which was not tested in this research. Lisle (1995) also suggested that the rivers closest to achieving equal mobility were laterally migrating braided rivers. Therefore, it may not be surprising that the braided rivers tested here were close to equal mobility, even at discharges below several times bankfull discharge.

$$y = 0.204x^{-0.792}$$
$$R^2 = 0.922$$
$$SE = 1.317$$
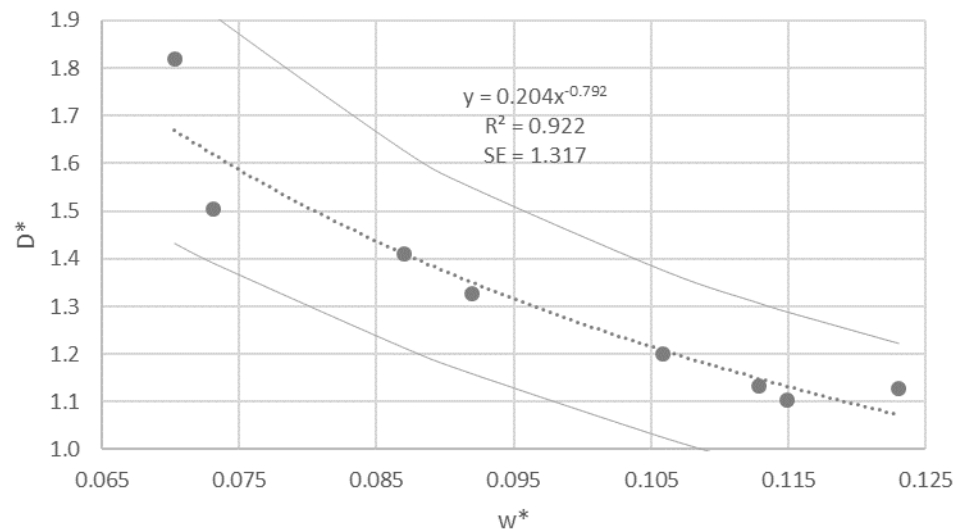
Figure 6.15 – The ratio of D_{50} in the subsurface to the D_{50} of the bedload (D^*) as a function of dimensionless stream power (w^*).

Lisle (1995) links his findings with the depth of scour and fill by suggesting that as stream power increases, the depth of scour (i.e., erosion) increases. Therefore, the active layer thickness, defined as the depth of bed incorporated into the bedload transport, increases with stream power so that bedload is entrained from greater and greater depths with

increasing dimensionless stream power. Figure 6.16 shows how different depths of change (e.g., depths of scour and fill) accounted for increasingly large areas with increasing discharge and therefore stream power for the hydrograph experiments. Under high discharges (>1.14 l s^{-1}), the depth of the active layer is well beyond the D_{90} of 3.5 mm so that all size fractions were available for transport (Figure 6.16 and Figure 6.17). Based on Lisle (1995) who suggested that equal mobility would require the active layer to be 8-10x the $D_{90,}$ it is possible that equal mobility can be achieved at, or close to, channel forming-discharges in gravel-bed braided rivers. While few runs achieved active depths greater than 28mm (8x D_{90}), depths greater than 24mm (7x D_{90}) were common above discharges of 1.65 l s^{-1}, again suggesting that this system was close to equal mobility at high discharges (Figure 6.17).
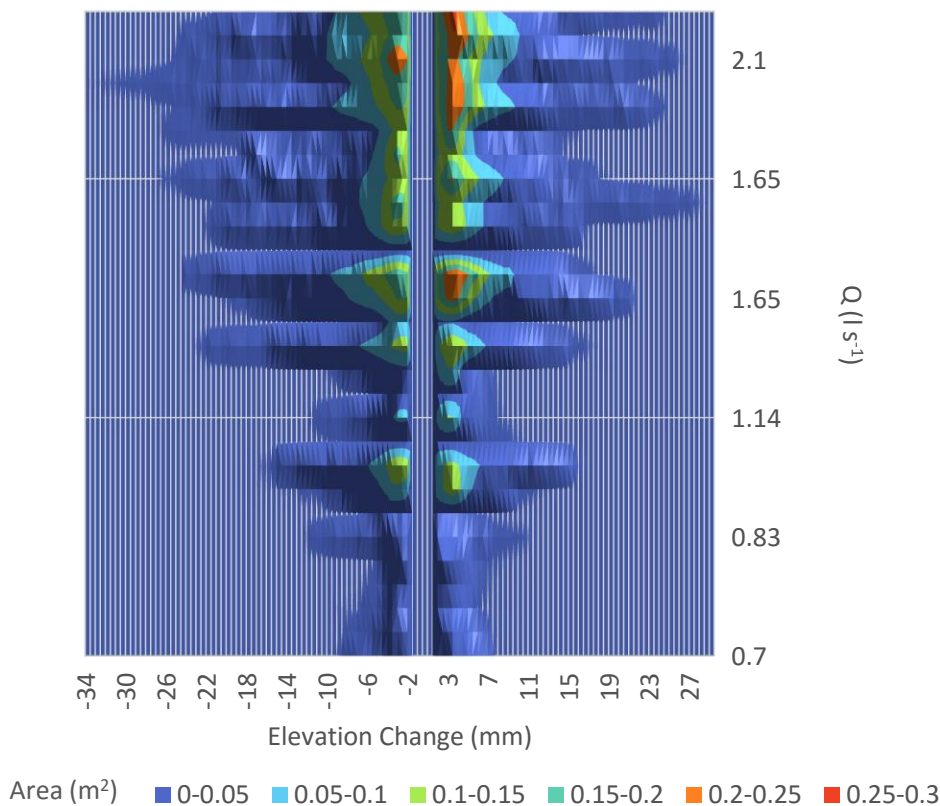
Figure 6.16 – The total active area covered by a range of elevation changes across the discharges (Q) used in the hydrograph experiments. Results shown were derived from the 2σ threshold.
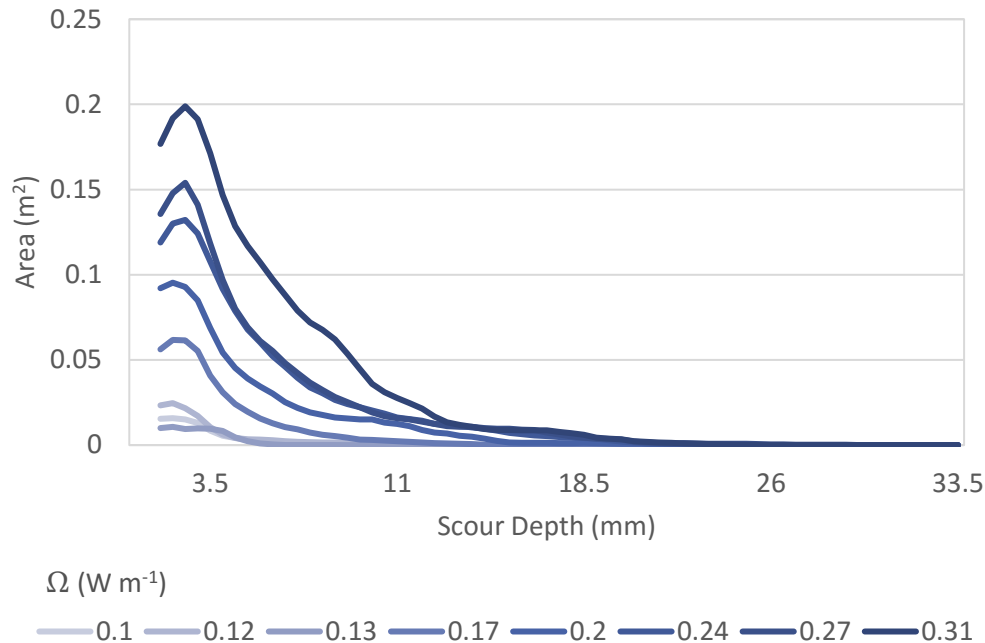
Figure 6.17 - Distribution of scour depths (erosion) as a function of total stream power (Ω). Results shown were derived using the 2σ threshold.

6.5 Summary and Conclusions

This chapter expands on the last two chapters by investigating the role of grain size distributions and their evolution with channel morphology and stream power. Overall, there are strong linkages between the thresholds for detectable morphological change, bedload transport rates, and coarse grain mobilization. The expansion and contraction of the active width, which is likely due to a lack of persistent armouring, is strongly related to the transition from a partially mobile bed towards equal mobility. Until now, there have been no studies, in the field or flume, that have been able to link channel morphology with grain size distributions in gravel-bed braided rivers in this way.

From these results the following conclusions are made:

- Fine grains were fully mobilized for all stream powers over three event hydrographs
- D_{50} and D_{90} can be highly variable, even under constant discharge conditions, but both tend to increase with stream power.
- Antecedent conditions may be important for determining the availability of grain sizes in the local sediment supply.

- While equal mobility is rarely achieved, these model braided rivers were generally selectively mobile and approached equal mobility at high discharges.

- The transition from Phase I to Phase II corresponds to the lower threshold of morphological change with a discharge of $1.14 \, l \, s^{-1}$ or dimensionless stream power of 0.08.

- The expansion of the active width and depth with increasing stream power is directly related to the mobilization of coarse grains as the active layer thickens, indicating that bedload size distributions are at least partially a function of channel morphodynamics.

- Braided rivers are likely different in bed mobility from their single-thread counterparts due to the lack of armouring and the lateral migration, allowing for active layers thickness up to 10x the size of D_{90}, rather than entrainment being limited to the surface and immediate subsurface.

- The results suggest that in a physical model of a braided river, armouring may be limited or non-existent, especially at high discharge and stream power.

Chapter 7

7 Summary and Conclusion

7.1 Overview

The purpose of this research was to contribute to current knowledge and understanding of the morphodynamics of gravel-bed braided rivers. Specifically, while there are clearly strong linkages between bedload transport and morphology in these spatially and temporally dynamic rivers, understanding of these linkages and the relation to other factors (e.g., channel hydraulics and bed-material mobility) in these river systems was incomplete. This was largely because bedload transport in braided rivers has been notoriously difficult to measure, either by direct sampling, or using hydraulically-based bedload formulae. As a result, and due to recent improvements in technology, the morphological method has provided an attractive alternative to traditional sampling and formulaic techniques for estimating bedload transport rates. In addition to inferring information about bedload transport from changes in topography and morphology, the morphological method allows for the investigation of spatial and temporal patterns of change not possible with other methods. In addition, given the ability to collect bedload from a physical model, this research further investigated the role of grain size fractional transport and bed mobility in braided rivers, which has not been done before.

This final chapter starts by summarizing the main results in terms of the original research objectives (Section 7.2). Next, there is a discussion about the possible contributions this research will have with respect to fundamental understanding as well as applied geomorphology and engineering (Section 7.3). Following this, Section 7.4 outlines some of the known research limitations of this research project along with ideas for future research prospects. The chapter (and thesis) ends with a few concluding statements.

7.2 Summary of Results

The goal of Chapter 4 was to address two main research objectives:

1. Quantify the morphological active width in a physical model over a range of gravel-bed river morphologies and characterize its relationship with wetted width, braiding indices, and dimensionless stream power over a range of flow conditions.
2. Characterize the relationship between the active width and bedload transport flux under channel forming conditions and variable discharge conditions

This chapter was based on results and analysis from 5 constant channel-forming discharge experiments as well as three event hydrograph experiments. The findings of this research confirm and extend previous work that found wetted width, braiding intensity, active braiding intensity, and the morphological active width all increase with increasing discharge and stream power (Ashmore & Sauks, 2006; Bertoldi et al., 2009a; Egozi & Ashmore, 2009). Measurements of bedload transport rate can be highly variable but in general increased with total stream power and dimensionless stream power (Ashmore, 1988; Bertoldi et al., 2009a). While there was substantial scatter, results from this research follow the general trends described by Bertoldi et al. (2009a) where active width as a proportion of the wetted width was positively correlated with dimensionless stream power and ABI. Novel contributions from this research include the characterization of the positive relationship between the morphological active width and measured bedload transport rates for both the constant discharge and hydrograph experiments.

In addition to these main results, it was found that the spatial distribution of the active area became more continuous and complex in terms of areas of erosion and deposition with increasing discharge and stream power. Furthermore, while the active depth was restricted to a relatively narrow range for the constant discharge experiments, it had a positive relationship with stream power in the hydrograph experiments. This could highlight differences between 'downstream' (i.e., constant channel-forming discharge experiments) and 'at-a-station' (i.e., event hydrograph) processes. Finally, based on the results of the hydrograph experiments, both morphological change and bedload transport rate share the same lower threshold for detection at a dimensionless stream power around 0.08 (1.14 l s⁻

[1]). This research is the first of its kind to illustrate the direct linkages between active width, bedload transport, and stream power both spatially and temporally for gravel-bed braided rivers.

Chapter 5 addressed the following objectives:

3. Calculate the morphological sediment budget for multi-thread gravel-bed rivers over a range of discharge and stream power conditions with a known sediment output and under the minimum budget conditions

4. Investigate the spatial and temporal dynamics of sediment transport in experimental gravel-bed braided rivers using morphological methods

As predicted, bedload transport rate was highly variable, both spatially and temporally. Likewise, volumes of erosion and deposition were spatially and temporally variable, but in general, similar in magnitude. Consequently, the total net change across all of the constant discharge experiments was low (-0.001- 0 m^3). The tendency for net change to be slightly negative could be related to a combination of morphodynamic processes and measurement techniques. For instance, areas of erosion may experience greater magnitudes of change than areas of deposition, and therefore are more likely to be detected during DoD differencing and subsequent thresholding (Rumsby et al., 2008; Wheaton et al., 2009). Also, morphological estimates of path lengths were reasonable with respect to previous findings from tracers, and similar across all the braided constant discharge experiments. This supports the general idea that morphology is determined by the movement of individual grains which are themselves influenced by the local morphology (Pyrce & Ashmore, 2003b; Kasprak et al., 2015).

Two morphological budgets were calculated, one based on the known bedload transport rate at the downstream end of the flume, and the other based on the assumptions of the minimum budget. Overall, the morphological budget provided reasonable estimates of bedload transport rates once propagated across 14 subsections of the study reach. The results suggest that while variable, rates of bedload transport are similar at all 14 cross-sections including the measured flux at the downstream baskets. These strong similarities in the spatial and temporal variability in bedload transport flux indicates a morphologically-dominated system. While it was expected that the minimum budget

would underestimate bedload transport rates, this research was able to compare it to measured values and found that it significantly underestimated the budget for all experiments analyzed, which could have implications for applied geomorphology and engineering that often rely on such estimates.

Finally, it was found that the bulk change was strongly correlated between adjacent sections but that the strength of the relationships decayed with distance. This spatial persistence was less noticeable at higher stream powers, and while the exact cause for this is not known it could be due to the increased morphological complexity found at high stream power.

The results Chapter 6, investigated the following objectives:

5. Characterize the evolution of grain size distributions across three experimental hydrographs, including fractional transport rates.
6. Characterize the range of bed mobility conditions in terms of partial, selective or equal mobility for a range of stream power conditions.

Unlike any other study before it, this chapter linked channel morphology, hydraulics, grain size distributions, and bed mobility in gravel-bed braided rivers. It was found that D_{10} was relatively constant under all experimental conditions, suggesting that fine grains were always fully mobilized in the braided systems. D_{50} and D_{90} were strongly influenced by stream power in the hydrograph experiments, but no clear trends were found in the constant discharge experiments. Plotting the grain size distributions of the hydrograph experiment with the subsurface of the flume, it was found that increasing discharge and stream power caused a shift from partial mobility towards equal mobility as the bedload began to mimic the distribution of the bed subsurface. This special case of selective mobility is expected to be rare in gravel-bed rivers but seems to be common in the event hydrographs modelled here (Venditti et al., 2017). In addition, the differences in the mobility of different size fractions can be directly linked to the expansion and contraction of the morphological active width and the expansion of the active layer into greater depths of the bed (Lisle, 1995; Haschenburger & Wilcock, 2003). Both types of expansions are likely to be more common in braided rivers due to the apparent lack of armouring in these systems. Based on previous research the lack of armouring could the related to the relatively high stream

powers and the high rates of sediment supply commonly found in braided rivers, that prevent the establishment of a coarse armour layer (Lisle, 1995). The sediment supply and availability of a variety of grain sizes is constantly being replenished from lateral migration and the erosion of bars. The lower threshold for the fractional transport of coarse sediment was around 1.14 l s^{-1} or a dimensionless stream power of 0.08 which coincides with the threshold for significant bedload transport occurring and for measurable morphological active width and depth (Chapter 4). This threshold also separates Phase I from Phase II transport, suggesting a strong link between channel morphology, bedload transport rate, and bed mobility.

7.3 Contributions

This research contributes to the larger goal of understanding the processes driving channel morphology, hydraulics, and bedload transport in gravel-bed braided rivers. For instance, the active width was already shown to have a strong relationship with hydraulic and morphologic parameters, but these relationships had not been adequately investigated. This research extended previous research that suggested active width could be predicted from simple hydraulic parameters (e.g., discharge, slope, grain size, and active braiding intensity) based on an extensive dataset across a range of stream power (Bertoldi et al., 2009a; Ashmore et al., 2011). Additionally, this research confirmed that the active width is related to bedload transport rates, which had not been characterized in previous research, and that both are highly variable spatially and temporally. A better understanding of the active width can now be used in river assessment as a general predictor of bulk change, active depth, and bedload transport rates in a given river. In addition, due to the relatively strong relationship with active braiding intensity (ABI), it might be possible to estimate the reach averaged-active width from field photos, where ABI can be estimated as a function of wetted width and braiding intensity. Therefore, the active width serves as a direct link between morphological change, bedload transport, and channel hydraulics. In response to increased stream power, the active width expands and becomes more continuous within active channels. As a result, bedload transport rates increase (i.e., Phase II flow) and in braided rivers, which seem to lack extensive armouring, this also results in a transition towards equal mobility as all the grains in the active layer are mobilized. Finally, given the

strong relationship between bedload transport and morphology, most of the particles that are mobilized will be transported and deposited on the next downstream bar (Pyrce & Ashmore, 2003b; Kasprak et al., 2015). Therefore, the active width serves as an indicator of bed stability, bedload transport rates, and rates of morphological change. Furthermore, the active width itself could be at least estimated from simple hydraulic and morphological parameters such as the active braiding intensity, wetted width, and total stream power (Ashmore et al., 2011).

One of the unexpected discoveries in this research was that the lower threshold for morphological change corresponded with the transition from Phase I (i.e., partial mobility) to Phase II flow (i.e., selective mobility). The importance of this discovery is that it confirms the fundamental linkages between morphological change and bedload transport. Below this threshold, there was no detectable morphological change and bedload transport was essentially negligible and restricted to fine particles only. Above this threshold, morphological change, bedload transport, and the fractional transport of coarse grains all increased with stream power. If such a threshold could be found in real rivers, it would have meaningful implications for classifying the stability of river systems, as well as the ecological functioning. While ecological considerations were not part of the current study, Haschenburger & Wilcock (2003) highlighted the importance of knowing the fractional transport rates of different grain sizes for the maintenance of benthic invertebrate habitats in gravel-bed rivers.

In addition to the main results, this research highlights the importance of experimental geomorphology and physical modelling for exploratory and confirmatory research. The data collected, with respect to the active width, bedload transport, and grain-size distributions would have been impossible in the field due to the challenges in collecting spatially continuous DEMs of braided gravel-bed river topography, and the notorious challenges with at-a-point sampling of bedload transport in the field. This research also confirmed that the use of close-range digital photogrammetry is effective for capturing channel topography at small spatial and temporal resolutions and that DEM differencing is an effective way to apply the morphological method to complex river systems. Furthermore, the control over the channel-forming discharge and stream power allowed for

a wide range of conditions to be investigated at a high spatial and temporal resolution. Additionally, given the ability to investigate the role of constant and variable discharge, this research has effectively characterized the differences in active width and depth for downstream and at-a-station conditions.

Beyond academic contributions, the knowledge gained from this research is expected to have many practical applications that will directly benefit geomorphologists, engineers, river managers and conservation authorities, and ecologists. Specifically, measurements of the wetted width and braiding intensity could be used to estimate active braiding intensity and the active width, both of which are positively related to bedload transport rates. While these would only provide estimates of bedload transport rates, the morphological method is in general less expensive, time-consuming and labour intensive than hydraulics-based methods or direct sampling in the field (McLean & Church, 1999). The focus on remote sensing or photogrammetric techniques could limit the time spent in the field, the number of personnel required, and the dangers of wading in rivers (McLean & Church, 1999). This method will be especially useful in larger rivers, including braided rivers, and remote areas where traditional field methods are impractical and numerical models still need improvement (Ashmore & Church, 1998). The morphological method also has the advantage of not needing hydraulic measurements that are difficult to measure such as local shear stress and near-bed velocity. Finally, remote sensing techniques make it possible to monitor large areas remotely and over time, providing insight into patterns of spatial variation and long-term processes.

The management of braided rivers can be generally classified into two main categories 1) reduce braiding for the protection of infrastructure or resources; 2) promote braiding for the restoration of hydrological ecological functioning (Piegay et al., 2006). Traditionally, to reduce braiding and flooding, gravel was extracted from the river to promote narrowing and incising of the channel. Unfortunately, excessive gravel extraction can have detrimental impacts on local infrastructure and ecological functioning. On the other hand, to promote or restore braiding, sediment is injected into the system. Both of these management strategies would benefit from knowledge on river evolution over time as well as estimates of bedload transport yields (Piegay et al., 2006). This is a good example of

how the morphological method can use historical maps and aerial photos to help inform best management practices.

Additionally, while many rivers in the world do not have gauging stations or active monitoring programs, there are large datasets of aerial photographs that are being under-utilized (McLean & Church, 1999) With clearer understandings of the linkages between morphology, hydraulics, and bedload transport it will possible to apply morphological methods to historical photographs, which can be used to quantify changing river morphology (Bakker & Lane, 2017). For example, it may be possible to describe how the active width or the prevailing sediment budget has changed over time. The advantage is that the historical images can provide information in areas where no other data is available while also providing a long-term dataset of river morphology change (McLean & Church, 1999). This could shed light on the impacts of land-use change, direct human interventions and in some areas, the success of restoration efforts.

Finally, this data will have direct contributions to improving the numerical modelling of gravel-bed braided rivers. One of the fundamental outcomes of this research is the >500 DEMs of braided river evolution that could be used in numerical modelling. In addition, a clearer understanding of morphologically driven transport is expected to improve numerical model predictions of bedload transport rates, especially over long-term channel evolution. Furthermore, information on fractional transport rates could prove invaluable to validate and refine numerical models (Brasington & Smart, 2003; Williams et al., 2016). With improved numerical models, it will be possible to investigate many questions that cannot be easily tackled in the field or flume, including scale invariance, self-organization, and long-term evolution (Brasington & Smart, 2003)

7.4 Limitations and Future Research Questions

This research is one of the most extensive of its kind, opening up the possibilities for many other research projects and questions to be answered. In some cases, this will involve improving on methods and techniques used in this research, or to expand on the data collected here for a more complete dataset. For example, two complete experiments were abandoned during early processing due to poor image quality and subsequent poor DEM

quality. The morphological method is very sensitive to data quality; therefore, more research should be done to investigate ways to improve SfM digital photogrammetry data collection. Some of the improvements made over the course of this research included extensive quality control (i.e., visually inspect photo quality at the end of each run), redundant coded targets and target checking as well as introducing two photo surveys of each surface. Additionally, it would be helpful to recreate the conditions of experiment 8 which was run at a constant channel-forming discharge of 1.14 l s^{-1}. As mentioned, this discharge was important for morphological change and bedload transport rates in the physical model based on the hydrograph experiments and therefore a recreation of this experiment would allow for a deeper investigation into that possible threshold of braiding morphodynamics.

Three experiments, experiments 9, 12, and 13, interacted with the flume edges. While this is largely unavoidable due to the self-forming nature of the channel morphologies, this effect is undesirable because of the possible implication on bedload transport rates and the evolution of channel morphology. Ideally, similar experiments could be done on a larger flume, where edge effects can be avoided.

The current research was done using a single grain size distribution scaled down from the Sunwapta River in Alberta, Canada. It would be interesting to see if the findings of this research were consistent for other grain size distributions. For example, it is expected that a bed of coarser grains and low sediment supply might promote armouring more than the current model, but these differences have not yet been investigated. Furthermore, the current research did not consider the surface grain size distribution specifically, but relied on the subsurface as a surrogate. Future research should look at the surface for a more detailed look at the linkages between surface armouring and the expansion of the active width and active depth spatially and temporally.

Estimates of path length in this study were based on morphological estimates of volumes of erosion and known bedload transport rates. While the values found were reasonable based on previous research, path length in braided rivers should be investigated used more extensive tracer studies, across a range of stream powers. This would extend the work of Kasprak et al., (2015) and help confirm that the variability in path length for a given

morphology is relatively limited and strongly linked to morphology (Ashmore & Church, 1998). Furthermore, tracer research could be extended to look at fractional transport rates to help provide additional insights into the morphological differences in Phase I and Phase II flow. Finally, some of the spatial correlations found in this research should be investigated in more detail. For example, the exact reason for the spatial decay in the correlation of bulk change between sections is not known, but seems to be related to morphology.

This dataset directly compared two different DoD thresholding methods, the classic simple threshold based on the standard deviation of the vertical error, and the dilation method which tried to account for neighbouring cells to create a more continuous active area. The simple thresholding method is commonly used in the literature, where some measure of DoD uncertainty (here, the 2σ of the vertical error) is used to create a minimum level of detection (LOD) (Wheaton et al., 2009). The literature has also shown that estimates of morphological change are highly sensitive to the chosen threshold, and therefore care must be taken in choosing a threshold that preserves the maximum amount of 'real' data while eliminating data noise. Wheaton et al. (2010) proposed that while the simple threshold is easy to apply it does not account for that fact that vertical error is not spatially uniform. As a result, more 'real' data can be preserved if the LOD is spatially varied to accommodate differences in elevation uncertainty. In their research, Wheaton et al. (2010) found that areas on the Feshie River with steep banks and high surface roughness were associated with higher elevation uncertainty than areas that were relatively flat and smooth. While Wheaton et al. (2010) used the principles of fuzzy modelling to manage their DoDs, here a dilation method was used which resulted in more continuous active areas in the DoDs. The purpose of including both thresholds was not to promote the use of one over the other, but simply to compare the differences between the methods throughout the data analysis stage. Overall, the dilation method resulted in significantly greater estimates of active width in both the constant and hydrograph experiments compared to the simple thresholding method. In terms of the active depth, the dilation method provided lower estimates than the simple thresholding method, but the differences were only significant for the hydrograph experiments. Moving into net change and subsequent morphological sediment budgeting, the two methods were not significantly different for the constant

discharge experiments. There also seemed to be greater agreement between the methods with increases in volumes of change, supporting the idea that the morphological method is ideally used in areas where change is greater than the uncertainty in the measurements. Based on these results, it is not clear if one method is better than another, but it seems both could appropriately be used for morphological budgeting. Additional research should investigate the implications of data lost between the two methods.

Building on the current research, additional work should be done on the changes in bed mobility for constant discharge experiments. The research here was limited by few samples taken at lower discharges, but it would be helpful to confirm the overall trends found in the hydrographs over a range of discharges. Similarly, additional hydrograph experiments should be done to further investigate the impacts of antecedent conditions, the number of discharge steps, and finally the changes in bed mobility with discharges above bankfull. Ryan et al. (2002) suggested that there may be a second breakpoint discharge when mobility changes, but since this likely occurs well above bankfull discharge, that second breakpoint was not investigated in this research.

Finally, while Froude-scale modelling has been used successfully in the past to measure and monitor gravel-bed braided river processes, it is important to validate model findings with field data. There are many ways model and prototype similarity can be verified but in general methods can be categorized into comparisons of form or comparisons of process. Comparisons of form include visual comparison of channel planform and braiding intensity, cross-section geometry, and long profile characteristics (Young & Warburton, 1996; Paola et al., 2009). Similarity of process usually relies on the comparison of non-dimensional parameters related to channel hydraulics and sediment transport (i.e., Froude-scale modelling). Additional process comparisons are relatively challenging because in many cases equivalent prototype data is unavailable (e.g., bedload transport rates) (Young & Warburton, 1996). While previous research has found that Froude-scaled models of braided rivers are qualitatively and quantitatively similar to their field prototypes, additional verification of this dataset is needed if the findings of this research are to be used for geomorphological and engineering applications (Paola et al., 2009). One possible approach would be to compare the rates and magnitudes of morphological change (i.e.,

active areas and active depths) in an experimental river to the rates and magnitudes of change the prototype (Sapozhnikov & Foufoula-Georgiou, 1997; Paola et al., 2009). While this comparison would have been challenging in the past, new techniques for capturing river topography are making it increasingly possible to collect high-resolutions DEMs at greater temporally frequencies in the field (Brasington et al., 2003; Picco et al., 2013; Wheaton et al., 2013). The main challenge to collecting a spatially continuous DEM in the field is achieving detailed elevation information in wetted areas. Therefore, while not the focus on the current analyses, future analyses should compare measurements of planform change (i.e., rate and magnitude) between the model and the prototype river.

7.5 Concluding Statements

The research presented in this thesis has confirmed and extended previous research while also making several novel contributions to the study of gravel-bed braided river morphodynamics. In terms of the dataset, the data collected for this research represents one of the largest and most comprehensive of its kind. Few studies have ever reported so many digital elevation models and DEMs of difference being created over such short time-intervals or over a range of channel morphologies. In addition to the extensive dataset on the model's surface topography, bedload transport measurements were made for each experimental run covering the same temporal interval as the DoDs. This dataset alone will be valuable to other researchers, including numerical modellers, for investigating additional questions on channel morphodynamics and bedload transport processes.

Overall, the results highlight some of the fundamental linkages between channel morphology, bedload transport processes, and evolution in bed mobility. All of the results support the idea that even chaotic looking braided rivers have systematic behaviour like their single-threaded counterparts but that they have unique attributes as a function of their intrinsically complex morphodynamics.

References

Ashmore, P. (1988). Bed load transport in braided gravel-bed stream models. *Earth Surface Processes and Landforms*, *13*(8), 677–695. https://doi.org/10.1002/esp.3290130803

Ashmore, P. (1991a). Channel Morphology and Bed Load Pulses in Braided, Gravel-Bed Streams. *Geografiska Annaler. Series A, Physical Geography*, *73*(1), 37. https://doi.org/10.2307/521212

Ashmore, P. (1991b). How do gravel-bed rivers braid? *Canadian Journal of Earth Sciences*, *28*(3), 326–341. https://doi.org/10.1139/e91-030

Ashmore, P. (1993). Anabranch confluence kinetics and sedimentation processes in gravel-braided streams. *Geological Society, London, Special Publications*, *75*(1), 129–146. https://doi.org/10.1144/GSL.SP.1993.075.01.08

Ashmore, P. (2007). Laboratory modelling of gravel braided stream morphology. *Earth Surface Processes and Landforms*, *7*(3), 201–225. https://doi.org/10.1002/esp.3290070301

Ashmore, P. (2009). Intensity and characteristic length of braided channel patterns. *Canadian Journal of Civil Engineering*, *36*, 1656–1666. https://doi.org/10.1139/L09-088

Ashmore, P. (2013). Morphology and Dynamics of Braided Rivers. In J. Shroder & E. Wohl (Eds.), *Treatise on Geomorphology* (pp. 289–312). San Diego: Elsevier. https://doi.org/10.1016/B978-0-12-374739-6.00242-6

Ashmore, P., Bertoldi, W., Tobias Gardner, J., & Gardner, J. T. (2011). Active width of gravel-bed braided rivers. *Earth Surface Processes and Landforms*, *36*(11), 1510–1521. https://doi.org/10.1002/esp.2182

Ashmore, P., & Church, M. (1998). Sediment transport and river morphology: a paradigm for study. In *Gravel-Bed Rivers in the Environment* (pp. 115–148).

Ashmore, P., & Gardner, J. T. (2008). Unconfined Confluences as Elements of Braided River Morphology. In S. P. Rice, A. G. Roy, & B. L. Rhoads (Eds.), *River Confluences, Tributaries and the Fluvial Network* (pp. 119–143). John Wiley & Sons Ltd.

Ashmore, P., & Sauks, E. (2006). Prediction of discharge from water surface width in a braided river with implications for at-a-station hydraulic geometry. *Water Resources Research*, *42*(3), 1–11. https://doi.org/10.1029/2005WR003993

Ashworth, P. J., & Ferguson, R. I. (1986). Interrelationships of Channel Processes, Changes and Sediments in a Proglacial Braided River. *Geografiska Annaler. Series A, Physical Geography*, *68*(4), 361. https://doi.org/10.2307/521527

Ashworth, P. J., Ferguson, R. I., Ashmore, P., Paola, C., Powell, D. M., Prestegaard, K. L., & Prestegaards, K. L. (1992). Measurements in a Braided River chute and lobe:

2. Sorting of bed load during entrainment, transport, and deposition. *Water Resources Research*, *28*(7), 1887–1896. https://doi.org/10.1029/92WR00702

Bakker, M., & Lane, S. N. (2017). Archival photogrammetric analysis of river–floodplain systems using Structure from Motion (SfM) methods. *Earth Surface Processes and Landforms*, *42*(8), 1274–1286. https://doi.org/10.1002/esp.4085

Bennett, S. J., Ashmore, P., & Neuman, C. M. (2015). Transformative geomorphic research using laboratory experimentation. *Geomorphology*, *244*, 1–8. https://doi.org/10.1016/j.geomorph.2014.11.002

Bertoldi, W., Ashmore, P., & Tubino, M. (2009a). A method for estimating the mean bed load flux in braided rivers. *Geomorphology*, *103*(3), 330–340. https://doi.org/10.1016/j.geomorph.2008.06.014

Bertoldi, W., Zanoni, L., & Tubino, M. (2009b). Planform dynamics of braided streams. *Earth Surface Processes and Landforms*, *34*(4), 547–557. https://doi.org/10.1002/esp

Blott, S. (2000). Gradistat Version 8.0. Kenneth Pye Associates Ltd.

Brasington, J., Langham, J. A., & Rumsby, B. T. (2003). Methodological sensitivity of morphometric estimates of coarse fluvial sediment transport. *Geomorphology*, *53*(3–4), 299–316. https://doi.org/10.1016/S0169-555X(02)00320-3

Brasington, J., & Smart, R. M. A. (2003). Close range digital photogrammetric analysis of experimental drainage basin evolution. *Earth Surface Processes and Landforms*, *28*(3), 231–247. https://doi.org/10.1002/esp.480

Brewer, P. A., & Passmore, D. G. (2002). Sediment budgeting techniques in gravel-bed rivers. *Geological Society, London, Special Publications*, *191*(1), 97–113. https://doi.org/10.1144/GSL.SP.2002.191.01.07

Bristow, C. S., & Best, J. L. (1993). Braided rivers: perspectives and problems. *Geological Society, London, Special Publications*, *75*(1), 1–11. https://doi.org/10.1144/GSL.SP.1993.075.01.01

Buffington, J. M. (2012). Changes in Channel Morphology Over Human Time Scales. In M. Church, P. Biron, & A. Roy (Eds.), *Gravel-Bed Rivers* (pp. 433–463). Chichester, UK: John Wiley & Sons, Ltd. https://doi.org/10.1002/9781119952497.ch32

Bunte, K., & Abt, S. R. (2001). Summary for Policymakers. In Intergovernmental Panel on Climate Change (Ed.), *Climate Change 2013 - The Physical Science Basis* (pp. 1–30). Cambridge: Cambridge University Press. https://doi.org/10.1017/CBO9781107415324.004

Chandler, J. (1999). Effective application of automated digital photogrammetry for geomorphological research. *Earth Surface Processes and Landforms*, *24*(1), 51–63. https://doi.org/10.1002/(SICI)1096-9837(199901)24:1<51::AID-ESP948>3.0.CO;2-H

Charlton, R. (2008). *Fundamentals of Fluvial Geomorphology*. Oxon: Routledge.

Chew, L. C., & Ashmore, P. (2001). Channel adjustment and a test of rational regime theory in a proglacial braided stream. *Geomorphology*, *37*(1–2), 43–63. https://doi.org/10.1016/S0169-555X(00)00062-3

Church, M. (2006). Bed Material Transport and the Morphology of Alluvial River Channels. *Annual Review of Earth and Planetary Sciences*, *34*(1), 325–354. https://doi.org/10.1146/annurev.earth.33.092203.122721

Church, M. (2011). *Observations and Experiments*. (K. J. Gregory & A. S. Goudie, Eds.), *The SAGE Handbook of Geomorphology*. 1 Oliver's Yard, 55 City Road, London EC1Y 1SP United Kingdom: SAGE Publications Ltd. https://doi.org/10.4135/9781446201053

Church, M., & Haschenburger, J. K. (2017). What is the "active layer"? *Water Resources Research*, *53*(1), 5–10. https://doi.org/10.1002/2016WR019675

Dingman, S. L. (2009). *Fluvial Hydraulics*. New York: Oxford University Press.

Diplas, P., Kuhnle, R., Gray, J., Glysson, D., & Edwards, T. (2008). Sediment Transport Measurements. In M. Gracia (Ed.), *Sedimentation Engineering* (pp. 307–353). Reston, VA: American Society of Civil Engineers. https://doi.org/10.1061/9780784408148.ch05

Doeschl, A. B., Ashmore, P., & Davison, M. (2006). Methods for Assessing Exploratory Computational Models of Braided Rivers. In *Braided Rivers: Process, Deposits, Ecology and Management* (pp. 177–197). Oxford, UK: Blackwell Publishing Ltd. https://doi.org/10.1002/9781444304374.ch8

Egozi, R., & Ashmore, P. (2008). Defining and measuring braiding intensity. *Earth Surface Processes and Landforms*, *33*(14), 2121–2138. https://doi.org/10.1002/esp.1658

Egozi, R., & Ashmore, P. (2009). Experimental analysis of braided channel pattern response to increased discharge. *Journal of Geophysical Research*, *114*(F2), F02012. https://doi.org/10.1029/2008JF001099

Ferguson, R. I. (1986). Hydraulics and hydraulic geometry. *Progress in Physical Geography*, *10*(1), 1–31. https://doi.org/10.1177/030913338601000101

Ferguson, R. I. (1993). Understanding braiding processes in gravel-bed rivers: progress and unsolved problems. *Geological Society, London, Special Publications*, *75*(1), 73–87. https://doi.org/10.1144/GSL.SP.1993.075.01.03

Ferguson, R. I., Ashmore, P., Ashworth, P. J., Paola, C., & Prestegaard, K. L. (1992). Measurements in a Braided River chute and lobe: 1. Flow pattern, sediment transport, and channel change. *Water Resources Research*, *28*(7), 1877–1886. https://doi.org/10.1029/92WR00700

Fonstad, M. A., Dietrich, J. T., Courville, B. C., Jensen, J. L., & Carbonneau, P. E. (2013). Topographic structure from motion: a new development in photogrammetric

measurement. *Earth Surface Processes and Landforms*, *38*(4), 421–430. https://doi.org/10.1002/esp.3366

Gardner, J. T., & Ashmore, P. (2011). Geometry and grain-size characteristics of the basal surface of a braided river deposit. *Geology*, *39*(3), 247–250. https://doi.org/10.1130/G31639.1

Goff, J. R., & Ashmore, P. (1994). Gravel Transport and Morphological Change in Braided Sunwapta River, Alberta, Canada. *Earth Surface Processes and Landforms*, *19*(3), 195–212. https://doi.org/10.1002/esp.3290190302

Gomez, B. (1991). Bedload transport. *Earth-Science Reviews*, *31*(2), 89–132. https://doi.org/10.1016/0012-8252(91)90017-A

Gurnell, A. M., Bertoldi, W., & Corenblit, D. (2012). Changing river channels: The roles of hydrological processes, plants and pioneer fluvial landforms in humid temperate, mixed load, gravel bed rivers. *Earth-Science Reviews*, *111*(1–2), 129–141. https://doi.org/10.1016/j.earscirev.2011.11.005

Haschenburger, J. K. (2013). Bedload Kinematics and Fluxes. In J. Shroder & E. Wohl (Eds.), *Treatise on Geomorphology* (pp. 103–123). San Diego: Academic Press.

Haschenburger, J. K., & Church, M. (1998). Bed material transport estimated from the virtual velocity of sediment. *Earth Surface Processes and Landforms*, *23*(9), 791–808. https://doi.org/10.1002/(SICI)1096-9837(199809)23:9<791::AID-ESP888>3.0.CO;2-X

Haschenburger, J. K., & Wilcock, P. R. (2003). Partial transport in a natural gravel bed channel. *Water Resources Research*, *39*(1), 1–9. https://doi.org/10.1029/2002WR001532

Head, K. (2006). *Manual of Soil Laboratory Testing* (3rd ed.). Scotland, UK: Whittles Publishing.

Hicks, D. M., Duncan M.J., Lane, S. N., Tal, M., & Westaway, R. M. (2008). Contemporary morphological change in braided gravel-bed rivers: new developments from field and laboratory studies, with particular reference to the influence of riparian vegetation. In H. Habersack, H. Piégay, & M. Rinaldi (Eds.), *Gravel-Bed Rivers VI: From Process Understanding to River Restoration* (pp. 557–586). Elsevier B.V.

Hoey, T. (1992). Temporal variations in bedload transport rates and sediment storage in gravel-bed rivers. *Progress in Physical Geography*, *16*(3), 319–338. https://doi.org/10.1177/030913339201600303

Hoey, T. B., & Sutherland, A. J. (1991). Channel morphology and bedload pulses in braided rivers: a laboratory study. *Earth Surface Processes and Landforms*, *16*(5), 447–462. https://doi.org/10.1002/esp.3290160506

Hundey, E. J., & Ashmore, P. (2009). Length scale of braided river morphology. *Water Resources Research*, *45*(8), 1–9. https://doi.org/10.1029/2008WR007521

James, L. A., Hodgson, M. E., Ghoshal, S., & Latiolais, M. M. (2012). Geomorphic change detection using historic maps and DEM differencing: The temporal dimension of geospatial analysis. *Geomorphology*, *137*(1), 181–198. https://doi.org/10.1016/j.geomorph.2010.10.039

Kasprak, A., Wheaton, J. M., Ashmore, P., Hensleigh, J. W., & Peirce, S. (2015). The relationship between particle travel distance and channel morphology: Results from physical models of braided rivers. *Journal of Geophysical Research: Earth Surface*, *120*(1), 55–74. https://doi.org/10.1002/2014JF003310

Kleinhans, M. G. (2010). Sorting out river channel patterns. *Progress in Physical Geography*, *34*(3), 287–326. https://doi.org/10.1177/0309133310365300

Kleinhans, M. G., & van den Berg, J. H. (2011). River channel and bar patterns explained and predicted by an empirical and a physics-based method. *Earth Surface Processes and Landforms*, *36*(6), 721–738. https://doi.org/10.1002/esp.2090

Lane, S. N. (1995). The Dynamics of Dynamic River Channels. *Geography*, *80*(2), 147–162. https://doi.org/10.1007/sl0869-009-9117-l

Lane, S. N. (2000). The Measurement of River Channel Morphology Using Digital Photogrammetry. *The Photogrammetric Record*, *16*(96), 937–961. https://doi.org/10.1111/0031-868X.00159

Lane, S. N., & Richards, K. S. (1997). Linking River Channel Form and Process : Time , Space and Causality Revisited, *22*, 249–260.

Leduc, P., Ashmore, P., & Gardner, J. T. (2015). Grain sorting in the morphological active layer of a braided river physical model. *Earth Surface Dynamics*, *3*(4), 577–585. https://doi.org/10.5194/esurf-3-577-2015

Lindsay, J. B., & Ashmore, P. (2002). The effects of survey frequency on estimates of scour and fill in a braided river model. *Earth Surface Processes and Landforms*, *27*(1), 27–43. https://doi.org/10.1002/esp.282

Lisle, T. E. (1995). Particle Size Variations Between Bed Load and Bed Material in Natural Gravel Bed Channels. *Water Resources Research*, *31*(4), 1107–1118. https://doi.org/10.1029/94WR02526

Martin, Y., & Church, M. (1995). Bed-material transport estimated from channel surveys: Vedder River, British Columbia. *Earth Surface Processes and Landforms*, *20*(4), 347–361. https://doi.org/10.1002/esp.3290200405

McKenna Neuman, C., Ashmore, P., & Bennett, S. J. (2013). 1.17 Laboratory and Experimental Geomorphology: Examples from Fluvial and Aeolian Systems. In *Treatise on Geomorphology* (Vol. 1, pp. 325–348). Elsevier. https://doi.org/10.1016/B978-0-12-374739-6.00017-8

McLean, D. G., & Church, M. (1999). Sediment transport along lower Fraser River: 2. Estimates based on the long-term gravel budget. *Water Resources Research*, *35*(8), 2549–2559. https://doi.org/10.1029/1999WR900102

Metivier, F., & Meunier, P. (2003). Input and output mass flux correlations in an experimental braided stream. Implications on the dynamics of bed load transport. *Journal of Hydrology*, *271*(1–4), 22–38. https://doi.org/10.1016/S0022-1694(02)00312-8

Morgan, J. A., Brogan, D. J., & Nelson, P. A. (2016). Application of Structure-from-Motion photogrammetry in laboratory flumes. *Geomorphology*, *276*, 125–143. https://doi.org/10.1016/j.geomorph.2016.10.021

Mosley, M. P., & Zimpfer, G. L. (1978). Hardware models in geomorphology. *Progress in Physical Geography*, *2*(3), 438–461. https://doi.org/10.1177/030913337800200303

Mueller, E. R., & Pitlick, J. (2013). Sediment supply and channel morphology in mountain river systems: 1. Relative importance of lithology, topography, and climate. *Journal of Geophysical Research: Earth Surface*, *118*(4), 2325–2342. https://doi.org/10.1002/2013JF002843

Mueller, E. R., & Pitlick, J. (2014). Sediment supply and channel morphology in mountain river systems: 2. Single thread to braided transitions. *Journal of Geophysical Research: Earth Surface*, *119*(7), 1516–1541. https://doi.org/10.1002/2013JF003045

Murray, A. B., & Paola, C. (2003). Modelling the effect of vegetation on channel pattern in bedload rivers. *Earth Surface Processes and Landforms*, *28*(2), 131–143. https://doi.org/10.1002/esp.428

Paola, C., Straub, K., Mohrig, D., & Reinhardt, L. (2009). The "unreasonable effectiveness" of stratigraphic and geomorphic experiments. *Earth-Science Reviews*, *97*(1–4), 1–43. https://doi.org/10.1016/j.earscirev.2009.05.003

Parker, G. (2008). Transport of Gravel and Sediment Mixtures. In M. Garcia (Ed.), *Sedimentation Engineering: Processes, Measurements, Modeling, and Practice* (pp. 165–252). Reston, VA: American Society of Civil Engineers. https://doi.org/10.1061/9780784408148.ch03

Parker, G., & Toro-Escobar, C. M. (2002). Equal mobility of gravel in streams: The remains of the day. *Water Resources Research*, *38*(11), 46-1-46–8. https://doi.org/10.1029/2001WR000669

Peakall, J., Ashworth, P. J., & Best, J. L. (1996). Physical Modelling in Fluvial Geomorphology : Principles , Applications and Unresolved Issues. John Wiley & Sons Ltd.

Picco, L., Mao, L., Cavalli, M., Buzzi, E., Rainato, R., & Lenzi, M. A. (2013). Evaluating short-term morphological changes in a gravel-bed braided river using terrestrial laser scanner. *Geomorphology*, *201*, 323–334. https://doi.org/10.1016/j.geomorph.2013.07.007

Piegay, H., Grant, G., Nakamura, F., & Trustrum, N. (2006). Braided River Management: from Assessment of River Behaviour to Improved Sustainable Development. In

Braided Rivers: Process, Deposits, Ecology and Management (pp. 257–275). Oxford, UK: Blackwell Publishing Ltd. https://doi.org/10.1002/9781444304374.ch12

Powell, D. M., Reid, I., & Laronne, J. . B. B. (2001). Evolution of bed load grain size distribution with increasing flow strength and the effect of flow duration on the caliber of bed load sediment yield in ephemeral gravel bed rivers. *Water Resources Research*, *37*(5), 1463–1474. https://doi.org/10.1029/2000WR900342

Pryor, B. S., Lisle, T. E., Montoya, D. S., & Hilton, S. (2011). Transport and storage of bed material in a gravel-bed channel during episodes of aggradation and degradation: a field and flume study. *Earth Surface Processes and Landforms*, *36*(15), 2028–2041. https://doi.org/10.1002/esp.2224

Pyrce, R. S., & Ashmore, P. (2003a). Particle path length distributions in meandering gravel-bed streams: results from physical models. *Earth Surface Processes and Landforms*, *28*(9), 951–966. https://doi.org/10.1002/esp.498

Pyrce, R. S., & Ashmore, P. (2003b). The relation between particle path length distributions and channel morphology in gravel-bed streams: a synthesis. *Geomorphology*, *56*(1–2), 167–187. https://doi.org/10.1016/S0169-555X(03)00077-1

Pyrce, R. S., & Ashmore, P. (2005). Bedload path length and point bar development in gravel-bed river models. *Sedimentology*, *52*(4), 839–857. https://doi.org/10.1111/j.1365-3091.2005.00714.x

Redolfi, M., Tubino, M., Bertoldi, W., & Brasington, J. (2016). Analysis of reach-scale elevation distribution in braided rivers: Definition of a new morphologic indicator and estimation of mean quantities. *Water Resources Research*, *52*(8), 5951–5970. https://doi.org/10.1002/2015WR017918

Rice, S., & Church, M. (1998). Grain size along two gravel-bed rivers: statistical variation, spatial pattern and sedimentary links. *Earth Surface Processes and Landforms*, *23*(4), 345–363. https://doi.org/10.1002/(SICI)1096-9837(199804)23:4<345::AID-ESP850>3.0.CO;2-B

Robert, A. (2003). *River Processes: An Introduction to Fluvial Dynamics*. London: Hodder Arnold.

Rumsby, B. T., Brasington, J., Langham, J. A., McLelland, S. J., Middleton, R., & Rollinson, G. (2008). Monitoring and modelling particle and reach-scale morphological change in gravel-bed rivers: Applications and challenges. *Geomorphology*, *93*(1–2), 40–54. https://doi.org/10.1016/j.geomorph.2006.12.017

Ryan, S. E., Porth, L. S., & Troendle, C. A. (2002). Defining phases of bedload transport using piecewise regression. *Earth Surface Processes and Landforms*, *27*(9), 971–990. https://doi.org/10.1002/esp.387

Sapozhnikov, V. B., & Foufoula-Georgiou, E. (1997). Experimental evidence of dynamic scaling and indications of self-organized criticality in braided rivers. *Water*

Resources Research, *33*(8), 1983–1991. https://doi.org/10.1029/97WR01233

Shvidchenko, A. B., & Kopaliani, Z. D. (1998). Hydraulic Modeling of Bed Load Transport in Gravel-Bed Laba River. *Journal of Hydraulic Engineering*, *124*(8), 778–785. https://doi.org/10.1061/(ASCE)0733-9429(1998)124:8(778)

Smith, M. W. W., Carrivick, J. L. L., & Quincey, D. J. J. (2016). Structure from motion photogrammetry in physical geography. *Progress in Physical Geography*, *40*(2), 247–275. https://doi.org/10.1177/0309133315615805

Surian, N., & Cisotto, A. (2007). Channel adjustments, bedload transport and sediment sources in a gravel-bed river, Brenta River, Italy. *Earth Surface Processes and Landforms*, *32*(11), 1641–1656. https://doi.org/10.1002/esp.1591

Tubino, M., & Bertoldi, W. (2007). Bifurcations in gravel-bed streams. In H. Habersack, H. Piégay, & M. Rinaldi (Eds.), *Gravel-Bed Rivers VI: From Process Understanding to River Restoration* (pp. 133–159). https://doi.org/10.1016/S0928-2025(07)11123-8

Venditti, J. G., Nelson, P. A., Bradley, R. W., Haught, D., & Gitto, A. B. (2017). Bedforms, Structures, Patches, and Sediment Supply in Gravel-Bed Rivers. In *Gravel-Bed Rivers* (pp. 439–466). Chichester, UK: John Wiley & Sons, Ltd. https://doi.org/10.1002/9781118971437.ch16

Wainwright, J., & Mulligan, M. (Eds.). (2013). *Environmental Modelling*. Chichester, UK: John Wiley & Sons, Ltd. https://doi.org/10.1002/9781118351475

Warburton, J. (1996). A brief review of hydraulic modelling of braided gravel-bed rivers in New Zealand. *Journal of Hydrology New Zealand*, *35*(2), 157–173.

Westoby, M. J. J., Brasington, J., Glasser, N. F. F., Hambrey, M. J. J., & Reynolds, J. M. M. (2012). "Structure-from-Motion" photogrammetry: A low-cost, effective tool for geoscience applications. *Geomorphology*, *179*, 300–314. https://doi.org/10.1016/j.geomorph.2012.08.021

Wheaton, J. M., Brasington, J., Darby, S. E., Kasprak, A., Sear, D. A., & Vericat, D. (2013). Morphodynamic signatures of braiding mechanisms as expressed through change in sediment storage in a gravel-bed river. *Journal of Geophysical Research: Earth Surface*, *118*(2), 759–779. https://doi.org/10.1002/jgrf.20060

Wheaton, J. M., Brasington, J., Darby, S. E., & Sear, D. A. (2009). Accounting for uncertainty in DEMs from repeat topographic surveys: improved sediment budgets. *Earth Surface Processes and Landforms*, *35*(2), n/a-n/a. https://doi.org/10.1002/esp.1886

Wickert, A. D., Martin, J. M., Tal, M., Kim, W., Sheets, B., & Paola, C. (2013). River channel lateral mobility: metrics, time scales, and controls. *Journal of Geophysical Research: Earth Surface*, *118*(2), 396–412. https://doi.org/10.1029/2012JF002386

Wilcock, P. R., & Southard, J. B. (1989). Bed-load transport of mixed-size sediment: fractional transport rates, bed forms, and the development of a coarse bed-surface layer. *Water Res. Res.*, *25*(7), 1629–1641.

Williams, R., Brasington, J., Vericat, D., Hicks, M., Labrosse, F., & Neal, M. (2011). Monitoring Braided River Change Using Terrestrial Laser Scanning and Optical Bathymetric Mapping. In *Developments in Earth Surface Processes* (Vol. 15, pp. 507–532). Elsevier B.V. https://doi.org/10.1016/B978-0-444-53446-0.00020-3

Williams, R. D. (2012). DEMs of Difference. *Geomorphological Techniques*, *2*(2), 1–17. https://doi.org/2047-0371

Williams, R. D., Measures, R., Hicks, D. M., & Brasington, J. (2016). Assessment of a numerical model to reproduce event-scale erosion and deposition distributions in a braided river. *Water Resources Research*, *52*(8), 6621–6642. https://doi.org/10.1002/2015WR018491

XLSTAT. (2017). Kolmogorov-Smirnov test in Excel tutorial. Retrieved from https://help.xlstat.com/customer/en/portal/articles/2062428-kolmogorov-smirnov-test-in-excel-tutorial?b_id=9283

Yager, E. M., Kenworthy, M., & Monsalve, A. (2015). Taking the river inside: Fundamental advances from laboratory experiments in measuring and understanding bedload transport processes. *Geomorphology*, *244*, 21–32. https://doi.org/10.1016/j.geomorph.2015.04.002

Yager, E. M., & Schott, H. E. (2013). The Initiation of Sediment Motion and Formation of Armor Layers. In J. F. Shroder (Ed.), *Treatise on Geomorphology* (pp. 87–102). San Diego: Elsevier. https://doi.org/10.1016/B978-0-12-374739-6.00232-3

Yalin, M. S. (1971). *Theory of Hydraulic Models*. London: Macmillan Education UK.

Young, W. J., & Davies, T. R. H. (1990). Prediction of bedload transport rates in braided rivers: a hydraulic model study. *Journal of Hydrology (NZ)*, *29*(2), 75–92.

Young, W. J., & Warburton, J. (1996). Principles and practice of hydraulic modelling of braided gravel-bed rivers. *Journal of Hydrology New Zealand*, *35*(2), 175–198. https://doi.org/10.1016/S0301-9322(97)80098-5

Zolezzi, G., Bertoldi, W., & Tubino, M. (2012). Morphodynamics of Bars in Gravel-Bed Rivers: Bridging Analytical Models and Field Observations. In M. Church, P. A. Biron, & A. Roy (Eds.), *Gravel-Bed Rivers* (pp. 69–89). Chichester, UK: John Wiley & Sons, Ltd. https://doi.org/10.1002/9781119952497.ch6

Appendices

Appendix A Principles of Similarity in Froude-Scaled Models

Similarity theory is based on the use of dimensionless parameters that characterize a system and can be kept equal between a model and prototype. The fundamental dimensionless parameters used in Froude scaling modelling can be determined using dimensional analysis and the Buckingham Π (pi) theorem (Peakall et al., 1996; Dingman, 2009). This method is used to reduce all relevant variables into their fundamental units and determine all the possible non-dimensional combinations of the variables. When considering a movable-bed model where the flow is two-phase flow (fluid and sediment particles) the fundamental variables can be defined by:

- The fluid properties: dynamic viscosity (μ) and density of the fluid (ρ)
- The sediment properties: sediment density (ρ_s) and grain diameter (D)
- The flow properties: slope (S); flow depth (d) or hydraulic radius (R); and the acceleration due to gravity (g)

In this example, shear velocity ($U^* = (gRS)^{0.5}$) is often used in place of slope and the immersed specific weight of the grains ($\gamma_s = g(\rho_s - \rho)$) is often used in place of g. This leaves us with μ, ρ, ρ_s, R, D, U^* and γ_s (Peakall et al., 1996; Young and Warburton, 1996).

Based on the Buckingham Π theorem, there are seven variables and three dimensions (mass, length and time) resulting in four dimensionless terms, called Π terms:

$$\Pi_1 = \frac{R}{D}$$

$$\Pi_2 = \frac{\rho_s}{\rho}$$

$$\Pi_3 = \frac{\rho U^* D}{\mu} = Re_*$$

$$\Pi_4 = \frac{\rho U_*^2}{\gamma_s D} = Fr_*$$

Π_1 and Π_2 are relative roughness and relative density, respectively. Π_3 is the grain Reynolds number (Re_*), which represents a ratio between inertial forces and viscous forces. Π_4 is the grain-size Froude number (Fr_*), representing the ratio between inertial and gravitational forces (Young and Warburton, 1996).

In a perfectly scaled model, the values of these dimensionless variables would be the same in the model and prototype. Unfortunately, it is generally not possible and in fluvial geomorphology the result is the Froude-scaled model (FSM), in which the Froude number is held constant between the model and prototype and the grain Reynolds number is relaxed but kept above the critical value $(Re_* > 70)$ for rough turbulent flow (Peakall et al., 1996; Young and Warburton, 1996). In addition, geometric similarity requires that all lengths are scaled by the same scale ratio. Therefore, the grain size distribution for graded sediment is scaled down by the same scale ratio for all grain sizes. Finally, the river slope is the same in the model and prototype (Young and Warburton, 1996). As a result, the Shields parameter (ϑ), which defines the shear stress required for entrainment, will be the same in the model and prototype:

$$\vartheta = \frac{\tau}{(\rho_s - \rho)gD}$$

where τ is the bed shear stress ($\tau = \rho gdS$, d is water depth and S is slope), ρ_s and ρ are the density of sediment and water respectively, g is the gravitational constant and D is grain size.

Appendix B Weir Calibration

Prior to the experiments a new weir was built and calibrated in January 2015. Calibration of the weir was done using a custom-built pool attached to the edges of the weir via a plastic sheet (Figure B.1). The sides of the pool had vertical scales that allowed the height of the water in the pool to be read at both the upstream and downstream ends. Using four people, the amount of time it took to fill the pool was measured 3 times across a series of slope and discharge settings. It was possible to find a linear relationship between the height of the water in the head tank and the discharge coming over the weir. There are several sources of error with this method, including the inherent subjectivity of starting the timer and reading the pool scales simultaneously, especially as water levels were often unsteady. This error was minimized by having the same person at each station for the duration of calibration and completing triplicates for all tests. The result of the calibration was estimated discharge based on the following equation:

$$Q = 0.5H - 0.4$$

where H is the water depth above the weir. The estimated relative error is shown in Table B.1, indicating that the discharge values have an estimated error of ~5 %.

Figure B.1 – Weir calibration using a custom-built pool.

Table B.1 - Relative error in discharge (Q) measurements as a function of head tank water depth.

Relative Error	Q
	$l\,s^{-1}$
Mean	0.045
Minimum	0.001
Maximum	0.15
Std. dev.	0.44

Appendix C Sediment Sorter Calibration

To determine that amount of water coming off the upstream sediment slide, the discharge contributions from the slide were measured at the end of the experiments. After starving the sediment recirculation system of sediment, an empty bucket positioned at the end of the sediment slide was filled with the output from the sediment sorter (i.e., water) for 30 seconds. The mass of water collected over 30 seconds was averaged for 10 samples to estimate the average contributing discharge from the sediment sorter (Table C.1).For the second round of testing, sediment was recirculated so that the water and sediment mixture going down the sediment slide mimicked the experimental conditions. Like the first round of tests, 10 samples were collected for 30 seconds each. The sediment was separated from the water using a small box with a fine mesh bottom attached to the top of the water collection bucket. Once separated the water and the sediment were weighed separately so that the discharge represents contributions from the water only (Table C.1).

Table C.1 - Summary statistics sediment sorter discharge (Q) contributions of water and sediment, where samples is the number of samples, mean Q is the average discharge, and σ is the standard deviation.

	Samples	Mean Q	σ
		$l\,s^{-1}$	$l\,s^{-1}$
Water Only	10	0.118	0.003
Water and Sediment	10	0.117	0.006

Appendix D Target Survey

The procedure used to complete the target surveys for each experimental condition was based on the following steps:

1) Set-up tripod and theodolite over Survey Station 1 marked by a target on the floor.
2) Measure and input instrument height into the theodolite (~1.965 m)
3) Set the horizontal angle (Hz) to zero on control point 1B.
4) Collect Hz and vertical (Z) coordinates for control points 1B, 3L, 3LB and Survey Station 2.
5) Collet Hz and Z coordinates for each survey target beginning with 253 in the bottom left of the flume and continuing with the targets along the left-hand side to target 295.
6) Collect Hz and Z coordinates for each survey target along the right-hand side of the flume, beginning with upstream target 283 and continuing to target 285.
7) Re-collect the Hz and Z coordinates for the control points 1B, 3L, 3LB and station 2. If values differ by greater than 0.002", restart the survey, otherwise continue to step 8.
8) Complete a second survey of each target so that there are two Hz and Z coordinates for each target from Survey Station 1. If values of control points differ by greater than 2 seconds, restart the survey.
9) If satisfied with coordinates from Survey Station 1, move tripod and theodolite over to Survey Station 2 as marked by the target on the floor.
10) Follow steps 4 – 8, this time taking coordinates for Survey Station 1.

One survey was used for each experiment, although sometimes multiple surveys would need to be completed to achieve the desired precision of < 0.002". Once a survey is completed, the resulting coordinates were used in Agisoft to determine the number of targets that could be detected. Targets that were consistently missing during automatic target detection component in Agisoft were adjusted and resurveyed. This was only done during the evolution stages of the experiments to ensure high quality surveys were used for the processing of experimental DEMs.

Appendix E Camera Settings

The camera setting used for the two Canon and two Olympus cameras are in Table E.1.

Table E.1 - Summary of camera settings.

	Canon EOS Rebel T5i	Olympus C-5060
Camera body	Digital SLR	Digital
Lens Focal Length	20 mm or 24 mm	wide angle 27-110 mm
Number of cameras	2	2
External Control	Yes	Yes
Location	Trolley	Ceiling
Camera Settings		
Mode	Manual	P; M
ISO	100	Auto; 80
Shutter Speed	1/8	1/30; 1/1000
Aperture	F 3.5	F 2.8
White Balance	Tungsten	Auto

Appendix F Sediment baskets

In total, 7 baskets were made and labelled A-G and weighed both dry and wet throughout the experiments as well as at the end of all the experiments (Table F.1). To determine the total mass of wet sediment at the end of each run, the value 16.35 kg (5*3.27) was subtracted from the combined total mass of the wet basket and wet sediment, leaving the mass of the wet sediment.

Table F.1 - Average dry and wet masses of the sediment baskets.

Basket	Average Dry Mass	Average Wet Mass
	Kg	Kg
A	3.22	3.26
B	3.23	3.27
C	3.23	3.27
D	3.22	3.27
E	3.23	3.27
F	3.22	3.26
G	3.23	3.26
Total Average	3.22	3.27
Total σ	0.005	0.004

To determine the effect of the moisture content of the sediment in the baskets as well as the conversion from a wet sediment mass to a dry sediment mass, a series of tests were completed at the end of the experiments. To begin, dry sediment of a known mass (e.g., 1, 2, 4, and 8 kg) was added to a basket hanging from the load cell (Figure F.1). The sediment was wet to mimic experimental conditions of flow going into the basket. A timer was started once the water had finished being poured and the wet weight of the sediment and basket was recorded every 60 seconds for 12 minutes. The result was that the wet mass of sediment stabilized after approximately 1 minute, and remained stable for the remaining 11 minutes of testing.
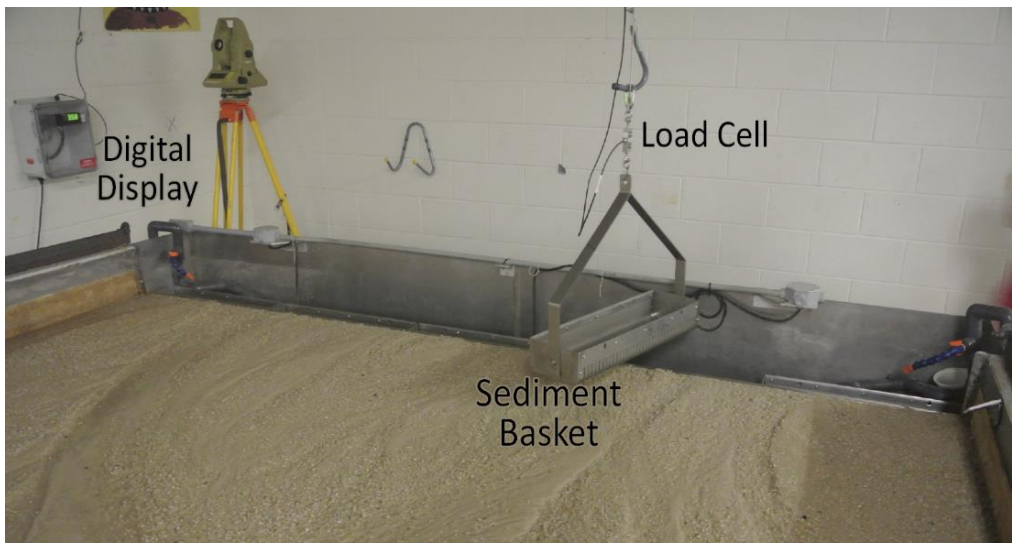
Figure F.1 – Image of a sediment basket hanging from the load cell.

The test also provided the conversion between wet and dry sediment. Since the sediment started from a known dry mass, once the sediment was wet and the mass stabilized, we were left with a conversion factor of 1.22kg (Figure F.2).
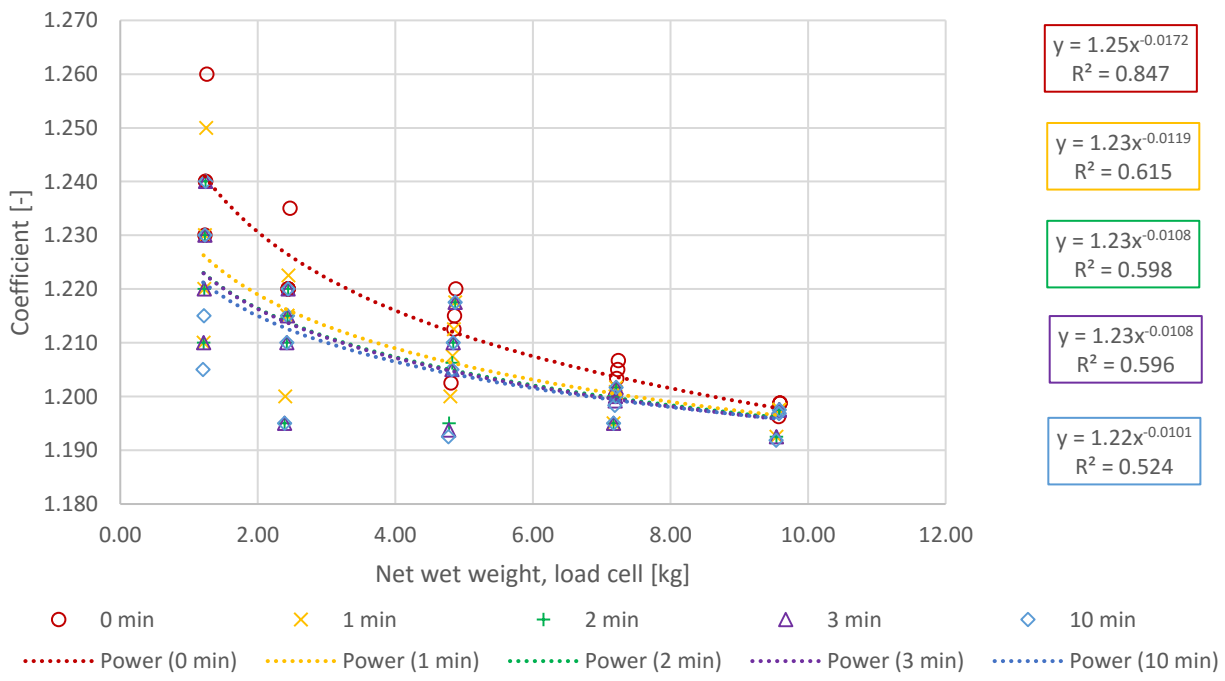
Figure F.2 – Wet and dry sediment coefficient for different dry sediment masses.

Appendix G Sediment Sieving

The standard dry sieving procedure is as follows (Head, 2006):

1. Oven dry the sample and weigh the cooled sample for an initial dry weight.
2. Select sieves (Table G.1)
3. Sieve the sample by passing it through the set of sieves by using a mechanical shaker for a period of 10 minutes. In some cases, this included riffling (i.e., splitting) the sample before sieving.
4. Weigh the samples using a balance (with an accuracy of 0.1 % or better) of the total initial mass
   a. As a check, calculate the sum of masses and if the total differs by more than 1 %, repeat steps 4 and 5
5. Clean sieves and repeat for other samples.

Before sieving began, all sieves were cleaned out to remove any residual grains stuck in the mesh from previous uses. Between samples, the sieves were cleaned out impeccably to 1mm, and all sieves below 1mm were cleaned using a wire brush designed for cleaning sieves.

Table G.1 - Sieve sizes used to sieve sediment samples from the downstream baskets.

Sieve Size	mm	5.6	4	2.8	2	1.4	1	0.71	0.5	0.35	0.25
	phi	-2.5	-2	-1.5	-1	-0.5	0	0.5	1	1.5	2

Appendix H Bulk Density

The bulk density of the bed sediment was determined using a water replacement method. To start, a small hole with a diameter of approximately 7 cm and depth of 3 cm was dug into the dry flume bed. The sediment removed was collected and weighed. A small piece of clear plastic wrap was placed carefully into the hole and gently pushed into the edges of the hole. Next, the hole was filled with water of a known volume (Figure H.1). Bulk density was calculated as the mass of sediment removed from the hole divided by the volume of water used to fill the hole (Figure H.2). 37 samples were taken using the water replacement method between 4.8 and 7 m from the upstream end of the flume covering a range of morphological features including in-channel, bar heads, and flat areas (Figure H.3). The water was dyed purple using marker ink so that it was easier to distinguish when the hole was filled.

Figure H.1 – Water replacement method for the estimating bulk density. Sediment removed from the hole was collected and the hole was lined with plastic and filled with water.
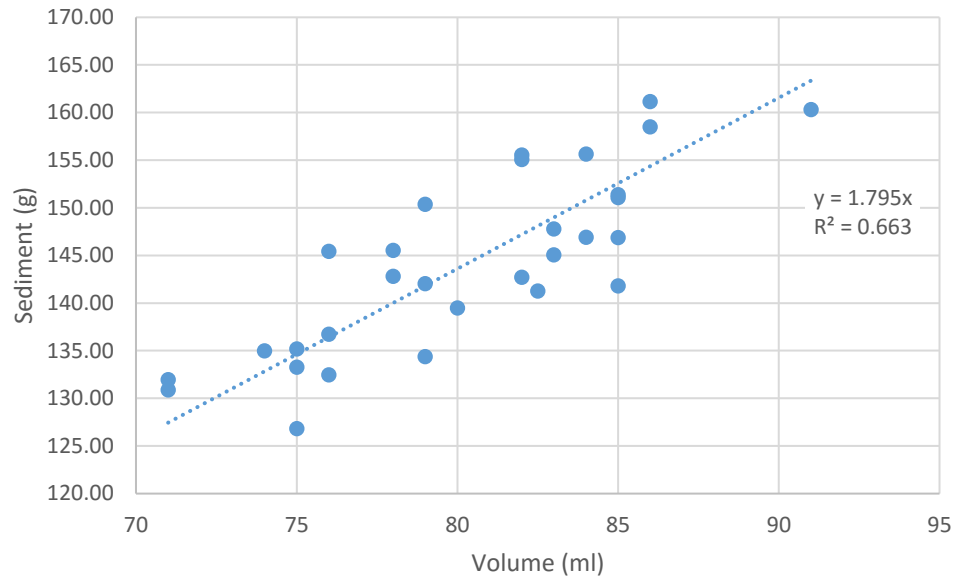
Figure H.2 – Bulk density calculation. The mass of sediment removed from the flume as a function of the volume of water used to fill the hole.

Figure H.3 – Bulk density sample locations. The bulk density samples were taken at the end of experiment 13, covering a range of morphological features including bars and in-channel locations. The water was dyed purple to improve the visibility of the water against the sand.

To account for any possible differences in moisture content, the bulk density samples were weighed immediately after collection and then again after being dried with a hair dryer for 2 minutes using a low-cool setting (Table H.1). On average there was a 0.46 % loss in sediment mass after drying. For this research the value of 1.79 g ml^{-1} was used for the conversion between dry volumes and dry masses of sediment.

Table H.1 - Summary statistics of bulk density measurements before and after drying.

	Before Drying	After Drying
	g ml^{-1}	g ml^{-1}
Minimum	1.67	1.66
Maximum	1.91	1.90
Average	1.80	1.79
σ	0.07	0.07

Appendix I Summary of T-tests

Table I.1 - Summary of statistics for the active width for the constant discharge experiments using the simple 2σ threshold and the dilation method, where n is the number of observations, mean is the average result, σ is the standard deviation, and the p-values are based on a Student's t-test using alpha = 0.05.

Experiment	Threshold Method	n	Mean	σ	p-value
			m	m	
1	Simple	37	0.011	0.008	0.063
	Dilation	37	0.015	0.011	
4	Simple	65	0.143	0.059	0.007
	Dilation	65	0.173	0.068	
9	Simple	67	0.166	0.054	0.001
	Dilation	67	0.201	0.062	
12	Simple	64	0.436	0.063	<0.0001
	Dilation	64	0.565	0.070	
13	Simple	66	0.607	0.061	<0.0001
	Dilation	66	0.797	0.088	

Table I.2 - Summary of statistics for the active depth for the constant-discharge experiments using the simple 2σ threshold and the dilation method, where n is the number of observations, mean is the average result, σ is the standard deviation, and the p-values are based on a Student's t-test using alpha= 0.05.

Experiment	Threshold Method	n	Mean	σ	p-value
			m	m	
1	Simple	37	0.003	0.000	1
	Dilation	37	0.003	0.000	
4	Simple	65	0.005	0.001	1
	Dilation	65	0.004	0.001	
9	Simple	67	0.006	0.001	1
	Dilation	67	0.005	0.001	
12	Simple	64	0.005	0.001	1
	Dilation	64	0.004	0.001	
13	Simple	66	0.005	0.000	1
	Dilation	66	0.004	0.000	

Table I.3 - Summary of statistics for the volumes of erosion and deposition for the constant discharge experiments based on the 2σ threshold where n is the number of observations, mean is the average result, σ is the standard deviation, and the p-values are based on a Student's t-test using alpha= 0.05.

Experiment	Threshold Method	n	Mean	σ	p-value
			m^3	m^3	
1	Erosion	37	0.000	0.000	0.829
	Deposition	37	0.000	0.000	
4	Erosion	65	0.005	0.003	0.793
	Deposition	65	0.005	0.003	
9	Erosion	67	0.008	0.003	0.953
	Deposition	67	0.007	0.003	
12	Erosion	64	0.017	0.004	0.820
	Deposition	64	0.016	0.004	
13	Erosion	66	0.023	0.003	0.992
	Deposition	66	0.022	0.003	

Table I.4 - Summary of statistics for the hydrograph active widths using the simple 2σ threshold and dilation threshold, where n is the number of observations, mean is the average result, σ is the standard deviation, and the p-values are based on a Student's t-test using alpha= 0.05.

Discharge	Threshold	n	Mean	σ	p-value
l s^{-1}			m	m	
0.7	Simple	15	0.012	0.009	0.186
	Dilation	15	0.017	0.012	
0.83	Simple	8	0.012	0.009	0.290
	Dilation	8	0.017	0.012	
0.93	Simple	3	0.014	0.004	0.149
	Dilation	3	0.021	0.006	
1.14	Simple	24	0.040	0.027	0.092
	Dilation	24	0.056	0.036	
1.35	Simple	8	0.126	0.071	0.353
	Dilation	8	0.164	0.088	
1.65	Simple	25	0.158	0.035	<0.0001
	Dilation	25	0.213	0.047	
1.86	Simple	15	0.244	0.059	0.012
	Dilation	15	0.308	0.070	
2.1	Simple	15	0.296	0.083	0.020
	Dilation	15	0.377	0.096	

Table I.5 - Summary of statistics for the hydrograph active depths using the simple 2σ threshold and dilation threshold, where n is the number of observations, mean is the average result, σ is the standard deviation, and the p-values are based on a Student's t-test using alpha= 0.05.

Discharge	Threshold	n	Mean	σ	p-value
l s^{-1}			m	m	
0.7	Simple	15	0.003	0.000	<0.0001
	Dilation	15	0.002	0.000	
0.83	Simple	8	0.003	0.000	0.000
	Dilation	8	0.002	0.000	
0.93	Simple	3	0.003	0.000	0.001
	Dilation	3	0.002	0.000	
1.14	Simple	24	0.003	0.000	<0.0001
	Dilation	24	0.003	0.000	
1.35	Simple	8	0.005	0.001	0.065
	Dilation	8	0.004	0.001	
1.65	Simple	25	0.005	0.001	<0.0001
	Dilation	25	0.004	0.000	
1.86	Simple	15	0.006	0.001	0.000
	Dilation	15	0.005	0.001	
2.1	Simple	15	0.006	0.001	0.000

Table I.6 - Summary of statistics for the erosional and depositional active depths, where n is the number of observations, mean is the average result, σ is the standard deviation, and the p-values are based on a Student's t-test using alpha= 0.05.

Discharge	n	Mean		σ		p-value
I s^{-1}		m		m		
		Erosion	Deposition	Erosion	Deposition	
0.7	15	0.006	0.006	0.005	0.005	0.842
0.83	8	0.013	0.009	0.011	0.004	0.356
0.93	3	0.008	0.005	0.004	0.001	0.295
1.14	24	0.020	0.020	0.013	0.014	0.829
1.35	8	0.062	0.064	0.034	0.038	0.914
1.65	25	0.081	0.078	0.014	0.024	0.596
1.86	17	0.112	0.125	0.028	0.037	0.275
2.1	17	0.141	0.157	0.035	0.047	0.289

Appendix J Tukey HSD Multiple Pairwise Comparisons

The following results are for the Tukey Honestly Significantly Different (HSD) Test, which was completed ad hoc to ANOVA tests for the bedload transport rates from the 14 reach subsections. The results shown are for the experiments which had significant differences between subsections (i.e., experiments 9, 12, and 13) and the results only show the values for those sections that had significant differences. The first table for each experiment displays the output for the Tukey HSD, followed by a summary table that groups subsections into 'similar' (i.e., not statistically significantly different) groups. Each Tukey test was completed with a confidence interval of 95%

Table J.1 - Significant results of the Tukey HSD test for experiment 9 for estimated bedload transport rates at 14 subsections where Tukey's d critical value = 4.756.

Contrast	Difference	Standardized difference	Critical value	Pr > Diff
1 vs 14	2.138	6.057	3.362	**< 0.0001**
1 vs 13	1.924	5.451	3.362	**< 0.0001**
1 vs 12	1.676	4.749	3.362	**0.000**
1 vs 11	1.238	3.507	3.362	**0.031**
2 vs 14	2.029	5.748	3.362	**< 0.0001**
2 vs 13	1.816	5.143	3.362	**< 0.0001**
2 vs 12	1.568	4.440	3.362	**0.001**
6 vs 14	1.883	5.334	3.362	**< 0.0001**
6 vs 13	1.669	4.728	3.362	**0.000**
6 vs 12	1.421	4.026	3.362	**0.005**
5 vs 14	1.859	5.266	3.362	**< 0.0001**
5 vs 13	1.645	4.661	3.362	**0.000**
5 vs 12	1.397	3.958	3.362	**0.006**
3 vs 14	1.839	5.208	3.362	**< 0.0001**
3 vs 13	1.625	4.603	3.362	**0.000**
3 vs 12	1.377	3.901	3.362	**0.008**
7 vs 14	1.814	5.138	3.362	**< 0.0001**
7 vs 13	1.600	4.532	3.362	**0.001**
7 vs 12	1.352	3.830	3.362	**0.010**
4 vs 14	1.739	4.927	3.362	**< 0.0001**
4 vs 13	1.526	4.322	3.362	**0.001**
4 vs 12	1.278	3.619	3.362	**0.021**
8 vs 14	1.562	4.424	3.362	**0.001**
8 vs 13	1.348	3.819	3.362	**0.011**
9 vs 14	1.330	3.769	3.362	**0.013**

Table J.2 - Summary of all-pairwise comparisons for experiment 9 from the Tukey HSD comparison of bedload transport rates.

Subsection	Groups				
1	A				
2	A	B			
6	A	B			
5	A	B			
3	A	B			
7	A	B			
4	A	B			
8	A	B	C		
9	A	B	C	D	
10	A	B	C	D	E
11		B	C	D	E
12			C	D	E
13				D	E
14					E

Table J.3 - Results of the Tukey HSD test for experiment 12 with respect to estimated bedload transport rates at 14 subsections where Tukey's d critical value = 4.756.

Contrast	Difference	Standardized difference	Critical value	Pr > Diff
1 vs 14	1.902	3.600	3.363	0.023
1 vs 10	1.778	3.365	3.363	0.050

Table J.4 - Summary of all-pairwise comparisons for experiment 12 from the Tukey HSD comparison of bedload transport rates.

Subsection	Groups	
1	A	
2	A	B
3	A	B
4	A	B
5	A	B
6	A	B
7	A	B
8	A	B
12	A	B
9	A	B
11	A	B
13	A	B
10		B
14		B

Table J.5 - Results of the Tukey HSD test for experiment 13 with respect to estimated bedload transport rates at 14 subsections where Tukey's d critical value = 4.756.

Contrast	Difference	Standardized difference	Critical value	Pr > Diff
1 vs 12	3.433	6.572	3.363	**< 0.0001**
1 vs 13	3.384	6.479	3.363	**< 0.0001**
1 vs 11	3.280	6.280	3.363	**< 0.0001**
1 vs 14	3.227	6.179	3.363	**< 0.0001**
1 vs 10	3.061	5.861	3.363	**< 0.0001**
1 vs 9	2.726	5.218	3.363	**< 0.0001**
1 vs 8	2.312	4.427	3.363	**0.001**
1 vs 7	1.991	3.812	3.363	**0.011**
2 vs 12	3.261	6.242	3.363	**< 0.0001**
2 vs 13	3.212	6.149	3.363	**< 0.0001**
2 vs 11	3.108	5.950	3.363	**< 0.0001**
2 vs 14	3.055	5.849	3.363	**< 0.0001**
2 vs 10	2.889	5.531	3.363	**< 0.0001**
2 vs 9	2.553	4.888	3.363	**0.000**
2 vs 8	2.140	4.097	3.363	**0.004**
2 vs 7	1.819	3.482	3.363	**0.034**
3 vs 12	2.964	5.675	3.363	**< 0.0001**
3 vs 13	2.915	5.581	3.363	**< 0.0001**
3 vs 11	2.811	5.382	3.363	**< 0.0001**
3 vs 14	2.759	5.281	3.363	**< 0.0001**
3 vs 10	2.592	4.963	3.363	**< 0.0001**
3 vs 9	2.257	4.321	3.363	**0.001**
3 vs 8	1.843	3.529	3.363	**0.029**
4 vs 12	2.551	4.884	3.363	**0.000**
4 vs 13	2.502	4.791	3.363	**0.000**
4 vs 11	2.398	4.592	3.363	**0.000**
4 vs 14	2.346	4.491	3.363	**0.001**
4 vs 10	2.180	4.173	3.363	**0.003**
4 vs 9	1.844	3.530	3.363	**0.029**
5 vs 12	2.068	3.959	3.363	**0.006**
5 vs 13	2.019	3.865	3.363	**0.009**
5 vs 11	1.915	3.666	3.363	**0.018**
5 vs 14	1.862	3.565	3.363	**0.026**

Table J.6 - Summary of all-pairwise comparisons for experiment 13 from the Tukey HSD comparison of bedload transport rates.

Subsection	Groups				
1	A				
2	A				
3	A	B			
4	A	B	C		
5	A	B	C	D	
6	A	B	C	D	E
7		B	C	D	E
8			C	D	E
9				D	E
10				D	E
14					E
11					E
13					E
12					E

Appendix K Correlation Matrices

The following p-value tables, which are outputs from XLSTAT, correspond with the correlation matrices in Figure 5.25, which looked at the spatial correlation between all 14 subsections of the study are in terms of bulk change (i.e. total volume of change in kg).

Table K.1 - Results of experiment 4 bulk change Pearson Correlation Matrix at all 14 subsections. Values in bold are different from 0 with a significant level of alpha= 0.05.

Section	1	2	3	4	5	6	7	8	9	10	11	12	13	14
1	**0**													
2	**< 0.0001**	**0**												
3	**< 0.0001**	**< 0.0001**	**0**											
4	**0.005**	**0.015**	**< 0.0001**	**0**										
5	0.741	0.808	0.199	**< 0.0001**	**0**									
6	0.164	0.356	0.435	0.113	**< 0.0001**	**0**								
7	0.220	0.258	0.172	0.800	**0.001**	**< 0.0001**	**0**							
8	0.262	0.229	0.438	0.223	**0.000**	**< 0.0001**	**< 0.0001**	**0**						
9	0.454	0.590	0.719	**0.015**	**< 0.0001**	**< 0.0001**	**< 0.0001**	**< 0.0001**	**0**					
10	0.335	0.202	0.097	**0.012**	**0.011**	**0.024**	**0.019**	**0.006**	**< 0.0001**	**0**				
11	0.215	0.162	0.071	0.053	**0.042**	**0.007**	**0.004**	**0.003**	**< 0.0001**	**< 0.0001**	**0**			
12	**0.006**	**< 0.0001**	**< 0.0001**	**0.009**	0.284	0.128	0.122	0.217	**0.001**	**< 0.0001**	**< 0.0001**	**0**		
13	0.375	0.285	0.142	0.922	0.071	0.427	0.407	0.846	0.188	0.805	**0.001**	**< 0.0001**	**0**	
14	0.666	0.782	0.292	0.500	0.830	0.269	0.248	0.385	0.428	0.877	0.088	0.124	**< 0.0001**	**0**

Table K.2 - Results of experiment 9 bulk change Pearson Correlation Matrix at all 14 subsections. Values in bold are different from 0 with a significant level of alpha= 0.05.

Section	1	2	3	4	5	6	7	8	9	10	11	12	13	14
1	**0**													
2	**< 0.0001**	**0**												
3	**0.008**	**< 0.0001**	**0**											
4	0.042	**< 0.0001**	**< 0.0001**	**0**										
5	0.704	0.498	0.019	**< 0.0001**	**0**									
6	0.438	0.091	0.127	**0.004**	**< 0.0001**	**0**								
7	0.926	0.100	0.268	**0.035**	**0.011**	**< 0.0001**	**0**							
8	0.456	0.747	0.854	0.255	0.080	**0.034**	**< 0.0001**	**0**						
9	0.616	0.588	0.916	0.558	0.087	0.103	0.070	**< 0.0001**	**0**					
10	0.456	0.747	0.854	0.255	0.080	**0.034**	**< 0.0001**	**< 0.0001**	**< 0.0001**	**0**				
11	0.081	0.545	0.545	0.741	0.584	0.919	0.577	0.460	**0.001**	0.460	**0**			
12	0.991	0.722	0.513	0.436	0.777	0.859	0.383	0.210	0.317	0.210	**0.017**	**0**		
13	**0.047**	0.259	0.446	0.714	0.222	0.407	0.859	0.949	0.593	0.949	0.090	**< 0.0001**	**0**	
14	0.389	0.716	0.629	0.052	**0.010**	0.360	0.386	0.174	0.319	0.174	0.219	**< 0.0001**	**< 0.0001**	0

Table K.3 - Results of experiment 12 bulk change Pearson Correlation Matrix at all 14 subsections. Values in bold are different from 0 with a significant level of alpha= 0.05.

Section	1	2	3	4	5	6	7	8	9	10	11	12	13	14
1	**0**													
2	**< 0.0001**	**0**												
3	**0.042**	**< 0.0001**	**0**											
4	**0.028**	**0.001**	**< 0.0001**	**0**										
5	0.179	**0.004**	**0.000**	**< 0.0001**	**0**									
6	0.560	**0.049**	0.150	0.283	**0.003**	**0**								
7	0.622	**0.029**	0.056	0.124	**0.013**	**< 0.0001**	**0**							
8	0.262	0.166	**0.016**	0.067	0.735	0.948	**0.002**	**0**						
9	0.180	0.088	**0.010**	**0.012**	0.601	0.401	0.294	**< 0.0001**	**0**					
10	0.954	0.509	0.371	0.939	0.222	0.643	0.802	**0.009**	**< 0.0001**	**0**				
11	0.786	0.215	0.887	0.374	0.828	0.776	0.462	0.808	0.109	**< 0.0001**	**0**			
12	**0.002**	0.071	0.533	0.279	0.390	0.988	0.198	0.849	0.194	**0.005**	**0.016**	**0**		
13	**0.020**	**0.010**	0.995	0.901	0.482	0.719	**0.005**	0.314	0.269	0.781	0.294	**< 0.0001**	**0**	
14	0.155	**0.013**	0.441	0.832	0.898	0.788	0.068	0.941	0.857	0.850	0.263	**0.000**	**< 0.0001**	**0**

Table K.4 - Results of experiment 13 bulk change Pearson Correlation Matrix at all 14 subsections. Values in bold are different from 0 with a significant level of alpha= 0.05.

Section	1	2	3	4	5	6	7	8	9	10	11	12	13	14
1	**0**													
2	**< 0.0001**	**0**												
3	**0.039**	**0.000**	**0**											
4	0.126	0.158	**0.001**	**0**										
5	0.065	0.099	0.682	**0.010**	**0**									
6	0.652	0.885	0.482	0.669	0.303	**0**								
7	0.870	0.556	0.874	0.868	0.739	0.107	**0**							
8	0.159	0.534	0.847	0.628	0.496	0.621	0.207	**0**						
9	0.187	0.384	0.704	0.208	**0.002**	0.272	0.851	**0.005**	**0**					
10	0.052	0.188	0.308	0.207	0.783	0.282	0.591	0.275	**0.013**	**0**				
11	0.815	0.904	0.886	0.783	0.548	0.214	0.396	0.304	0.266	**0.001**	**0**			
12	0.164	**0.032**	0.379	0.262	0.298	0.409	0.169	0.706	0.984	**0.019**	**0.001**	**0**		
13	0.888	0.822	0.368	0.292	**0.037**	0.751	0.107	0.801	0.549	0.331	**0.005**	**< 0.0001**	**0**	
14	**0.017**	0.136	0.085	**0.045**	0.733	0.083	0.963	0.248	0.601	0.077	0.069	0.179	**< 0.0001**	**0**

Curriculum Vitae

Name: Sarah E. K. Peirce

Post-secondary Education and Degrees:

University of Guelph
Guelph, Ontario, Canada
2005-2010 B.A.S.

University of Guelph
Guelph, Ontario, Canada
2010-2012 M.Sc.

The University of Western Ontario
London, Ontario, Canada
2012-2017 Ph.D.

Honours and Awards:

USC Teaching Honour Roll, 2015-2016
Vanier Canada Graduate Scholarship, 2013-2016
E.G., Pleva Teaching Assistantship in Geography Award, 2013
Ontario Graduate Scholarship, 2011-2012, 2012-2013
University of Guelph Dean's Scholarship, 2010, 2012
Second-Team All-Canadian 2010, 2012
Canadian Water Resources Assoc. Graduate Scholarship, 2011
Ontario Graduate Scholarship in Science and Technology, 2011
Professor Victor Matthews Track and Field Award, 2010-2011
Canadian Association of Geographers Undergraduate Award, 2010
Ontario University Athletics Women of Influence Award, 2009
University of Guelph President's Award, 2009

Related Work Experience

Instructor
The University of Western Ontario
2016, 2017

Research Assistant
The University of Western Ontario
2013-2016

Teaching Assistant
The University of Western Ontario
2012-2015

Teaching Assistant
University of Guelph
2010-2012

Publications: **Peirce, S**. 2016. Making Learning Mobile: Using Mobile Technologies to Bring GIS into the Geography Classroom. *Teaching Innovation Projects.* Vol. 6(1) Article 2.

Kasprak, A., Wheaton, J.M., Ashmore, P.E., Hensleigh, J.W. and **Peirce, S**. 2015. The relationship between particle travel distance and channel morphology: Results from physical models of braided rivers. *Journal of Geophysical Research: Earth Surface.* Vol 120(1): 55-74.

Peirce, S. and Lindsay J. 2015. Characterizing ephemeral streams in a Southern Ontario watershed using electrical resistance sensors. *Hydrological Processes*. Vol. 29(1): 103-111.